Advanced Modeling, Control, and Design of an Electromechanical Engine Valve Drive System with a Limited-Angle Actuator

by

Yihui Qiu

Submitted to the Department of Electrical Engineering and Computer Science

in partial fulfillment of the requirements for the degree of

Doctor of Philosophy

at the

MASSACHUSETTS INSTITUTE OF TECHNOLOGY

February 2009

Author……..….

Department of Electrical Engineering and Computer Science

January 9, 2009

Certified by……..….

John G. Kassakian

Professor, Electrical Engineering and Computer Science

Thesis Supervisor

Certified by……...….

Thomas A. Keim

Principal Research Engineer, Laboratory for Electromagnetic and Electronic Systems

Thesis Supervisor

Accepted by……..…….

Terry P. Orlando

Chairman, Department Committee on Graduate Students

Advanced Modeling, Control, and Design of an Electromechanical Engine Valve Drive System with a Limited-Angle Actuator

by

Yihui Qiu

Submitted to the Department of Electrical Engineering and Computer Science

on February 2009, in partial fulfillment of the

requirements for the degree of

Doctor of Philosophy

Abstract

This thesis addresses a specific variable valve actuation (VVA) system ---- an electromechanical valvetrain ---- in order to provide variable valve timing (VVT) in internal combustion (IC) engines. This electromechanical valve drive (EMV) system was proposed by Dr. Woo Sok Chang and his colleagues in the Laboratory for Electromagnetic and Electronic Systems (LEES), who also validated the feasibility of the design to provide VVT. The goal of this thesis is to bring the MIT EMV system to a more practical level by achieving a smaller package (to fit in the limited space over the engine head), a faster transition time (to accommodate faster engine speed), and a lower power consumption, while still offering satisfactory valve transitions with timing control. This thesis reports four major achievements.

First, a more accurate system model, including dynamics, loss flow and distributions, and nonlinear friction, has been established for better guidance in system control and design via numerical simulations.

Second, different control strategies and cam designs have been explored in order to determine the most appropriate control strategy and cam design to achieve a lower torque requirement, reduced power consumption and a faster transition time.

Third, a limited-angle actuator was custom designed and built for the valve actuation application in order to reduce the actuator size while maintaining the necessary torque and power output.

Fourth, with the limited-angle actuator in place, the EMV system was evaluated experimentally for intake valve actuation and numerically for exhaust valve actuation with gas force disturbance taken into consideration. Based on this system evaluation, we are able to project the system's applicability to a real 4-cylinder 16-valve engine with independent valve control for each intake and exhaust valve.

At the end of the thesis, the power consumption has been reduced from 140 W to 50 W (about 64%), the transition time has been reduced from 3.3 ms to 2.7 ms, and the final actuator volume has been reduced to 1/7 of that of the original motor. These significant improvements enabled the projection of independent valve actuation for a 4-cylinder 16-valve IC engine with reasonable power consumption and high engine speed.

Thesis Committee:

Prof. John G. Kassakian (co-supervisor)
Professor of Electrical Engineering and Computer Science

Dr. Thomas A. Keim (co-supervisor)
Principal Research Engineer of Laboratory for Electromagnetic and Electronic Systems

Prof. David J. Perreault (Thesis reader)
Associate Professor of Electrical Engineering and Computer Science

Prof. Wai K. Cheng (Thesis reader)
Professor of Mechanical Engineering

Acknowledgments

First of all, I would like to thank my committee members. I am extremely grateful to my co-supervisors Prof. John Kassakian and Dr. Thomas Keim for their constant guidance, patience, support, and understanding during these six and half years. I would not be at this position without their tremendous help. I owe great gratitude to Prof. David Perreault, who has constantly devoted his precious time, brilliant ideas, and strong support to my project. I deeply appreciate Prof. Wai Cheng's agreement to be my committee member and offer valuable opinions from an engine expert's point of view.

I also want to thank my former colleagues who worked on this project. Dr. Woo Sok Chang, Dr. Tushar Parlikar, Mr. Michael Seeman, Mr. Fergus Hurley, Mr. James Otten, and Mr. Ryan Slaughter, whose work has been very meaningful and helpful to my thesis research.

I also want to extend my sincere thanks to the whole LEES, including professors, staff, and students, who are always there when I need their help.

Prof. Zahn generously gave me the Maxwell® license so I could use Maxwell® in my research; Prof. Leeb has always been patient whenever I bugged him from time to time to borrow all kinds of instruments; Prof. Kirtley, my RQE committee member, helped me learn a lot about permanent magnets and motor design; Prof. Lang was very kind to help me to find an appropriate storage place of epoxy related product and also offered me a TA position when I had a funding problem; Prof. Schindall, another RQE committee member of mine, offered great ideas during our discussion on the project; and Prof. Verghese, also actively helped me to find a TA position so I could be supported financially.

And speaking of LEES staff, Wayne, Vivian, Dave (Otten), Gary, Dimonika, Makiko, Miwa, Kiyomi, Karen, thank you all for your tremendous support for my project and thank you for the wonderful times, too.

My fellow graduate students in LEES, Warit, Riccardo, Yehui, Jiankang, Bernard, Natalija, Kevin, Steve, Tony, Jackie, Robert, Al, and the list goes on and on, thank you all for being around, being supportive, being available when I needed some help, or needed somebody to share excitements or frustrations.

Special thanks goes to the EECS graduate office staffs, who have been taking care of all the trivial stuff so I can focus on my research and class work; Dr. James Bales from the MIT Edgerton Center, who generously lent me the high speed camera and patiently trained me on how to use it; GWG of MIT and GW6 of EECS which offered me a place where I could share my academic and personal experiences with my fellow women graduate students; Mr. William Beck of the MIT Plasma Science and Fusion Center, who offered excellent suggestions on armature fabrication and also gave me many samples of fiber glass sleeves for this purpose; Peter, Andrew, Mike, and other staff of the MIT machine shop, who helped me build and assemble the actuator; Mr. George Yundt and

Mr. Bill Fejes of Danaher Motion Corporation, who shared with us some great thoughts on motion control; The Ford Motor Company and the Eaton Corporation for their donation of a conventional valvetrain each; and The Industrial Technology Research Institute of Taiwan for their half-year financial support and technical cooperation.

This project was mainly funded by the Sheila and Emanuel Landsman Foundation and the Herbert R Stewart Memorial Fund.

And last but not the least, I owe my family the deepest gratitude. My parents and my brothers back in China, my husband, my mother-in-law and my two-year-old son here in Boston, all have been extremely supportive and understanding in their own way along this long journey of mine at MIT. I wouldn't be where I am without their backing me up with substantial and irreplaceable love.

This thesis would not be possible to finish without the help and support from all the people I mentioned above. Thank you all so very much.

Table of Contents

List of Illustrations

List of Tables

CHAPTER 1 INTRODUCTION

1.1 Introduction

Energy challenges and environmental pollutions are becoming more and more serious problems in today's world. Automobiles, which consume oil and output emissions, are an important contribution to these two critical problems. People have been actively seeking solutions to minimize oil consumption and exhaust emission of automobiles via different ways for decades. The research work can be roughly summarized in two directions. One direction is to give up partially or totally the current internal combustion (IC) engine, as in hybrid cars. The other direction is to stay with the internal combustion engine but try to optimize its performance under any load and speed condition via advanced control and design techniques. This thesis addresses a specific IC engine improvement ---- an electromechanical valvetrain.

As early as a few decades ago, people recognized that despite the simple design and low cost of conventional crankshaft-synchronized cam driven valve actuation, it can offer optimized engine performance at only one point on the engine torque-speed operating map. Commonly, valve lift profile and timing are chosen to give good performance of high load and high speed, in part because such a choice gives reasonable engine operation over much of the engine map. But at load conditions away from high speed and high load, other valve strategies, were they achievable, might offer reasonable engine performance with better fuel economy or lower emissions, or both.

In particular, research has shown that variable valve timing can achieve significant improvements including fuel efficiency, emissions, torque output, and other possible benefits. As a result, many new types of variable valve actuation have been proposed and studied. However, commercialization of those techniques has been difficult for many reasons, which will be discussed in more detail in Chapter 2. Based on the study of previous proposals for variable valve actuation, a novel electromechanical valve drive (EMV) system was proposed by a group of MIT researchers several years ago. As will

become evident shortly, the fundamental contribution of the MIT EMV system is the flexibility to separately control the starting timing of valve opening and closing events. We call this capability variable valve timing (VVT). This novel system also introduced a deliberately non-linear element called a nonlinear mechanical transformer (NMT) in order to achieve inherent soft landing and zero power consumption between valve transitions. Feasibility of the concept has been validated by previous work [18]. Further enhancement of the system performance in several practical aspects via advanced modeling, control, and design will be the main focus of this thesis.

1.2 Thesis Goals

The objective of this research is to bring the proposed MIT EMV system to a more practical level by achieving a smaller package (to fit in the limited space over the engine head), a faster transition time (to accommodate faster engine speed), and a lower power consumption, while still offering satisfactory valve transitions with timing control.

The objective is described in more detail below:

1. To establish a more accurate nonlinear system model of the EMV system to help with more effective system dynamic analysis;

2. To model and simulate the EMV system, including the mechanical structure and electrical components, by using a simulation software package (20-sim®) as a platform for better control and design decisions;

3. To evaluate different control strategies by simulations and experiments in order to decrease torque requirement and power consumption of the actuator;

4. To study the possibility of obtaining an optimal design of the nonlinear mechanical transformer, which will offer a lower torque and power requirement and a faster transition;

5. To propose a novel actuator design customized for the application --- a limited-angle actuator --- which is able to provide satisfactory VVT function and is small enough to fit into the limited space on an engine head;

6. To design a limited-angle actuator using 3-dimensional design software SolidWorks® before building and assembling the actuator;

7. To evaluate the EMV system with the custom designed actuator by simulations and by experiments and confirm the benefits of the proposed system with experimental results;

8. To introduce gas force into the simulation for the case of an exhaust valve and confirm with simulation results the feasibility of the EMV system with the limited-angle actuator in this case;

9. To predict a full picture of variable valve actuation (VVA) for both intake and exhaust valve of a real engine before offering some insights on possible future work.

1.3 Thesis Organization

This thesis is organized as follows:

In Chapter 2, the background and motivation of this project is presented. The starting point of this thesis, i.e., the proposed EMV system and the preliminary experimental results, will be reviewed in Chapter 3. Chapter 4 will discuss the dynamic model, loss structure, and nonlinear friction model of the system developed here. The evolution of the simulation structure of the EMV system will also be described. With the help of the more advanced system modeling, different control strategies are described and improved experimental results are obtained in Chapter 5. Also, relying on numerical simulations

based on the effective system modeling, Chapter 6 targets an optimal design of the NMT and confirms the expected advancement of system performance through experiments. A novel actuator design customized for the application, a limited-angle actuator, is proposed and analyzed in Chapter 7, while the practical design and fabrication of the actuator are discussed in Chapter 8. Chapter 9 presents experimental evaluation of the EMV system with the new limited-angle actuator, and projects performance of full VVA of a 4-cylinder 16-valve engine based on both experimental and simulation results. Finally, Chapter 10 concludes the thesis and offers some perspectives on possible future work.

CHAPTER 2 BACKGROUND AND MOTIVATION

2.1 Introduction

This Chapter provides more detailed background on VVT and VVA. Several different approaches to realize VVA will be reviewed and compared. Emphasis is placed on electromechanical valve drive systems, including the Pischinger EMV system [9] and the MIT EMV system [17]. The motivation behind this project will be obvious at the end of this chapter.

2.2 VVT

After many decades of continuous development, researchers are still trying to get even better engine performance out of IC engines. Higher fuel efficiency and lower exhaust emissions have always been on the top of the most important goals and are becoming more urgent and critical objectives lately due to the increase of automobile usage, the rapid consumption of the limited oil source, and the increasingly severe pollution of the atmosphere. VVT is one of the most promising emerging technologies in support of the evolution towards better engine performance [1]-[3]. To some extent, electromechanical variable valve actuation can be seen as the ultimate solution to achieving infinite adjustability of valve timing, as will be discussed in this and the following sections [4].

In conventional IC engines, the valves are actuated by cams that are located on a belt- or chain-driven camshaft. As a long developed valve drive, the system has a simple structure, low cost, and offers smooth valve motion. However, the valve timing of the traditional valvetrain is fixed with respect to the crankshaft angle because the position profile of the valve is determined purely by the shape of the cam. Meanwhile, the valve timing desired at different load conditions and speeds could be very different in order to increase torque/power output, minimize fuel consumption, and reduce exhaust emissions. In other words, a cam that idles well with clean emissions typically can't generate much power at high speed, while another high-power cam design will have more emissions at

idle and be balky at low speed. As a result of the inherent compromises in cam design, the optimal engine performance with one cam design is only possible at certain operating conditions (traditionally at high speed, wide-open throttle and full load conditions) [1]. If instead, the valve timing can be decoupled from the crankshaft angle and can be adjusted adaptively for different situations, then the engine performance can be optimized with respect to higher torque/power output, increased gas mileage, and reduced emissions, at any point of the engine map. This flexibly controlled valve timing is called variable valve timing and the corresponding valve drive system is called variable valve actuation. From the research of engine scientists, the main benefits from variable valve timing can be summarized in specific numbers: a fuel economy improvement of approximately 5~20%, a torque improvement of 5~13%, an emission reduction of 5 ~10% in HC, and 40~60% in NO_x [1]-[7]. Other possible gains include enabling a smaller starter/battery, a combined starter/alternator and the replacement or elimination of many mechanical components.

2.3 VVA

To achieve VVT, substantial research on different kinds of engine valve actuation has been done. There are three main categories: pure mechanical [6], [8], [12], electro-hydraulic [1], and electromechanical valve drives [4], [9]-[16].

The various mechanical actuators are mainly improved designs based on the current valvetrain. One basic type is to switch between two completely different cam profiles [6]. Another popular drive changes valve timing by advancing and retarding one set of cams, while the valve duration stays the same [8]. Both concepts are simple and widely accepted as effective valve drives. But the control flexibility is still very limited and discrete, compared to the ultimate goal of continuously adjusted valve timing of both phase and duration, plus individual control of each valve in order to achieve single valve/cylinder deactivation/activation and engine idle at low speeds.

The electro-hydraulic device, on the other hand, offers much more flexibility in terms of VVT control. But the use of a hydraulic system makes it expensive and cumbersome, compromising its practicality for automobile manufacture.

The concept of electromechanical actuation has become more feasible and attractive recently owing to its simple structure, continuous VVT control, and independent action for each valve and each cylinder. Although there are several different approaches to electrify the original mechanical valve drive, the bi-positional electromechanical valve drive (BPVD, also referred to as the Pischinger EMV system) has become a popular research topic and has gotten closest to real engine application [9]-[16]. As shown in Fig. 2.1, the Pischinger EMV system, proposed by Pischinger et. al. [9], consists of two normal force actuators and a spring-valve system.

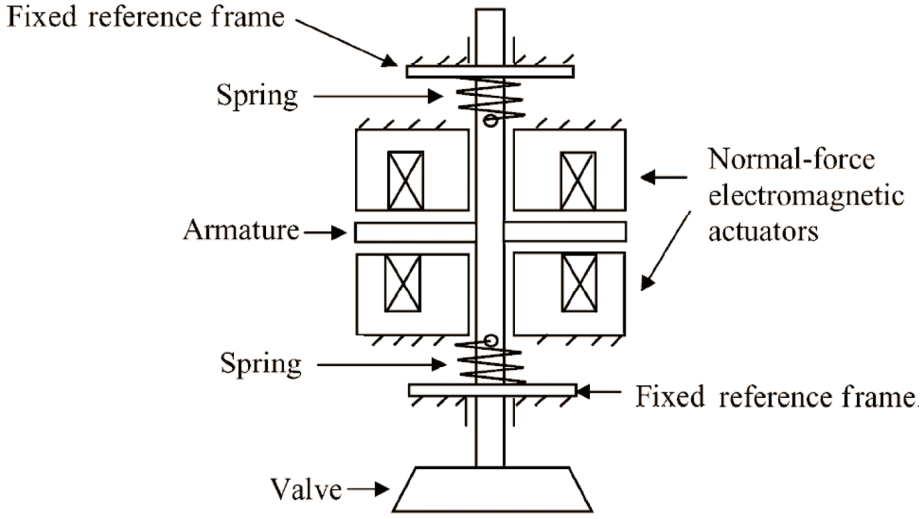

Fig. 2.1. The Pischinger EMV system [20].

The springs are introduced into the system in order to provide the large force needed for valve acceleration and deceleration during each transition. The force requirements of the actuator are thereby substantially reduced. The normal force actuator can only exert an attracting force to the armature. It cannot repel the armature. The force constant of the normal force actuator is proportional to the inverse of the square of the air gap between the active actuator and the armature connected to the valve stem. In other words, the

force constant is small at the beginning of the transition but is very large when reaching the end of the transition. The good side of these features is that only a very small current will be needed to hold the valve at either the closed or open position due to the large force constant at the end of each transition. However, the down side of the large and unidirectional force constant turns out to be the difficulty of achieving soft landing when the valve is approaching the valve seat. Soft landing, i.e., low valve seating velocity, at the end of each transition, is very critical in terms of acoustic noise and lifespan of the valves. This situation could be more severe in the presence of a high gas force, as will occur with an exhaust valve. In recent literature, soft landing has been achieved by a complicated nonlinear control scheme under certain circumstances [14][15]. However, the impact of gas force disturbance has yet been taken into consideration.

As discussed above, the main cause of the landing problem in the Pischinger EMV system is that the normal force actuators are unidirectional actuators with a nonuniform and nonlinear force constant versus valve position. To solve this problem, Dr. Woo Sok Chang and his colleagues proposed a new type of electromechanical valve drive [17], referred to hereafter as the MIT EMV system. This MIT EMV system inherits the valve-spring system and its regenerative benefits from the Pischinger EMV system, while using a bi-directional shear force actuator with a uniform torque constant. As shown in Fig. 2.2, the motor shaft is connected to the valve system via a nonlinear mechanical transformer (NMT). Inherent soft landing is guaranteed by a special design of the NMT, as will be discussed in Chapter 3. The experimental results of the first prototype proved the feasibility of the system up to 6000 rpm engine speed, as also will be reviewed in Chapter 3.

2.4 Motivation of Further Research

Although Dr. Chang and his colleagues have shown some exciting results, there still are several challenges that need to be addressed in order to put the proposed system into a real engine.

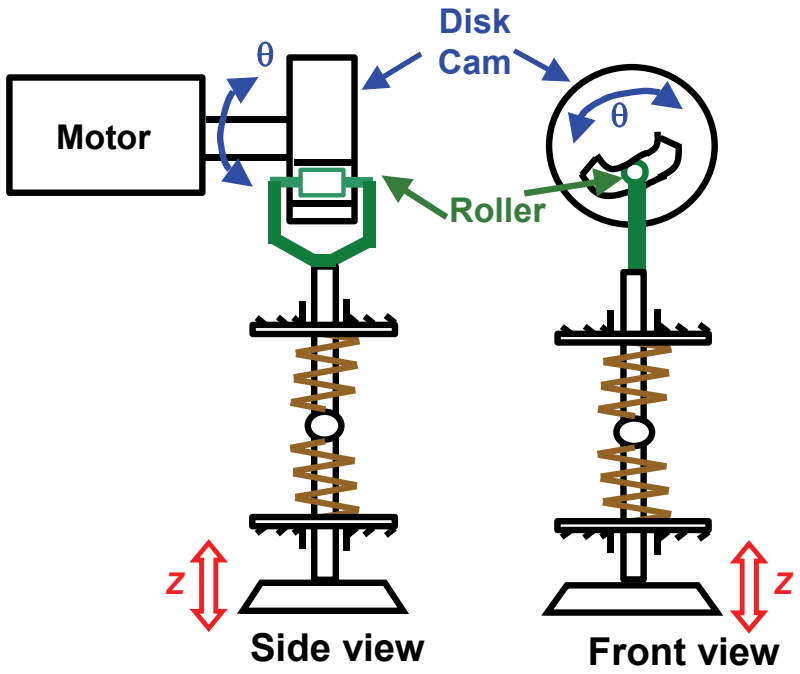

Fig. 2.2. The MIT EMV system [19].

One of the most important challenges is size: the motor used in the first prototype was far too big compared to the limited space over the engine head, considering that there are 16 valves on a modern four cylinder engine and independent control over each valve is preferred. Another challenge is to lower the electrical power consumption of the system. A third issue regards the transition time. It is very desirable to achieve a faster transition time since modern IC engines are pursuing higher and higher engine speed where 6000 rpm is not high enough anymore. Last but not least, the gas force has not been taken into consideration yet. This needs to be addressed especially for the case of an exhaust valve.

CHAPTER 3 THE PROPOSED EMV SYSTEM

3.1 Introduction

This chapter reviews the MIT EMV system originally proposed by Dr. Woo Sok Chang et. al. [17], starting by explaining the basic concept and discussing the prominent features of the system mainly owing to the nonlinear mechanical transformer (NMT). Then the preliminary control scheme, the initial design of the nonlinear mechanical transformer, and the first prototype are described. Finally, the preliminary experimental results are studied, which not only prove the feasibility of the idea, but also offer valuable insights on directions for future research. All of the analytical and experimental work of the proposed EMV system reported in sections 3.2 to 3.4, and essentially all of the interpretation thereof, are the work of Dr. Woo Sok Chang and his colleagues Tushar Parlikar and Michael Seeman [17]-[21]. The author of this thesis joined the MIT EMV research group at August 2002 just in time to observe and then conduct the preliminary experiments and process experimental data afterwards. Section 3.5 summarizes the author's observations and thoughts on how to improve the EMV system performance for the purpose of this thesis.

3.2 Basic Concept of the MIT EMV System

In order to solve the problems associated with the previously discussed VVT systems, a new EMV system was proposed by Dr. Woo Sok Chang and his colleagues, who were members of MIT's Laboratory for Electromagnetic and Electronic Systems (LEES) [17]-[18]. This EMV system comprises an electric motor that is coupled to a resonant valve spring system via a NMT. As already shown in Fig. 2.2. The NMT is implemented by a slotted cam connected to a motor shaft and roller follower which in turn is connected to the valve stem via a valve holder. It is straightforward to see how this device works based on Fig. 2.2. When the motor swings back and forth within the angle range limited by the cam slot design, the roller follower moves back and forth within the slotted cam, allowing

the valve to move up and down between fully open and fully closed positions. Note that the angular range of motor rotation, i.e., the angular range of the cam slot, is a design parameter of this system, while the full stroke of the valve usually will be determined by engine design.

In the proposed EMV system, the shear force motor acts as a uniform–force–constant and bi-directional actuator, through which the valve timing is controlled and the friction force and gas force during transitions are overcome. Compared to the Pischinger EMV system [9], which uses two normal force actuators, this design allows valve transition in two opposite directions via one control channel.

For the same reason described when discussing the Pischinger EMV system, a pair of springs is introduced into this system to offer the large force needed to accelerate and decelerate the valve mass and rotor inertia during each transition. In other words, the springs store and regenerate the kinetic energy (transferring between potential energy in the springs and kinetic energy in the valve) as the valve moves between the two ends of the stroke, which will sharply reduce the power and torque requirements of the motor. The two springs are identical, so the equilibrium point of the springs is designed to be the middle position of a full stroke, i.e., half-open position.

The mechanical transformer is responsible for transferring the rotation of the rotor into the translation of the valve in a desired way. In particular, we desire to achieve small seating velocity of the valve at the end of each transition, zero holding power/torque when the valve needs to stay at fully open or closed positions, and reduced peak torque and hence rms torque requirements of the motor. In order to accomplish these goals, a NMT with a $z-\theta$ characteristic like that is shown in Fig. 3.1, is designed and will be discussed in the next section.

3.3 Prominent Features Due to the NMT

This section will describe the merits of using a NMT, in terms of at least four aspects. More details on the idea of MIT EMV system with a shear force actuator, a spring valve assembly, and a NMT can be found in Dr. Woo Sok Chang's PhD thesis [17] and other publications on the MIT EMV system [18]-[20].

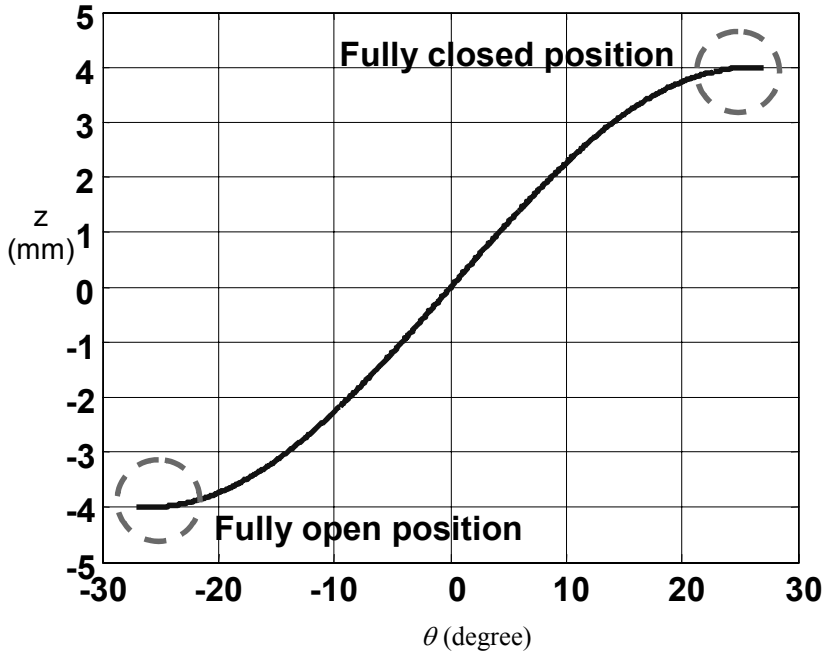

Fig. 3.1. A desirable transfer characteristic for the NMT.

For the valve-spring system, the spring forces are the largest at the ends of the stroke because the spring forces increase linearly with valve displacement from the middle of the stroke. If the relationship between valve motion and motor shaft motion were linear, these large spring forces would make it difficult to hold the valve in the open or closed position without using a large motor torque, and thus substantial electrical power. The same issue will arise when we try to open the exhaust valve, where, under some engine conditions, the large gas force will be at its peak at the beginning of the transition. With a linear mechanical transformer, a much larger starting torque, and hence a much larger peak/rms torque of the motor are required to complete the transition. The high torque and power requirements will result in the need for large-size motor as well as reduced fuel

efficiency of the engine. In addition, precise control of the valve seating velocity would require precise control of the motor velocity, which would impose exacting standards on control. A cam profile such as that in Fig. 3.1 allows all these problems to be solved, as we will show below.

Let us define the displacement of the rotor as θ and that of the valve as z, then obviously θ is a function of z and vice-versa. Assume that the NMT implies the following relation between θ and z,

$$z = g(\theta) \tag{3.1}$$

$$\frac{dz}{dt} = \frac{dg}{d\theta} \cdot \frac{d\theta}{dt} \tag{3.2}$$

$$\frac{\mathrm{d}^2 z}{\mathrm{d}t^2} = \frac{\mathrm{d}^2 g}{\mathrm{d}\theta^2}\left(\frac{\mathrm{d}\theta}{\mathrm{d}t}\right)^2 + \frac{\mathrm{d}g}{\mathrm{d}\theta}\frac{\mathrm{d}^2\theta}{\mathrm{d}t^2} \tag{3.3}$$

Assume the nonlinear mechanical transformer provides an ideal coupling between the z-domain and the θ-domain, that is to say, there is no power loss or energy storage inside the coupling. Therefore we can equate the power in the z and θ domains as shown in (3.4) and obtain the following relations as shown in (3.5) by using the NMT characteristic as shown in (3.2):

$$\tau_\theta \cdot \frac{d\theta}{dt} = F_z \cdot \frac{dz}{dt} \tag{3.4}$$

$$\tau_\theta = \frac{dg}{d\theta} F_z \tag{3.5}$$

where τ_θ is the torque in the θ-domain and F_z is the force in the z-domain.

There are essential benefits obtained by using this nonlinear mechanical transformer. At either end of the stroke, the slope of the cam characteristic $\frac{dg}{d\theta}$ is designed to be very close to zero, as shown in Fig. 3.1. Thus, the reflected motor inertia in the z-domain is very large, creating inherently smooth valve kinematics profiles since the valve is slowed down by the large effective inertia near the ends of the stroke. This characteristic makes

it easier to control the motor velocity near the ends of the stroke in the sense that possible high rotation speed and hence overshoot in the θ-domain will not prevent small seating velocity of the valve at the end of each transition. Also, overshoot of the rotor is allowed by extending the flat slope area in the θ-domain. Moreover, the large spring forces at the ends of the stroke in the z-domain are transformed into small torques in the θ-domain, also due to the flat end of the transformer. Therefore static friction is enough to hold the valve at open or closed positions without any power or torque input from the motor. This is a big energy saver for the engine, especially at lower speed conditions where the valve spends much more time at closed or open positions than in a transition. In addition, because the gas force on the exhaust valve is largest at the beginning of the opening transition, the reflected gas force obtained in the θ-domain is also small, making it easier to open the exhaust valve against a large gas force. Compared to the linear case, the peak torque is both reduced in magnitude and delayed until later in the transition.

In summary, the nonlinear design of the transformer which has flat ends will ensure an inherent soft landing, allow some overshoot of the motor, realize zero torque/power valve holding, and reduce peak torque and hence the rms torque requirements of the motor.

3.4 Preliminary Experimental Results

In this section we will present the first prototype setup and the control scheme used to obtain the first satisfactory transition. Then the experimental results of that transition are discussed [17]-[20].

3.4.1 First Prototype Setup

In order to prove the concept of the proposed EMV system, an experimental apparatus was designed, constructed, and integrated into a computer-controlled experimental test stand, which is hereafter referred as our first prototype.

The test stand consists of a computer-controlled digital signal processor (DSP) board (the DS1104 from dSPACE, Novi, MI), a motor drive, a shear-force motor with an optical

shaft angle encoder, a valve-spring assembly, and a disk cam and roller follower to implement the NMT. The dSPACE control board is used to receive the shaft angle feedback signal, to process the signal to implement the controller transfer function, and also to generate the output current/torque command. It is supported by software that allows us to construct the input and output terminals and controller in a MATLAB® SIMULINK® file before compiling and to conveniently implement the whole structure on the DSP board. The motor drive is used to receive a current/torque command and inject the desired amount of current into the motor, which then will initiate and complete a valve transition with the help of the springs. An oscilloscope is used to record position, current, and voltage information. These data can be acquired to a .txt file by Labview® for later computational analysis. The whole setup is shown in Fig. 3.2 [20] as below. More details on the setup design can be found in Dr. Tushar Parlikar's Master's degree thesis [18].

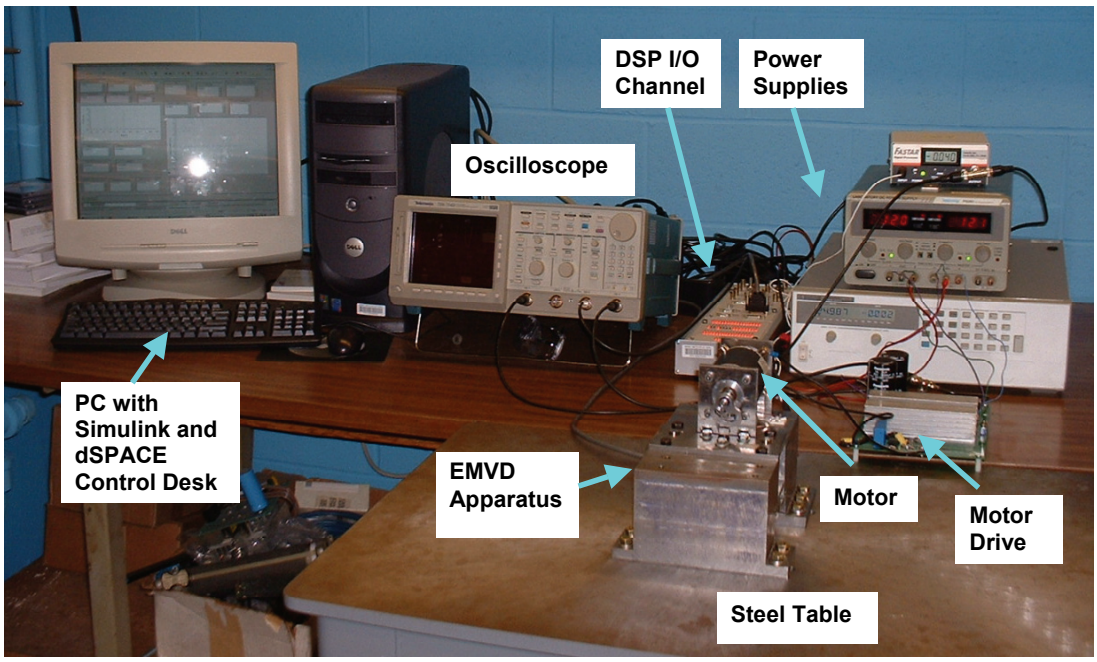

Fig. 3.2. The whole EMV system [20].

An off-the-shelf permanent magnet dc motor (the 4N63-100 from Pacific Scientific, Rockford, IL), as shown in Fig. 3.2, was picked for our preliminary evaluation because it has a very high torque-to-rotor inertia ratio while meeting other requirements such as

power consumption, appropriate speed rating, good electrical and mechanical time constants, and so on. However, this motor is large in size --- too large to fit into the limited space over the engine head. Therefore even though this motor proves the concept of the MIT EMV system, a much smaller motor will be required to practically implement the proposed EMV system, which is one main target of this thesis.

To achieve the intended control system bandwidth, a high-bandwidth motor drive circuit realizing hysteretic current control has been developed; details of this design can be found in [21].

To meet the transition time requirement of no less than 3.5 ms for 6000 rpm engine speed, a pair of die springs having the appropriate stiffness (56 kN/m) were selected based on the known valve mass, rotor inertia, and disk cam inertia [17]. A pair of these springs was used together with a standard exhaust engine valve from a 16 valve, 2.0 L Ford Zetec® cylinder head to form a valve-spring assembly, as shown in Fig. 3.3.

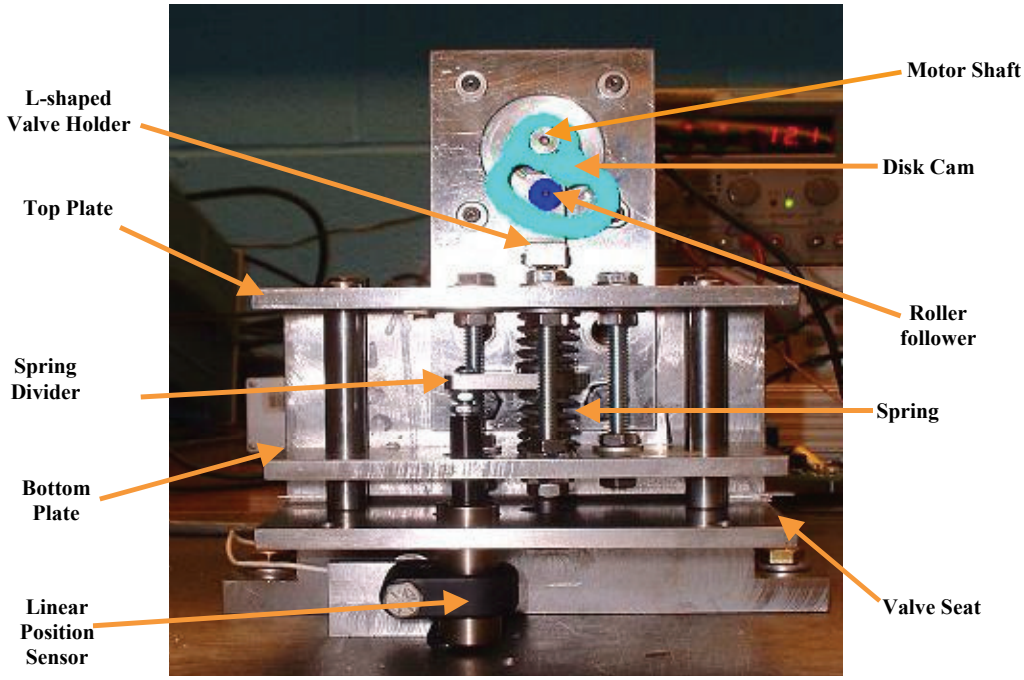

Fig. 3.3. Front view of the system including motor and spring assembly [20].

A differential optical encoder with an 8192-line resolution (E6D from US Digital, Vancouver, WA) was selected for rotary position sensing.

The disk cam is one of the most important parts in this EMV system due to its nonlinear characteristics as discussed in the previous section. To realize the zero-slope design at both ends of the stroke, a sinusoidal function with an effective rotation range of ± 26 degrees was initially chosen to fulfill the desired NMT characteristics. A few extra degrees are added at both ends to extend the flat end to allow overshoot of the rotor without affecting the finishing positions of the valve. The designed NMT part is shown in Fig. 3.4. The desired NMT characteristics within the effective angular range and the extended flat range are given by (3.6) and (3.7) respectively,

$$z = f(\theta) = 4\sin(3.46\theta) \text{ mm} \quad |\theta| \le 26°, or, 0.454 \text{ rad} \tag{3.6}$$

$$z = f(\theta) = 4 \cdot sign(\theta) \text{ mm} \quad |\theta| \ge 26°, or, 0.454 \text{ rad} \tag{3.7}$$

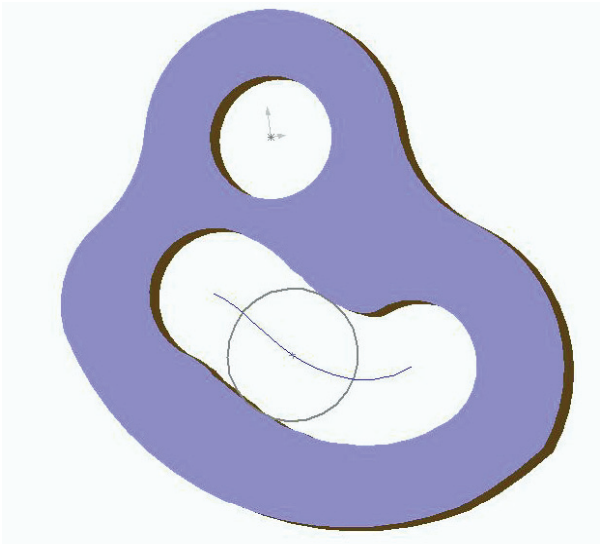

Fig. 3.4. The nonlinear mechanical transformer [17].

3.4.2 Operation Modes and Control Schemes

The operation of the EMV system can be separated into three modes: initial, transition and holding. In the initial mode, the valve is moved from its resting position (the middle

of the stroke) to one end of the stroke (closed or open). Friction will keep a resting valve firmly at the open or closed end of a stroke, even in the absence of an electromagnetic holding torque. It may be possible to manage engine shutdown in such a way that all the valves are parked either closed or open, as is more appropriate for the subsequent engine-starting event. If this is possible, the initial mode may not be used often, if ever.

The valve is moved from one end of the stroke to the other end during the transition mode within a limited time and with a small seating velocity. Both initial mode and transition mode are followed by the holding mode during which the valve is held at the arrival end with a variable holding time. The three modes are illustrated in Fig. 3.5 [17]. Two different control schemes were designed for these three modes: one was designed to realize both transition and holding mode by shaping the reference input appropriately, while the other was designed to carry out initial mode control.

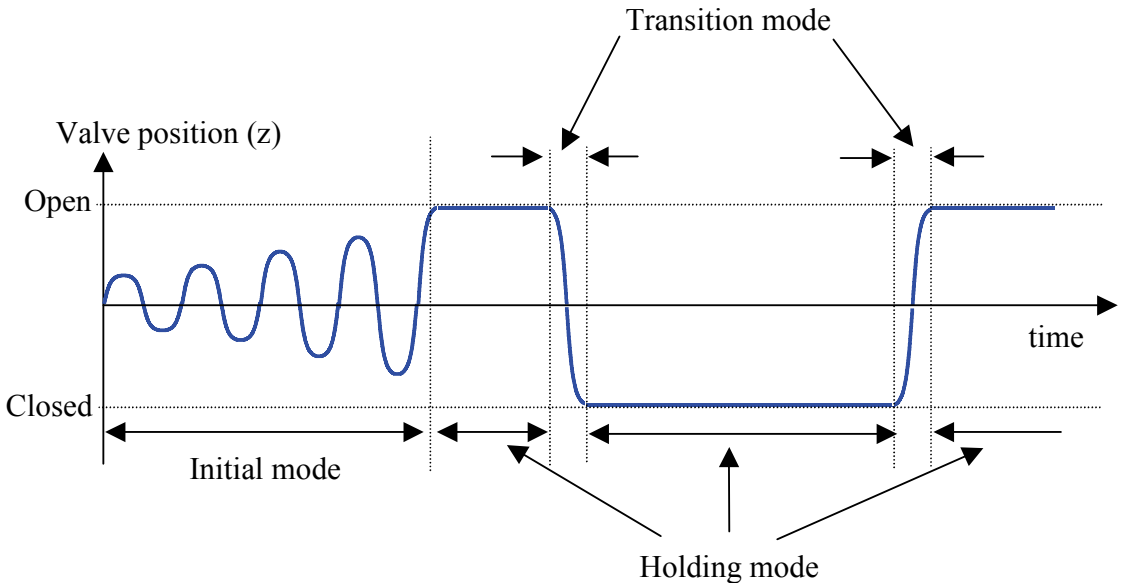

Fig. 3.5. Three operation modes of engine valve motion [17].

- **Transition Mode Control**

During the transition mode, the valve is driven between the fully closed and fully open positions. Thus a position feedback control strategy was chosen when we were trying to evaluate the system via simulations and experiments. Because the motor is the control

unit in the system and the valve position is rigidly related to the rotor position via the NMT, the rotor position θ was chosen to be the feedback variable and control target. Currently, an optical encoder is used to detect the rotor position. A block diagram of the closed-looped EMV system is shown in Fig. 3.6. The EMV plant is comprised of the motor drive, motor, NMT, and the valve-spring system. The reference position input is a position trajectory, which includes the desired starting and finishing motor positions, corresponding to the valve starting and finishing positions respectively. The reference trajectory, a half cycle of a sinusoidal signal for simplicity here, is chosen with proper frequency in order to achieve the desired transition time. The system output is actual motor position detected by the position sensor. The difference between the actual motor position and the reference position is passed into a controller, which provides a current control input to the motor drive. The motor drive then supplies the desired current to the motor.

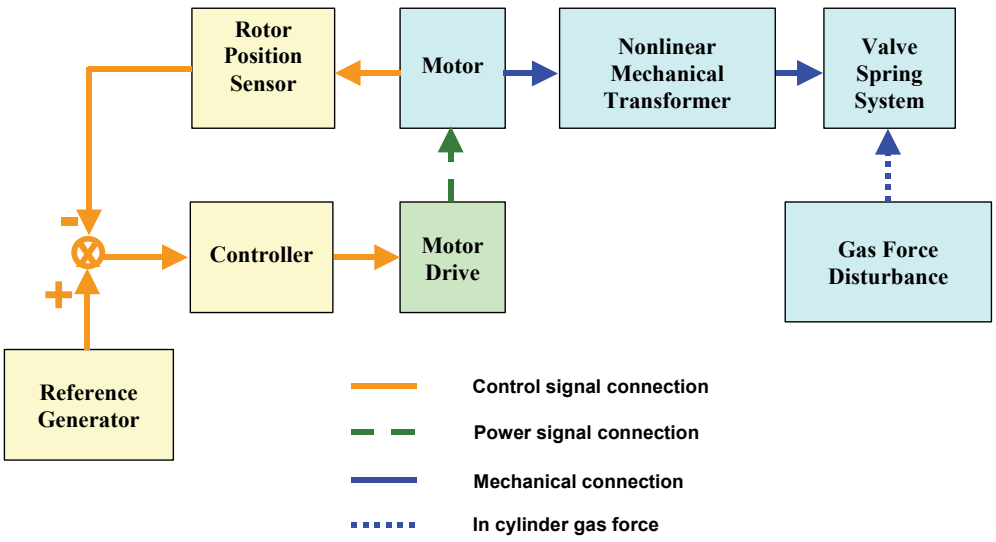

Fig. 3.6. Block diagram of the closed-looped EMV system.

In practice, a fixed-gain lead compensator was used for our first try to obtain a successful transition measured by transition time and seating velocity, as will be presented in section 3.4.3. The transfer function of the lead compensator is given by (3.8) [17],

$$G(S) = K\frac{1+S/Z}{1+S/P} \tag{3.8}$$

where K is the controller gain, Z is the zero location of the lead compensator, and P is the pole location of the compensator. The selection of the three constants is discussed in more detail in [17] and [18].

The objective of the holding mode is to hold the valve at either end of the stroke for a controllable time. This control of holding mode was combined into transition mode control by shaping the reference input to stay constant when it reaches the maximum position in either direction, using the same control law as for the transition mode. After the motor has been observed to be motionless at the end positions, zero current control is implemented. The presence of flats at the ends or of near-flat conditions near the ends is enough to overcome the spring force attempting to initiate a transition. It would be relatively simple to introduce small detents for "parking" if necessary, but that is not treated here.

- **Initial Mode Control**

As discussed above, the initial mode control may be valuable if we want to move the valve from its equilibrium position to either end position before engine start-up after a failed valve transition. To avoid requiring the motor to overcome the full static force of the springs, we drive the system at its resonant frequency by applying a series of current/torque pulses to the EMV system until the valve reaches the desired end position. During this process, the sign of the current/torque pulses will be flipped when the motor/valve velocity changes its sign. When the valve is close enough to the desired end position, the system switches to transition mode control to assure a soft valve landing.

The control law of the initial mode is given by (3.9) [17]:

$$i = \alpha \cdot \omega / |\omega| \tag{3.9}$$

where i is the current command sent to the motor and motor drive, ω is the nonzero angular velocity of the motor and α is a pre-determined constant. In a discrete implementation, i keeps its previous value whenever $\omega = 0$.

3.4.3 Preliminary Experimental Results

As discussed in section 3.4.1, a single-valve experimental apparatus was designed and constructed in order to validate that the proposed EMV system is technically feasible for up to 6000 rpm engine speed. A simple closed-loop control is used, as shown in section 3.4.2, where the displacement in the θ-domain is the control target. Based on previous hardware and software implementation, we now present and discuss some preliminary experimental results [17]-[20].

- **Initial Mode Behavior**

As shown in Fig. 3.7, the initial mode is completed within 35 ms with 8 A current pulses, which is sufficiently fast for practical applications. The average power during the initial mode period is approximately 150 W [17], which is acceptable since this is a one-time operation.

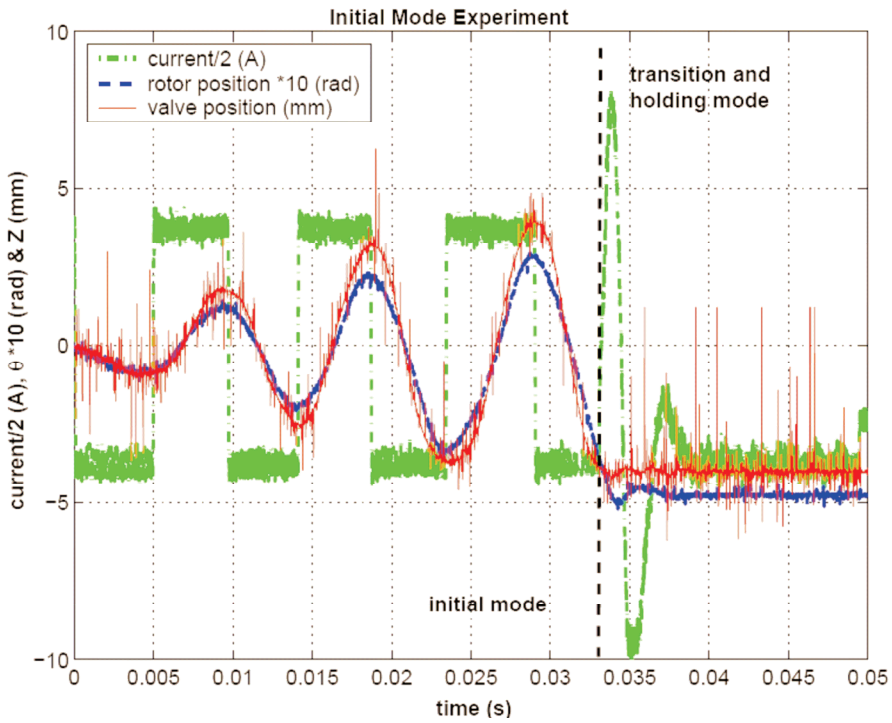

Fig. 3.7. Experimental results for the initial mode [19].

When the valve was sufficiently close to the desired end, the initial mode control was switched to the transition/holding mode control to ensure a soft valve landing. After reaching the stroke end, the valve was retained in the holding mode. A non-zero holding current was due to the nonzero static position error, as shown in Fig. 3.7. However, in the laboratory, we observed that after turning off the motor drive, the valve was still held at the end owing to static friction, demonstrating the expected zero holding current/power feature of the proposed EMV system.

- **Transition Mode and Holding Mode Behavior**

In preliminary experiments, for simplicity a 180° section of a sinusoidal function (from negative peak to positive peak or vice versa) was used as the position reference. The peak-to-peak value is the whole rotation range, while the frequency is designed to meet the requirement of the transition time. The position and current profiles from experiment are shown in Figs. 3.8 and 3.9 [19].

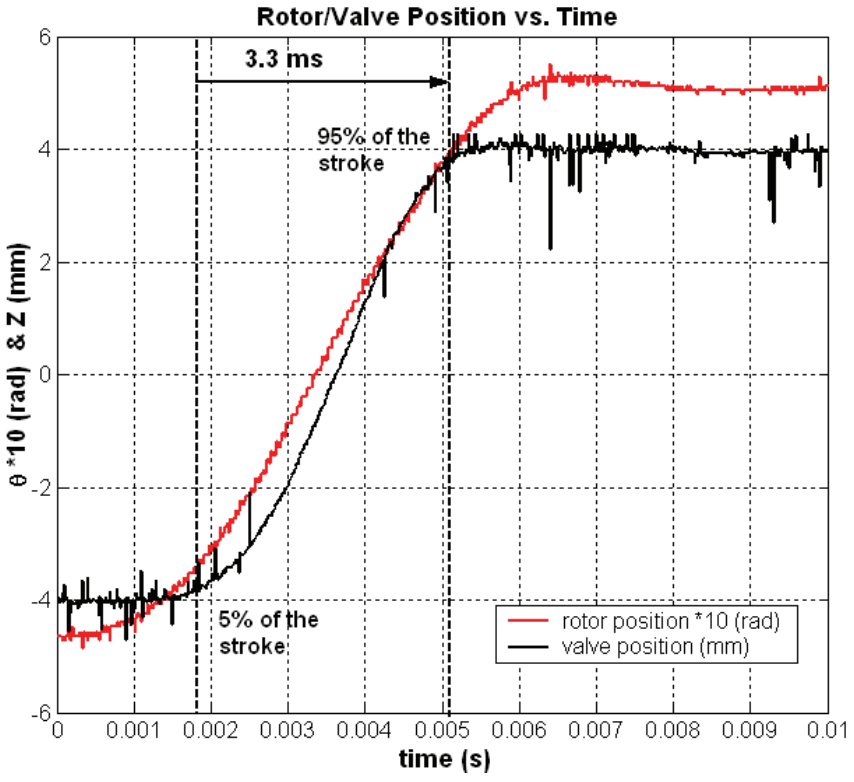

Fig. 3.8. Rotor and valve position profiles during transition mode.

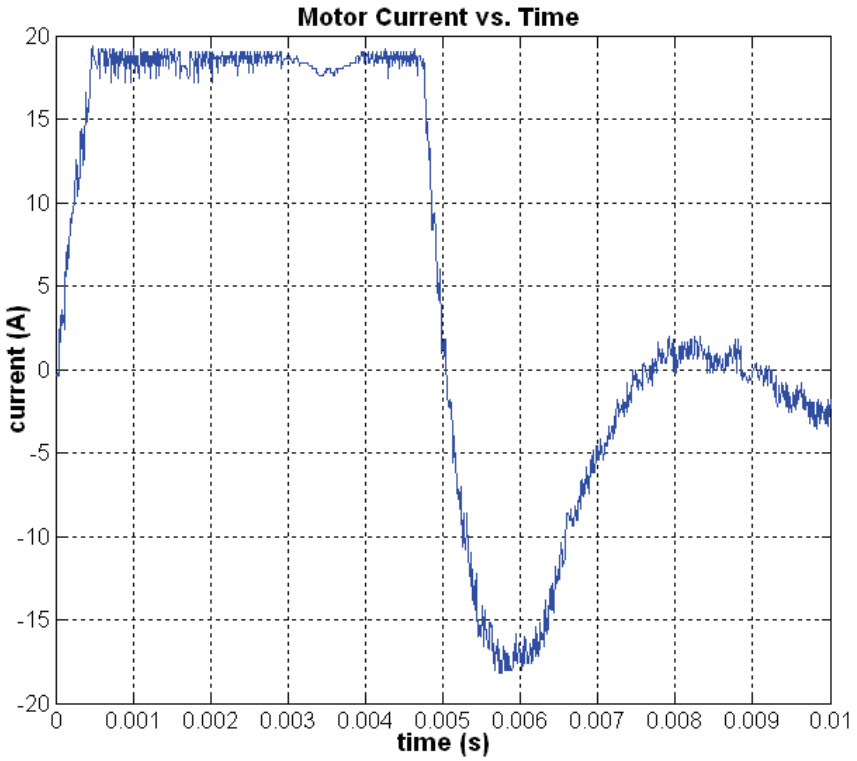

Fig. 3.9. Current profile during transition mode.

In the experiment, the motor drive current is limited to ±18 A due to thermal constraints on the motor. The most important performance parameters in an engine valve drive are transition time, valve seating velocity, and power consumption, as shown in Table 3.1. The transition time, defined as the period during which the valve moves from 5% to 95% of the full stroke (8 mm), was approximately 3.3 ms, which is fast enough for the target 6000 rpm engine speed. The valve seating velocity was measured by a high-speed camera with a mean of 21.3 cm/s [17][18]. This is less than the seating velocity of 30 cm/s at 6000 rpm in a conventional valve drive, and therefore we have achieved soft landing under such circumstances. From the experimental data, an average power per valve per half cycle at 6000 rpm was estimated as of 140 W [17]. The peak torque shown in Table 3.1 is not necessarily important for engine performance, but is very crucial as a metric for the size of the motor. For this reason, it is included in the table for future study.

TABLE 3.1. PRELIMINARY EXPERIMENTAL RESULTS.

Power Consumption	Peak Torque	Transition Time	Mean Seating Velocity
140 (W)	1.33 (N-m)	3.3 (ms)	21.3 (cm/s)

3.5 Challenges and Solutions

The experiments confirmed that the system offers consistent VVT with an expected soft landing up to an engine speed of 6000 rpm. However, in order to supply the large power and high torque shown in Table 3.1, a motor of large size was necessary in our prototype, which by no means can be fit into a regular engine. We also want to minimize power consumption to be more competitive with other valve actuators and to improve fuel efficiency. In addition, it is also very desirable to achieve a faster transition time since more and more modern engines are targeting engine speeds higher than 6000 rpm. And last but not least, the gas force has not been taken into consideration yet, and needs to be addressed, especially for the case of the exhaust valve.

In order to meet the challenges mentioned above, a two-step solution is offered.
Step 1: Minimize the power and torque requirement to achieve a satisfactory and faster transition based on a more advanced system model, an improved control strategy, and an optimal NMT design;

Step 2: Obtain a reasonable sized system package based on customized design of a limited-angle actuator.

The feasibility of Step 1 is supported by observation of the experimental results and several simplifications in the preliminary modeling, control, and design choices of the first prototype. First of all, from the current profile of the transition mode, we can observe that the motor drives the system very hard during the first half of the transition and then brakes equally hard during the second half, which suggests a lot of wasted energy in the motor winding. Secondly, the sinusoidal functions used for both position reference and NMT design were selected just for simplicity, and have yet to be proven to be optimal in

terms of power consumption and torque requirement. Thirdly, the friction in the system was assumed to be linear viscous friction with a constant coefficient, which is not necessarily true given the nonlinearity of the NMT, and leads to suboptimal control performance. These simplifications, as well as the experimental results, suggest a huge potential to decrease the power and torque requirements, as will be confirmed in Chapters 4, 5, and 6.

Custom-designing a limited-angle actuator is possible due to the system feature that the motor only swings back and forth within a limited angle range instead of rotating continuously as in a conventional motor. This will allow us to design a novel iron and armature structure specific to the application. The detailed design, fabrication, and validation of the limited-angle actuator will be discussed in Chapters 7, 8 and 9.

CHAPTER 4 NONLINEAR SYSTEM MODELING

4.1 Introduction

The goal of this chapter is to provide a more advanced system model which can predict system behavior fairly accurately via numerical simulation and hence can be relied on to guide us during further system control and design decisions.

The dynamic system model as developed in [17]-[20] will be presented before a thorough discussion of power distribution and loss structure of the system is offered. More importantly, a nonlinear friction model will be proposed. With this particular model, the simulation results match experimental results very well.

4.2 Dynamic System Model

From what we have discussed in Chapter 3, the dynamic system model can be represented by equations of motion as follows:

$$F_z = m_z \frac{d^2 z}{dt^2} + f_z + K_z \cdot z + f_{gas} \tag{4.1}$$

$$K_T \cdot I = J_\theta \frac{d^2 \theta}{dt^2} + f_\theta + \tau_\theta \tag{4.2}$$

where τ_θ is the transformer torque in the θ-domain, F_z is the transformer force in the z-domain, J_θ is the total inertia in the θ-domain, m_z is the total mass in the z-domain, $f_\theta = f_\theta(\theta)$ is the friction in the θ-domain, $f_z = f_z(z)$ and $f_{gas} = f_{gas}(z)$ are the friction force and gas force respectively in the z-domain, K_T is the motor torque constant, K_z is the effective spring constant from the two springs, I is the motor current, θ is the displacement in the rotational domain, and z is the displacement in the vertical domain.

(4.1) and (4.2) can be combined by using the NTF characteristic relations shown in (3.1)-(3.3). In this manner, we can obtain a single equation of motion in either the z or θ domains. Because we will use rotor position as our control target as discussed previously, the single equation of motion in the θ-domain is shown in (4.3),

$$K_T \cdot I = (J_\theta + (\frac{dg}{d\theta})^2 \cdot m_z) \cdot \frac{d^2\theta}{dt^2} + f_\theta + \frac{dg}{d\theta} \cdot ((\frac{d^2g}{d\theta^2}) \cdot (\frac{d\theta}{dt})^2 + h_z(\theta) + h_{gas}(\theta)) \tag{4.3}$$

where $z = g(\theta)$, $h_z(\theta) = f_z(z) = f_z(g(\theta))$ and $h_{gas}(\theta) = f_{gas}(z) = f_{gas}(g(\theta))$ are the z-domain friction force and gas force represented with respect to rotor position θ.

Based on (4.3), we also can write an array of state equations for the EMV system. If we set up two states as,

$$\begin{aligned} x_1 &= \theta \\ x_2 &= \dot{\theta} \end{aligned} \tag{4.4}$$

then we can write state equations as follows,

$$\begin{aligned} \dot{x}_1 &= x_2 \\ \dot{x}_2 &= (K_T \cdot I - f_\theta - \frac{dg}{d\theta} \cdot ((\frac{d^2g}{d\theta^2}) \cdot (x_2)^2 + h_z(x_1) + h_{gas}(x_1))) / (J_\theta + (\frac{dg}{d\theta})^2 \cdot m_z) \end{aligned} \tag{4.5}$$

In effect, the system represented by (4.4) and (4.5) resembles a typical second-order time-varying differential equation with nonlinear mass/inertia and nonlinear damping owing to the nonlinear relation between the θ and z domains. Also, it is important to note that because $\frac{dg}{d\theta}$ is different for each point in the valve stroke, the dynamic characteristics of the EMV system change at every point in the stroke. For first order analysis of the system, we can linearize the system at the end position and the middle position, respectively, if we ignore the gas force disturbance. At the ends of the stroke where the

motor is essentially decoupled from the engine valve-spring system (because the cam slope is almost 0), the state equations reduce to:

$$\begin{aligned} \dot{x}_1 &= x_2 \\ \dot{x}_2 &= (K_T \cdot I - f_\theta)/J_\theta \end{aligned} \tag{4.6}$$

In the middle of the stroke, assuming the slope of the NTF relation is equal to the constant r, the state equations can be rewritten as:

$$\begin{aligned} \dot{x}_1 &= x_2 \\ \dot{x}_2 &= (K_T \cdot I - f_\theta - r \cdot (h_z(x_1) + h_{gas}(x_1)))/(J_\theta + r^2 \cdot m_z) \end{aligned} \tag{4.7}$$

However, if we want to predict the system behavior accurately, we have to seek help from numerical simulation, as will be discussed shortly.

From the system dynamic model above, we can see that the friction forces play an important role in the system dynamics. More importantly, the frictional loss is one of the two main loss sources of the system as will be shown in the section 4.3, especially as the gas force is not significant for the intake valve. Therefore, a good model to describe the friction forces of the system is necessary, as will be discussed in section 4.4.

4.3 Loss Structure

In order to minimize the power consumption and torque requirement of the system, it is important to have a clear understanding of the power distribution and loss structure of the system. In other words, in one successful transition, where does the input power flow and what is the original cause? In this electromechanical system, in terms of the motor, there are two main power flows: electrical loss associated with the winding resistance and mechanical power output at the shaft, which is determined by the torque and speed. Furthermore, the mechanical output can be divided into two parts: the frictional loss in the θ-domain and in the z-domain respectively, when we ignore gas force in the case of intake valve actuation. Therefore, because the energy in the springs is the same at the

start and at the end of a transition, the total input work over one stroke goes completely to compensate electrical and frictional losses and nothing else. The loss flow of the system is shown in Fig. 4.1.

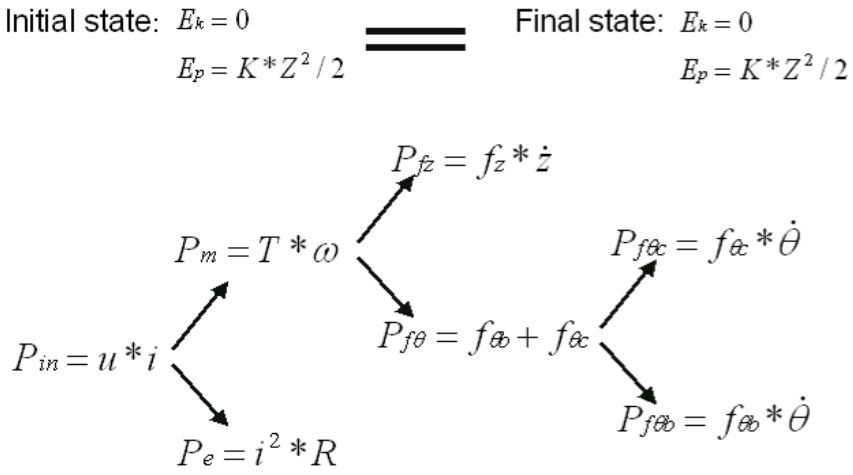

Fig. 4.1. Loss flow of the EMV system.

There are two electrical losses associated with the winding resistance. One is associated with the low-frequency portion of the current and the other is associated with the high switching frequency portion of the current. The resistance associated with the former loss is essentially the dc winding resistance. This is basically the resistance that can be looked up in the specification of the motor, which is 0.89 Ω in the brush dc motor in the first prototype. The resistance associated with the latter loss is called ac resistance in this thesis. Ac resistance and dc resistance are different owing to skin and proximity affects in the conductors and core loss in the magnetic material. We refer to the two losses as dc resistance loss and ac resistance loss, respectively. The two losses can be demonstrated separately and together by the simple experiments discussed below.

Experiment 1: Bypass the motor drive and connect a dc power supply directly to the motor with the shaft locked. Power on the power supply with certain output voltage, such as 4 V. Measure the voltage and current profile at the end of the motor leads, as shown in Fig.4.2. Calculate the input power by multiplying input voltage and current, which should equal the output power, i.e., the dc electrical loss i^2R. By matching input and output

power, we can estimate the actual dc resistance, which is about 0.80 Ω, very close to the value in the specification.

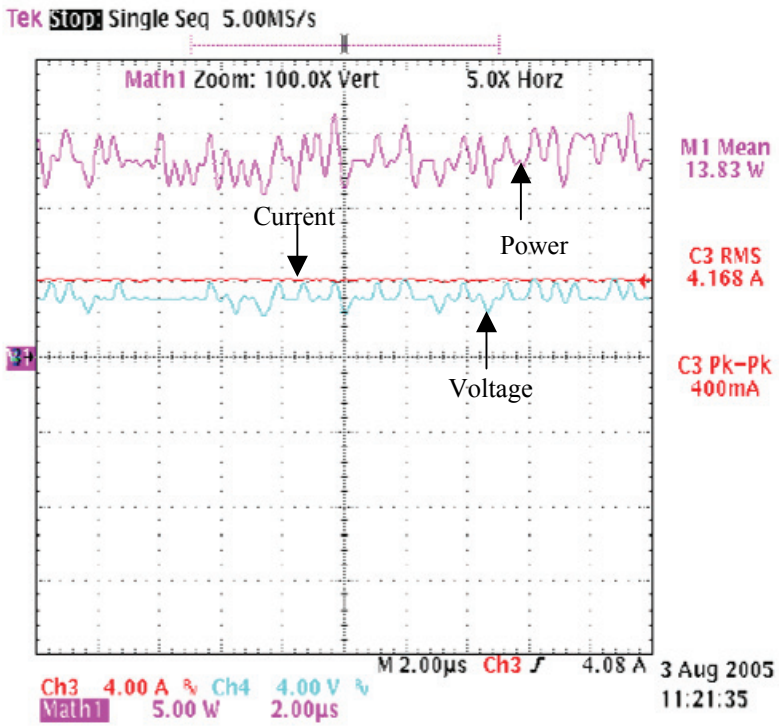

Fig. 4.2. Experiment 1 --- 4 V dc input directly to the motor.

Experiment 2: Use the motor drive to drive the motor with the shaft locked, and give the motor drive a zero current command. The measured current profile shows a mean current value of almost zero, so the dc loss is negligible, as shown in Fig. 4.3.

But the high frequency current ripple has a nonzero rms value, resulting in a nonzero ac resistance loss as well as a nonzero input power. From the rms current and power measurement, we can calculate an equivalent ac resistance, which is about 31 Ω.

Experiment 3: With a nonzero current command, e.g., 5 A, as shown in Fig. 4.4, the current has two components --- the dc component (approximately 4.9 A) and the ac component. Accordingly, the loss has two portions as well. With the ac resistance and dc resistance obtained in experiments 1 and 2, we can verify that the input power is matched by the sum of the predicted dc loss and ac loss.

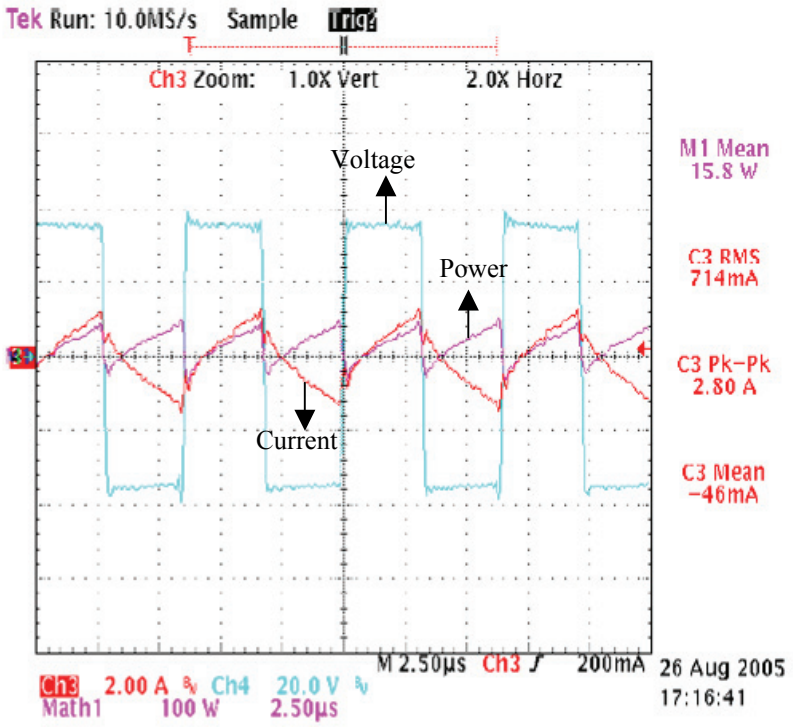

Fig. 4.3. Experiment 2 --- 0 A current command to motor drive.

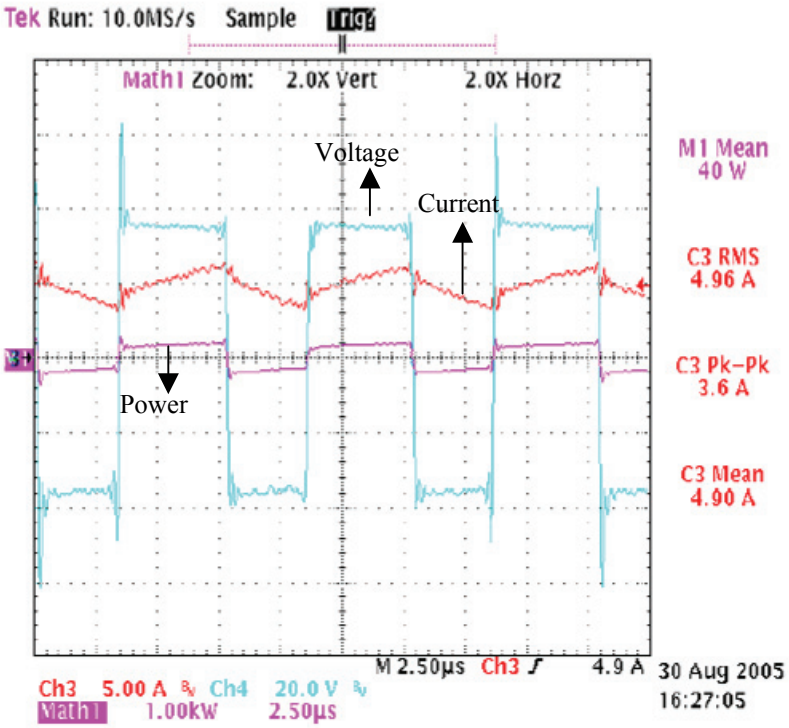

Fig. 4.4. Experiment 3 --- 5 A current command to motor drive.

It is valuable to observe that the dc loss is very much a function of the local average current profile, while the ac loss is more or less constant as long as the local average current profile varies slowly as compared to the switching frequency and thus has its content at much lower frequencies. Fortunately, this is usually the case in this application. Assume we can achieve a full transition in the θ-domain within 5 ms, which gives a basic frequency of about 200 Hz. By comparison, the switching frequency, i.e., the basic frequency of the current ripple, has a frequency as high as 150 kHz. This leads to different solutions to reduce the two different losses. The dc loss can be decreased if a local average current profile having lower peak and rms values can be used to achieve a satisfactory transition. This solution also yields the reductions of the peak torque and rms torque requirement of the motor. On the other hand, the ac loss can be cut by reducing the switching frequency and the ac current ripple. Means to reduce electrical losses and torque requirement will be discussed in more details in Chapters 5 and 6.

As for frictional loss, it is determined largely by the friction forces along the transition. The friction forces also affect the motor torque requirement directly. Hence, a detailed analysis and modeling of the friction force is very crucial, as discussed in next section.

4.4 Nonlinear Friction Model

In Chang's preliminary analysis, it was assumed that friction can be represented by viscous friction with constant coefficients in both domains [17], as shown in (4.8),

$$\begin{aligned} f_\theta &= B_\theta \frac{d\theta}{dt} \\ f_z &= B_z \frac{dz}{dt} \end{aligned} \tag{4.8}$$

However, based on that assumption, the simulation results could not predict the experimental results very well, suggesting an improved understanding of friction is necessary, especially as regards the θ-domain. Therefore, in our analysis, we keep the assumption that the friction in the z-domain is only viscous friction proportional the valve

velocity exclusively, as shown in (4.8). In the θ-domain, the situation is somewhat complicated for three reasons. First, there are at least three friction sources --- windage, contact friction from the shaft bearing, and contact friction from the roller follower. Secondly, contact friction includes not only viscous friction but also coulomb friction. Thirdly, due to the spring force acting between the disk cam and roller follower, contact friction between them is affected by normal force, which is not constant during the transition. Therefore, a friction model taking all these effects into consideration is proposed, as shown in (4.9):

$$f_\theta = B_{\theta b}\frac{d\theta}{dt} + F_n \cdot (B_{\theta v}\frac{d\theta}{dt} + B_{\theta c}\,\mathrm{sgn}(\frac{d\theta}{dt})) \tag{4.9}$$

In this model, part of the viscous friction, mainly due to windage and contact friction from the shaft bearing, is independent of spring force or normal force, and therefore has a constant coefficient $B_{\theta b}$, while the other portion of viscous friction, $B_{\theta v}\frac{d\theta}{dt}$, and coulomb friction, $B_{\theta c}\,\mathrm{sgn}(\frac{d\theta}{dt})$, depend very much on the normal force F_n exerted at the contact surface owing to contact friction between the disk cam and roller follower.

The normal force exerted on the rolling surface varies along the valve transition because it is affected by multiple factors, as shown in (4.10),

$$F_n = (K_s z - f_z - m_z\frac{d^2 z}{dt^2}) \cdot \cos(\alpha) \tag{4.10}$$

where $K_s z$ is the spring force, f_z is the friction force in the z-domain, $m_z\frac{d^2 z}{dt^2}$ is the inertial force, and α is the angle between the tangent to the contact surface presented by the line C-C and the horizontal plane which is perpendicular to vertical valve motion presented by the line A-A, as shown in Fig. 4.5.

As derived in Appendix I, for a given NMT function as shown in (4.11), the cam slot surface slope, $\tan(\alpha)$, and its variation, $\cos(\alpha)$, used in (4.10) at different θ positions, can be described as in (4.12) and (4.13).

$$\begin{aligned} z &= f(\theta) = a \cdot \sin(b \cdot \theta) \\ a &= z_{\max} \\ b &= \pi / 2\theta_{\max} \end{aligned} \tag{4.11}$$

$$\tan(\alpha) = (a \cdot b \cdot \cos(b \cdot \theta)) / (a \cdot \sin(b \cdot \theta) + h) \quad |\theta| \le \pi / 2b \tag{4.12}$$

$$\cos(\alpha) = 1 / \sqrt{1 + (a \cdot b \cdot \cos(b \cdot \theta) / (a \cdot \sin(b \cdot \theta) + h))^2} \quad |\theta| \le \pi / 2b \tag{4.13}$$

where, as shown in Fig. 4.5, $2z_{\max}$ is the full stroke of the valve, $2\theta_{\max}$ is the total rotation range of the motor, and h is the vertical distance between the motor shaft center and the roller center when the roller as well as the valve is in the middle of the stroke, i.e., the equilibrium point of the system.

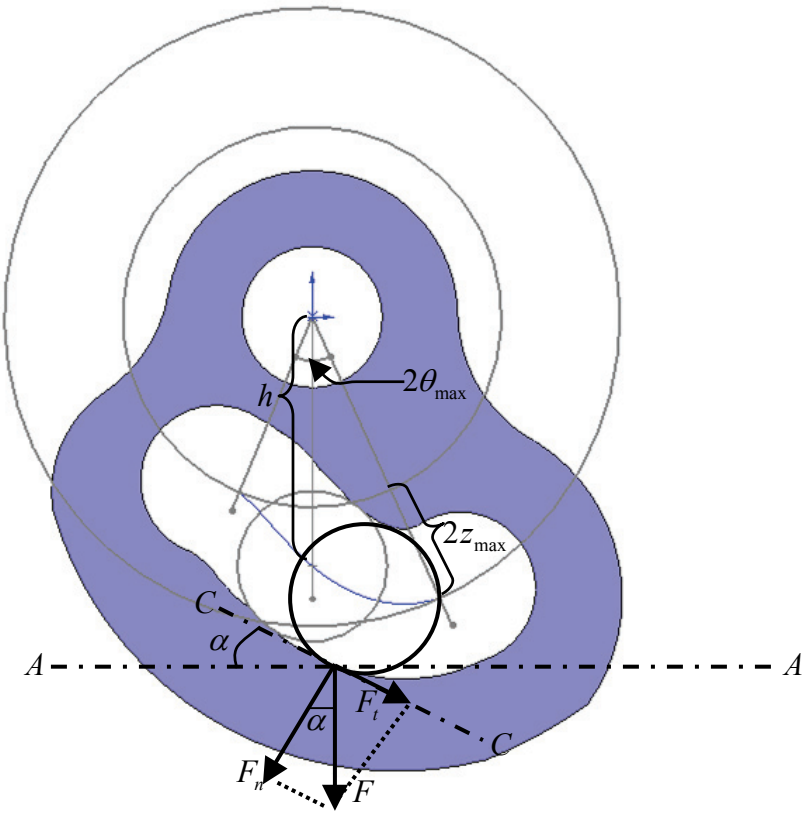

Fig. 4.5. The design parameters of the NMT.

Obviously, this friction model in the θ-domain is a nonlinear model, not only because the coulomb friction is related to the direction of the valve velocity, but also because a large portion of the friction is related to a varying normal force which is a nonlinear function with respect to θ or z. If we want to summarize the total frictional force in either the θ or z domain, then due to the nonlinear translation of the NMT, an additional layer of nonlinearity is added to the whole friction model. Therefore, in order to identify system parameters and predict system performance, we have to rely heavily on numerical simulation owing to the inherent nonlinearity of the whole system. The setup of the numerical simulation, extraction of friction coefficients, and validation of the proposed nonlinear friction model by comparing simulation to experimental results will be discussed in the following sections.

4.5 Simulation Setup

4.5.1 Introduction of 20-sim®

The software package 20-sim®, developed by Controllab Products (CLP), originates from the 20-sim®, MAX, CAMAS and TUTSIM prototypes that were developed by the Control Laboratory of the University of Twente in the Netherlands.

20-sim® is a modeling and simulation program that allows us to enter models graphically, similar to drawing an engineering schematic. With these models we can simulate the behavior of most dynamic systems, such as electrical, mechanical or hydraulic systems, including their closed-loop controls. It fully supports graphical modeling and allows us to design and analyze dynamic systems in an intuitive and user-friendly way. It also supports the use of components, which helps us to enter models as in an engineering schematic; by choosing components from library and connecting them, we can build our system scheme without the use of equations.

4.5.2 Summary of System Scheme and Parameters

From the discussion in last chapter and this chapter, we already have a big picture of the system model, including equations in the θ-domain, in the z-domain, and in the NMT in between. The summary of the EMV system scheme is shown in Fig. 4.6.

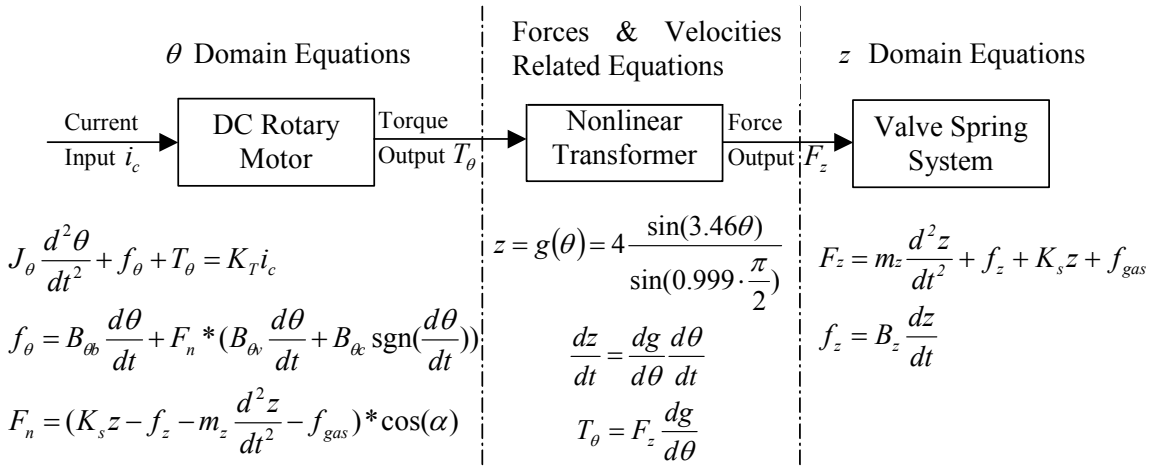

Fig. 4.6. Summary of the EMV system scheme.

In order to conduct a meaningful simulation, we need to identify all the system parameters. The motor-related parameters, including the rotor inertia $J_{\theta m}$, torque constant K_T, and winding resistance R are taken from the specification of the commercial motor after they are verified by simple testing and measurements. The inertia of the disk cam, $J_{\theta c}$, is calculated by the 3D design software SolidWorks®. The sum of the rotor inertia, $J_{\theta m}$, and cam inertia, $J_{\theta c}$, is the total inertia J_θ in the θ-domain, as shown in (4.14). The cam inertia $J_{\theta c}$ actually dominates the total inertia in the θ-domain.

$$J_\theta = J_{\theta m} + J_{\theta c} \tag{4.14}$$

$$m_z = m_{zv} + m_{zh} + m_{zs} \cdot 2/3 + m_{zr} + m_{zd} \tag{4.15}$$

The total mass in the *z*-domain consists of the mass of the valve, m_{zv}, valve holder, m_{zh}, spring divider, m_{zd}, springs, m_{zs}, and roller follower, m_{zr}, as shown in (4.15), which are all measured using an accurate scale. The effective mass of the springs used in the dynamic simulation is $2/3$ of their actual mass due to the fact that different points on the spring undergo different accelerations [22]. The spring constant K_s is taken from the spring specification and confirmed by testing. The rotational range of the rotor, $2\theta_{\max}$, is

determined by the design of the disk cam while the stroke of the valve, $2z_{\max}$, is determined by the design of the engine. The frictional coefficients are extracted from the experimental and simulation results, as will be discussed in the next section. A summary of the system parameters is shown in Table 4.1. Note that the gas force is assumed to be negligible in the case of intake valve actuation and therefore is not present in the table.

TABLE 4.1. SIMULATION PARAMETERS OF INTAKE VALVE ACTUATION.

Parameters Description	Intake Valve
$J_{\theta m}$	$5.9 \cdot 10^{-6}$ Kg·m^2/s
$J_{\theta c}$	$1.23 \cdot 10^{-5}$ Kg·m^2/s
J_{θ}	$1.82 \cdot 10^{-5}$ Kg·m^2/s
K_T	70 mN/A
R	0.89 Ω
$B_{\theta b}$	500 μN-m·s/rad
$B_{\theta v}$	10 μm·s/rad
$B_{\theta c}$	8 μm·s/rad
$\theta_{\max}$	26º
$z_{\max}$	4 mm
m_{zv}	40 g
m_{zh}	29 g
m_{zs}	14 g
m_{zd}	32 g
m_{zr}	7 g
m_z	117.3 g
K_s	112 N/mm
B_z	12 N-m/s

4.5.3 Evaluation of System Performance

In this section we will demonstrate how to estimate the system performance including transition time and power consumption with simulated data and experimental data. The definitions will apply to the whole thesis unless specially addressed.

- **Transition Time**

We define the transition time, t_z, as the period during which the valve travels from 5% to 95% of the stroke in the z-domain, as shown in (4.16),

$$t_z = t(0.95 \cdot 2z_{\max}) - t(0.05 \cdot 2z_{\max}) \tag{4.16}$$

- **Average Power Consumption**

Unless specially addressed, whenever the phrase "power consumption" is used in this thesis, it represents the average power consumed per valve per cycle at 6000 rpm engine speed, where a full cycle equals a duration of 20 ms. The average power consumption per valve per cycle at any other engine speed N can then be estimated as (4.17),

$$P_N = P_{6000} \cdot N / 6000 \tag{4.17}$$

For 6000 rpm engine speed, one complete combustion cycle (20 ms) includes one opening transition and one closing transition for each valve. Although the total power required to operate one valve includes both the power required to open and the power required to close the valve, the simulations presented here cover only one transition because we assume that, in the absence of gas force, the opening and closing transitions will be identical. If we want to predict both intake and exhaust valve actuation by simulation, we can conduct simulations under three different circumstances as listed below:

- Intake valve opening (or closing) without gas force to predict intake valve actuation for both directions.
- Exhaust valve opening (or closing) without gas force to predict exhaust valve closing actuation.
- Exhaust valve opening with maximum gas force under full load condition to predict exhaust valve opening actuation.

In each case, transient winding loss, $i_c^2 R$, and motor power output, $e \cdot i_c$, will be integrated along the transition in our simulation. Winding loss, $i_c^2 R$, is the heat load imposed on the cooling system, while motor power output, $e \cdot i_c$, reflects all friction losses in both the θ and z domains because the system has the same potential energy ($\frac{1}{2} K_s z_{amx}{}^2$) and kinetic energy ($0$) at both ends of the transition, as discussed in section 4.3. Therefore heat energy $E_{\text{winding\_open}}$ and friction energy $E_{\text{friction\_open}}$ in one opening transition can be determined by (4.18),

$$\begin{aligned} E_{\text{winding\_open}} &= \int i_c^2 R dt \\ E_{\text{friction\_open}} &= \int e i_c dt \end{aligned} \tag{4.18}$$

where the integral covers the entire interval during which the valve opening current is non-zero. The particular function i_c depends on the case being simulated.

Hence the average winding loss $P_{\text{winding\_open}}$ and the friction loss $P_{\text{friction\_open}}$ over one cycle ($20\,\text{ms}$ @ 6000 rpm engine speed) can be calculated by (4.19),

$$\begin{aligned} P_{\text{winding\_open}} &= E_{\text{winding\_open}} / 20\text{ms} \\ P_{\text{frction\_open}} &= E_{\text{friction\_open}} / 20\text{ms} \end{aligned} \tag{4.19}$$

The sum of the average winding loss $P_{\text{winding\_open}}$ and the average friction loss $P_{\text{friction\_open}}$ is the average power consumed during one opening transition P_{open}, as shown in (4.20),

$$P_{\text{open}} = P_{\text{wind\_open}} + P_{\text{friction\_open}} \tag{4.20}$$

For an intake valve where gas force is negligible, we assume opening and closing transitions in one cycle are totally separate and symmetric events. Therefore the average

winding loss, the average friction loss, and therefore the average power associated with closing a valve, is the same as that associated with opening. Hence the total average winding loss, $P_{\text{intake\_winding}}$, the total average friction loss, $P_{\text{intake\_friction}}$, and the total average power consumption of one cycle, P_{intake}, i.e., the sum of that required to open and that required to close, equals twice that required to open, as shown in (4.21),

$$\begin{aligned} P_{\text{intake\_winding}} &= 2 \cdot P_{\text{intake\_winding\_open}} \\ P_{\text{intake\_friction}} &= 2 \cdot P_{\text{intake\_friction\_open}} \\ P_{\text{intake}} &= 2 \cdot P_{\text{intake\_open}} \end{aligned} \tag{4.21}$$

Equation (4.21) presents the complete contribution to average power of the operation of one intake valve.

For an exhaust valve with no gas force disturbance, the situation is identical to that of the intake valve discussed above. Therefore the total average winding loss $P_{\text{exhaust\_winding\_nogasforce}}$, the total average friction loss $P_{\text{exhaust\_friction\_nogasforce}}$, and the total average power consumption $P_{\text{exhaust\_nogasforce}}$ in one cycle also equals twice that needed for one opening transition, as shown in (4.22),

$$\begin{aligned} P_{\text{exhaust\_winding\_nogasforce}} &= 2 \cdot P_{\text{exhaust\_winding\_open\_nogasforce}} \\ P_{\text{exhaust\_friction\_nogasforce}} &= 2 \cdot P_{\text{exhaust\_friction\_open\_nogasforce}} \\ P_{\text{exhaust\_nogasforce}} &= 2 \cdot P_{\text{exhaust\_open\_nogasforce}} \end{aligned} \tag{4.22}$$

Equation (4.22) presents the complete contribution to average power of the operation of one exhaust valve with no gas force.

For an exhaust valve with gas force, the average winding loss $P_{\text{exhaust\_winding\_close\_gasforce}}$, the average friction loss $P_{\text{exhaust\_friction\_close\_gasforce}}$, and the average power consumption

$P_{\text{exhaust\_close\_gasforce}}$ associated with closing the valve equal those required to open/close the valve without gas force, i.e.,

$$\begin{aligned} P_{\text{exhaust\_winding\_close\_gasforce}} &= P_{\text{exhaust\_winding\_open\_nogasforce}} \\ P_{\text{exhaust\_friction\_close\_gasforce}} &= P_{\text{exhaust\_friction\_open\_nogasforce}} \\ P_{\text{exhaust\_close\_gasforce}} &= P_{\text{exhaust\_open\_nogasforce}} \end{aligned} \tag{4.23}$$

However, the average power associated with opening $P_{\text{exhaust\_open\_gasforce}}$ is different and needs to be simulated as a separate case. The total average winding loss $P_{\text{exhaust\_winding\_gasforce}}$, the total average friction loss $P_{\text{exhaust\_friction\_gasforce}}$, and the total power consumption $P_{\text{exhaust\_gasforce}}$ therefore can be evaluated by (4.24),

$$\begin{aligned} P_{\text{exhaust\_winding\_gasforce}} &= P_{\text{exhaust\_winding\_open\_gasforce}} + P_{\text{exhaust\_winding\_open\_nogasforce}} \\ P_{\text{exhaust\_friction\_gasforce}} &= P_{\text{exhaust\_friction\_open\_gasforce}} + P_{\text{exhaust\_friction\_open\_nogasforce}} \\ P_{\text{exhaust\_gasforce}} &= P_{\text{exhaust\_open\_gasforce}} + P_{\text{exhaust\_open\_nogasforce}} \end{aligned} \tag{4.24}$$

Equation (4.24) presents the complete contribution to average power of the operation of one exhaust valve with gas force.

4.6 Validated Simulation Results

4.6.1 Simulation Model

The latest version of the EMV system schematic in 20-sim® is shown in Fig. 4.7, where the nonlinear system model, including the nonlinear friction and NMT models are included. A combination of open-loop control and closed-loop (feed-back) control is also shown in this schematic, for the purpose of not only initial mode control but also different transition mode control strategies, as will be discussed in Chapter 5.

The basic simulation results describing the valve transition, the reference and actual rotor positions, and the motor current input, are plotted in the window shown in Fig. 4.8. Extra

windows can be added in order to observe and study other system parameters, such as winding loss, frictional loss, motor torque output, and friction torque in both θ and z domains. In Fig. 4.9, the motor torque output (i.e., the frictional loss) and the motor winding loss are integrated with respect to time and the resulting energy profiles are plotted for one transition. The final energy number can be used to estimate power consumption per cycle, as discussed in the previous section. All simulation data can be exported to a TXT or BINARY data file, which can be read and further reprocessed by other software like MATLAB®. For example, friction torque information is exported to and replotted in MATLAB®. This becomes valuable if we want to compare simulation results and experimental results.

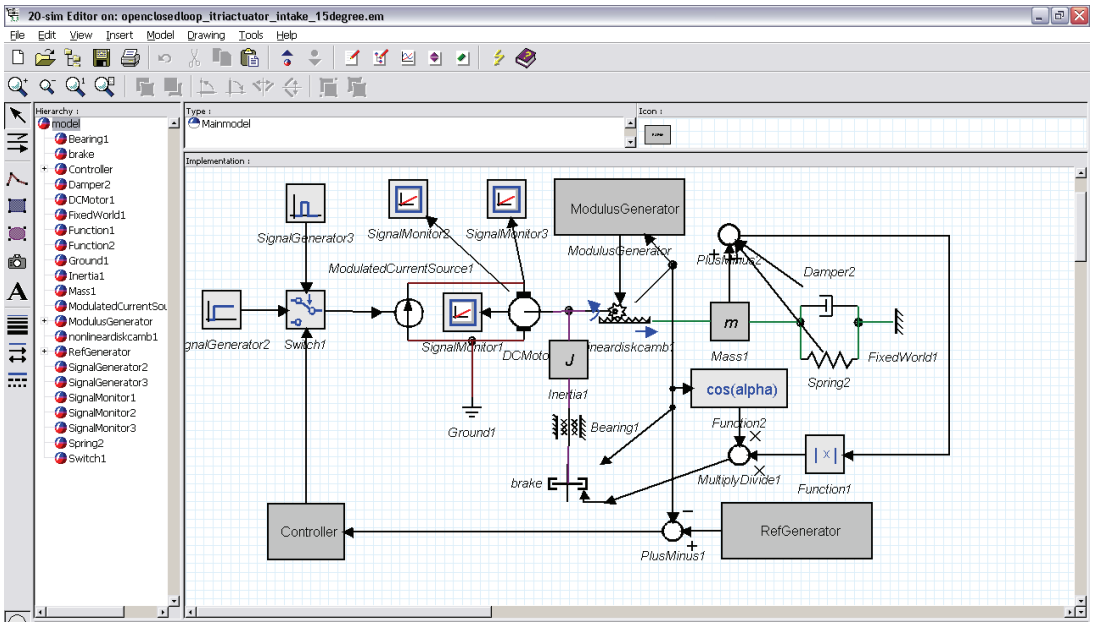

Fig. 4.7. Latest version of the EMV system schematic in 20-sim®.

4.6.2 Extraction of Friction Coefficients

In order to extract the friction coefficients, especially the three friction coefficients in the θ-domain, we did a simple open-loop experiment. Starting with the system at rest in the closed or open position, we injected a pre-selected square current pulse into the motor, to set the system into motion. The motor was then turned off and the resulting damped oscillation recorded. A time-matching numerical solution was also done using 20-sim®, where the nonlinear friction model is plugged in. We varied the three friction coefficients

to minimize the difference between the experimental data and the numerical simulation with different current pulse inputs. The measured trace for one trial is shown in Fig. 4.10, along with the result of the simulation. The extracted friction coefficients are shown in Table 4.1.

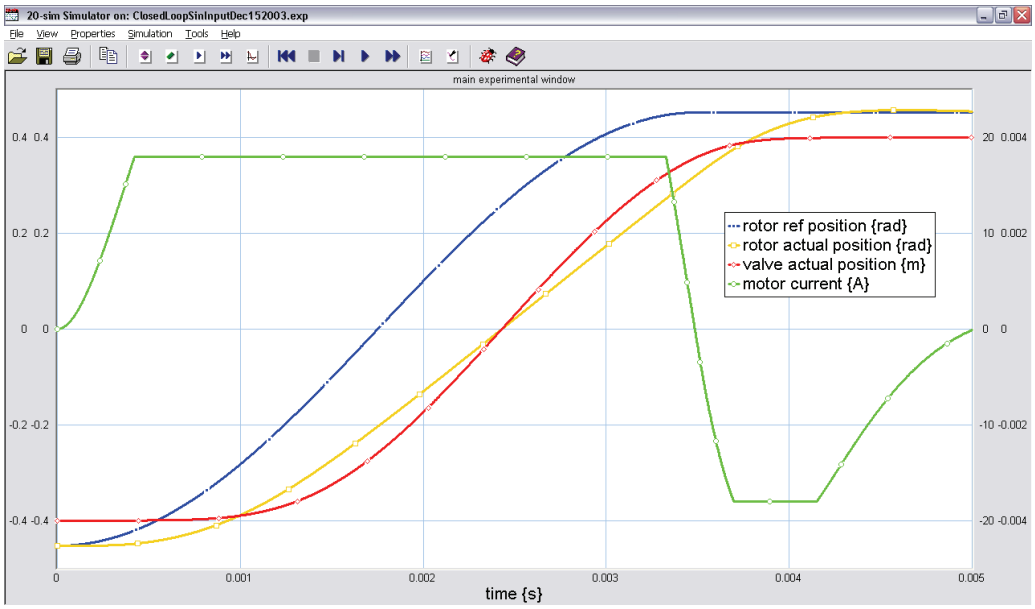

Fig. 4.8. Position and current profiles in 20-sim® simulation.

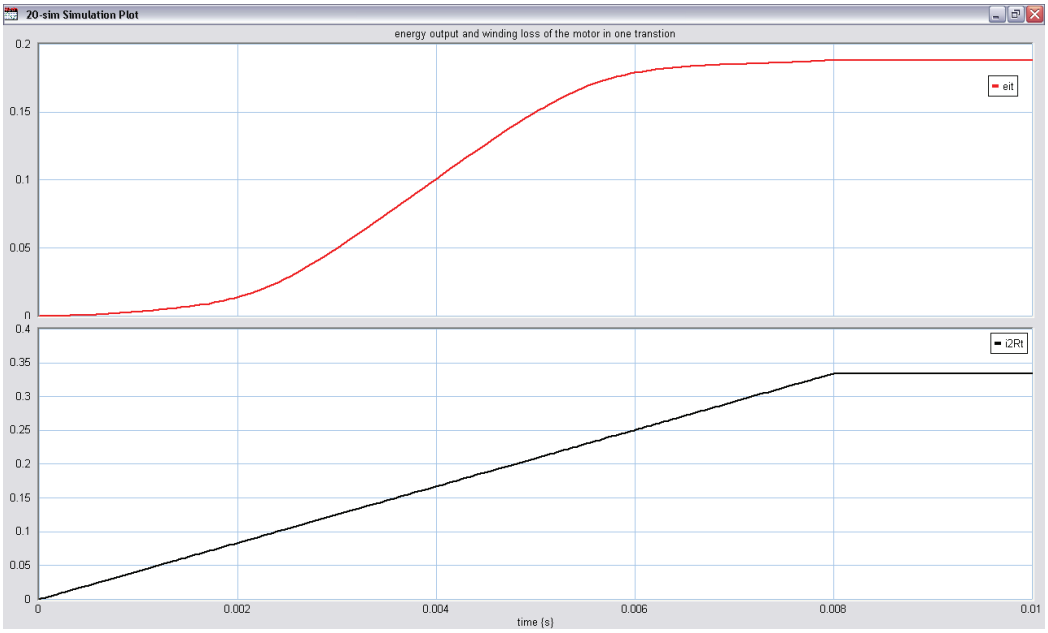

Fig. 4.9. Friction and winding loss tracking in 20-sim® simulation.

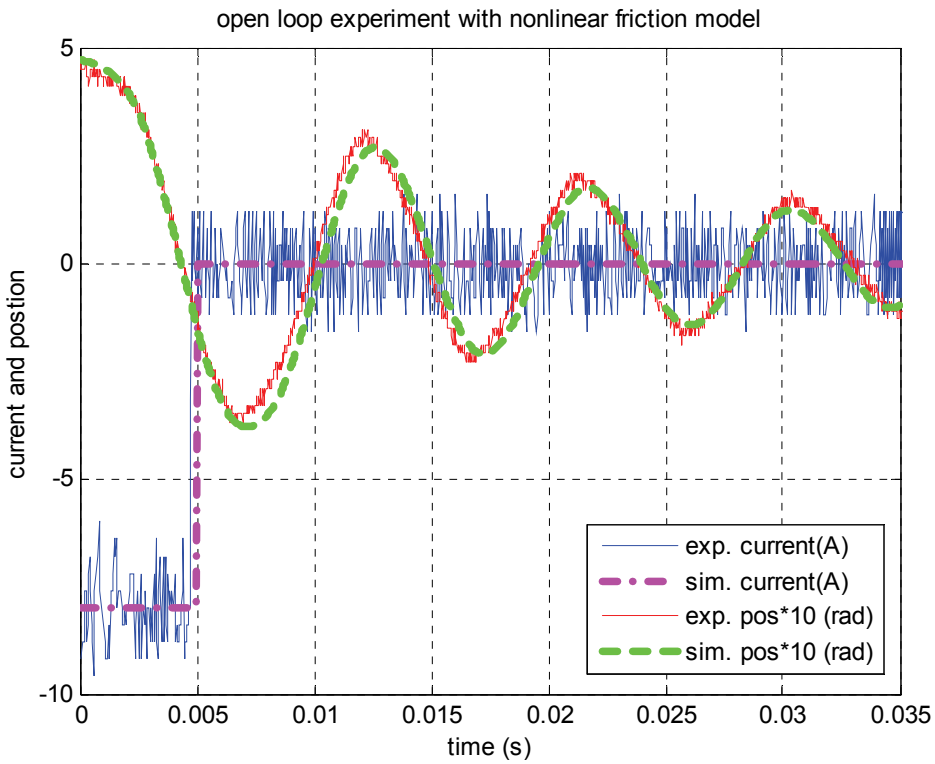

Fig. 4.10. Open-loop experiments to extract friction coefficients.

4.6.3 Validation of the Nonlinear Friction Model

The verification of this nonlinear friction model in a closed-loop experiment is shown in Figs. 4.11 to 4.14. Figures 4.11 and 4.12 present the simulation and experimental results respectively of the initial mode. Both simulation and experimental results of transition mode, including position and current profiles, are shown in Figs. 4.13 and 4.14 respectively. In both cases, the simulation results using the updated nonlinear friction model match the experimental data every well. Therefore, we can rely on this system model to predict system performance and hence guide us when we try to improve control strategy and hardware design.

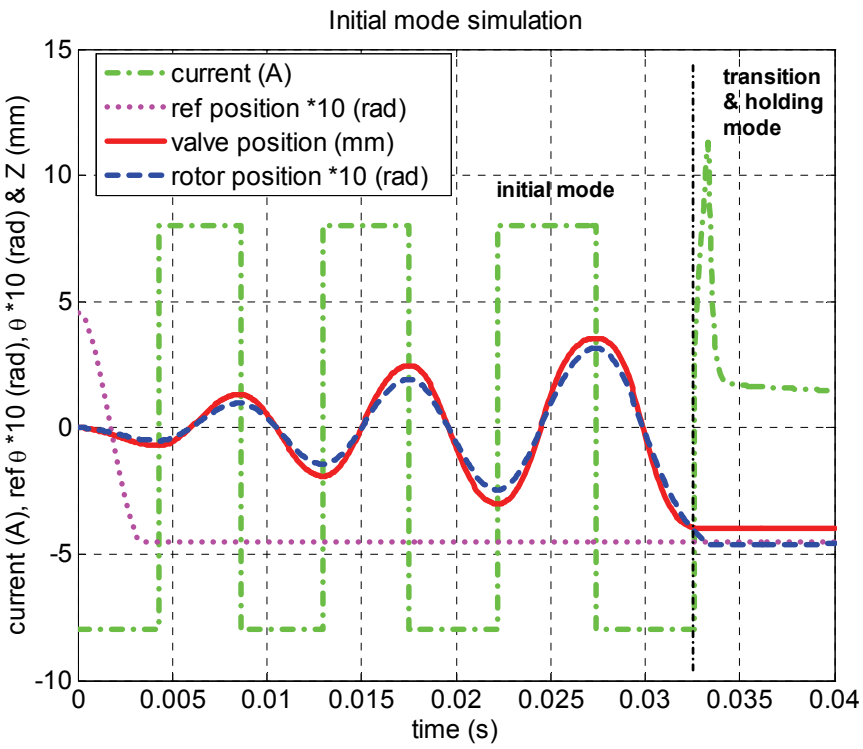

Fig. 4.11. Simulation results of initial mode.

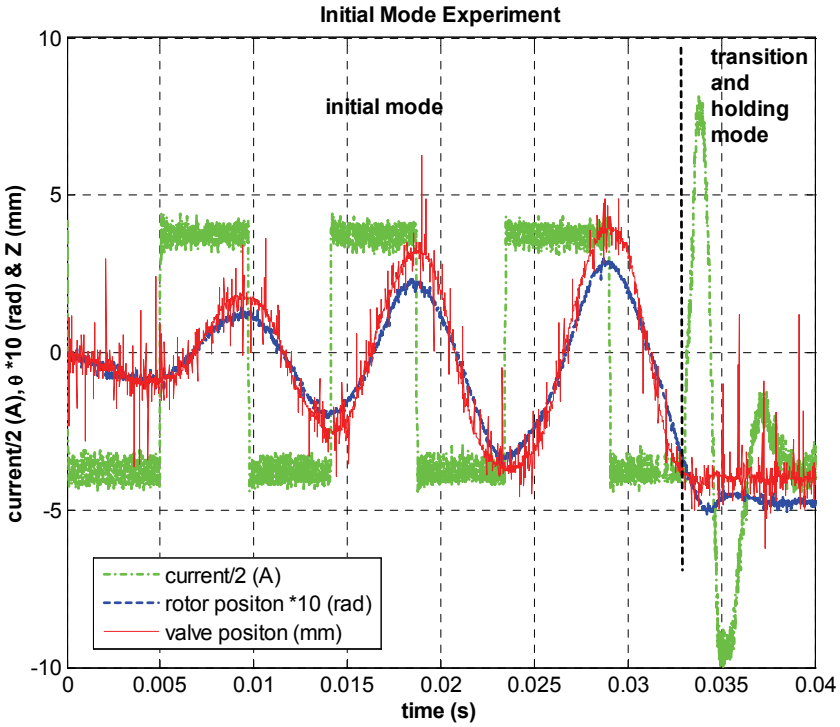

Fig. 4.12. Experimental results of initial mode.

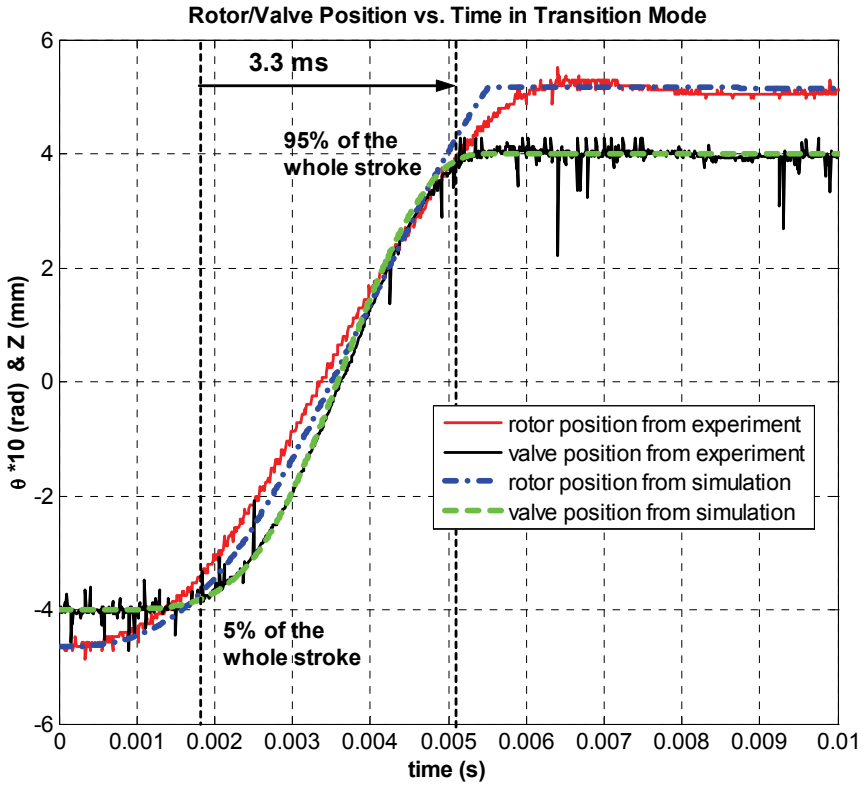

Fig. 4.13. Position profiles of transition mode from experiment and simulation.

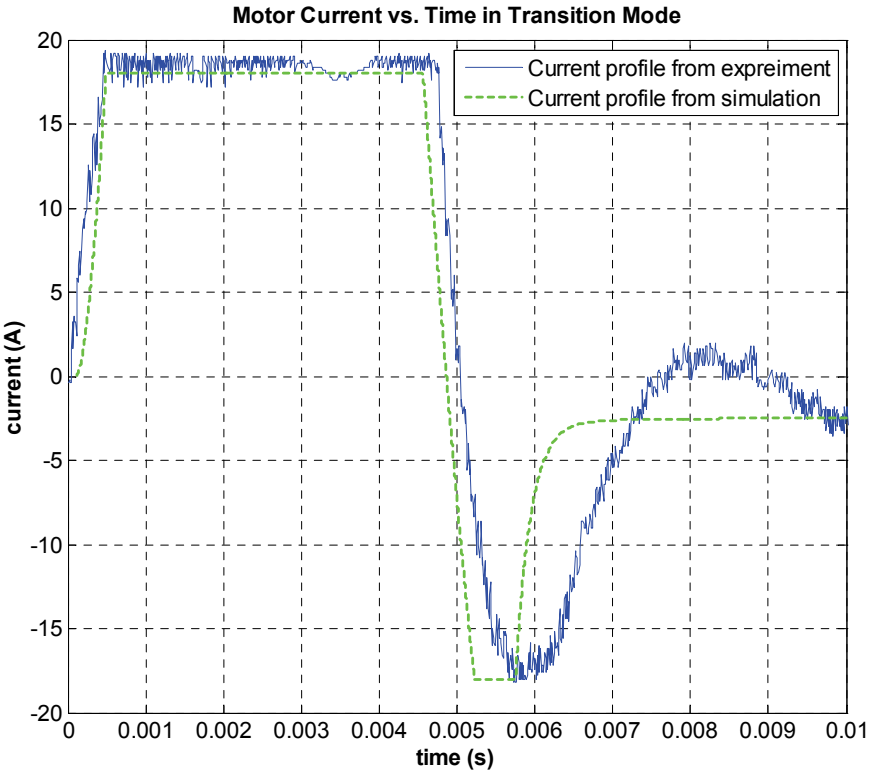

Fig. 4.14. Current profiles of transition mode from experiment and simulation.

Note that in Fig. 4.14, the nonzero current at the end of transition is due to the nonzero static error between actual position and reference position.

Simulation results of friction profiles along one complete transition, using the current nonlinear model as well as the previous linear model, are shown in Fig. 4.15. The substantial difference between these two θ-domain friction profiles is very obvious. The previous linear model, representing by a viscous friction with constant coefficient, gives us a profile with maximum value at the middle of the transition. This is because the speed will be the highest in the middle of the transition. With the nonlinear model, there are two local maximum values close to the starting and ending position and one local minimum value in the middle of the transition instead. This unique profile is due to the normal-force-dependent viscous friction force, which dominates the total friction force in θ-domain, as will be discussed next.

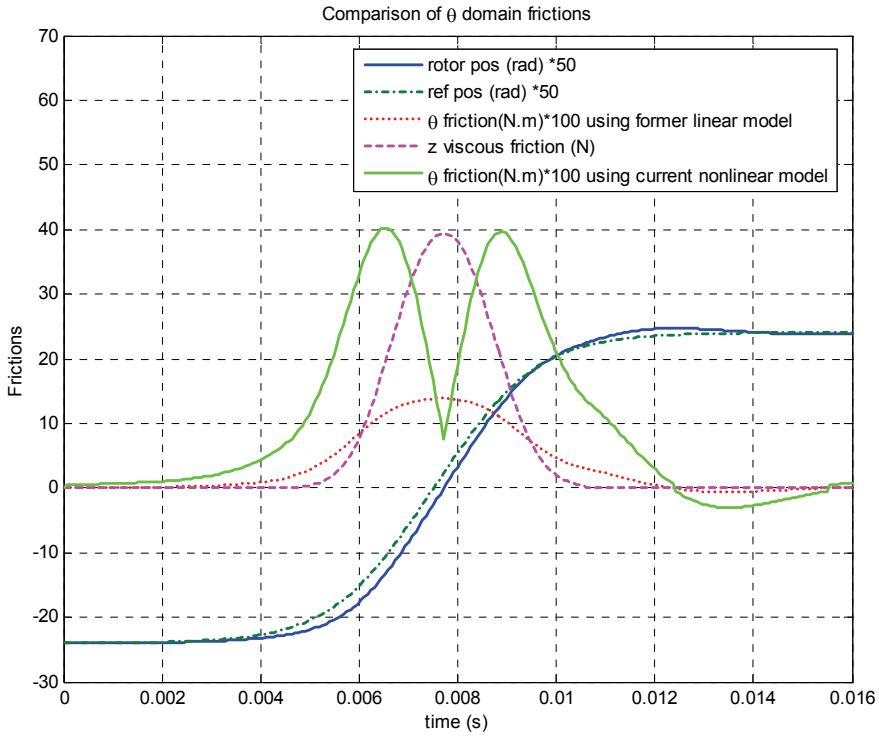

Fig. 4.15. Comparison of current and previous friction models.

Among the three parts of the total friction in the θ-domain, the coulomb friction turns out to be the smallest, with a peak value less than one tenth of the peak value of the two viscous friction forces. In other words, if we picked the two viscous friction coefficients in the right ranges, system performance will be quite insensitive to the coulomb friction coefficient. Meantime, the normal force dependent friction force dominates the independent viscous friction force by a factor of more than 5 in peak value. The linear or independent viscous friction reaches its peak value when the rotor rotational speed is the highest around the middle of the stroke. The normal-force-dependent viscous friction is more complicated, since it is affected by normal force and rotational speed at the same time. The normal force is the highest at both ends and is zero at the middle of the stroke while the rotational speed is zero at both ends and the highest at the middle of the stroke. The combined distributions of normal force and rotational speed lead to three local minimums (zero) and two local maximums (peak) of profile of the nonlinear viscous friction force. The three zeros are at the ends and the middle of the stroke while the two peaks are located between end and middle positions symmetrically. Moreover, due to the different weights of these friction forces, the sensitivity of their respective coefficients to the system performance is also different. Obviously, the normal force dependent friction force is the most sensitive while the coulomb friction force has the least sensitivity. With this more detailed and accurate friction model at hand, it is possible to use feed forward control (or open-loop control) to counteract friction in the future.

CHAPTER 5 CONTROL STRATEGIES AND INPUT FILTER

5.1 Introduction

As discussed in Chapter 4, the electrical loss of the motor consists of principally two components --- dc resistance loss and ac resistance loss. In this chapter we will discuss different control strategies for the purpose of minimizing dc electrical resistance loss, and input filter design in order to reduce ac resistance loss. First we will review the pure closed-loop control used in the preliminary experiment presented in Chapter 3, but we will change the position reference from a sine wave to the loss-free, free-flight trajectory of the system. Secondly, a combination of open-loop and closed-loop control is proposed in order to reduce power consumption further and speed up the initiation of the transition. Thirdly, the case of pure open-loop control using a current pulse with controlled amplitude and duration is discussed, including the tradeoff between power consumption and transition time. Each control strategy will be simulated using the improved system model described in Chapter 4, and then verified by experiments. Finally, the input filter design for our first prototype is presented at the end of this chapter.

5.2 Pure Closed-loop Position Control

5.2.1 Free-flight Trajectory as Reference

As discussed in Chapter 4, the dc resistance loss is determined by the mean current profile. As shown in Fig. 3.9 in Chapter 3, in the first half of the transition the motor current reaches a positive saturation limit while trying to inject as much energy into the system as possible to accelerate the valve, while in the second half the current reaches the negative limit, trying to pull out as much energy as possible from the system to decelerate the valve. The dc resistance loss associated with this reactive energy exchange is substantial. The mechanical power loss and the peak torque requirement can also be larger than necessary due to the increased frictional loss and the unnecessary fighting with the springs. One reason for this energy waste is the convenient but not optimized

sinusoidal position reference, which causes the motor to over-accelerate first and then over-decelerate.

Imagine an ideal world, where there is no friction, gas force or electrical input. In this world, if the valve were pushed to the fully open or closed position and then let go from that point, the whole system would oscillate forever between the two end positions. The spring would provide the inertial power to accelerate and decelerate the valve mass and motor inertia during each transition. Figure 5.1 shows the free oscillation trajectory of the EMV system, obtained by simulation, ignoring friction and gas forces. For comparison, the original sinusoidal reference is also plotted in the same figure. We believe this natural free-flight trajectory could be a better reference in our closed-loop control. With this reference, if the controller works perfectly and our system model is accurate, the motor will act only to cancel friction (and gas force if any) at each point along the trajectory. The springs do exactly what they are intended to do in the ideal case: they provide the reactive power associated with the acceleration and deceleration of the system.

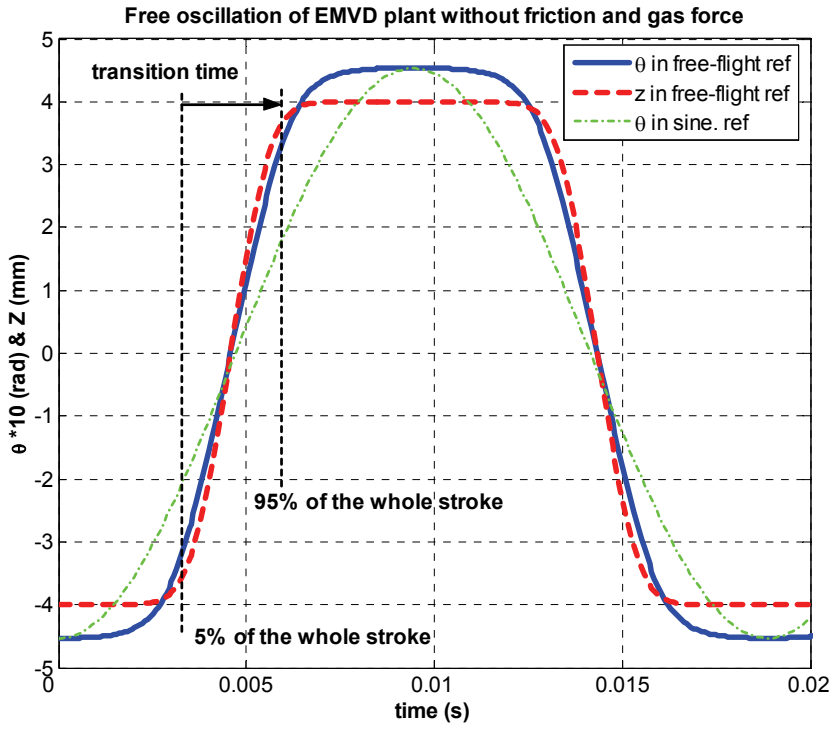

Fig. 5.1. Free-flight trajectory of the EMV system from simulation.

Figures. 5.2 and 5.3 show the simulation and experimental results using the new free-flight trajectory as the position reference. The current profile was improved significantly compared to that with sine trajectory as the position reference shown in Fig. 4.14. An identical transition time of 3.3 ms is achieved while the power consumption is reduced from 140 W to 99 W and the peak torque is lowered from 1.26 N-m to 1.05 N-m.

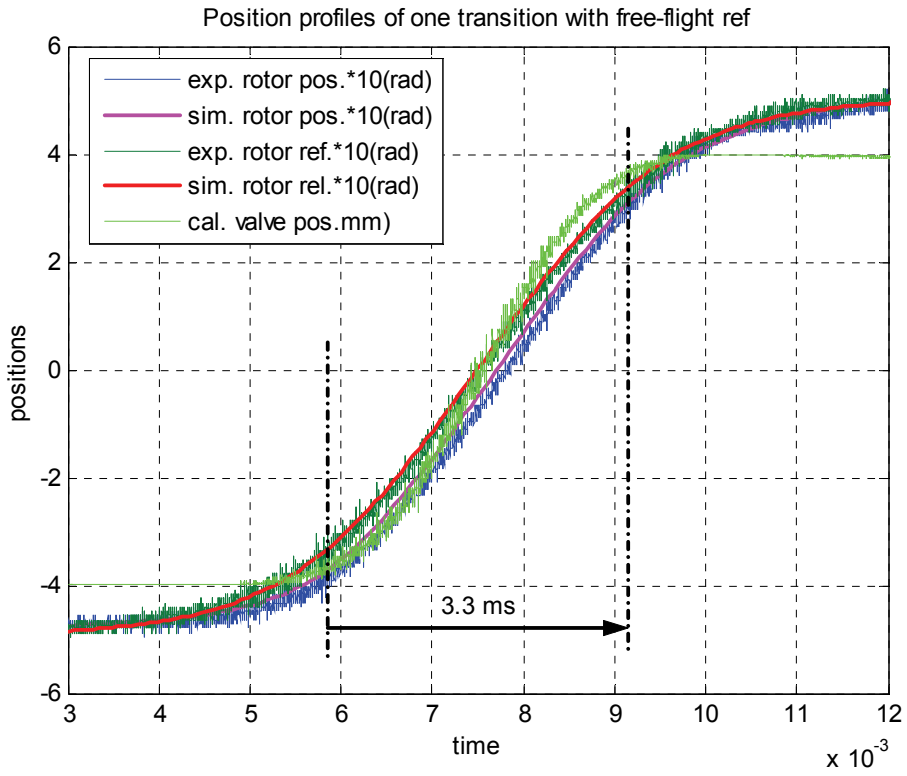

Fig. 5.2. Sim. and exp. position profiles with free-flight position reference.

5.2.2 Low Current Limit Control

With the more accurate friction model, it is possible to predict the profile of total friction torque in the θ-domain, including the friction torque originally generated in the θ-domain and the friction torque reflected into the θ-domain from the friction force in the z-domain. Therefore the concept of feed forward control can be added into our control scheme to achieve lower power consumption and smaller torque requirement, as discussed in this section.

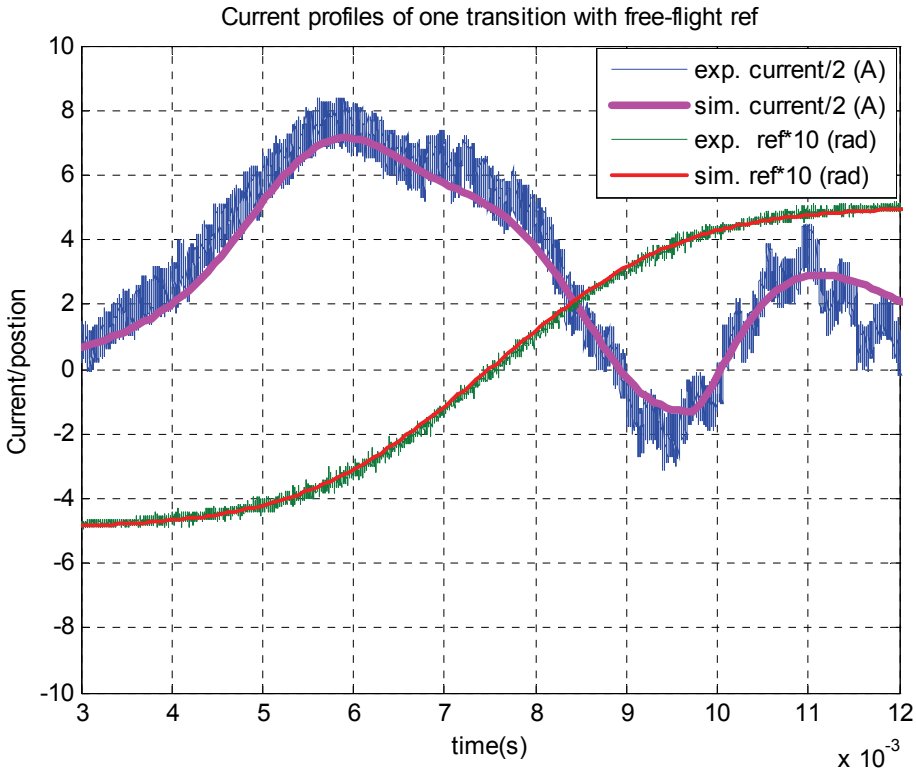

Fig. 5.3. Sim. and exp. current profiles with free-flight position reference.

In Fig. 5.4, the simulation results of one transition with the free-flight trajectory as the position reference are shown, including the actual rotor position, the valve position, the torque generated by the motor and the equivalent total friction torque in the θ-domain. Probably due to a not-so-perfect controller, the motor torque is still much larger than the friction torque during the first half of the transition, thus over-driving the rotor, while the motor has to reverse the torque direction in the second half of the transition to slow down the rotor and make sure it reaches the end with a suitably low velocity. Understandably, there are unnecessary electrical and frictional losses associated with the first over-drive then slow-down process due to the inefficiency of the system. Because the profile of the total friction torque looks more or less like a square wave, a simple idea to improve the situation is to clamp the current and limit the motor torque to a value not in excess of the actual friction torque. Fig. 5.5 shows the simulation results of a successful transition with an 8 A current. A much lower peak torque and rms torque requirement has been achieved with this simple idea, as shown in Table 5.1, which suggests much less energy waste and hence a much lower power consumption.

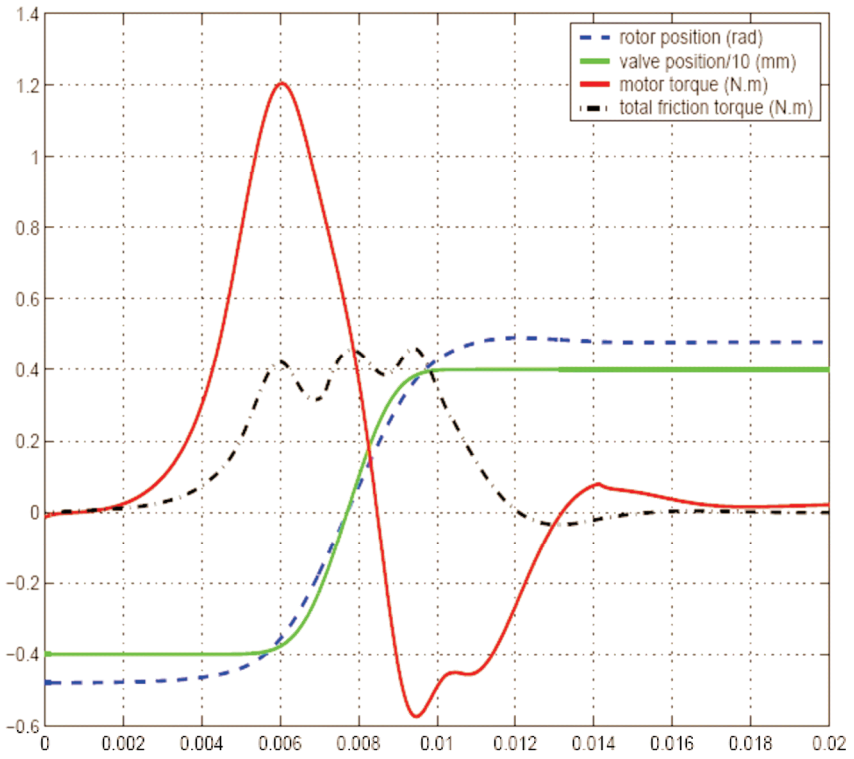

Fig. 5.4. Sim. results with free-flight position reference, no current limit.

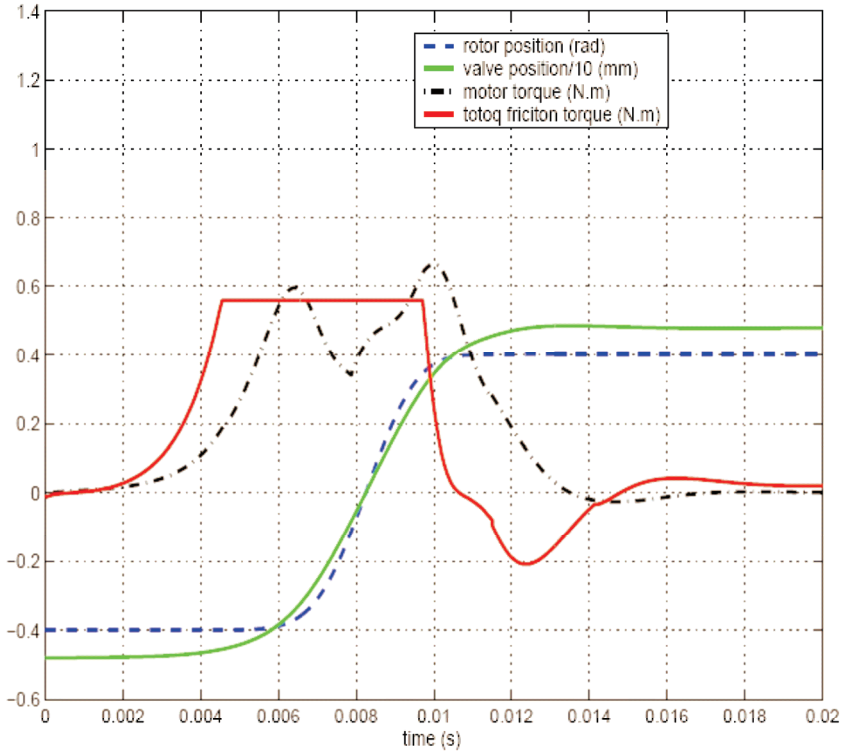

Fig. 5.5. Sim. results with free-flight position reference, 8 A current limit.

The benefits discussed above can be verified by experiment. Figs. 5.6 and 5.7 show position and current profiles of one transition with an 8 A current limit. The power consumption of one transition, including electrical loss and mechanical loss, is reduced further from 99 W to 76 W, peak torque is now reduced from 1.05 N-m to 0.56 N-m while the transition time is 3.4 ms, only a bit slower than previous experiments.

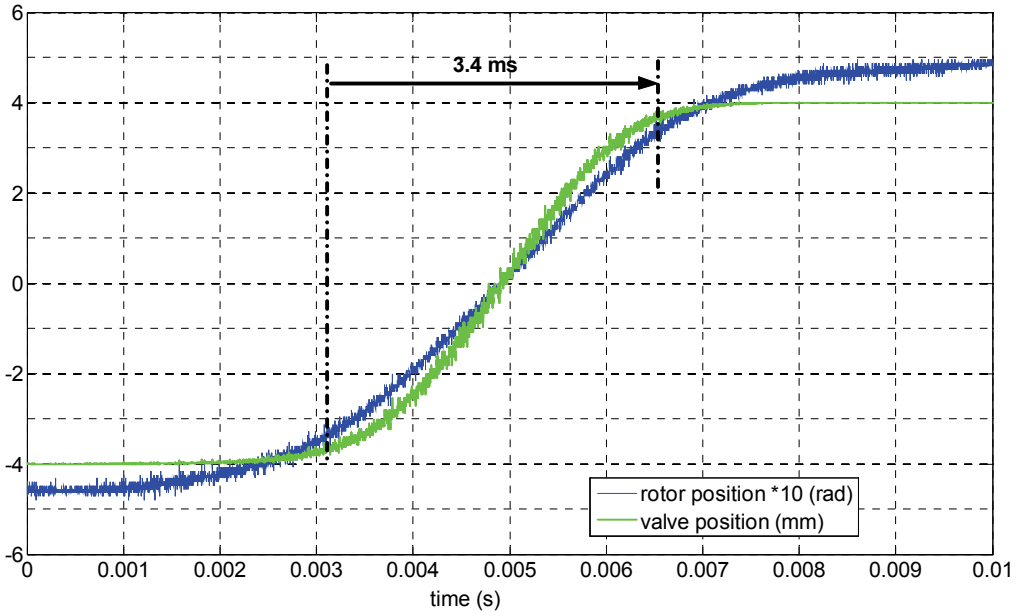

Fig. 5.6. Rotor and valve position profiles from experiment with 8 A limit.

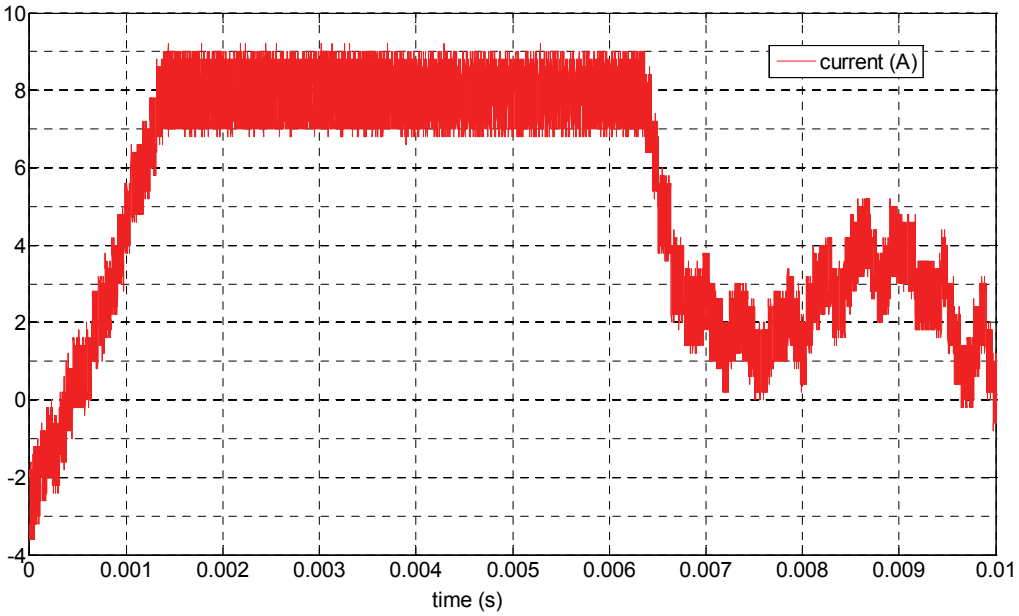

Fig. 5.7. Current profile from experiment with 8 A limit.

TABLE 5.1. TORQUE REQUIREMENTS W/ AND W/O CURRENT LIMIT FROM SIMULATION.

One transition	Peak torque (N-m)	rms torque (N-m)
With no current limit	1.2	0.44
With 8 A current limit	0.56	0.31

5.3 Combination of Closed-loop and Open-loop Control

As discussed in the previous section, the closed-loop position controller forces the actual position to follow the reference position at each point along the transition. However, if we look into the must-have requirements of this project, including the transition time, final position, seating velocity, power consumption, and so on, we realize that we will not care about the position in the initial and middle part of valve trajectory as long as it arrives at the desired final position in the required time with the required velocity. Of course, we can achieve these goals by setting up a reference and forcing the valve to follow it, as was done in the pure closed-loop control discussed in section 5.2. On the other hand, we can go with open-loop control at the initial and middle part of the transition and switch back to closed-loop control during the later part of the transition to ensure a smooth and accurate seating process. In this case, as an alternative of a position versus time reference, a constant position command representing the desired final position will be used in the portion of the closed-loop control.

This kind of combination of closed-loop and open-loop control sometime will be referred to in this thesis as the "kick and capture" strategy, because the initial open-loop current pulse will kick off the transition, the later closed-loop control will capture the valve at its designated position. However, there might be slightly different forms of this same idea, due to the large number of controllable factors in this scheme as well as the different control tradeoffs that we may have under different situations. The controllable parameters include the amplitude and duration of the kick off current pulse, the switching point from open-loop to closed-loop control, the closed-loop control with a constant position command or with a partial free-flight position reference, the closed-loop control with or without current limit, and the current limit of the closed-loop control if applicable. The main tradeoff in this control strategy is power/torque vs. transition time, as will be discussed in more detail next.

The main motivation behind the proposal of this control scheme is the possible benefit of a faster transition owing to the kick-off current pulse from the starting point of each transition. We can take the following experiment for example to show this benefit, whose position trajectories are shown in Fig. 5.8. Figure 5.9 gives out the current profile of this experiment, which starts with a kick-off current pulse of 12 A amplitude and 4 ms duration. Between the end point of kick-off current pulse and the time when the actual position reaches the threshold position, zero command current or torque will apply. After the actual position reaches the threshold position, closed-loop control with a constant position command will take over to ensure smooth valve seating. From the experimental data, we have the transition time reduced from 3.3 ms to 3.0 ms, as shown in Fig. 5.8, a big improvement compared to the pure closed-loop control discussed in section 5.2. However, the power consumption in this experiment is raised back to 140 W, about the same level compared to our starting point where pure closed-loop control with sinusoidal trajectory as the position reference was used as discussed and reviewed in section 3.4.3.

As will be discussed thoroughly in Chapter 6, research on optimization of the cam design, which was conduct in parallel to the study of different control strategies, suggested an optimal cam design in terms of power consumption, torque requirement, and transition time. With this different cam built and fitted into the EMV system, we continued our investigation on control strategies with open-loop control involved. Great results were achieved, as will be presented shortly. Therefore, from this point on, all experimental and simulated results are based on the newly designed cam presented in Chapter 6.

With the new cam fitted in our EMV system, a 8 A kick off current pulse plus closed-loop control with free-flight trajectory as reference offers a transition as fast as 2.5 ms while the power consumption is 82 W. Figs 5.10 and 5.11 show position and current profiles for this case.

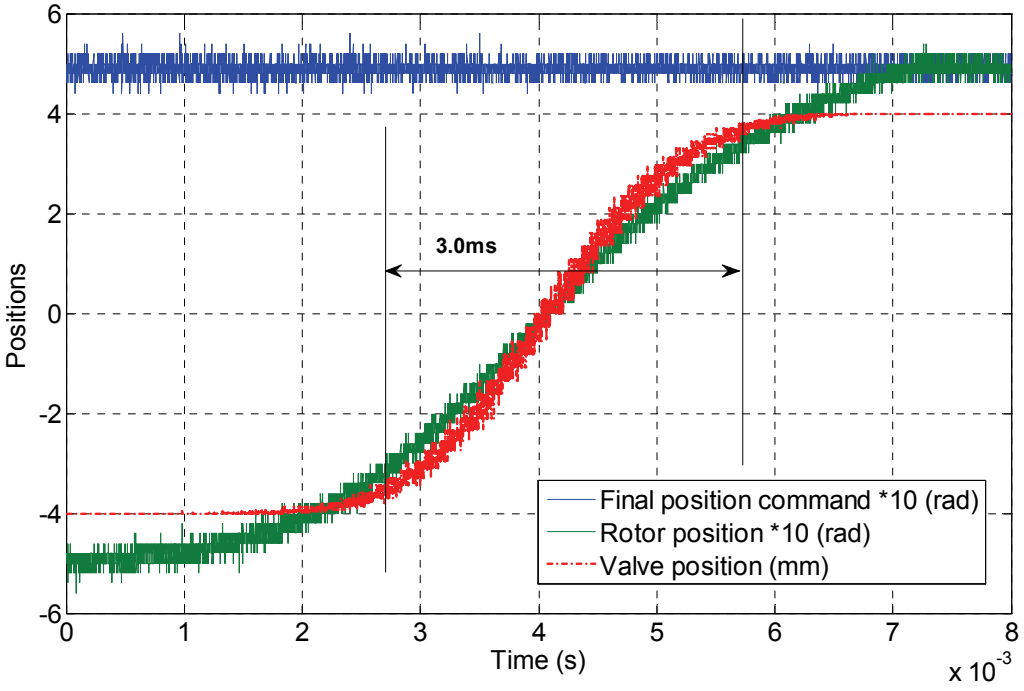

Fig. 5.8. Position profiles with the kick off and capture strategy.

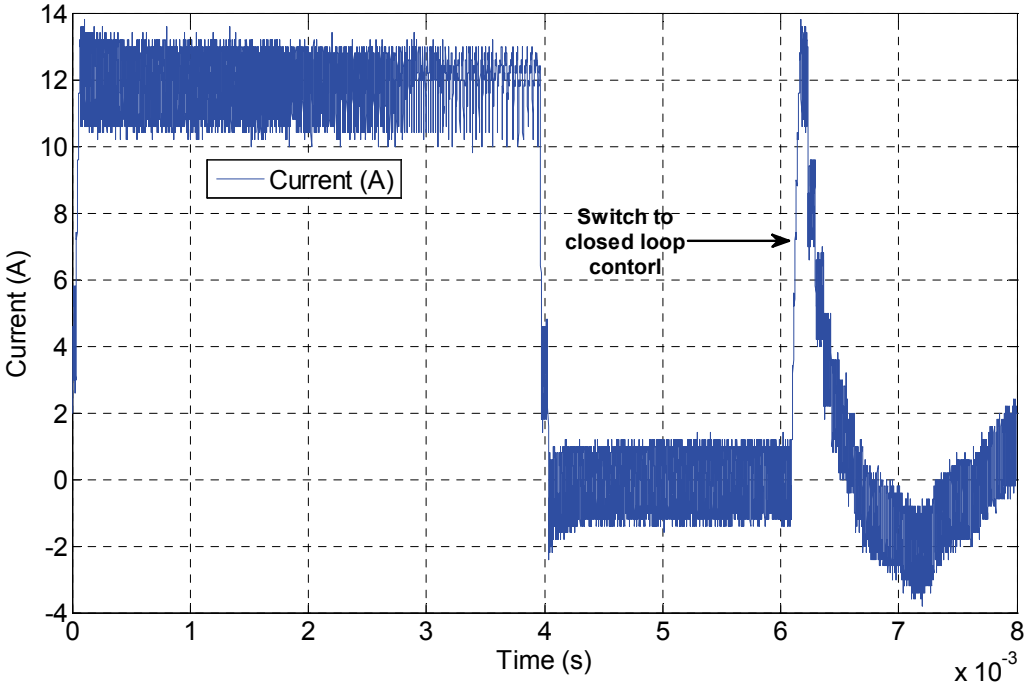

Fig. 5.9. Current profile with the kick off and capture strategy.

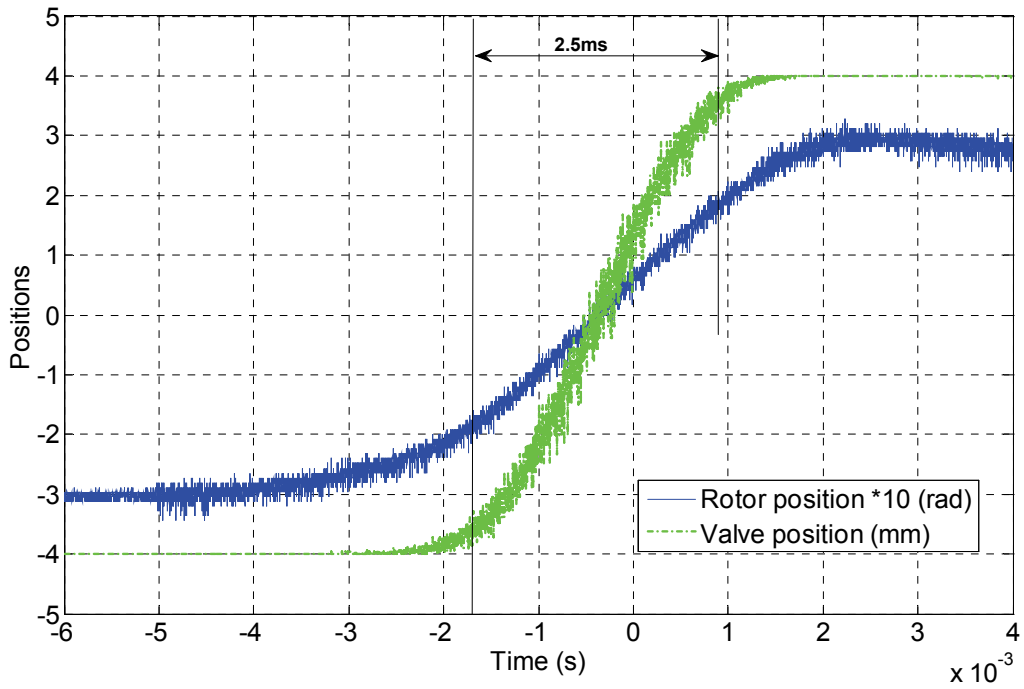

Fig. 5.10. Position profiles with 8 A kick off current pulse.

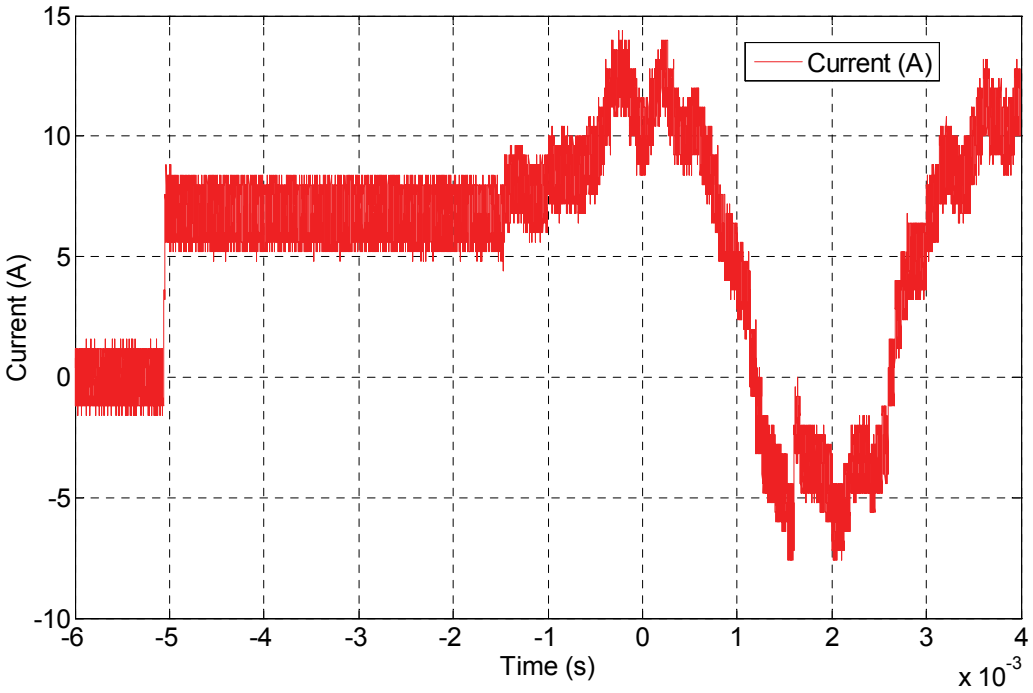

Fig. 5.11. Current profile with 8 A kick off current pulse.

We can reduce power consumption and torque requirement at the expense of longer transition time by adjusting the amplitude and duration of the kick-off pulse. Again, with the new cam fitted in our EMV system, a 5 A kick-off current pulse with free-flight trajectory as reference plus a current limit of ± 5 A, give us a much lower power consumption of 49 W and a bit slower transition time of 2.7 ms instead. The experimental results are shown in Figs. 5.12 and 5.13.

In both experiments described above, we chose to use the later portion of the free-flight position reference instead of final position command during the portion closed-loop control. We also chose to switch to the closed-loop control instantly at the end of the kick off current pulse. These specific control decisions are made mainly based on simulations by trial and error and then confirmed in experiments that they help to require less power and offer smoother landing during transitions.

We have been emphasizing that low power consumption is a highly desirable attribute and the ability to achieve it over most engine operating conditions is very valuable. Nevertheless, at the very highest engine speed, a fast transition is very desirable, and an acceptable penalty in power consumption may be a reasonable price to pay for faster transition. Therefore while keeping low power consumption at common engine speeds, the ability to achieve a quicker transition with an acceptable power increase at fairly high engine speeds will be another attractive benefit owing to the involvement of open-loop control. More discussion in this aspect will be presented in section 5.4.

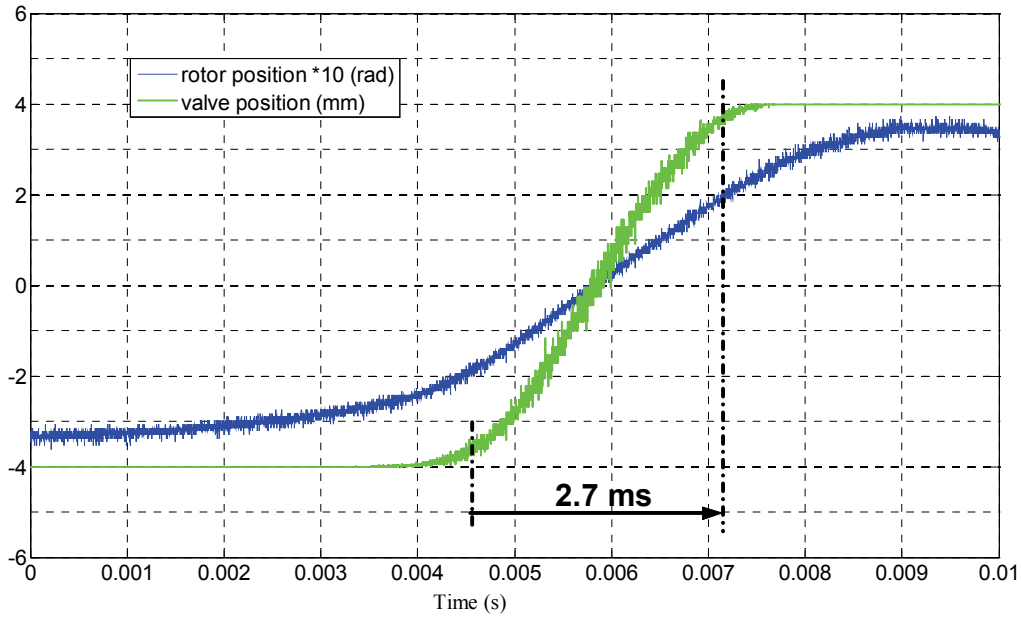

Fig. 5.12. Position profiles with 5 A kick off current pulse.

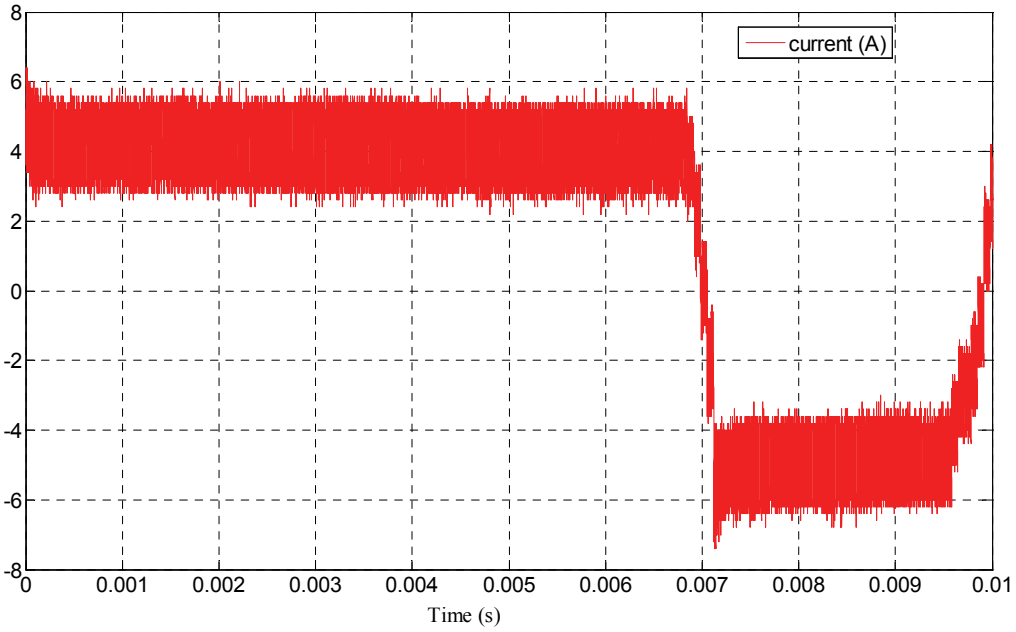

Fig. 5.13. Current profile with 5 A kick off current pulse.

5.4 Pure Open-loop Control

The study of combinations of initial open-loop control and later closed-loop control not only gives us another option to achieve a successful transition, but also indicates to us another way to think about this project, if we dig into the tradeoffs between power consumption and transition time. In other words, we have been considering our control from the perspective of valve position so far. What if we forget about the position for a few seconds, and look at the project from an energy point of view instead?

It is instructive to think of the problem as follows. Consider first 6000 rpm and 3.5 ms as the nominal peak engine speed and valve transition time in this thesis. If we inject just enough energy into the system, the valve will travel pretty much like its free-flight trajectory in an ideal world and give us a transition time very close to the nominal transition time for the nominal engine speed. If we inject more than enough energy early in a transition, the extra energy will speed up the transition, allowing an engine speed higher than the nominal engine speed or more flexibility in engine operation at or below the nominal speed. On the other hand, if we inject less than the enough energy for a nominal transition, the initial transition will proceed more slowly. During this initial interval, both friction and electrical loss power levels will be lower. If we compensate later in the transition with more control effort to achieve the target transition time, the increased power consumption in the later transition will most likely more than compensate the early-reduced energy consumption due to the fight with the springs, producing a higher loss for the complete event. If, instead, we respond to a slower start by continuing to use less control effort, the transition will take longer than the nominal time. But the integrated loss, over the entire transition will, for at least some trajectories, be less than for the nominal case. For slower engine speeds, this may be the preferred choice. Obviously, this is a very attractive combination, enabling optimization of the engine performance at each point.

We will not discuss how to achieve optimal engine performance at different load and speed conditions in this thesis. However, we will apply the energy view to the EMV

system control by investigating the possibility of using pure open-loop control based on single square-shaped current pulse. By adjusting the duration and amplitude of the open-loop current pulse, we achieve successful transitions with different power consumptions and transition times suitable for different engine conditions. Besides the control flexibility it offers, open-loop control is also a simpler and less expensive option than closed-loop controls and may be preferred by the automotive industry for this reason.

At this point, we will focus on low power consumption and low torque requirement for a single transition. In order to reduce power consumption, we need to minimize electrical loss, a main source of power consumption in this application. We also want to decrease the peak torque requirement because it is an important constraint to actuator size. Both objectives are achieved by an open-loop current pulse with as long a duration and as low a constant amplitude as possible for a successful transition.

Satisfactory transitions have been achieved repeatedly with our EMV system after we fitted a new disk cam, as discussed in Chapter 6. The lowest observed power and torque required to guarantee a successful transition were 49 W and 0.3 N-m respectively, achieved by a current pulse with a 4.2 A amplitude and 9 ms duration. The experimental profiles are shown in Figs. 5.14 and 5.15.

Compared to pure closed-loop control, this experiment gives us better results in both power and torque while the transition is a bit slower, for reasons discussed above. On the other hand, we can conclude that this strategy is better than the combination control because this strategy needs an even smaller torque while offering the same power consumption and transition time, and being much easier to implement and maintain in the real world.

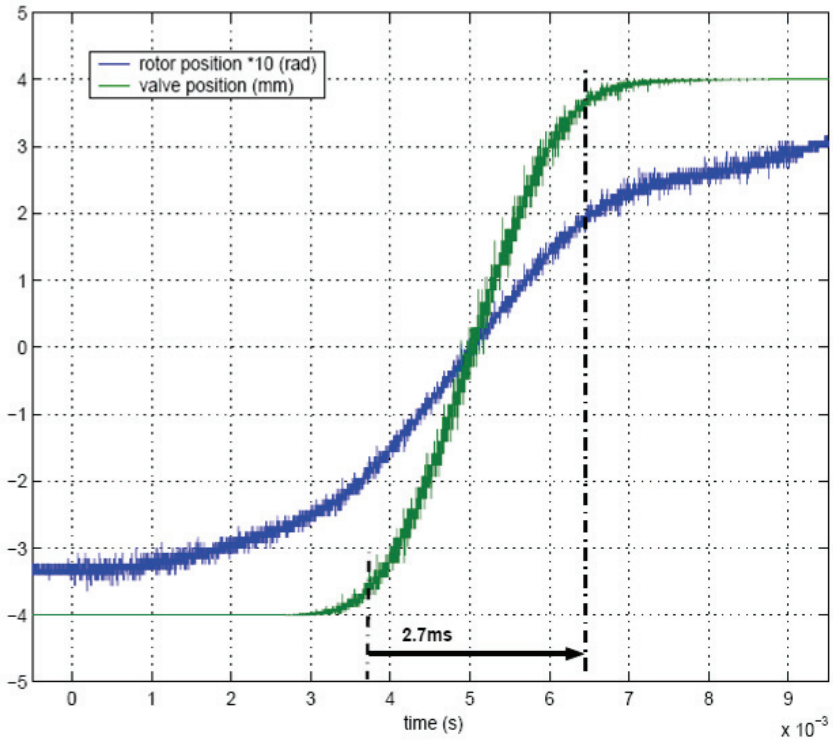

Fig. 5.14. Position profiles with pure open-loop control.

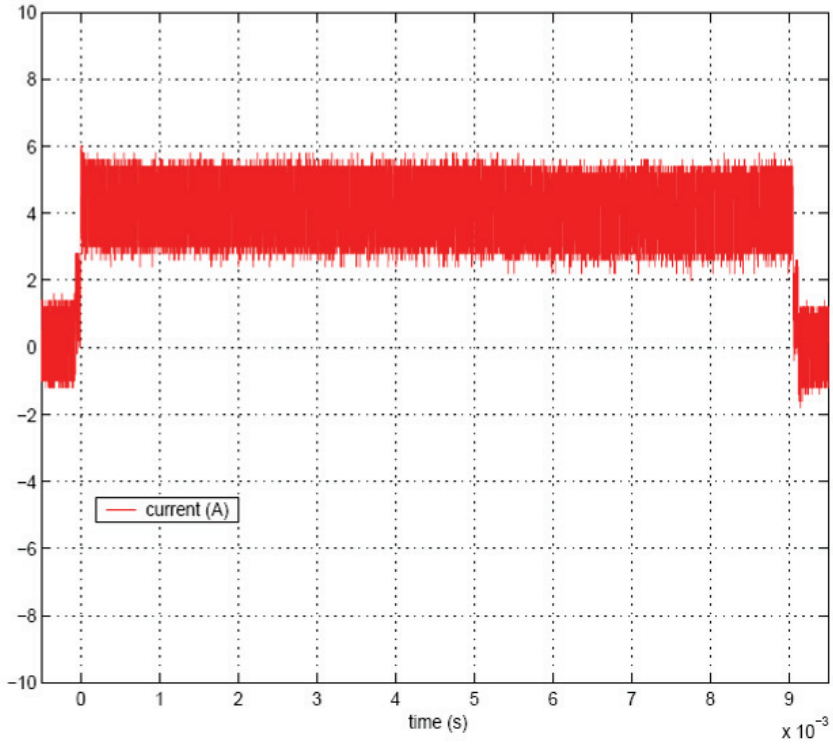

Fig. 5.15. Current profile with pure open-loop control.

To this point, we have discussed three control strategies used in our EMV system: pure closed-loop control, combination of initial open-loop control, and later closed-loop control, and pure open-loop control. Each has its own strengths and drawbacks, as discussed above. For easy comparison of system performance with different control strategies and conditions, all experiments discussed in this chapter have been summarized in Table 5.2. In Table 5.2, the control strategies and hardware conditions of each experiment are described briefly in the first column, while the power consumption, peak torque requirement, and transition time of each experiment are listed in the second to the fourth column respectively.

TABLE 5.2. PERFORMANCE COMPARISON WITH DIFFERENT CONTROL STRATEGIES AND CAMS.

Exp. Setup	Power Consumption (W)	Peak Torque (N-m)	Transition Time (ms)
Starting Point: Old cam, sine ref, and ± 18 A current limit	140	1.26	3.3
Old cam, free-flight ref, and ± 18 A current limit	99	1.05	3.3
Old cam, free-flight ref, ± 8 A current limit	76	0.56	3.4
Old cam, 12 A kick off current pulse, final position command	140	0.84	3.0
New cam, kick off 8 A current pulse, free-flight ref	82	0.88	2.5
New cam, kick off 5 A current pulse, and ± 5 A current limit, free-flight ref	49	0.35	2.7
New cam and 4.2 A, 9 ms open-loop current pulse	49	0.30	2.7

5.5 Input Filter Design

As mentioned in Chapter 4, there are two portions of power loss associated with the winding resistance. Previous sections in this Chapter focus on improving current profile, in terms of peak and rms value, which reduces mainly dc resistance loss. This section will aim at the ac resistance loss instead.

Also briefly discussed in Chapter 4, there are two possible directions to reduce ac loss. One way is to reduce the ripple amplitude and rms value. In the current system, this objective can be achieved by narrowing the hysteresis band in the motor drive. However, the narrower the hysteresis band, the higher the switching frequency, which will increase the equivalent ac resistance and possibly the loss, which is most likely related to frequency quadratically. This approach also imposes a larger stress on switching devices. Therefore this work will focus on the other approach to cut the switching frequency by inserting an input filter, simply a large inductor in this case, in series with the motor. As the switching frequency decreases, so does the equivalent ac resistance. Therefore the ac loss will decrease quickly as desired.

In order to prove the feasibility of this approach, two sets of experiments have been redone with an additional inductor inserted in front of the motor: the zero current command experiment discussed in Chapter 4 and the full transition experiments discussed in sections 5.2-5.4 of this Chapter. The experimental results are discussed below.

- **Zero Current Command Experiments**

In this experiment, we have inserted inductors of 112 μH and 380 μH in series with the brush dc motor in two separate events. The measured ac resistance loss, switching frequency, and equivalent ac resistance in all cases are summarized in Table 5.3. The method to estimate equivalent ac resistance has been discussed in detail in Chapter 4.

TABLE 5.3. AC LOSS W/ OR W/O EXTRA INDUCTOR IN ZERO CURRENT COMMAND EXPERIMENTS.

Zero current command experiments	Ac resistance loss (W)	Ac equivalent resistance (Ω)	Switching frequency (kHz)
Brush dc motor only	16.34	27	150
Brush dc motor with 112 μH inductor	3.77	7.7	40
Brush dc motor with 380 μH inductor	0.97	3.5	14

- **Full Transition Experiments**

An additional inductor has been inserted in series with the motor during most full transition experiments discussed in the previous sections, which confirms the improvements of motor electrical loss, mainly the huge reduction of ac resistance loss. By using this simple approach, we can get rid of most of the ac resistance loss. It is also interesting to notice that the reduced ac resistance loss is almost fixed, as shown in Table 5.4. This is because the hysteretic band in the motor drive is fixed, resulting in the same rms value of the current ripple and the same switch frequency and hence ac resistance of the motor.

TABLE 5.4. POWER CONSUMPTION W/ OR W/O EXTRA INDUCTOR IN ONE TRANSITION.

Exp. Setup	Power Consumption w/o extra inductor (W)	Power Consumption w/ extra inductor of 380 μH (W)	Reduced ac resistance loss (W)
New cam, free-flight ref, ± 8 A current limit	60	42	18
New cam, 5 A kick off current pulse, free-flight ref, and ± 5 A current limit	49	32	17
New cam, 4.2 A, 9 ms	49	31	18

At this point, we have discussed different control strategies, including the pure closed-loop control, the combination of open-loop and closed-loop control, and the pure open-loop control, in order to minimize the dc resistance loss. From the preceding, we can summarize that the dc resistance loss can be reduced significantly and more flexibility in transition time can be achieved when open-loop control is exploited. We have also shown that with a simple inductor design, we can eliminate most of the ac resistance loss.

In the next chapter, we focus on mechanical loss (or frictional loss) minimization. Because the cam friction dominates the total friction force, we will explore the possibility of a better cam design which generates less friction force during the valve transition and therefore requires less power compensation and torque drive. As already partially

revealed in the later portion of this chapter, and as will be discussed in detail in the next chapter, the new design of the cam not only reduces frictional loss, but also reduces electrical loss and transition time.

CHAPTER 6 OPTIMIZATION OF THE NMT DESIGN

6.1 Introduction

In Chapter 5, we have discussed different control strategies based on more effective system modeling. Similarly, from the nonlinear friction model discussed in Chapter 4, we have shown that the friction force in the EMV system is dominated by the nonlinear friction force existing at the rotor shaft of the motor and roller follower in the disk cam. Naturally, a more thorough study of the disk cam design becomes important as it will affect this component of friction force and hence the system performance significantly.

For the first disk cam design, Dr. Chang chose a sinusoidal function for simplicity to fulfill the relation between displacements in two domains, and an angular range of $\pm 26^o$ in the θ-domain was used based on analyzing a linearized EMV system in the middle of the stroke [17]. This chapter poses two design questions:

1. Other than the sinusoidal function, is there a function which will offer better system performance while maintaining the desired features of being flat at both ends?

2. Based on numerical simulation of the whole system dynamics, will there be an optimal angular range other than $\pm 26^o$?

The ultimate goal of this chapter is to answer these two questions.

In this chapter, we will start by reviewing design considerations for a NMT before presenting two possible directions of optimization in order to answer these questions. A simplified analysis is presented, which predicts benefits in torque requirement, power consumption, and transition time from θ-range optimization. An NMT design with an optimal θ-range and sinusoidal function was found based on numerical simulations in

20-sim®. Then a new disk cam was designed via Matlab® and SolidWorks®. Finally, experimental results confirm the expected improvements in torque, power, and transition time before some other possible designs, which could enhance certain aspects of the system performance, are discussed briefly.

6.2 Design Considerations of the NMT

6.2.1 Pros and Cons of the NMT

As discussed in Chapter 3, there are at least three strengths of the NMT design. They are inherent soft landing, zero holding power, and reduced peak torque and rms torque. However, discussion in the last several chapters has already revealed that the nonlinear design can also cause some complications for our control and design because it makes the whole system inherently nonlinear, making it very difficult to analyze system dynamics by analytical methods. Therefore, we have to rely heavily on numerical simulations to help predict effects of different control strategies and hardware designs, as partially shown in the last two chapters.

6.2.2 Design Goals of the NMT

Changing the design of the NMT will affect the performance of the whole EMV system in the following ways. First of all, the friction force, including amplitude and distribution, will be different, which in turn will require a different motor torque output to achieve the transition. This change will also affect the power consumption of the motor due to the differences in both frictional and winding losses. Secondly, the natural frequency of the system may also be changed, not only because the transformer may have a different value of inertia but also because the total inertia in the θ-domain will be translated into a different value of mass in the z-domain due to the different ratio. The change in the natural frequency will have an impact on transition time of the system. It will also affect the friction force related to velocity and hence the torque requirement and power consumption.

As a result of the previous discussion, we will summarize our design objective as follows. We will pick a design which will not only have a smaller friction force requiring a

smaller torque and power requirement and but also offer a smaller effective mass in the z-domain for a faster transition.

6.3 Two Possible Directions for a Better Design

As mentioned previously, in our first experimental apparatus, the relation between θ and z over the range of valve stroke is a sinusoidal function, as shown in (6.1).

$$z = g(\theta) = 4\frac{\sin(3.46\theta)}{\sin(0.999\pi/2)} \text{ mm} \qquad |\theta| \le 0.454 \text{ rad } (26°) \tag{6.1}$$

With a motor rotation within $\pm 26^o$, the valve will move up and down ± 4 mm to provide a stroke of 8 mm.

The relation between modulus (or slope $\frac{dz}{d\theta}$) and θ can be derived as a cosine relation, as shown in (6.2),

$$\frac{dz}{d\theta} = 4 \cdot 3.46 \cdot \frac{\cos(3.46\theta)}{\sin(0.999\pi/2)} \frac{\text{mm}}{\text{rad}} \qquad |\theta| \le 0.454 \text{ rad}(26°) \tag{6.2}$$

Note that in the relation represented by the NMT, only the length of the valve stroke is fixed by the application as 8 mm. In other words, the function between θ and z as well as the rotating range of the motor in the θ-domain are both flexible and can be designed differently to meet different purposes, which represents two major directions in terms of NMT design optimization. We call these two directions as "function optimization" and "θ-range optimization", which will be discussed next.

6.3.1 Function Optimization

To do research on function optimization, we first need to explore what kind of function we could use to implement the desired modulus characteristics? We set the necessary requirements of the NMT function as follows:

1. Zero modulus (slope) at both ends;
2. Only one maximum modulus in the middle of the stroke;
3. Smooth profile from one end to the other;
4. Symmetric profile with respect to zero position (i.e., equilibrium point) for simplicity.

Note that the fourth requirement may be relaxed (perhaps with great benefits) in the case of an exhaust valve, because of the asymmetric requirements for opening and closing, as will be discussed in the last section of this chapter.

Besides the cosine function used in our preliminary experiments, we have done some research searching for possible modulus functions for our NMT design. There are at least three other function families which have been identified as possible candidates in our application.

The first is the family of power functions, where the exponent is an even number, as shown in (6.3),

$$\frac{dz}{d\theta} = -a \cdot \theta^{2b} + c \tag{6.3}$$

where a and c are positive numbers and b is a positive integer to ensure the desired modulus characteristics.

The second is the family of secant functions, i.e., the reciprocal of cosine functions. The general formula of this family is shown in (6.4),

$$\frac{dz}{d\theta} = -a \cdot \sec(b \cdot \theta) + c \tag{6.4}$$

where a, b and c are all positive numbers to ensure the desired modulus characteristics.

The third candidate function is called “sinc” as well as “sampling function”, where it is defined as follows,

$$\frac{dz}{d\theta} = a \cdot \sin(b \cdot \theta)/\theta + c \quad \theta \neq 0$$
$$\frac{dz}{d\theta} = 1 \quad \theta = 0 \tag{6.5}$$

where a, b and c are all positive numbers to ensure the desired modulus characteristics.

Figure 6.1 shows one example of each function family in terms of modulus versus θ displacement, including the cosine function used in our early work. All offer the same peak modulus and same θ rotation range.

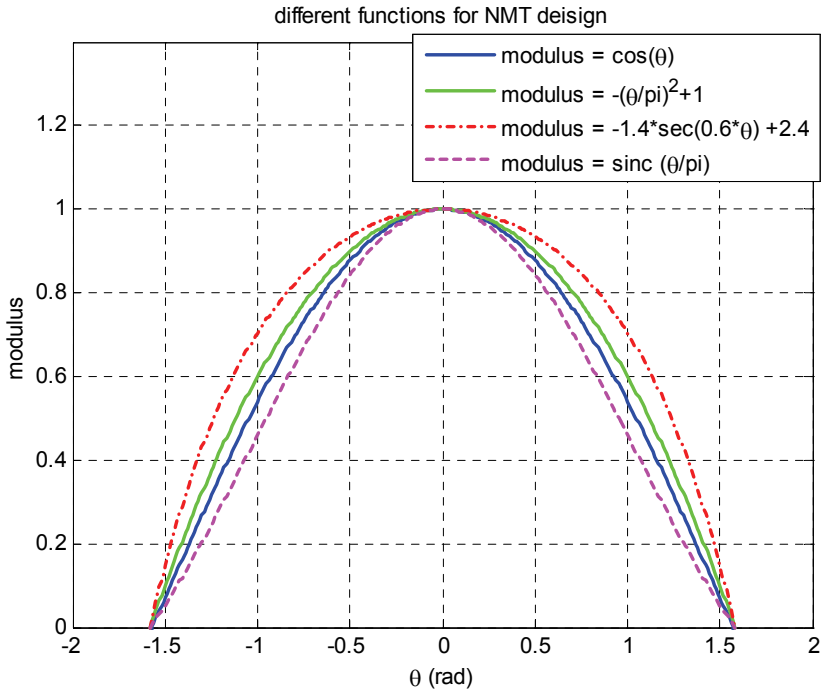

Fig. 6.1. Different modulus functions.

Because analytically there are no obvious clues pointing to large impacts on power consumption and torque requirements of different modulus functions, they were plugged

into the system in our simulation package. Simulation results showed that there are no big performance differences among different modulus function within the same θ-range. This result leads us to focus our attention on another approach of different transformer design, i.e., the θ-range optimization.

6.3.2 θ-range Optimization

To clarify θ-range optimization in the sense of minimum power consumption and torque requirement, let's assume the mechanical transformer has a constant modulus, rather than a varying one, along the stroke. If $\theta_{\max}$ is the half range of rotor rotation and $z_{\max}$ is the half range of valve lift, then we define the nominal modulus M as in (6.6),

$$M = z_{\max} / \theta_{\max} \tag{6.6}$$

Therefore, we can rewrite the transformer equations (3.1), (3.2), and (3.5) in Chapter 3 as follows,

$$z = M \cdot \theta \tag{6.7}$$

$$\frac{dz}{dt} = M \cdot \frac{d\theta}{dt} \tag{6.8}$$

$$\tau_\theta = M \cdot f_z \tag{6.9}$$

And the inertia in the θ-domain, J_θ, can be reflected into the z-domain as m_θ, via the relation shown in (6.10),

$$m_\theta = J_\theta / M^2 \tag{6.10}$$

From the equations above, we can make two simple arguments. First, if given fixed valve lift of 8 mm and fixed transition time requirement of 3.5 ms, the average valve velocity during one transition is also fixed. Therefore, from (6.8), the average rotor angular velocity under those conditions will be purely decided by the ratio M. In other words,

with a bigger M, we will have a smaller average rotating velocity of the rotor and vice versa. This will affect those friction forces that are function of rotating velocity and hence the torque and power needed to complete a transition. Secondly, from the perspective of the springs, the total driven mass includes the mass in the *z*-domain and the reflected mass of the inertia in the θ-domain. From (6.10), a bigger M results in a smaller reflected inertial mass and hence a smaller total effective mass in the *z*-domain. Therefore with a given spring constant, the natural frequency of the whole system will be higher, which will very likely result in a faster valve transition. Alternatively, a lower spring constant can be specified, with a possible further reduction of friction.

The impacts on system performance from having different ratio M can be more complicated. As thoroughly discussed in Chapter 4, we obtain the equations describing friction force in the θ-domain for an intake valve where gas force disturbance is ignored, as represented in (6.11) and (6.12),

$$f_\theta = B_{\theta b}\frac{d\theta}{dt} + F_n \cdot (B_{\theta v}\frac{d\theta}{dt} + B_{\theta c}\,\mathrm{sgn}(\frac{d\theta}{dt})) \tag{6.11}$$

$$f_{cam} = F_n \cdot (B_{\theta v}\frac{d\theta}{dt} + B_{\theta c}\,\mathrm{sgn}(\frac{d\theta}{dt})) \tag{6.12}$$

where f_θ is the total friction force in the θ-domain and f_{cam} represents the nonlinear portion related to the normal force F_n which varies along the transition.

As discussed above, a different M will result in a different average rotating speed $\frac{d\theta}{dt}$. Now we will show that a different M will also change the normal force F_n at the rolling contact between the roller surface and cam slot surface. As shown in Chapter 4, the normal force F_n is determined by several factors including spring force F_s, *z*-domain friction force f_z, *z*-domain inertial force f_m, and nominal ratio M, as shown in (6.13)-(6.17),

$$F_n = (F_s - f_z - f_m) \cdot \cos(\alpha) \tag{6.13}$$

$$F_s = K_s z \tag{6.14}$$

$$f_z = b_z \frac{dz}{dt} \tag{6.15}$$

$$f_m = m_z \frac{d^2 z}{dt^2} \tag{6.16}$$

$$\alpha = \text{atan}(M) \tag{6.17}$$

As discussed above, the reflected mass m_θ from the θ-domain inertia J_θ will be smaller if given a bigger ratio M. The decreased m_θ means the inertial force offered by the springs to the cam and rotor, $(F_s - f_z - f_m)$, will decrease, too, if $(F_s - f_z)$ remains unchanged. Furthermore, a bigger cam ratio M will result a smaller slope factor $\cos(\alpha)$. Both changes will reduce the normal force F_n and hence the related friction force.

On the other hand, given the constant travel distance of the valve and the faster transition time, a higher valve velocity and therefore a larger viscous friction forces f_z in the z-domain can be expected. At the same time, from (6.13), we can tell that this increased valve friction f_z will reduce the normal force F_n and, accordingly, the nonlinear friction force f_{cam} in the θ-domain. In other words, with M increasing, the nonlinear friction force f_{cam} will be decreasing while the valve friction force f_z will be increasing. Additionally, with M increasing, the same amount of friction force in the *z*-domain will be reflected into a bigger friction torque in the θ-domain, as shown in (6.9). As a result, when increasing M to certain point, from the actuator's perspective, the nonlinear friction force f_{cam} in the θ-domain will no longer dominate the linear friction force f_z in the *z*-domain and a minimum friction torque in total can be expected. If we increase M beyond that point, the total friction torque in the θ-domain will begin to increase again.

As for the impact on the viscous friction of the motor bearing, the linear portion of the friction force in the θ-domain, there are contradicting trends owing to a smaller θ-range

with a faster transition. Nevertheless, simulation suggests that for our current setup, the change of the bearing friction, if any, will not affect the whole friction torque much due to its small percentage. So it will not be our focus of discussion at this moment.

From discussion above, we can make two main points regarding a linear transformer with a differing nominal cam ratios M. First, with a bigger M, a higher natural frequency and a shorter transition time is expected; Second, with a bigger M, the nonlinear friction force related to the normal force in the cam will be reduced while the linear friction force in the *z*-domain will be increased. There should be at least one M which will give us the minimum value of total friction force/torque from the motor's perspective, which will result in the lowest torque requirement and power consumption. Therefore, for the case of a linear transformer, it is very promising to find the best ratio M which gives a faster transition with the lowest power consumption and torque requirement. We believe that the principles discussed above for a linear transformer apply equally to NMTs, although we have to rely on numerical simulations to confirm those possible improvements for a nonlinear transformer.

6.4 An Optimal Design for Our Purpose

6.4.1 Optimal Angular Range

With the direction pointed out above by the analysis for a linear transformer with different angular ranges, we conducted a series of numerical simulations of our EMV system using a nonlinear transformer which maintains a sinusoidal relation between a fixed valve lift of 8 mm and a angular range varying from $\pm 26^o$ to $\pm 7.5^o$ in the θ-domain. The simulation results of peak torque, rms torque and transition time are shown in Fig. 6.2.

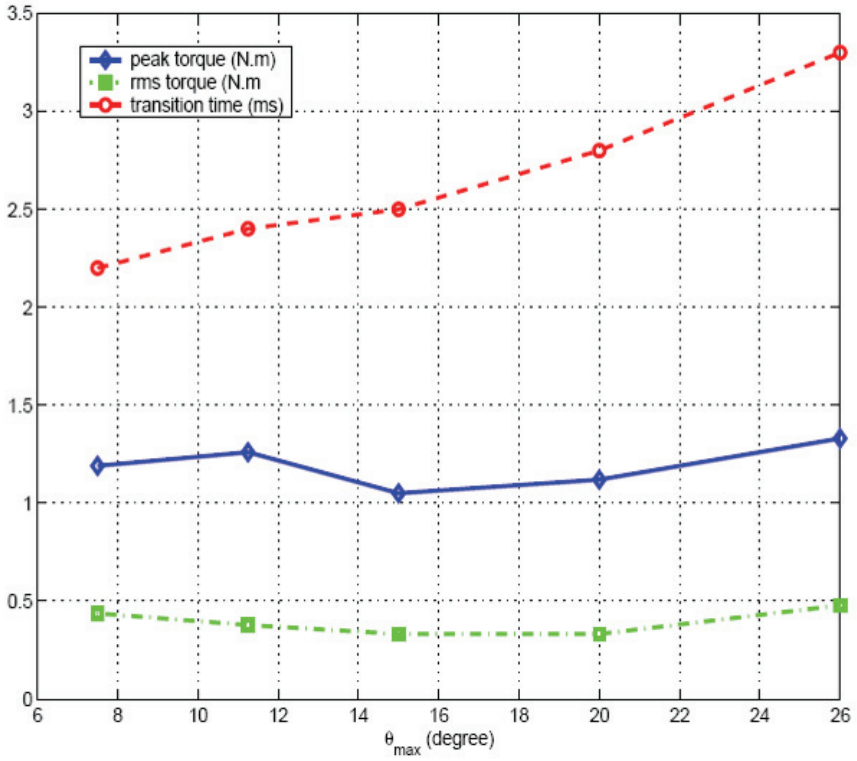

Fig. 6.2. Peak torque, rms torque, and transition time as a function of θ-range.

From Fig. 6.2, we can see that the transition time decreases with decreasing angular range. On the other hand, the peak torque and rms torque both decrease first and then increase with decreasing angular range. The simulation results confirm the previous analysis and the local optimal θ-range is $\pm 15^o$ as shown in Fig. 6.2. Therefore, the desired z vs. θ characteristics can be described in (6.18). With the θ-range of $\pm 15^o$, we can expect about 40% decrease in power consumption loss and a faster transition time of 2.5 ms.

$$z = g(\theta) = 4\frac{\sin(6\theta)}{\sin(0.999\pi/2)} mm \qquad |\theta| \le 0.262 rad(15^o) \tag{6.18}$$

6.4.2 Design of the New Cam

Figure 6.3 is the first cam used in our EMV system. There are at least six physical dimensions that we care about in its design --- the thickness of the cam s (vertical to the picture and not shown in the figure), the diameter of motor shaft hole $D1$, the diameter of

roller follower $D2$, the effective angular range $\pm\theta_{\max}$, the extended flat length range L_e and accordingly the corresponding flat angular range θ_e at each end, and the distance h between the motor shaft and roller follower centers when the cam is located at the equilibrium point $\theta = 0^o$.

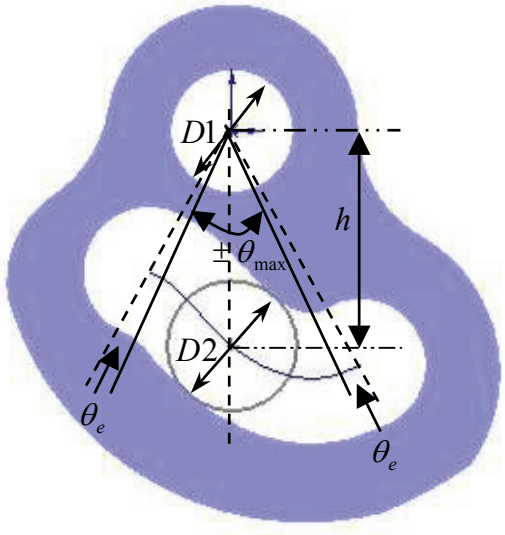

Fig. 6.3. Important physical parameters in a cam design.

At this point, the dimensions $D1$ and $D2$ are unchanged and $\theta_{\max} = 15^o$ is assumed for reasons explained in the previous subsection. Selecting the distance h for the new cam turns out to be tricky because it has to be bigger than h for the old cam to guarantee a smooth slot at both ends, as will be discussed shortly. At the same time, it cannot be too big, in order to keep the cam inertia low enough. Also, to minimize inertia, a reduced but still adequate cam thickness s will be chosen and nonfunctional holes will be added. Therefore, we follow these steps to finish the new cam design:

1. Use Matlab® to find the minimum $h_{\min}$ to ensure a smooth (continuous derivative) slot profile from end to end including extended flat area;

2. Pick h slightly bigger than $h_{\min}$ for our cam design to offer some tolerance where $h_{\min}$ is the minimum height to assure a smooth slot at both ends.

3. Set the extended flat length range L_e and the flat angular range θ_e at each end accordingly;

4. Based on the slot profile generated in Matlab®, design a new cam in 3D SolidWorks®;

5. Adjust the thickness of the cam and create nonfunctional hole if necessary to meet the requirements of both inertia limitation and enough mechanical strength.

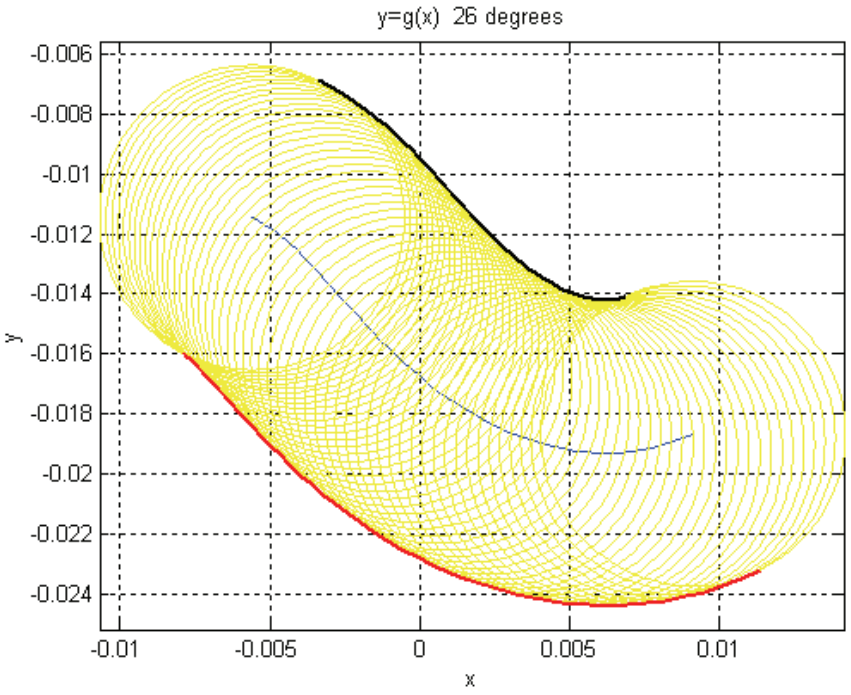

Fig. 6.4. Roller trajectory with $h = 16.75$ mm and $\theta_{\max} = 26^o$ in the x-y plane.

Function-wise the most important element of the cam follower is the cam slot. Our basic approach of slot design is as follows: first, we will put a cross section of the roller follower inside the desired slot at the equilibrium point $\theta = 0^o$, as shown in Fig. 6.3; then we will let the circle roll to the two end positions $\theta = \pm\theta_{\max}$ respectively with its center trajectory following the expected modulus function. By keeping all the circumferences of the circle at each position during the full transition, a slot shaped for the desired motion is obtained, as shown in Fig. 6.4 for $\theta_{\max} = 26^o$ of the old cam.

However, if we keep the distance h constant while decreasing $\theta_{\max}$, there will be a point where the roller follower begins to roll backwards at both end areas to meet the z vs. θ relation, which will result a non-smooth slot surface with abrupt turnings at both ends, as shown in Figs. 6.5 and 6.6.

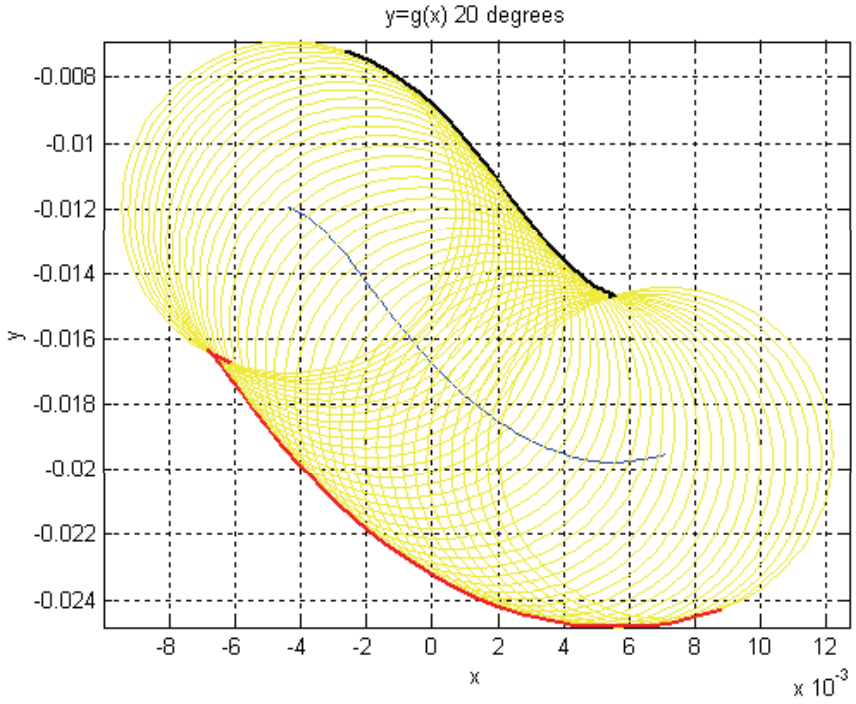

Fig. 6.5. Roller trajectory with $h = 16.75\,\text{mm}$ and $\theta_{\max} = 20^o$ in the x-y plane.

In order to obtain a smooth slot design between the two ends, we have to increase h to compensate for the problem caused by a decrease of $\theta_{\max}$. For $\theta_{\max} = 15^o$, calculations shows that we need a $h \geq 28.55\,\text{mm}$ to ensure smooth surface at both ends of the slot. Taking consideration the need for extended regions at both ends, we chose $h = 28.75\,\text{mm}$, which results in the slot design shown in Figs. 6.7 and 6.8, which show the trajectories with and without the extended areas, respectively.

We designed the extend area at both ends with $L_e = 2mm$, which results in an extended angular range $\theta_e = 4^o$ at the closing end and $\theta_e = 5^o$ at the opening end, as shown in Fig. 6.9.

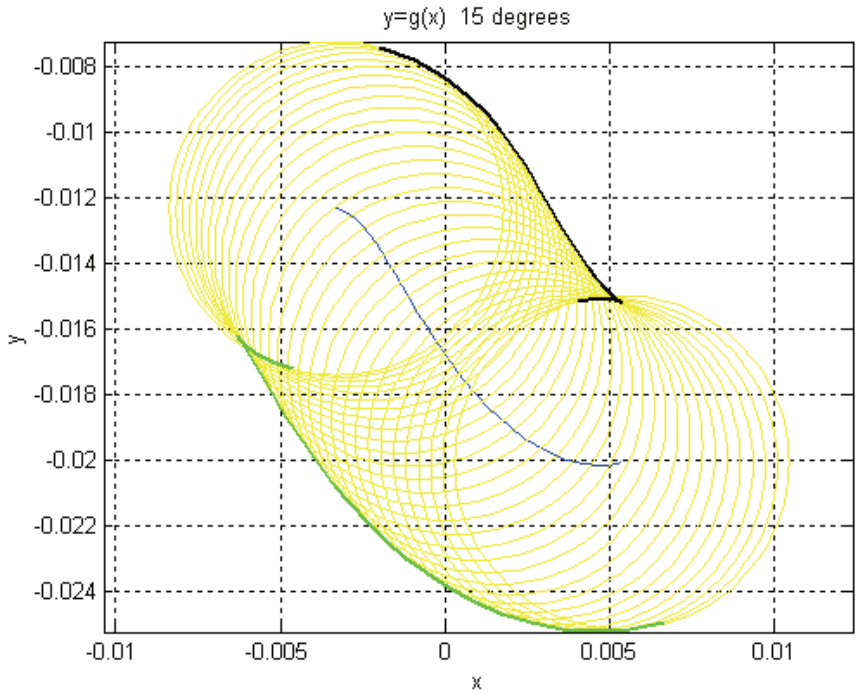

Fig. 6.6. Roller trajectory with $h = 16.75\,\text{mm}$ and $\theta_{\max} = 15^{o}$ in the x-y plane.

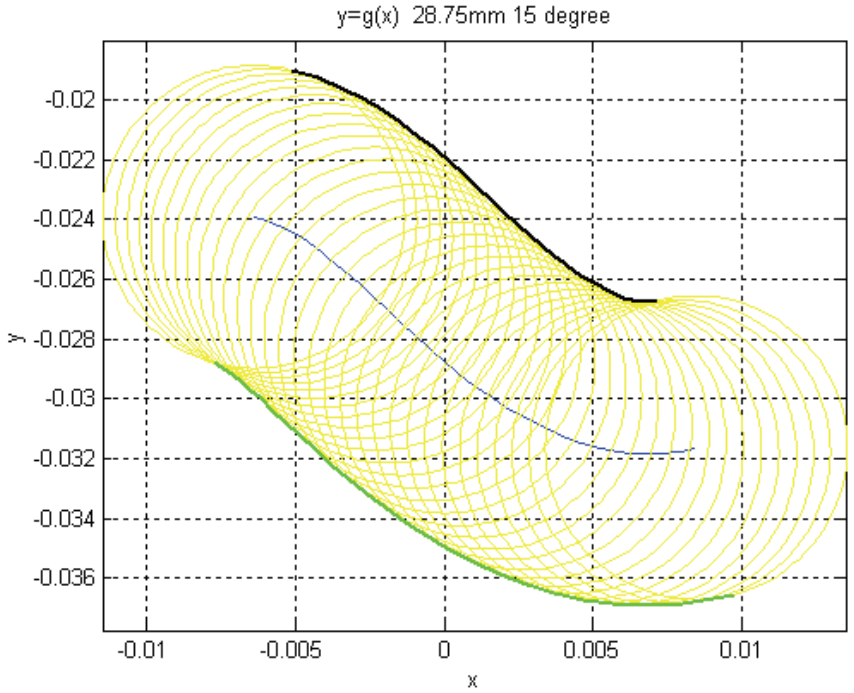

Fig. 6.7. Roller trajectory with $h = 28.75\,\text{mm}$ and $\theta_{\max} = 15^{o}$ in the x-y plane.

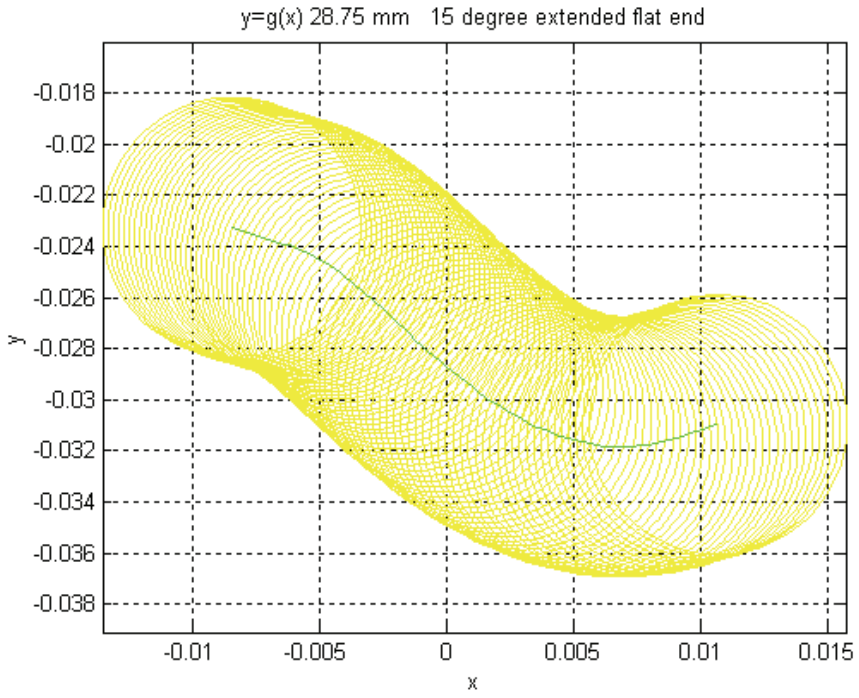

Fig. 6.8. Roller trajectory with $h = 28.75\,\text{mm}$, $\theta_{\max} = 15^o$, $L_e = 2\,\text{mm}$ in the x-y plane.

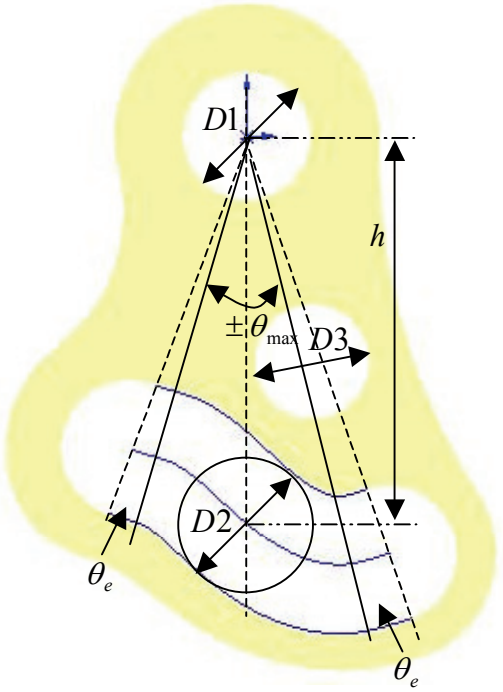

Fig. 6.9. Final design of the new $\pm 15^o$ cam.

In order to maintain the same inertia compared to the old disk cam, we have to reduce the thickness of the cam from 6 mm to 4.75 mm and add the nonfunctional hole shown in Fig. 6.9. Finite element analysis in SolidWorks® has been done to make sure the new cam with reduced thickness and added extra hole has enough mechanical strength for this application.

The final design of the new cam with $\theta_{\max} = 15^o$ is shown in Fig. 6.9. The cam drawing in SolidWorks® is attached in Appendix II. The physical parameters of both the old cam and the new cam are summarized in Table 6.1.

TABLE 6.1. COMPARISON OF THE OLD CAM AND THE NEW CAM DESIGNS.

	Old Cam	New Cam
Shaft Hole Diameter $D1$	9.5 mm	9.5 mm
Roller Hole Diameter $D2$	10 mm	10 mm
Effective Range $\pm\theta_{\max}$	$\pm 26^o$	$\pm 15^o$
Extended Range L_e	2 mm	2 mm
Distance h	16.75 mm	28.75 mm
Thickness s	6 mm	4.75 mm
Extra Hole Diameter $D3$	N/A	8.5 mm
Cam Inertia J	$1.23 \cdot 10^{-5}$ Kg·m^2/s	$1.23 \cdot 10^{-5}$ Kg·m^2/s

6.4.3 Experimental Verification

This section will present the experimental results using the new cam under several different control strategies, including pure closed-loop control, combination of closed-loop and open-loop control, and pure open-loop control. Although some experimental results have already been presented in Chapter 5 when we discussed different control strategies, we will repeat them in this chapter for reader's convenience.

We now present the experimental results of tests using the new cam with the three control strategies. Table 6.2 presents these experiments compared with those using the old cam as described in Chapter 5.

- **Pure closed-loop control with the free flight trajectory as reference**

After replacing the old $\pm 26^o$ cam with the new $\pm 15^o$ cam in our EMV system, we first tried the pure closed-loop control with the free flight trajectory as the position reference and set the current limit as $\pm 8\,\mathrm{A}$, the same setup used in the experiment with the old cam. Figs 6.10 and 6.11 show the position and current profiles during one transition. Improvements in power consumption, torque requirement, and transition time have been achieved, as shown in Table 6.2.

- **Combination of open-loop and closed-loop control**

Two different directions of this control strategy were explored in this experiment. First, in order to speed up the transition, we start with an $8\,\mathrm{A}$ open-loop current pulse and then switch back to closed-loop control at the end of the pulse, still using the free flight trajectory as the reference. The position and current profiles of one transition with this control arrangement were shown in Figs. 5.10 and 5.11. Then, in order to further reduce power consumption and torque requirement, we start with a 5 A open-loop current pulse and then switch back to closed-loop control with a $\pm 5\,\mathrm{A}$ current limit. The position and current profiles of one transition with this control arrangement are shown in Figs. 5.12 and 5.13.

- **Pure open-loop control with a 4.2 A, 9 ms current pulse**

This experiment explores pure open-loop control using one current pulse to initiate the transition. The amplitude and duration of the current pulse can be adjusted in order to meet different performance goals. As discussed in Chapter 5, a current pulse with lower amplitude but longer duration will generally yield lower power consumption but a slower transition. On the other hand, a current pulse with higher amplitude but shorter duration will result in a faster transition but a higher power consumption. Figs 5.14 and 5.15 present the position and current profiles with a 4.2 A, 9 ms open-loop current pulse.

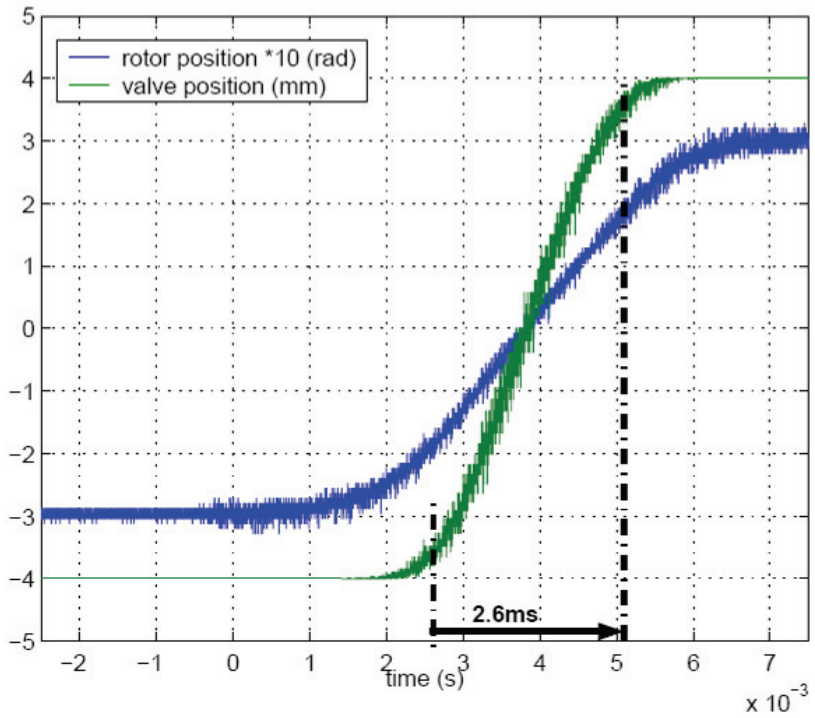

Fig. 6.10. Position profiles with new cam and pure closed-loop control.

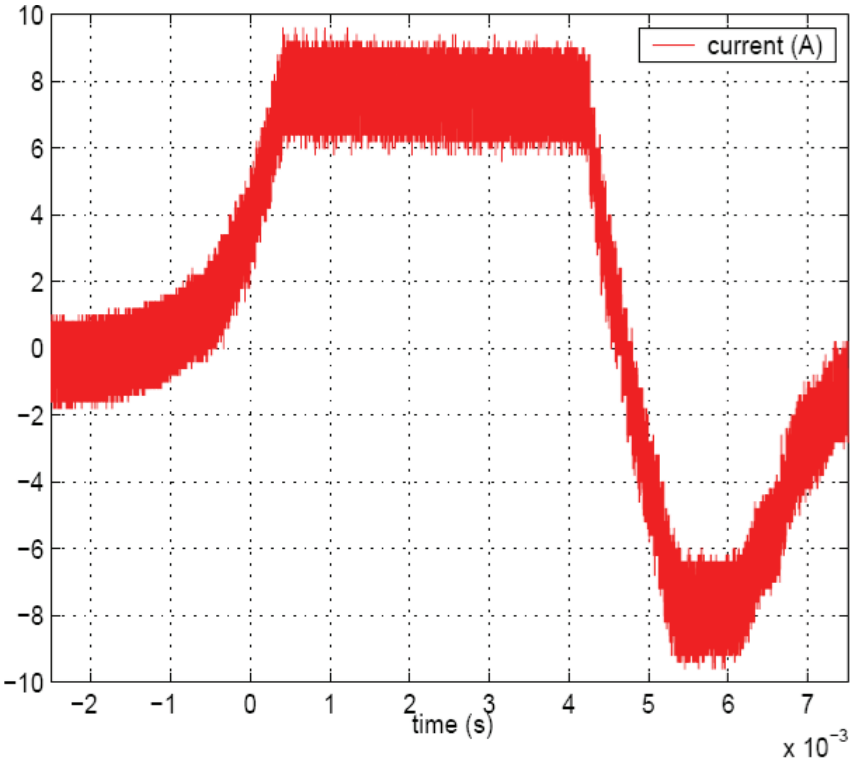

Fig. 6.11. Current profile with new cam and pure closed-loop control.

TABLE 6.2. COMPARISON OF SYSTEM PERFORMANCE WITH THE NEW CAM AND OLD CAM.

Exp. Setup	Power Consumption (W)	Peak Torque (N-m)	Transition Time (ms)
Old cam, closed-loop, free-flight ref, ± 8 A current limit	76	0.56	3.4
New cam, closed-loop, free-flight ref, ± 8 A current limit	60	0.56	2.6
New cam, kick off 8 A current pulse, then closed-loop, free-flight ref	82	0.88	2.5
New cam, kick off 5 A current pulse, then closed-loop, free-flight ref, and ± 5 A current limit	49	0.35	2.7
New cam and ± 4.2 A current pulse, open-loop	49	0.30	2.7

6.5 Test with a Much Smaller Motor

The optimal cam design also enables us to replace our dc brush motor with a much smaller dc brushless motor. The brushless motor yields satisfactory experimental results except for power consumption due to its low efficiency. This result leads to the design of a custom actuator that combines the high efficiency of the 1st dc brush motor and the small size of the 2nd dc brushless motor.

Table 6.2 has summarized our EMV system performance with the optimal cam in terms of power consumption, peak torque requirement, and transition time under different control strategies. Figures 6.12-6.14 show the reductions in power, torque, and transition time that have been achieved from the starting point obtained by Dr. Woo Sok Chang and Dr. Tushar Parlikar [17][18].

All these efforts, including the open-loop control, the new optimized cam design, and the input filter, lead to much lower peak torque requirement and power consumption, which sets the stage for a second prototype with a much smaller motor for an even higher engine speed situation.

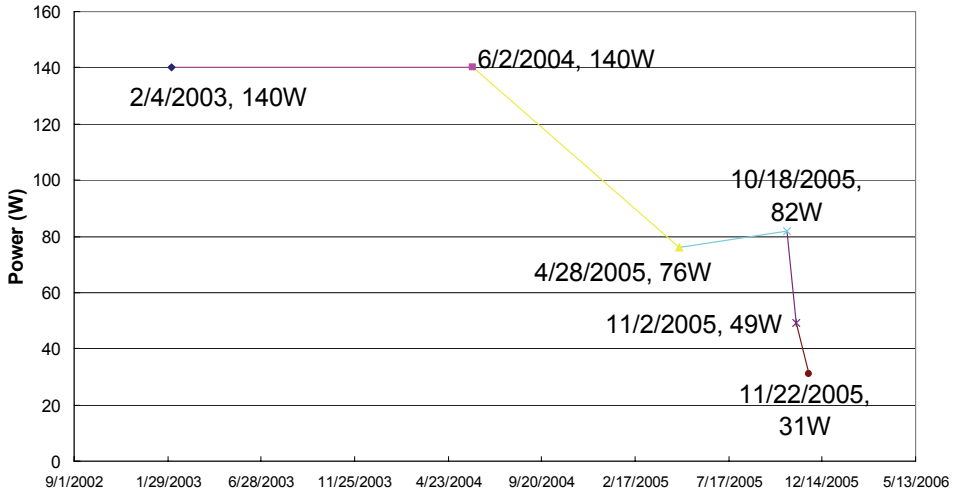

Fig. 6.12. Sequential improvements in power consumption.

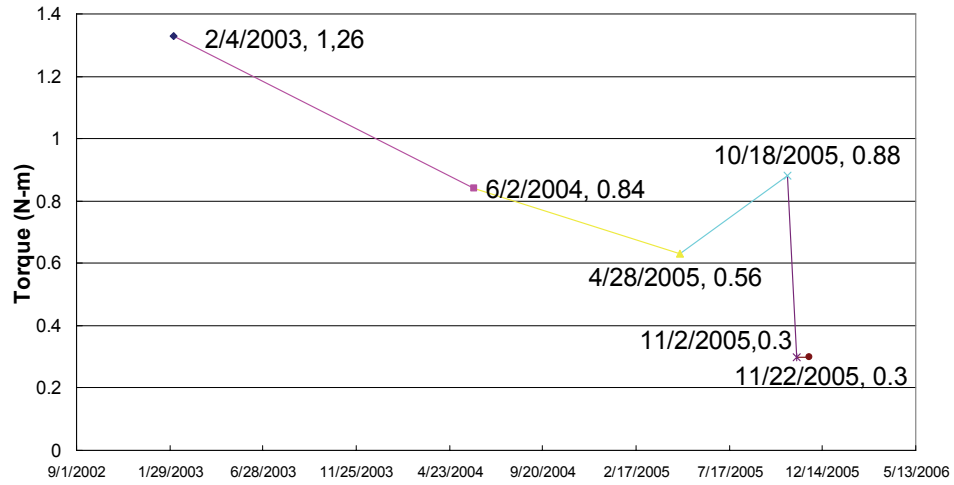

Fig. 6.13. Sequential improvements in peak torque requirement.

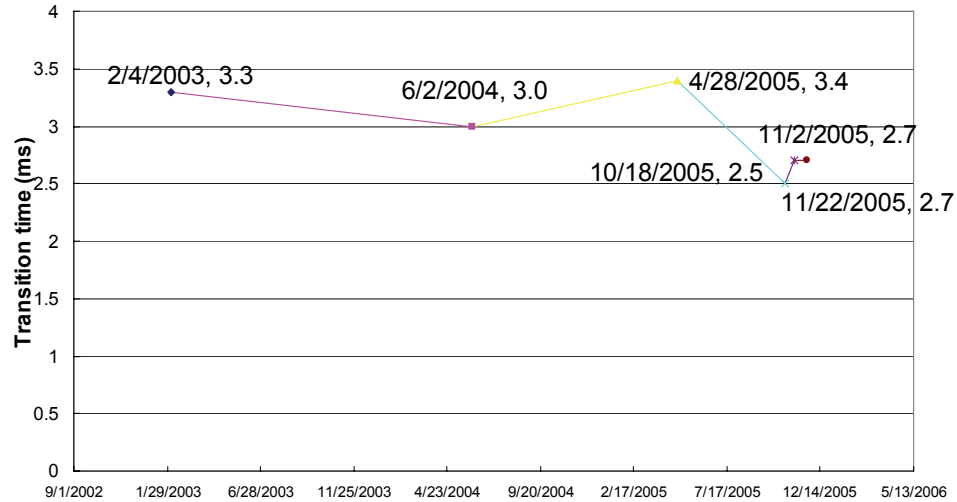

Fig. 6.14. Sequential improvements in transition time.

The new motor is a brushless dc motor (Portescap B1118-050A), as shown in Fig. 6.15, which has an even lower inertia (about one third that of the old brush dc motor) and a much smaller size (about one seventh that of the old dc brush motor). The experimental results with the new motor and new cam are shown in Figs. 6.16 and 6.17, and compared with those of the old motor in Table 6.3.

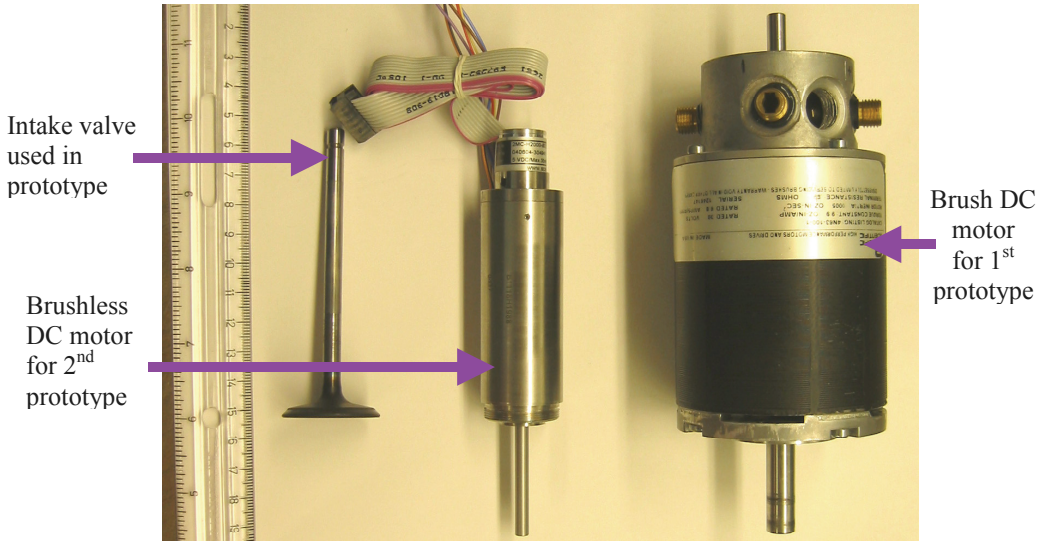

Fig. 6.15. The intake valve, the brush dc motor, and the new brushless dc motor.

However, this brushless dc motor does have a fatal flaw due to its low efficiency. As shown in Table 6.3, the power consumption with the new motor jumps back to 138 W, about the same level as that of our starting point of 140 W with the old cam, the old motor, and the pure closed-loop control with sinusoidal position reference. Within the power consumption of 138 W, 118 W is the winding loss, the cause of the extremely low efficiency. Since we are already using a carefully selected control strategy to minimize the torque requirement and winding loss, there is little room for improvement using this motor. This has motivated the custom design of an actuator, taking advantage of its requirements of limited angle rotation and intermittent working duty cycle, as will be discussed in Chapters 7-9. The goal of the customized actuator is to combine the high efficiency of our brush dc motor and the small size of the brushless dc motor.

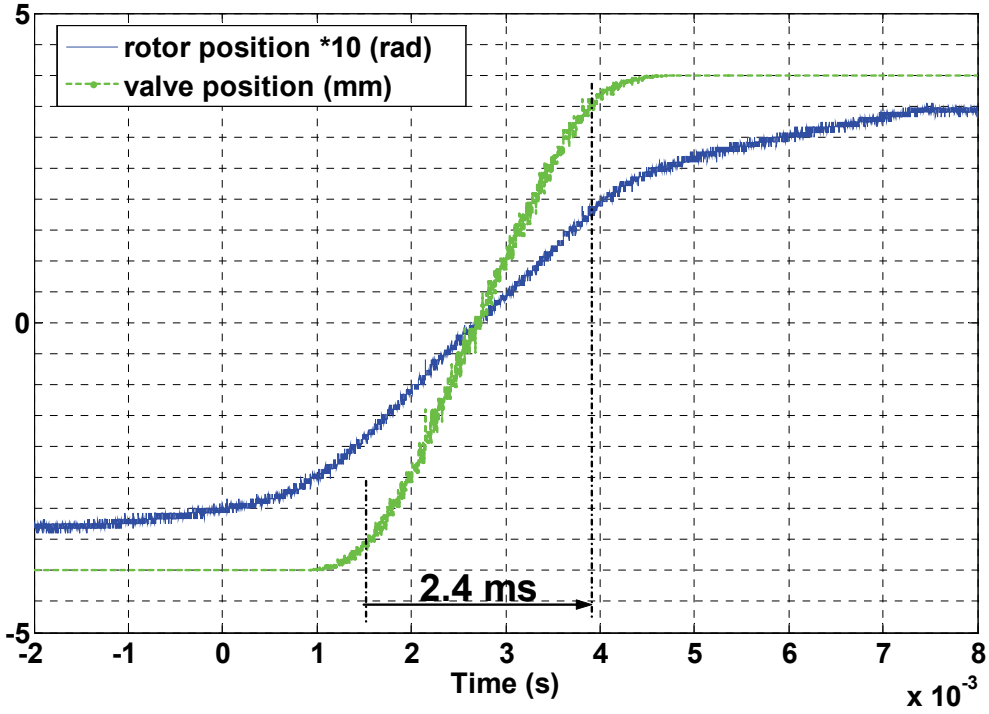

Fig. 6.16. Position profiles with the brushless dc motor.

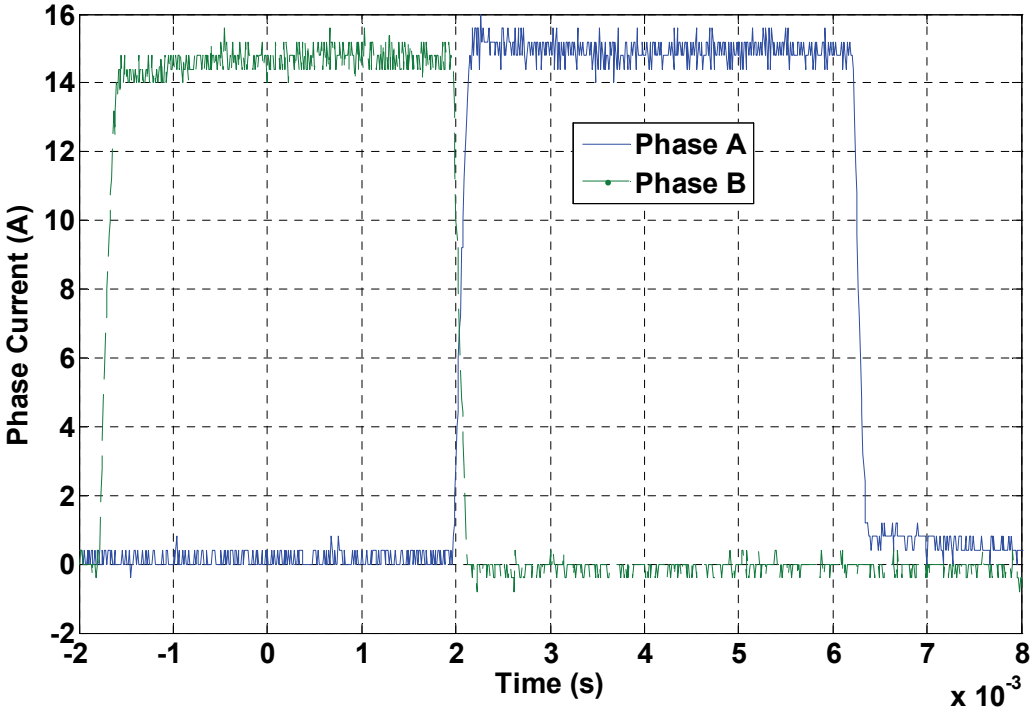

Fig. 6.17. Current profile with the brushless dc motor.

TABLE 6.3. PERFORMANCE COMPARISON WITH BRUSH AND BRUSHLESS DC MOTOR.

Exp. Setup	Exp. Date	Power Consumption (W)		Peak Torque (N-m)	Transition Time (ms)
		Electrical loss	Frictional loss		
Starting point with brush dc motor: Old cam, sin ref, and ± 18 A current limit	02/04/2003	140		1.26	3.3
		105	35		
Best performance with brush dc motor: new cam, 4.2 A, 9 ms current pulse, and input filter	11/22/2005	31		0.30	2.7
		13	18		
High loss with brushless dc motor: new cam and 15A 8 ms current pulse	04/05/2006	138		0.30	2.4
		118	20		

6.6 Other Possible Implementations of the NMT

In this section, other possible designs of the NMT are briefly discussed, which offers some insights on future research on the NMT.

6.6.1 Two-lift Design for Lift Control

So far, our focus is on variable valve timing. The valve lift is fixed. However, if the valve lift also can be adjusted under different circumstances, great benefits can be achieved in fuel economy and emission reduction, especially in the case of the intake valve [1]-[4].

If we follow the idea using a disk cam and a roller follower to implement the NMT, it is quite straightforward to stretch that idea into the following two-lift design. That is, if we set the valve closed position as the middle point in the cam slot, then the cam can have two different slot designs at each side of the middle position. One side can be designed to produce full opening while the other side is designed to achieve partial opening, such as half or one third.

The challenge of this cam design will be control other than design because the partial opening valve position will not allow the springs to exert their normal function in the full opening case.

6.6.2 Optimal Design for Exhaust Valve

Although in Chapter 9 we show in simulation that we can obtain satisfactory performance of exhaust valve actuation with the current optimal cam design and the custom designed actuator discussed in Chapter 7 and 8, we still want to discuss the possibility to design an even better cam for an exhaust valve due to its more complicated scenario.

The closed-to-open transition of an exhaust valve is very different from that of an intake valve, because of the large negative gas force exerted on the valve requiring an opening force higher than that for the intake valve. Figure 6.18 (provided courtesy of the MIT Sloan Automotive Laboratory [24]) shows a typical gas force profile as a function of crank angle in a conventional IC engine, at full load and high speed. The gas force affects system dynamics significantly so that the exhaust valve might need a different cam for better performance of the closed-to-open transitions.

Conversely, the open-to-closed transition of an exhaust valve is very similar to that of an intake valve. So the optimized θ-ranges will very likely be different for the two transition directions of an exhaust valve. There are two possible solutions to solve this problem. First, we can follow the idea of the separate slot design discussed in subsection 6.6.1, and design the cam and possibly some accessory parts in a way such that the transitions in opposite direction follow their own optimal cam profile. Or, a seemingly simpler solution could be an asymmetric cam design, which has different gear functions/ratios in two sides. One side is favored for opening transitions and the other side is in favor of closing transitions. The power consumption of a single transition might not be optimal, but the power consumption of the two transitions in one cycle prevails. This solution combines function and θ-range together in optimization, which will demand extensive simulations to find the best combination.

6.6.3 Four-bar Linkage Implementation of NMT

The current implementation of the NMT is a disk cam plus a roller follower. This is a very handy design in terms of laboratory experiments. However, considering the

requirements of automotive applications, reliability of this disk cam design is unknown and hence it could raise issues in life span and maintenance.

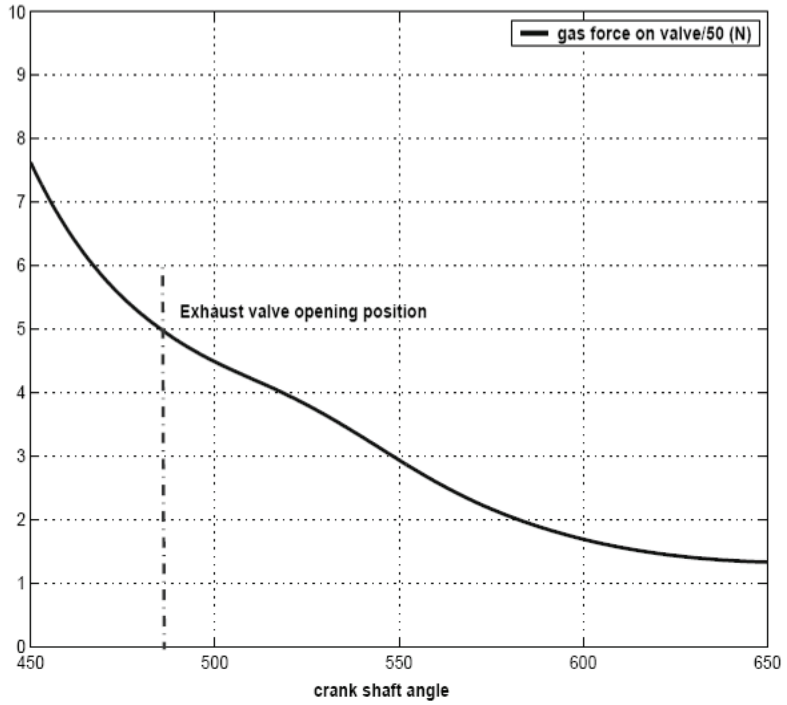

Fig. 6.18. A typical gas force profile at exhaust valve opening transition.

One the other hand, simple rotating joints are used in many places in automotive engines and a four-bar linkage can create an NTF function using only simple rotating joints. Therefore, some preliminary research to create a four-bar linkage implementation of NMT has been done by LEES Research Scientist Dr. Thomas Keim and MIT undergraduate student Corinna Hui. A promising candidate has been found, whose modulus characteristic and conceptual design are shown in Figs. 6.19 and 6.20.

At this point we have established a more accurate system model in Chapter 4, compared three different control strategies in Chapter 5, and obtained a revised cam design in this Chapter. Based on all these improvements in system modeling, control, and design, we have shown a significant reduction in power consumption and torque requirement for our EMV system. While it is still very difficult to solve the size issue with a standard commercial motor, as discussed in this chapter, all these achievements have set a

promising base for us to explore the possibility of customizing the actuator design in order to meet the size requirement. The next three chapters will focus of the subject of custom actuator design. Chapter 7 presents the conceptual design of our special actuator, Chapter 8 discusses the details of building a real actuator, and Chapter 9 confirms the feasibility of the actuator by experimental evaluation.

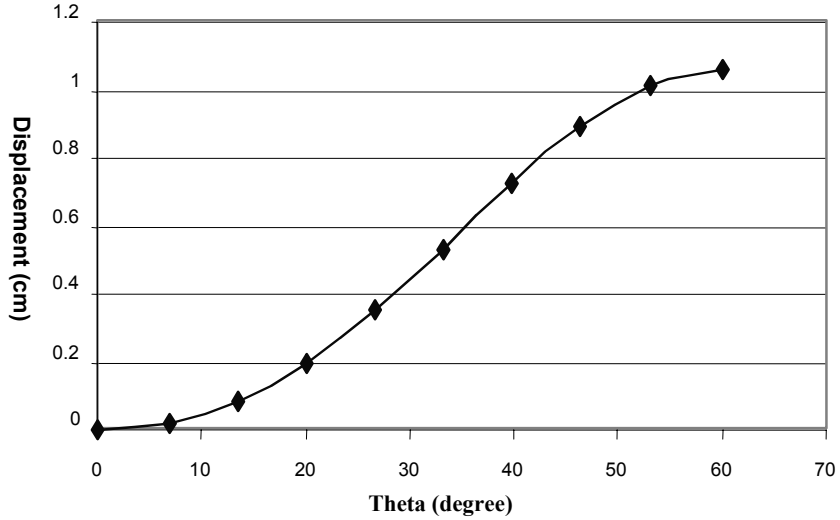

Fig. 6.19. Modulus characteristics of a promising 4-bar linkage design.

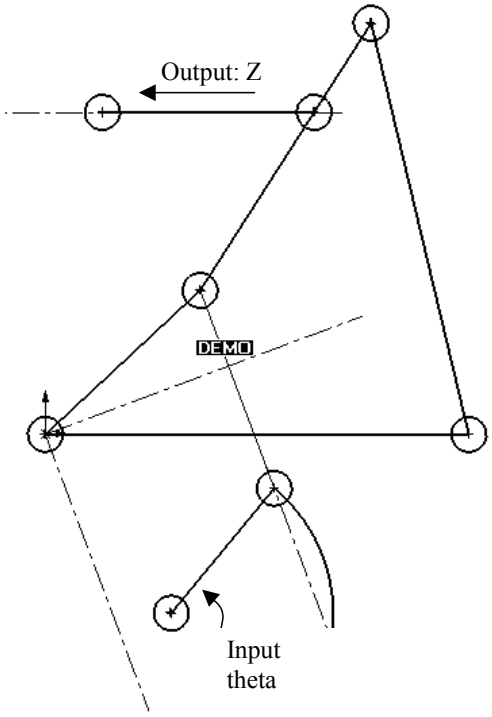

Fig. 6.20. Conceptual design of a promising 4-bar linkage.

CHAPTER 7 CUSTOMIZATION OF THE ACTUATOR DESIGN

7.1 Introduction

Two commercial motors have been tested in our EMV system. Obviously, both can achieve fast-enough valve transitions with the proposed improved control strategy and optimal cam design. However, the first dc brush motor has an unacceptable size but great efficiency, while the second dc brushless motor has manageable size but the ohmic loss in the armature winding is too high, resulting in a relatively high level of energy consumption. This suggests that a conventional motor design is not the best choice for the valve actuation application and that a custom-designed actuator is needed in order to meet all the requirements of engine valve actuation, including fast valve actuation, low power consumption, and small physical dimensions.

In this application, the rotor only needs to swing back and forth within a limited angle range (no more than 40 degrees including the extended flat area at both ends). This limited angle rotation allows us to design a yoke structure and hence flux path that could not be used in a conventional motor. In this chapter, we explore design possibilities for an actuator with such a yoke structure as well as other design techniques. We refer to such actuators as limited-angle actuators. Importantly, a new type of limited-angle actuator is proposed, which offers all the attributes needed for the application: in particular, low inertia, high torque, low ohmic loss, and small size.

In this chapter, we first discuss the challenges and objectives of this custom actuator design. Several possible topologies of a limited-angle actuator for valve actuation will then be proposed before the nominal actuator design is picked based on the torque constant estimated by Maxwell®, a numerical computation software for electromagnetic field applications using the finite element method. Extensive study has been done with the nominal actuator design, including optimal dimension search, further enhancement of torque output, minimization of armature inertia and resistance, calculation of torque variation at different rotor positions, and winding inductance manipulation via an extra

air gap. The final conceptual design will be compared with the two commercial motors used in our previous experiments, with respect to both actuator package and valve system performance. The comparison has given us assurances regarding the feasibility of this customized actuator for the valve actuation application and has provided us a strong foundation to fabricate a prototype of the actuator which will be discussed in Chapter 8.

7.2 Design Challenges

There are at least four big challenges that we need to face in order to design a satisfactory actuator.

First of all, the inertia of the rotor needs to be extremely low. We already know that the transition time is mainly determined by the stiffness of the springs, the mass of the valve and the inertia of the rotor and the disk cam. The springs used in our system have a fairly high stiffness. A large increase would require many changes to our proposed valve actuation system. The valve used in our system is an ordinary valve taken from a common 4-cylinder IC engine. There is not much that can be done to reduce the mass of the valve, either. Therefore, the only variable that we can control is the inertia of the rotor and the disk cam. We have already tried very hard to reduce cam inertia as discussed in Chapter 6. In order to ensure the required rapid transition, we chose both commercial motors to have extra low inertias, $3.5 \cdot 10^{-6}$ $Kg \cdot m^2/s$ for the first motor and $1.2 \cdot 10^{-6}$ $Kg \cdot m^2/s$ in the second case. For the same reason we need to design the actuator to have an inertia of no more than $3.5 \cdot 10^{-6}$ $Kg \cdot m^2/s$.

Secondly, high torque output is also a requisite for this application. We need high enough torque to overcome the friction force and gas force during transitions. Preferably, an even higher torque is desired, for faster transition and more robust response. From previous experience, we set 0.3 N-m as the lower end of the rated torque output of the actuator. The torque constant also affects the ohmic loss of the winding, which will be discussed shortly.

Thirdly, high efficiency, encompassing low ohmic winding loss and low frictional loss, is another very important requirement of this design. If the ohmic loss and/or frictional loss is too high, the temperature of the armature will reach an undesirable level, which will shorten the armature's life, require higher-grade insulation material and cooling system, and increase the maintenance cost of the actuator. From another point of view, a high ohmic and/or frictional loss will result in a high power consumption (i.e., a low efficiency) of the actuator. This will detract from the benefits of our EMV system and could result in a decision not to use the technology. From previous experiments, the frictional loss in the system seems to be well controlled with the optimized cam discussed in Chapter 6. The principal failing of the second motor was that its ohmic loss was too high. Therefore, our focus in this study was how to minimize the ohmic loss of the winding. Our general goal in this respect is no more than 100 W/valve, i.e., 1.6 kW for a 4-cylinder 16-valve engine, at 6000 rpm engine speed.

Fourthly, to fit the EMV system into the limited space over the engine head and to realize independent valve actuation, i.e., one actuator for each valve, we need to make the actuator small. The dc brushless motor has a feasible size to fulfill this purpose, so its size will be used as our benchmark. Special attention will be paid to meet the dimensional constraints coming from valve pitch, which is about 37.5 mm in a common 4-cylinder 16-valve IC engine. This means the width of the actuator should be no more than 37.5 mm, which will allow two actuators to stand side by side to drive two valves independently.

Needless to say, there are some other inevitable requirements for the actuator design if we want to commercialize the whole system into the automotive environment, such as low cost, robustness, being easy to maintain or maintenance free, and so on. But this thesis will focus on how to meet the four challenges mentioned above and summarized in Table 7.1 below.

TABLE 7.1. DESIGN OBJECTIVES OF THE ACTUATOR

	Inertia ($Kg \cdot m^2/s$)	Power (W)	Torque (N-m)	Size (mm*mm*mm)
Objective	$<=3.5x10^{-6}$	<=100	>=0.3	<=70560 (28*28*90) Side dimension <=37.5 mm

The design flow can be described as following:

Step 1: Propose possible topologies which meet the idea of the limited-angle actuator.

Sept 2: Choose the nominal topology mainly based on the torque output estimated by Maxwell®;

Step 3: Search among all possible combinations of physical dimensions of the nominal design by using a self-coded Matlab® program, and find those combination(s) which satisfy the size constraint, inertia constraint, and loss constraint based on first order estimation;

Step 4: From the suitable set of combinations, pick the one which has lowest loss, and confirm the torque output and winding loss using Maxwell®;

Step 5: Study in Maxwell® the variation of torque output at different rotor positions and different ambient temperatures and the change of winding inductance with extra air gap design.

Step 6: Plug the actuator model into 20-sim® and estimate power consumption and transition time for a successful transition.

We will discuss this process step by step in this chapter.

7.3 A Limited-Angle Actuator

From experiences with the first dc brush motor and the second dc brushless motor and study of the commercial market, we realize that there is no known commercial motor design which can meet all four requirements mentioned in section 7.2. We conclude that commercial motors are all designed for full turn rotations, which is not a fit or requirement for our application where the rotor swings back and forth only within a

limited angle. There do exist commercial motors called limited angle torque motors, which offer limited-angle rotation. However, most of them employ a conventional yoke structure as used in regular motors, and their inertia and size are always outside of our limits if they offer high enough torque and low enough power consumption. Therefore, we decided to design a limited angle actuator with a special yoke structure. This structure allows effective rotation only in a limited angle range, but can meet all the design challenges discussed in section 7.2.

7.3.1 Nominal Topology

From our study, there are 5 possible topologies that we have taken into consideration, as shown in Figs. 7.1-7.5 [23]. In all topologies, the armature is the only moving element (shown in green). Considering only configurations in which the armature is the sole moving member helps to minimize rotor inertia. We use the fact that rotation happens only within a limited angle range to reduce actuator size. The iron (shown in blue) and permanent magnets (shown in yellow) form the stator of the actuator. The main differences among those topologies are the shape of the iron yoke and the orientation of the flux field.

Figure 7.1 shows cross section view of the first limited-angle actuator topology. There are two permanent magnets placed 180^{o} apart with opposite poles facing each other.

Figure 7.2 presents cross section view of the second the limited-angle actuator topology, which looks just like half of a regular motor. The two permanent magnets are placed such that they are separated by 90^{o}, as shown in Fig. 7.2. Note that the angle between the permanent magnets, defined as σ, can be different from 90^{o}, which will affect the feasible width of the permanent magnets and the winding and hence the rotational angle and torque constant of the actuator.

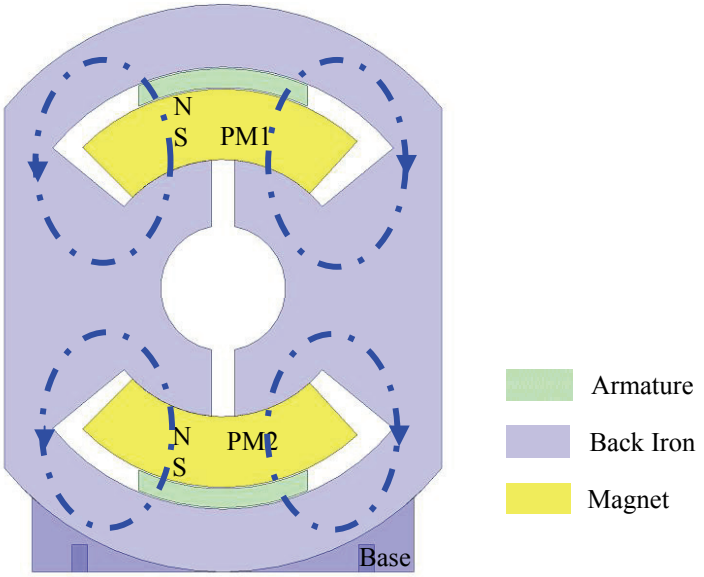

Fig. 7.1. Topology I of a limited-angle actuator.

Figure 7.3 shows cross section view of the third topology of the limited-angle actuator, in which the two permanent magnets are placed parallel to each other with opposite magnetic poles facing each other. Unlike the first two topologies, the two permanent magnets and two active portions of the winding used in this topology are different in size in order to maintain the same angular dimension at different radii.

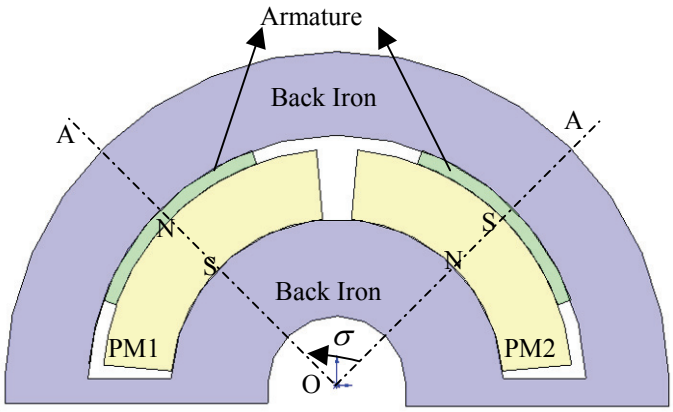

Fig. 7.2. Topology II of a limited-angle actuator.

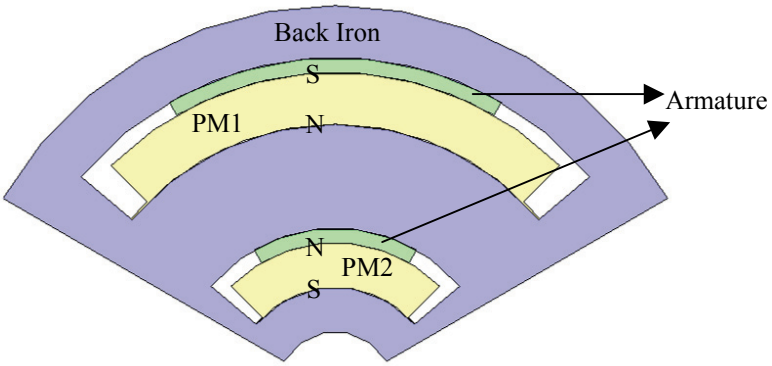

Fig. 7.3. Topology III of a limited-angle actuator.

Figures 7.1-7.3 are focusing on actuators which have radial flux fields. Fig. 7.4 below presents a topology of the limited angle actuator with an axial flux field, i.e., a variation of the conventional disk motor. There are four permanent magnets in this design.

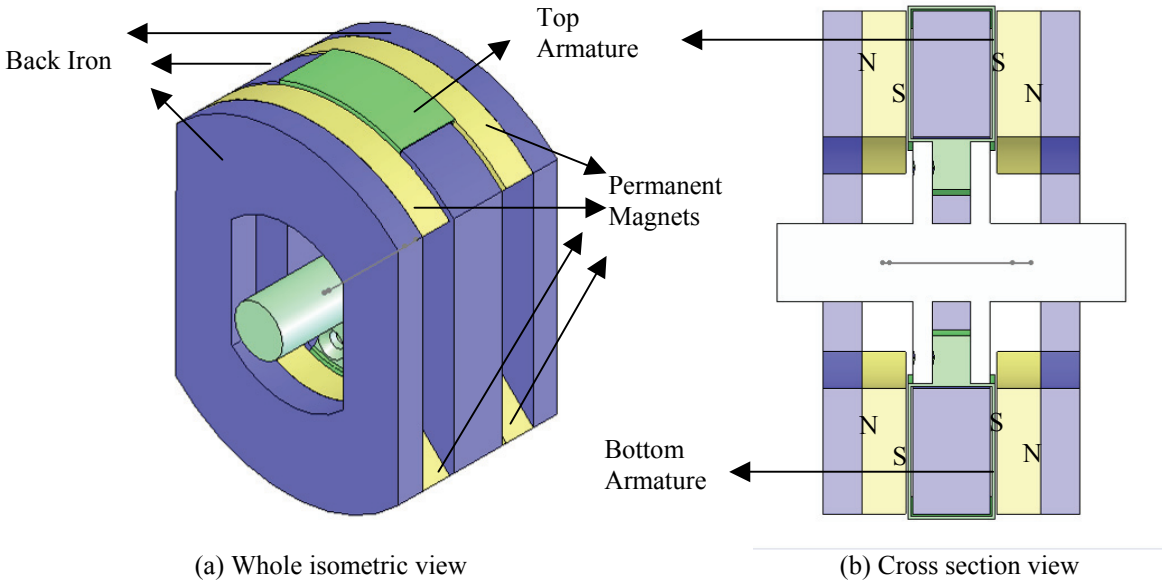

(a) Whole isometric view (b) Cross section view

Fig. 7.4. Topology IV of a limited-angle actuator.

In Fig. 7.5, a combination of axial flux field and radial flux field is presented, which is actually a combination of designs shown in Fig. 7.1 and Fig. 7.4. Therefore six permanent magnets are used in this design.

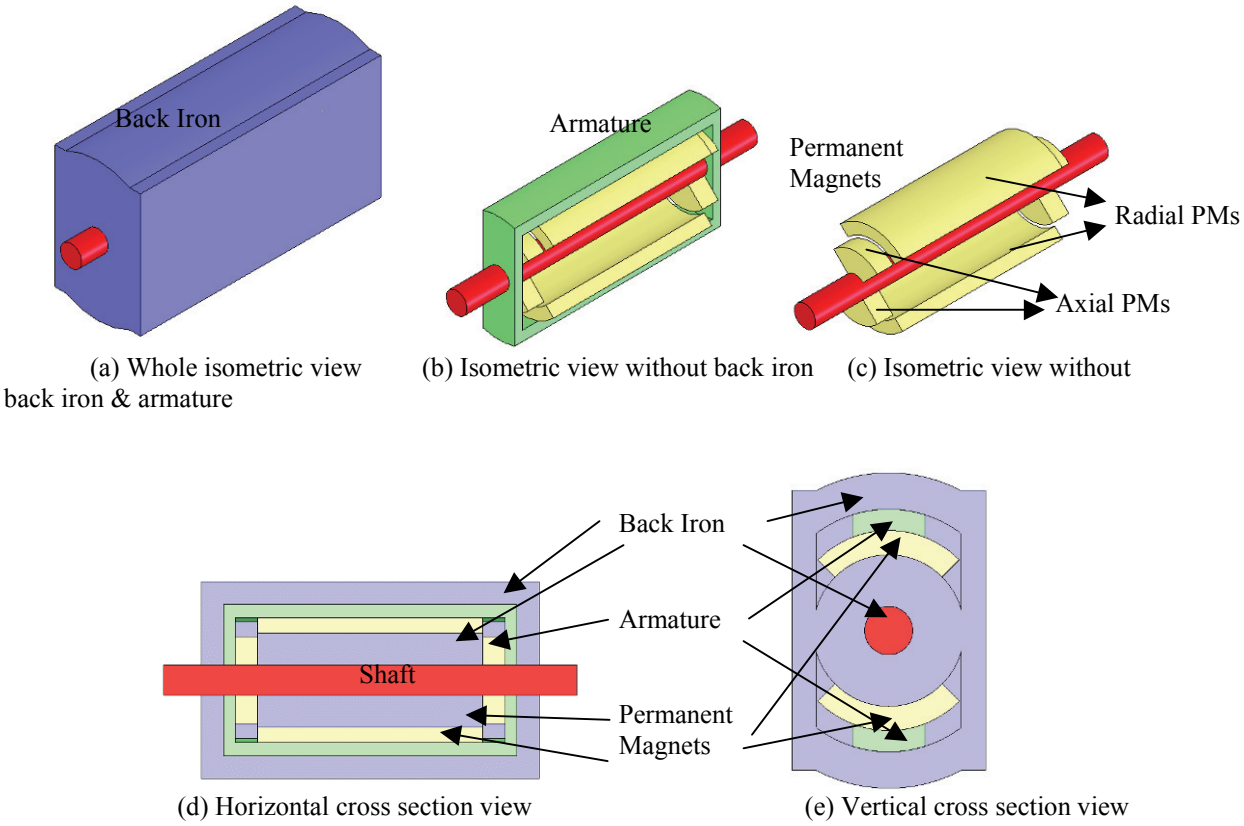

Fig. 7.5. Topology V of a limited-angle actuator.

All five topologies discussed above have been put into Maxwell® for torque constant estimation. The initial designs are mainly based on size constraints and a single-turn winding design. The comparison of each topology is summarized in Table 7.2.

TABLE 7.2. COMPARISON OF DIFFERENT TOPOLOGIES OF THE LIMITED-ANGLE ACTUATOR.

	Actuator Size (mm*mm*mm)	Torque Constant (N-m/100 A)
Topology I	60*36*28	0.143
Topology II	60*35*18	0.130
Topology III	60*34*30	0.118
Topology IV	54*38*50	0.098
Topology V	60*46*24	0.113

From Table 7.2, it is quite obvious that Topology I has the highest torque output as well as a simple structure while meeting the size constraints. Another advantage of this design

is that its slim width will help meet the valve pitch requirement when two actuators are placed side by side for two valves. Therefore we chose topology I as our nominal topology and conducted an extensive study of it.

7.3.2 Armature Design Considerations

This subsection will discuss design considerations of the limited-angle actuator, especially the armature of the nominal topology that we chose in the previous subsection.

As discussed before, all of the iron which forms the magnetic circuit is stationary, as are the permanent magnets used in the actuator. The flat surfaces at both sides of the iron yoke allow two actuators to be mounted closer to each other than a pair of round actuators with the same air gap radius. The only moving element in this actuator is the one-phase hollow-shaped winding, which is centered on, and rotates relative to, the axis of the actuator. This design minimizes the rotor inertia. Additionally, this design potentially eliminates the need for brushes, another notable advantage.

Figure 7.6 shows an isometric view of the concept of the moving armature of the actuator. The structure of the end turns is reasonably apparent from the figure. Each axial pass down the air gap is connected to the next axial path by a conductor lying in a plane normal to the axis of the armature. The paths are very direct and short. The red cylinder is the actuator shaft. It is attached to the conductor/polymer structure of the armature while passing through the end turns of the armature at both ends. The detail of the attachment will be defined when discussing how to build the actuator in Chapter 8.

In the design shown in Fig. 7.6, one end (usually the rear end) will be connected to the optical encoder and the other end (usually the front end) will be connected to the disk cam. However, the optical encoder is relatively expensive and impractical for an automotive application. In the future, it will be replaced with another type of position sensor which is cheaper and more robust in an automotive environment and yet has high resolution, such as an anisotropic magnetoresistive (AMR) sensor. The resistance of an AMR sensor changes when the angle between the direction of the applied field outside

and the direction of its own current flow inside changes. To fit in an AMR angular position sensor, the armature (including shaft and winding) could be designed slightly differently, as shown in Fig. 7.7, where the rear end of the shaft will not pass through the end turns such that these rear side end turns can be formed as straight conductors instead of arc conductors as used in the front-side end turns. Thus, when the position of the armature changes, the direction of the flux field generated by the current flowing through the rear end turns will also change, which can be captured by the AMR sensor for the purpose of position sensing.

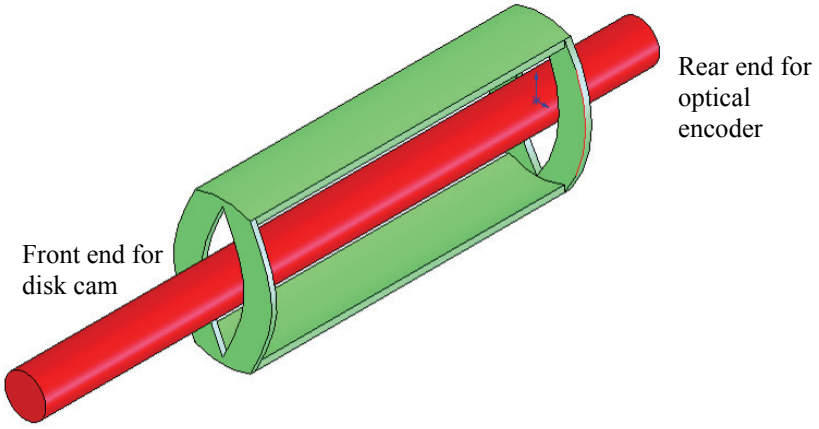

Fig. 7.6. Conceptual design of the moving armature.

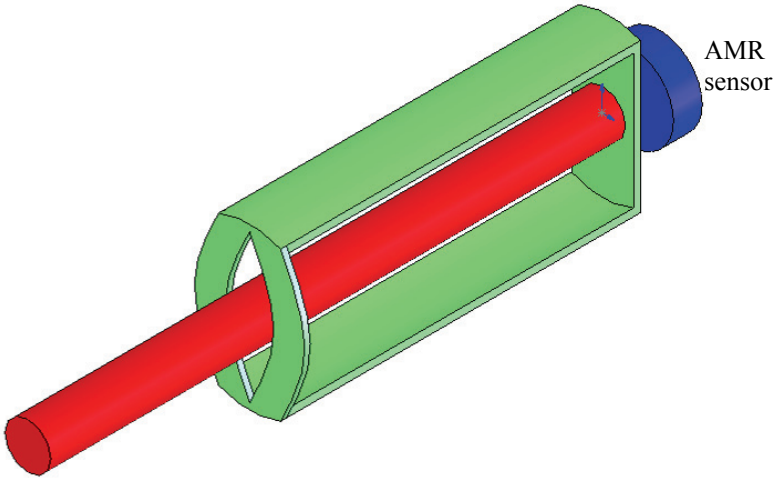

Fig. 7.7. Another conceptual design of the moving armature.

Figure 7.8 shows a close-up isometric view of a portion of the armature. The portion shown is presented as if cut from the effective portion of the armature which passes axially through the arc-shaped gap in the iron/permanent magnet structure. The armature is constructed of an array of conductors with rectangular cross section. Note that the number of the conductors shown in Fig. 7.8 is not necessarily the number we used in our real design (four turns), as discussed in Chapter 8. In the foreground of the figure, only the wire conductors are shown. These conductors are bonded together by a polymer, which forms the structural element of the armature. The green portion of the figure represents the polymer, which fills the gaps between the conductors in addition to providing a surface coating. The rectangular cross section of the wire allows a higher packing factor than round wire, while the polymer allows a low mass density structure.

As for the material choice of the winding conductor, aluminum is preferable to copper due to the special requirements of extra low inertia for fast transitions and low resistance for acceptable winding loss, as developed below.

The formula for electrical resistance is shown in (7.1),

$$R = \rho \cdot L / A \tag{7.1}$$

where R is resistance, ρ is electrical resistivity and L and A represent the length and cross-section area of the conductor path respectively.

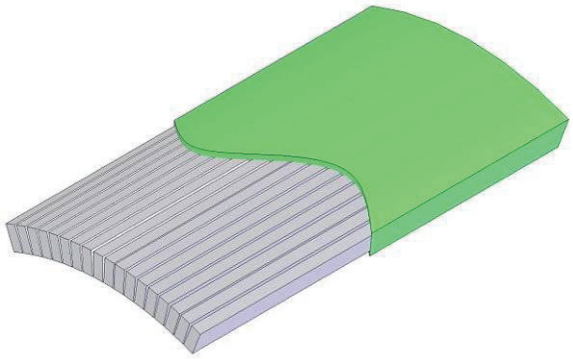

Fig. 7.8. A closer look of the active portion of the armature.

The length of conductor is principally determined by the geometric parameters of the magnetic circuit and the number of the turns, which are independent of conductor material. The electrical resistivity is directly determined by conductor material. However, besides the physical space limit, the allowable cross-sectional area A for the conductor is an indirect function of the choice of material if given an inertia limit. For the armature construction proposed here, the inertia of the moving element is very substantially determined by the mass of the conductor. More explicitly, assuming the thickness of the winding is much smaller than its mean radius, the inertia of the armature is approximately proportional to its mass given the same mean radius. The mass of conductor is proportional to the mass density and to the cross-section area. So if we choose to limit the mass of the conductor to be constant, independent of conductor material choice (to achieve equivalent inertia), the allowable cross-section area is inversely proportional to the conductor mass density, as shown in (7.2), while the mean radius of the winding is much larger than the thickness of the winding.

$$I \propto m \propto \rho_m \propto \frac{1}{A} \tag{7.2}$$

where I is the winding inertia, m is the winding mass, ρ_m is the mass density of the conductor, and A is the cross section area of the conductor.

Therefore if we design for constant inertia with two different conductor materials, the resistance ratio of each winding will be mainly decided by the electrical resistivity and the mass density, as shown in (7.3).

$$\frac{R_1}{R_2} = \frac{\rho_1}{\rho_2} \cdot \frac{A_2}{A_1} = \frac{\rho_1}{\rho_2} \cdot \frac{\rho_{m1}}{\rho_{m2}} \tag{7.3}$$

where R_1 and R_2 are the resistances of windings 1 and 2, respectively, ρ_1 and ρ_2 are the electrical resistivities of the two conductor materials, A_1 and A_2 are the conductor cross sections, and ρ_{m1} and ρ_{m2} are the mass densities of the two conductor materials.

For the aluminum conductor we choose (ASM grade 1350), with a conductivity 0.61 times that of copper, so the electrical resistivity is 1.64 times as great. On the other hand, the mass density ratio of copper to aluminum is 3.2. Therefore the net electrical resistance ratio of the two windings will be,

$$\frac{R_{Al}}{R_{Cu}} = \frac{1.64}{3.2} = 0.51 \tag{7.4}$$

So when the volume of a conductor is constrained to limit the inertia of the moving winding to a given value, the electrical resistance achievable with an aluminum conductor is about half of that achievable with copper.

7.3.3 Optimal Geometric Dimensions

After choosing the nominal topology of our limited-angle actuator, we need to optimize the physical dimensions in terms of torque output, rotor inertia, and physical size. These dimensional parameters are listed in Table 7.3 and also shown in Fig. 7.9.

TABLE 7.3. DEFINED PHYSICAL DIMENSIONS OF THE LIMITED-ANGLE ACTUATOR.

Dimension Description	Math Symbol
Thickness of the circumferential air gap	δ
Thickness of the permanent magnets	h_m
Angular range of the permanent magnets	θ_m
Thickness of the armature	h_a
Angular range of the armature	θ_a
Thickness of the iron yoke	h_y
Side width of the iron yoke	w
Angular range of the iron yoke	θ_y
Length of the permanent magnets and the iron yoke	l
Diameter of the shaft	d
Diameter of the clearance hole to fit the shaft	d_1
Thickness of the vertical air gap	δ_v

A search program in Matlab® based on the first-order principles of a magnetic circuit was used to find the best combination of the first ten dimensions shown in Table 7.3. The shaft diameter d was made as big as possible while keeping the rotor inertia within its limit in order to have a strong rotor structure with the cup-shaped armature. Therefore we set $d = 8.4\,\text{mm}$, much bigger than the 5 mm shaft of the second motor and very close to the 9 mm shaft of the first motor. In order to obtain high flux density, we want the air gap as small as possible. Due to limitations of fabrication and assembling clearance, we set $\delta = 0.2\,\text{mm}$ in this program. As for possible variations of the other eight parameters, we also set up five constraints to limit qualified combinations. First, the winding loss is constrained to be no more than half of the winding loss of the second motor when providing the same torque. This condition actually checks both torque capacity and winding resistance of the actuator at the same time. Second, the rotor inertia is constrained to be no more than that of the first motor. Third, the size of the actuator is constrained to be no more than that of the second motor as measured by the product of length and cross section area. Fourth, the side dimension of the actuator can be no more than the valve pitch in the engine, which we take to be 37.5 mm. Fifth, the angle rotation range is constrained to be no less than 40^o in total, 20^o at each side. All geometric dimensions except the length of the actuator are also labeled in Fig. 7.9.

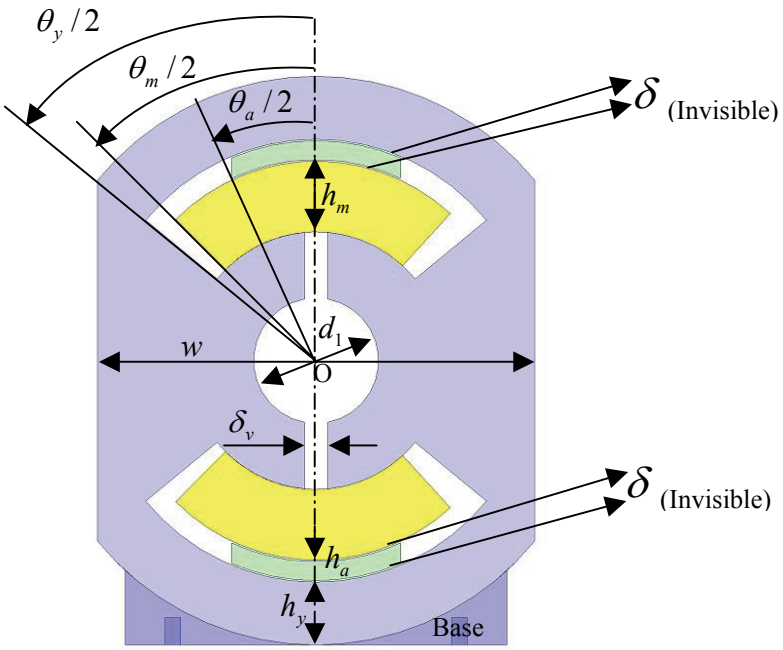

Fig. 7.9. Nominal topology with geometric parameters labeled.

It turns out that there is more than one combination meeting all the limits, therefore we picked the one which has the smallest winding loss for further study. The selected combination was then put into Maxwell® for more accurate finite element analysis, as shown in Fig. 7.10, in order to confirm the torque capacity of the actuator with the selected dimensions. Note that all the computations done by Maxwell® so far are based on three assumptions: single turn winding, $20^{o}C$ temperature inside the actuator, and the armature positioned in the middle of its rotational range. Considerations of a multi-turn winding, higher temperature, and different rotor positions will be discussed in the next section.

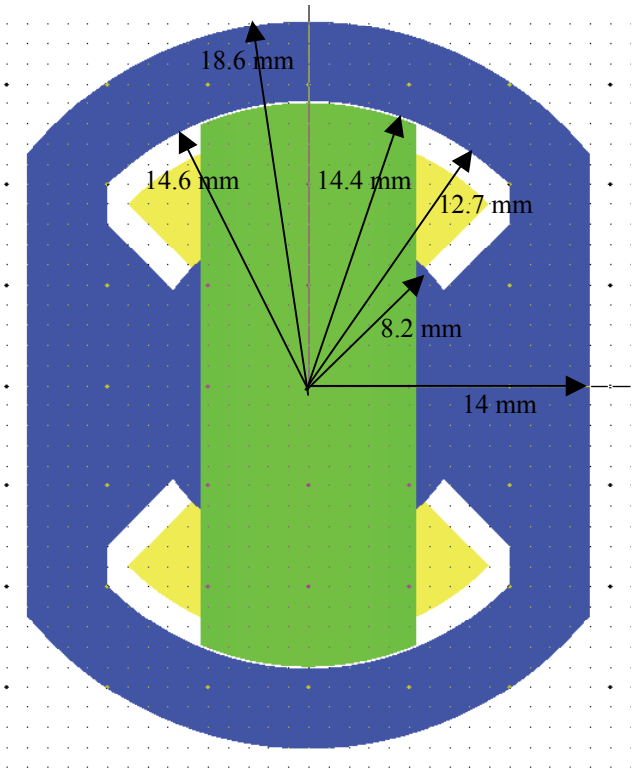

Fig. 7.10. Optimal dimensions for the limited-angle actuator.

Also, Maxwell® helped to determine a proper number for the thickness of the vertical air gap, δ_v, which offers a low enough winding inductance without affecting torque output. The torque output and winding inductance estimated by Maxwell®, with different vertical air gaps δ_v, are summarized in Table 7.4. We chose $\delta_v = 1\,\text{mm}$ for our final design which offers fast enough electrical response without affecting the torque output.

TABLE 7.4. TORQUE OUTPUT AND WINDING INDUCTANCE WITH DIFFERENT VERTICAL AIR GAPS.

Vertical air gap δ_v (mm)	Torque output (N-m/100 A)	Winding inductance (μH @ 1-turn)
0	0.143	5.57
0.1	0.143	2.97
0.5	0.143	1.43
1.0	0.143	0.93
1.2	0.142	0.86
1.5	0.141	0.75
2	0.140	0.62
4	0.134	0.43

The final geometric dimensions are listed in Table 7.5 and shown partially in Fig. 7.10. Figure 7.11 shows a size comparison of the proposed new actuator with the second dc brushless motor. Both images are drawn to the same scale. While they share the same width in the direction perpendicular to the paper, the shorter axial build of the new actuator is a significant packaging advantage. The fact that the new actuator does not need to be round makes it possible to respect the desired valve center-to-center dimension.

TABLE 7.5. FINAL PHYSICAL DIMENSIONS OF THE LIMITED-ANGLE ACTUATOR.

Dimension Description	Math Symbol
Thickness of the circumferential air gap	$\delta = 0.2\,\text{mm}$
Thickness of the permanent magnets	$h_m = 4.5\,\text{mm}$
Angular range of the permanent magnets	$\theta_m = 90^o$
Thickness of the armature	$h_a = 1.5\,\text{mm}$
Angular range of the armature	$\theta_a = 45^o$
Thickness of the iron yoke	$h_y = 4\,\text{mm}$
Side width of the iron yoke	$w = 28\,\text{mm}$
Angular range of the iron yoke	$\theta_y = 101^o$
Length of the permanent magnets and the iron yoke	$l = 60\,\text{mm}$
Diameter of the shaft	$d = 8.4\,\text{mm}$
Thickness of the vertical air gap	$\delta_v = 1\,\text{mm}$

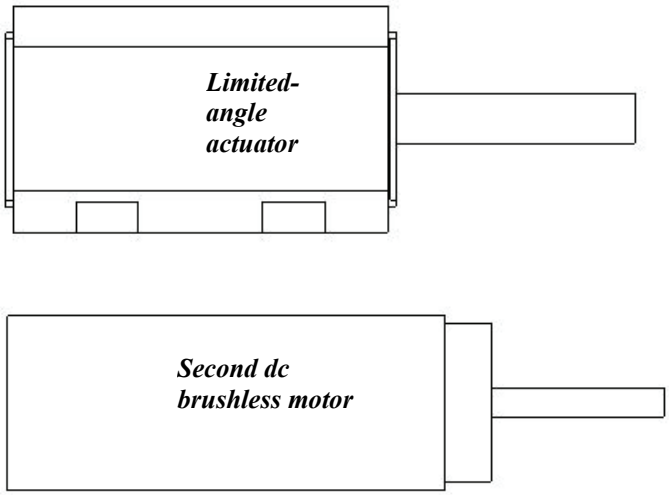

Fig. 7.11. Size comparison of the limited-angle actuator and the dc brushless motor.

7.4 Performance Estimation

7.4.1 Single Transition

To this point, a single turn armature has been used in the Maxwell® simulation for simplicity. However, in order to have a good match of the 12 V voltage bus in automotive application, a 4-turn winding seems more realistic. In Chapter 8, a 4-turn winding will be constructed for the prototype limited-angle actuator. Therefore, we will use parameters of a 4-turn armature in the thesis from now on. The resulting calculated torque constant of the actuator is now 5.09 mN-m/A while the electrical resistance is about $6.8\,\text{m}\Omega$ at $20^{o}C$. By comparison, the second motor has a published torque constant of 20.3 mN-m/A, and operating experience indicates that it may achieve in practice perhaps 90% of this value, or 18 mN-m/A. The observed resistance of the second motor is $0.67\,\Omega$. Considering both the torque constant and the resistance component, the new actuator should exhibit about 1/4 as much ohmic loss as the second motor in order to produce the same amount of torque.

In particular, when we use the parameters of the new design in a system simulation to drive an intake valve transition with an open-loop current pulse, a predicted power consumption of 56 W (ohmic loss 34 W and frictional loss 22 W) is obtained, much

lower than our upper bound ---- 100 W. This is huge improvement over the 138 W power consumption of the second motor (ohmic loss 118 W and frictional loss 20 W). The EMV system simulation with the custom designed actuator also predicts a fast transition of 2.8 ms, as shown in Fig.7.12.

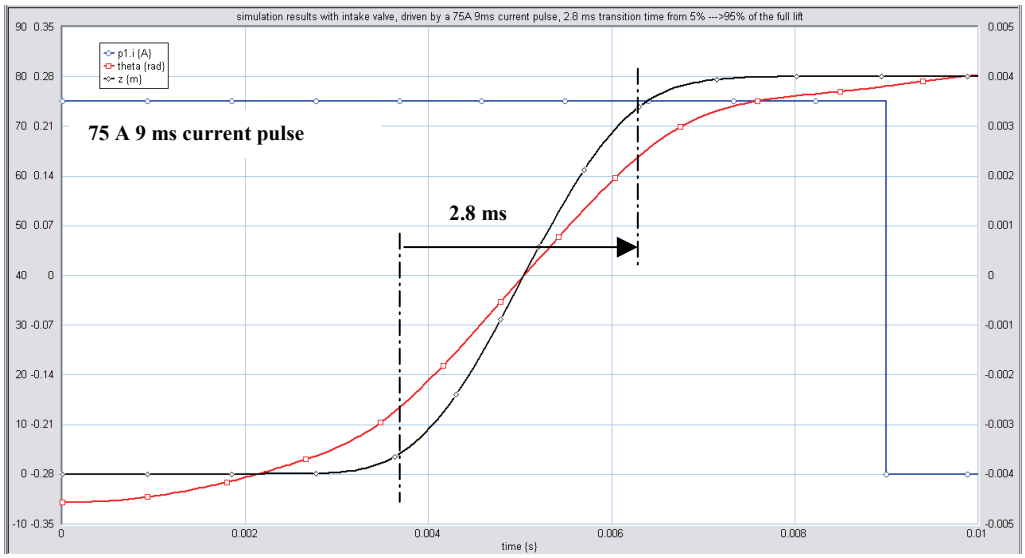

Fig. 7.12. Simulation profiles with the limited-angle actuator.

A summarized comparison between the two commercial motors and the limited-angle actuator is shown in Table 7.6. All the normalized numbers are based on the second motor. Note that the inertia of limited-angle actuator shown in Table 7.6 is only the inertia of the pure winding at this point, calculated by SolidWorks®. After we figure out the detailed design of the shaft, the connection parts between the shaft and the winding, and the optical encoder we are going to use, a larger total rotor inertia will be expected, as will be discussed in Chapter 9. Also note that the entries in the bottom three rows are not functions of the actuator alone, but of the actuator, the balance of the EMV, and the control strategy. These entries present each option as favorably as possible and the limited-angle actuator stands out with low enough power consumption and fast enough transition.

TABLE 7.6. COMPARISON OF TWO COMMERCIAL MOTORS AND THE LIMITED-ANGLE ACTUATOR.

	First motor **(from experiments)**	Second motor **(from experiments)**	New actuator **(from simulation)**
Size **(mm*mm*mm)**	69*69*119	28*28*90	28*36*60
Volume **(mm^3/normalized)**	566559/8	70560/1	64480/0.86
Rotor Inertia **($10^{-6}Kg{\cdot}m^2/s$ /normalized)**	3.5/2.9	1.2/1	1.3/1.08
Torque Constant **(N-m/A /normalized)**	0.07/3.5	0.02/1	0.00509/0.255
Winding Resistance **(Ohm/normalized)**	0.89/1.33	0.67/1	0.0068/0.01
Winding Loss **(W/normalized)**	31/0.26	118/1	34/0.29
Power Consumption **(W/normalized)**	49/0.36	138/1	56/0.405
Transition Time **(ms)**	2.7	2.4	2.8

7.4.2 Back-to-back Transitions

At high engine speed, not only do we want fast transitions, but we also want back-to-back transitions in one cycle, i.e., a closing transition following right after the opening transition.

One example is shown in Fig. 7.13, where current pulses with ± 125 A will give a back-to-back transition with a transition time of 8.3 ms from 5% of full stroke to the full lift and back to 5% of full stroke. Although the valve travels from 5% of full stroke to 95% of full stroke within 2.6ms, fast enough for 6000 rpm engine speed, the turn-around duration turns out to be even longer (about 3.1 ms) due to the almost flat ends of the NMT. The total transition time of 8.3 ms will be a bit short for 6000 rpm engine speed in reality.

It is possible to improve the situation by letting the valve not travel to the full lift, but for example, 98% of full lift instead, before coming back to the fully closed position. Fig. 7.14 presents such an example with current pulses of ± 160 A, offering a transition time

as fast as 6.8ms from 5% to 98% of full lift and back to 5% of the full lift. Similarly, in this scenario, although the transition time of single transition is only the 2.4 ms, fast enough for engine speed higher than 6000 rpm, the total transition time of 6.8ms (including a turn-around time of 3.0 ms) is able to meet the time constraint at 6000 rpm. Still higher engine speeds can be supported by using an even smaller fraction of full lift.

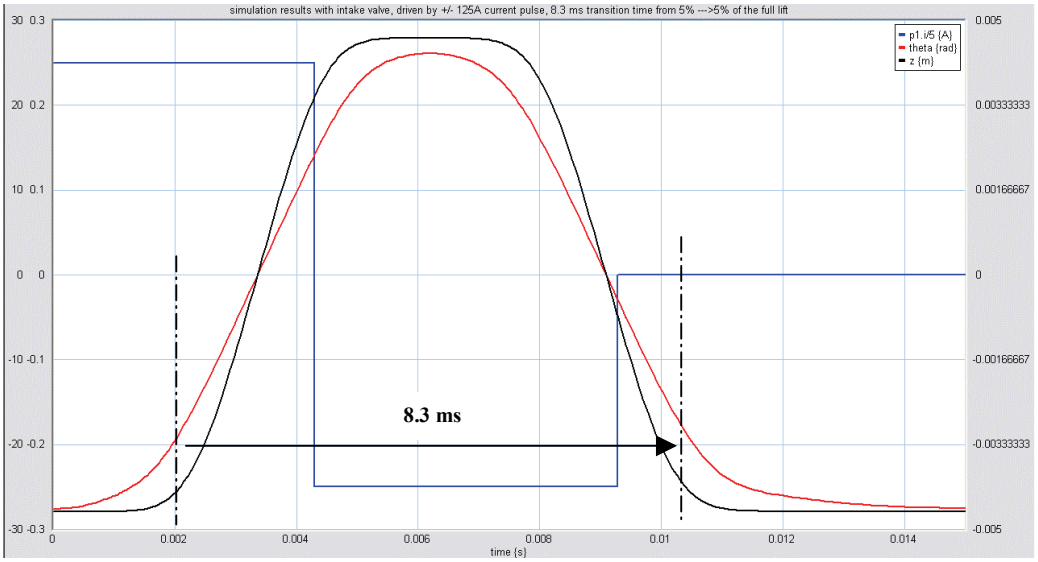

Fig. 7.13. Back-to-back transitions with current pulses of ± 125 A.

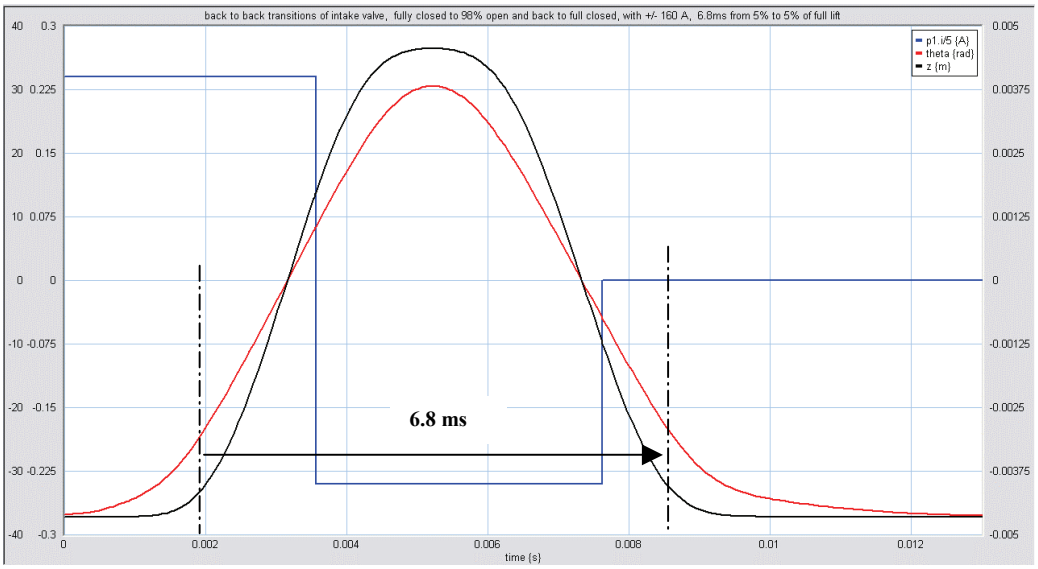

Fig. 7.14. Back-to-back transitions with 98% lift and current pulses of ± 160 A.

Therefore, we have concluded previously that the flat end of the NMT bring us inherent soft landing and other benefits such as zero holding torque and low driving torque. However, its penalty, a longer turn-around duration, compared to single transition time, is shown in the back-to-back transitions discussed above.

7.4.3 Performance at High Temperature and End Positions

In order to make sure this actuator will function reasonably under either a hotter or colder thermal environment, further investigations on the torque output and winding resistance at different temperatures have been conducted.

The change in torque output is mainly due to the change of properties of the permanent magnets as a function of temperature. Additionally, torque output at different rotor positions has also been studied for the purpose of control and design. Figure 7.15 shows the rotor position considered, including left end ($\theta = -20^o$), middle position ($\theta = 0^o$), and right end ($\theta = +20^o$) from left to right. For the two purposes above, extensive Maxwell® computations have been done, as summarized in Table 7.7. For temperatures higher than $20^o C$, such as $140^o C$, we use the B-H curves given by the manufacturer of the NdFeB permanent magnets. For temperature lower than $20^o C$, such as $0^o C$, we basically construct the B-H curve by extrapolating from the B-H curves given by the manufacturer at higher temperatures.

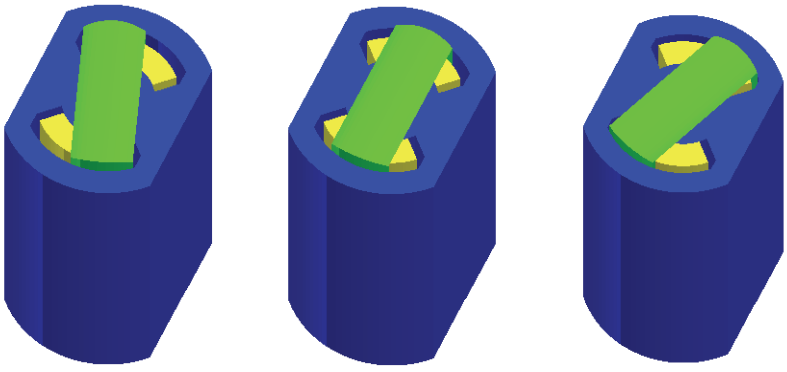

Fig. 7.15. Different rotor positions for torque output.

Note that in Table 7.7, all torque outputs at end positions and different temperatures are normalized based on the torque output at middle position ($\theta = 0^o$) and $20^o C$. The left-right asymmetry of torque production at the two end positions is mainly due to the distortion of the total flux field caused by the armature flux field. In other words, if we reverse the current direction in the Maxwell® model, we will obtain the opposite asymmetry of torque output, as also presented in Table 7.7 for the case of $20^o C$.

TABLE 7.7. TORQUE OUTPUT AT DIFFERENT TEMPERATURES AND ROTOR POSITIONS.

Normalized torque output	Left end (rotor @ -20 degrees)	Middle position (rotor @ 0 degree)	Right end (rotor @ +20 degrees)
20^O C w/ positive current	0.840	1	0.874
20^O C w/ negative current	-0.874	-1	-0.840
140^O C w/ positive current	0.785	0.935	0.819
0^O C w/ positive current	0.887	1.045	0.911

The higher torque output at lower temperature will benefit start performance since the friction from the cold oil will increase and hence need a larger starting torque.

The lower torque output at higher temperature, on the other hand, will require higher current input to maintain proper valve actuation, increasing the winding loss. The higher winding resistance at higher temperatures will also result in higher winding loss. In order to estimate the winding loss at a higher temperature, we need to consider both the change in winding resistance and the change in torque output. For simplicity, we use the torque output of the armature at the middle position ($\theta = 0^o$) when estimating winding loss at different temperatures. As shown in Table 7.8, the total power consumption with a higher winding loss at a higher temperature ($140^o C$) is still fairly reasonable compared to our expectation of 100 W consumption per valve, if we assume the frictional loss will not be affected by temperature. This evaluation further confirms our EMV system as a practical candidate for the high temperature environment in automotive engines.

TABLE 7.8. COMPARISON OF WINDING LOSS AT DIFFERENT TEMPERATURES.

	Normalized torque output	Normalized winding resistance	Actual/normalized winding loss of the actuator	Actual/normalized total power consumption of the EMV System
20 ºC	1	1	34W/1	56W/1
140 ºC	0.935	1.45	68W/2	90W/1.61

At this point, we have shown conceptually the feasibility of our custom designed limited-angle actuator in the valve actuation system. Based on this conceptual design, we built our prototype of the actuator in order to confirm our idea experimentally, as will be discussed in Chapter 8 and 9.

CHAPTER 8 CUSTOMIZED ACTUATOR FABRICATION

8.1 Introduction

In Chapter 7, we discussed the concept of and benefits of a limited-angle actuator ---- a novel design which is so far the best fit for the EMV application.

This chapter will focus on how to transfer the conceptual design into a detailed practical design so we can build a prototype actuator for experimental evaluation. We will start this chapter by discussing how to build the hollow rotor winding ---- the most important part of the actuator ---- and how to connect the winding with the shaft to form a rotating armature. Then we will discuss material choices and design considerations of other components, including the iron yoke, permanent magnets, magnet spacers, bearings, shaft, and so on. Finally, we will illustrate how to assemble the actuator step by step.

Design drawings of each part in SolidWorks® format will be shown in Appendix II.

8.2 Armature

The conceptual design discussed in Chapter 7 established thickness and the angle range of the armature. Here we determine the number of turns, what kind of insulation we will use, and how to construct the winding and with what materials.

For preliminary analysis in the last chapter, we designed a 4-turn winding for a 12 V bus. The simulations showed that this design has great potential. Therefore we will stick with the 4-turn design for our prototype actuator. Each turn is designed as an aluminum rectangular conductor with a height of 1.3 mm and a width of 2.3 mm. We will strive to insure that insulation will have a thickness of 0.1 mm or less at each side to satisfy the 1.5 mm thickness and 45^{o} angular range of the conceptual design.

Because we leave an air gap of only 0.2 mm between each side of the armature and the stator, we need the winding thickness to be very accurate. In the conceptual design, the

active flux will be available within an angular range of 90^o while the armature will occupy an angular range of 45^o. The armature will rotate within an angular range of 40^o, which leaves only 5^o of tolerance in the θ-domain. Therefore we need to make sure the angular range of the winding is also very accurate. In short, we need to find a way to make the armature so that it will have a very accurate shape in every dimension.

To solve this problem, we designed a mold for making the armature. The mold consists of 7 parts, as labeled in Fig. 8.1. The first three parts (mold 1-3) form a cylinder whose diameter is the same as that of the inner diameter of the armature. Mold parts 4 and 5 are two identical arc portions of a hollow cylinder, which have the same inner and outer diameters as the armature. Mold parts 1 to 5 can be screwed together to create a fixture. Mold parts 6 and 7 again are two identical arc portions of a hollow cylinder, which have an inner diameter the same as the outer diameter of the armature. These two parts will be clamped over parts 4 and 5, as shown in Fig. 8.1. The two air spaces between these parts define the exact shape of the active portions of the armature.

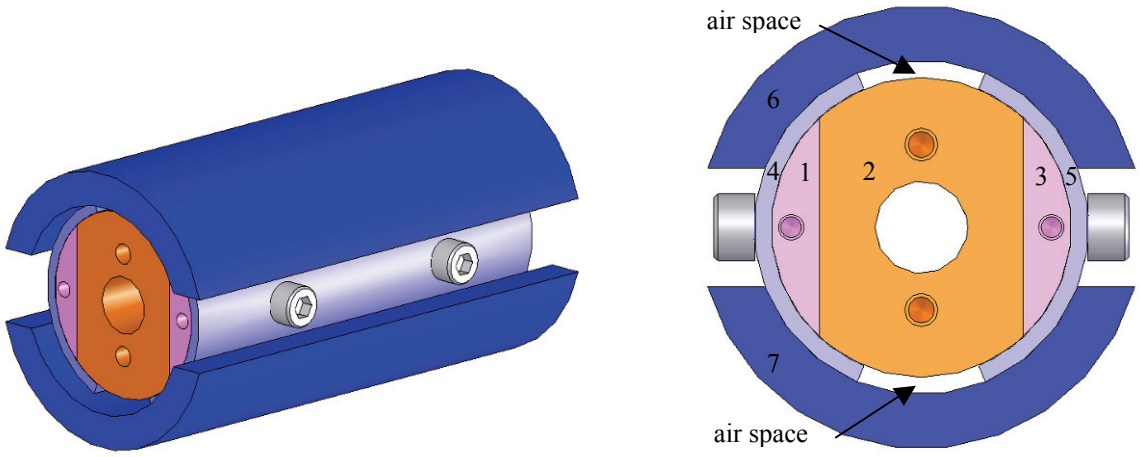

Fig. 8.1. Mold to make the armature.

We also need to connect the armature and shaft together to form the rotor of the actuator. First, we designed two parts called the front-end clamp and back-end clamp. The end turns of the armature are placed between the two clamps and screws are used to clamp the

two parts and the end turns together. Finally we connect the front-end clamps to the shaft via spring pins. The structure is shown in Fig. 8.2.

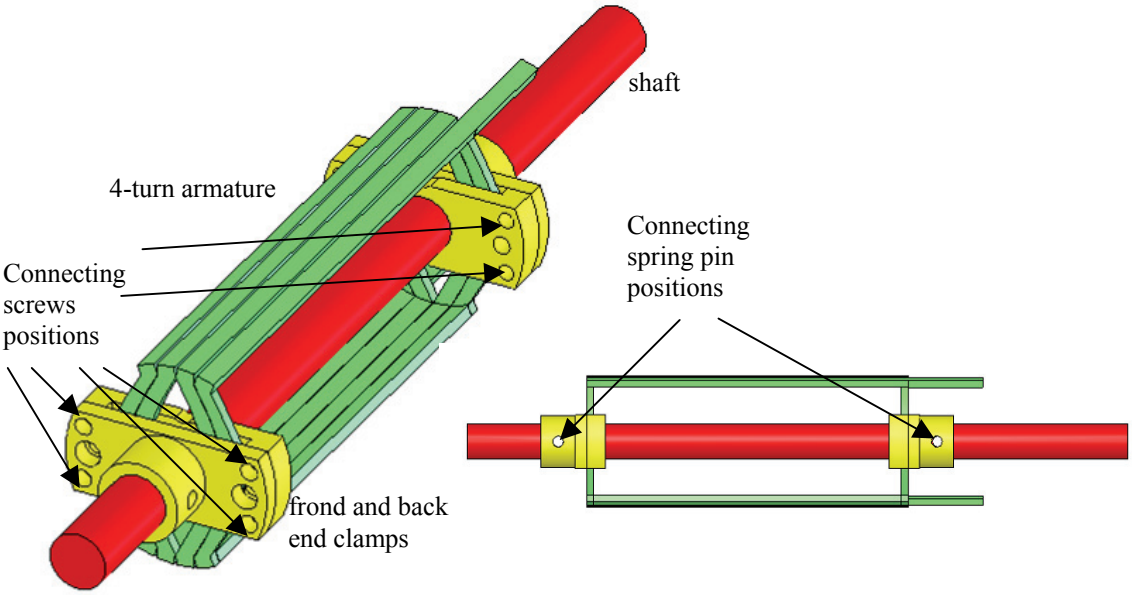

Fig. 8.2. Armature-shaft structure.

Next we will discuss how to achieve a properly insulated and strong enough armature structure by taking advantage of epoxy pre-impregnated (pre-preg) fiberglass tape and fiberglass woven sleeve. There are several wave patterns potentially suitable for this application. The cross section figures of these patterns are shown in Figs. 8.3–8.6, where the light green represents conductor and the dark blue represents insulation. The first three patterns fall into a similar category in the sense that we need to install the arrangement using insulating steps interspersed with winding steps. We also need to treat active turns and end turns of the armature differently. For active turns, we use the epoxy pre-preg fiberglass tape while for end turns, fiberglass woven sleeves are used instead. The last two patterns, on the other hand, can be implemented by wrapping the tape around the conductor before the winding process. If we use the last two patterns, we don't necessarily need to separately treat the end turns.

Due to the dimension constraints of the armature and the thickness of available pre-preg tape, only patterns 1-4 satisfy the dimension requirements. The first pattern shown in

Figure 8.3 obviously offers the most mechanical force to hold the turns together. Therefore we chose to try pattern 1 as well as pattern 4 shown in Fig.8.6 in making the armature.

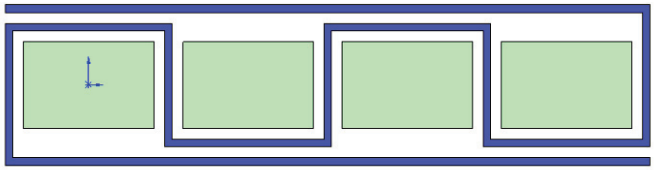

Fig. 8.3. Insulation pattern 1.

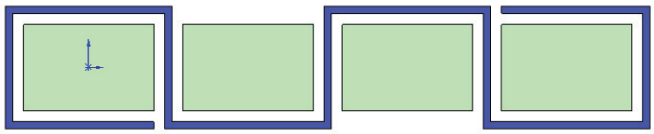

Fig. 8.4. Insulation pattern 2.

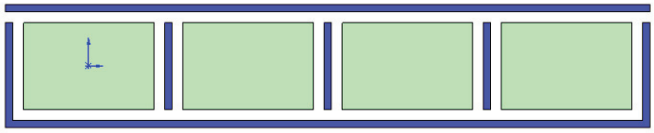

Fig. 8.5. Insulation pattern 3.

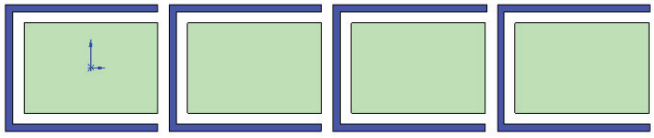

Fig. 8.6. Insulation pattern 4.

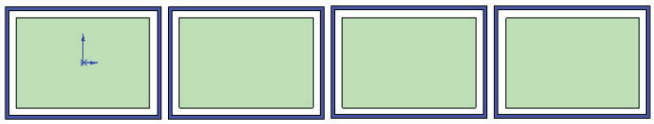

Fig. 8.7. Insulation pattern 5.

The end turns of the winding need to be pushed into the air space between the two end clamps after the winding process while also making sure there is enough space between turns for the shaft, as shown in Fig. 8.2. If we go with the pattern 4 of Fig. 8.6, then we don't need to treat each end turn separately since we can wrap the whole conductor with the pre-preg tape before winding. This tape may produce adequate end turn insulation. But if we use the pattern 1 shown in Fig. 8.3, the pre-preg tape will need to be woven between conductors during the winding process. The same technique cannot be applied to the end turns because after winding, the positions of the end turns will be changed dramatically to fit into the end clamps and to allow the shaft to pass through, requiring the end turns to be insulated separately. A fiberglass woven sleeve is chosen to fulfill this purpose. For mechanical reasons, epoxy resin is dripped onto the sleeved end turns to ensure strong connections between all end turns and between the end turns and the clamps.

As will be discussed in Chapter 9, pulling tests were done on armatures constructed using the two chosen insulation patterns. The results showed that the armature with the insulation pattern 1 of Fig. 8.3 has a much higher mechanical strength. Therefore we will focus on the armature fabricated with the first insulation pattern 1 of Fig. 8.3.

With all the design considerations of the armature explained, we now illustrate how to build the armature-shaft structure step by step.

Step 1: Preparation Work

- Clean all mold parts, end clamps, and spray mold release on all the surfaces of the mold parts and two inner end clamps which will have possible contact with the winding, as shown in Fig. 8.8. (The mold release is Sprayon S00311 dry film PTFE mold release from Krylon Products Group);

- Assemble mold parts 1-5 together. Use caliper to make sure the cavities which receive the winding are even and symmetric before tightening all the screws;

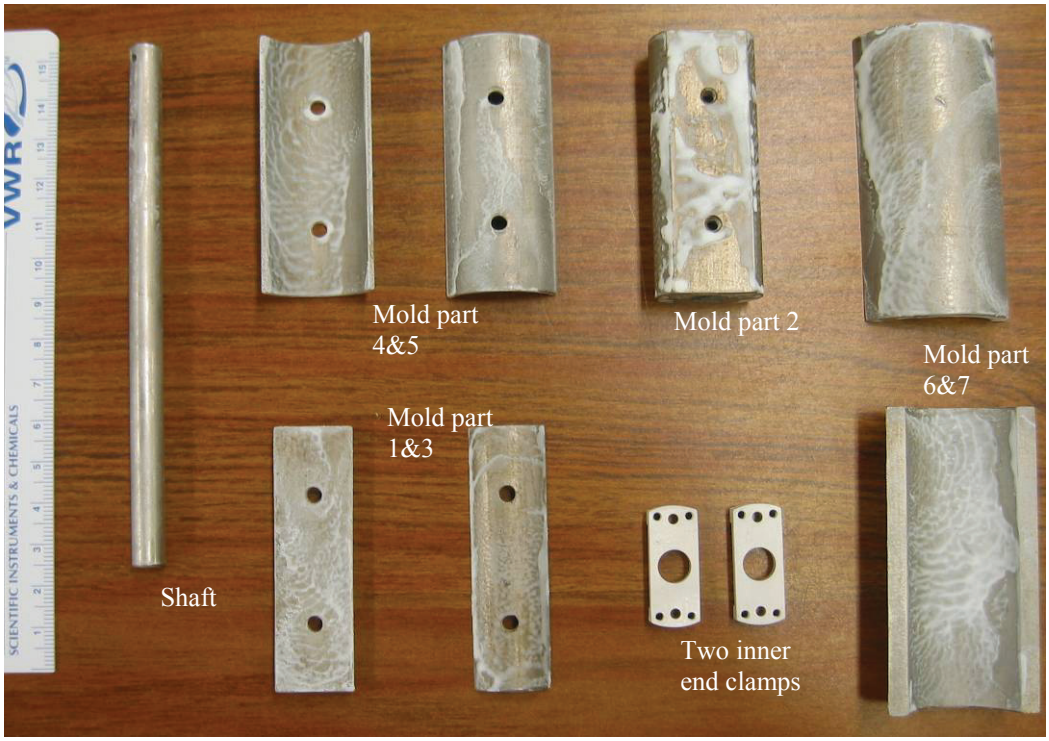

Fig. 8.8. All mold parts with mold release coatings.

- The inner clamps are attached to the axial ends of the mold assembly at this point in the process. Temporarily insert the shaft to ensure good clearance and alignment before tightening all the screws, as shown in Fig. 8.9;

- Prepare an aluminum conductor with a length no less than 720 mm (The aluminum grade is 1050A with as-rolled dimensions of 1.3 mm (± 0.03 mm) x 2.3 mm (± 0.05 mm). This product is purchased from AirCraftMaterialsUK.com Ltd, United Kingdom);

- Cut 7 sections of fiberglass sleeve of 30 mm length each and slide them onto the aluminum conductor (The sleeve is product Varglas Litewall from Varflex Corp, Rome, NY);

- Cut two pieces of pre-preg tape (E-761 with 120-Eglass reinforced) with a length a bit greater than 60 mm and a width no less than 35 mm (This product is offered by Park Electrochemical Corp, Waterbury, CT);

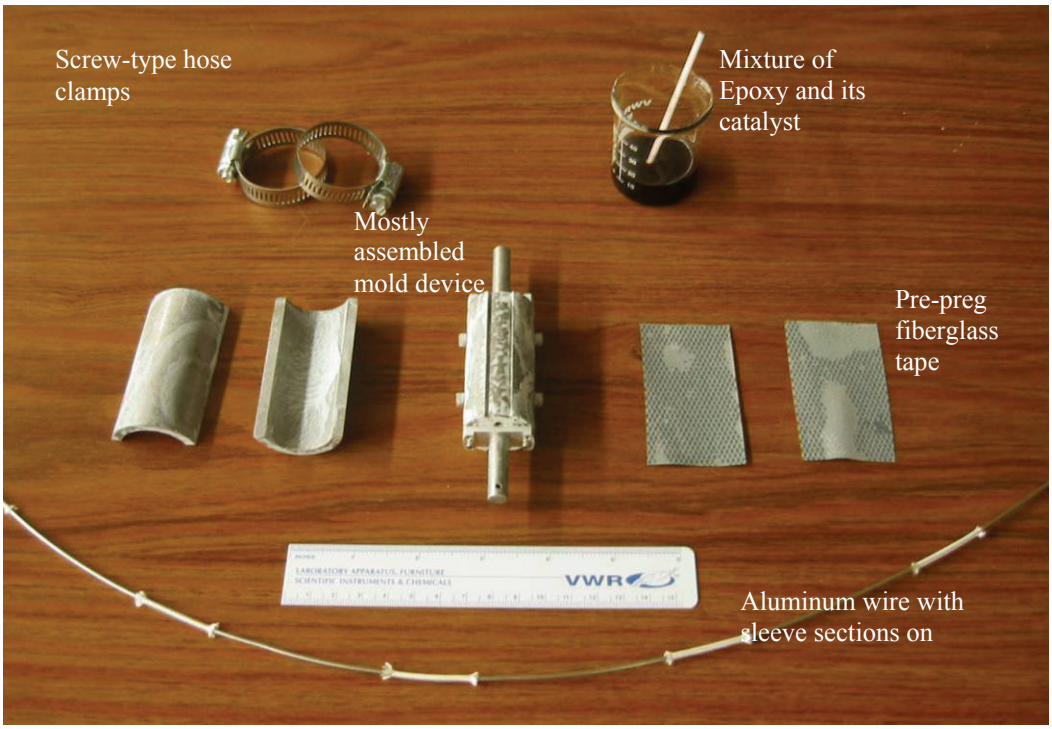

Fig. 8.9. Picture of all materials prepared for winding process.

- Mix about 5.7 gram of epoxy (W19) and 1.0 gram of its catalyst (catalyst 11) together in a container in advance (Both products are from Emerson & Cuming, Billerica, MA). It is a good idea to mix the epoxy and the catalyst about 18 hours before the winding and curing steps. The objective is a mixture thick enough to sink into the end turns without flowing outside;

- Prepare 2 or 3 screw-type hose clamps to clamp the winding within the mold in later steps;

All prepared materials are shown in Fig. 8.9.

Step 2: Winding Formation

The first step of the winding process is to attach the two pieces of pre-preg tape symmetrically on the inner surface of the winding pocket arc section on each side of the mold fixture, with one long edge of the tape touching the mold boundary. Use one hand to fix the positions of the tapes and use the other hand to put one end of the conductor on the surface of the winding pocket section of the mold and then start winding. During the process, the 7 sleeve sections should be properly positioned prior to making the subsequent bend in the conductor at the end of the mold. Also during the process, the two pieces of pre-preg tape will be woven alternatively over and under turns to form an insulating and supporting structure as shown in Fig. 8.3. After finishing the winding, the two outside pieces of the mold are put on and hose clamps used to clamp together the whole mold with the winding inside. Figure 8.10 shows how it looks like at the end of this process.

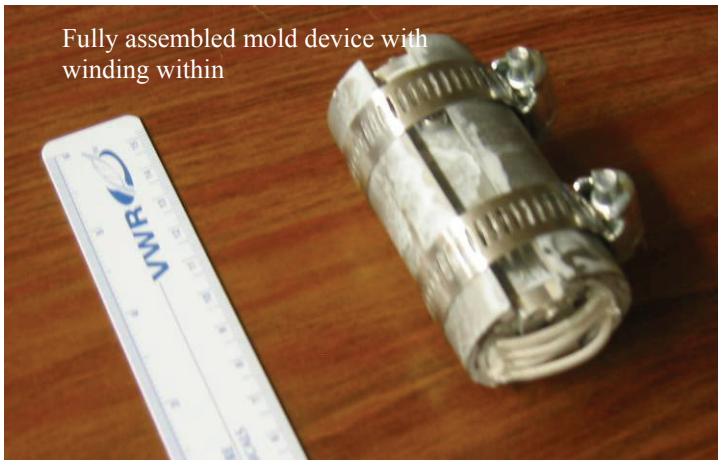

Fig. 8.10. Picture of the winding in mold with hose clamps put on.

Step 3: End Turn Treatment

The active portions of the winding are now tightly clamped within the mold pieces and we can work on the end turns without affecting the shape and position of the active turns. The entire assembly is clamped into a vice and tools such as a screwdriver are to put each end turn into the desired position while being careful not to damage the sleeves. The desired positions are the positions that enable the end turns to fit into the back-end clamps and which also enable the shaft to pass through the end turns easily, as shown in

Fig. 8.11. After this treatment, the assembly is removed from the vice. We then apply onto the glass sleeves enough catalyzed epoxy to thoroughly impregnate the sleeves, as shown in Fig. 8.12. Then we put on the front-end clamps and use screws to completely close the space between the front-end and back-end clamps. The end turns should be tightly clamped between the mounting clamps. The shaft is inserted as before to make sure there is enough clearance around it and the end clamps are nicely aligned axially. Now the armature is ready to be put into the oven to begin the curing process. The finished armature is shown in Fig. 8.13.

Fig. 8.11. Picture of the end turns in desired positions.

Step 4: The Curing Process

Due to the special requirements of pre-preg material, the curing process has three stages:

1. Increase oven temperature from room temperature to 255 ^{o}F (124 ^{o}C) with an increase rate in the range of 2-5 ^{o}F/minute;
2. Hold the oven temperature at 255 ^{o}F for a period of 90-120 minutes;
3. Decrease the oven temperature back to room temperature at a rate of around 8 degree F/minute.

Fig. 8.12. Picture of the end turns impregnated with epoxy.

Fig. 8.13. Picture of the armature structure before curing.

The oven we have doesn't have any rate control. However, from previous testing, we observed that the natural rate of increase of this oven, with full duty cycle (100%) on the heater, is about 3 ^{o}F/minute, which is in the recommended range.

However, when decreasing the oven temperature, if we do so by setting the target temperature to room temperature, the temperature will drop much slower than what is

specified above. So we chose to turn off the oven and open its door to accelerate the temperature drop. This process seems to have worked fine for our purpose.

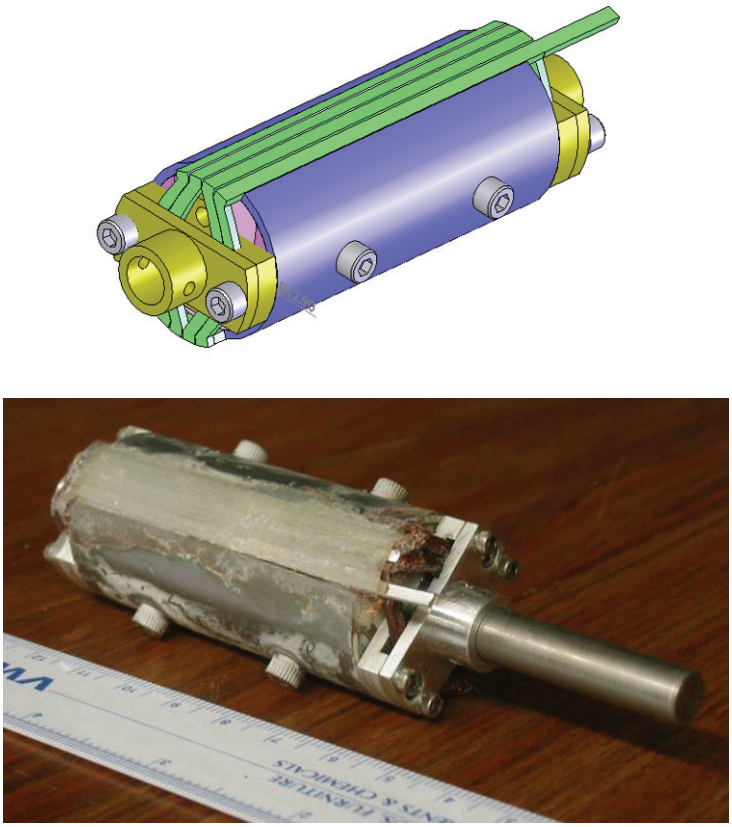

Fig. 8.14. SolidWorks® model and picture of mold without clamping pieces.

Step 5: Removal from Mold

After the curing process, the armature is removed from the mold. The hose clamps are loosened and the clamping parts (mold parts 6 and 7) are taken off, as shown in Fig. 8.14. Then the side screws, which hold parts 1-5 together, are loosened. Mold parts 4 and 5 should fall off or be very easily removed. The screws which hold back end clamps to part 1 and 3 of the mold are now removed. Parts 1 and 3 can then be removed. Now the only part left behind is part 2 of the mold, the middle piece of the three pieces forming a hollow cylinder, as shown in Fig. 8.15. In order to remove this part, we put the assembly, with the shaft inserted temporally, back into a vice, with the vice jaws clamping the arcuate outer surfaces of the end clamps at both ends. Hand tools, for example, a small screwdriver or a wrench, can be used to rotate the mold part 2 with respect to the shaft about 90^{o}. The shaft is then slid out of the armature structure and part 2 of the mold can

be removed, leaving the armature structure without the shaft, as shown in Fig. 8.16. For convenience in assembling, the shaft will be permanently connected to the armature via spring pins at the last stage of the assembly process, as will be discussed shortly.

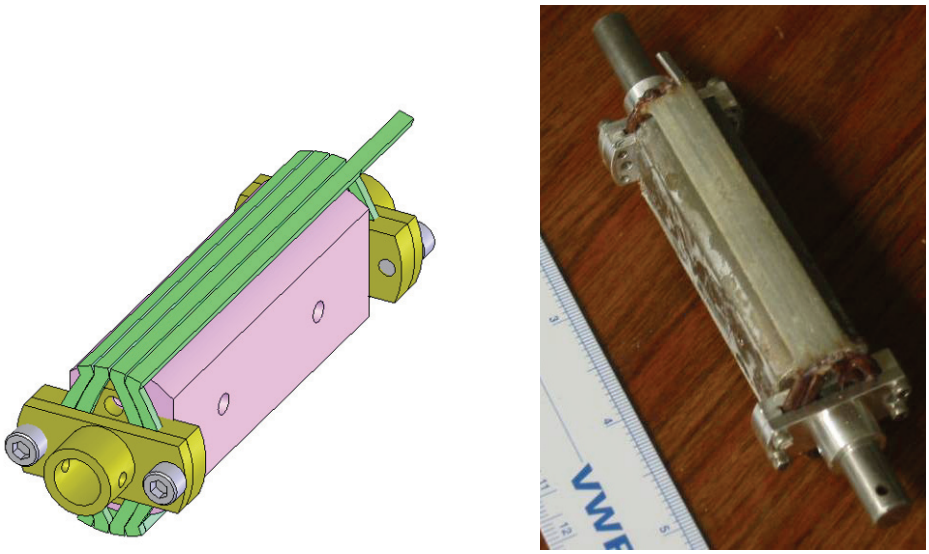

Fig. 8.15. SolidWorks® model and picture of the armature with only mold part 2.

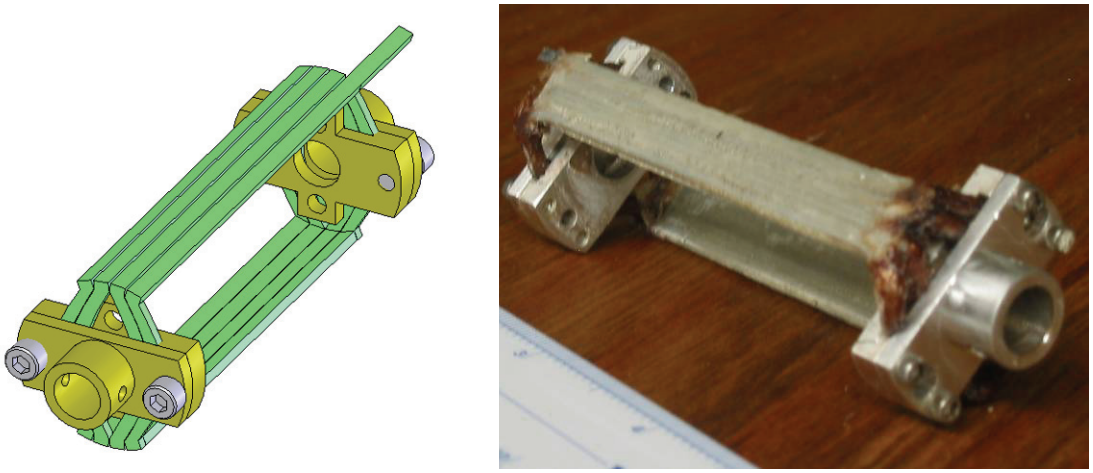

Fig. 8.16. SolidWorks® model and picture of the cured armature structure w/o shaft.

8.3 Other Components

8.3.1 Iron Yoke

Considering only its own function, we could make the yoke a single piece of mild steel. However, we need to install the armature and the permanent magnets within it, so as a practical matter, we chose to build it in multiple pieces. There are many possible

approaches to do this, depending on the procedure to be used to assemble the whole actuator. Here we choose to build the iron yoke from three layers and five pieces, as shown in Fig. 8.17, with screws in the sides to hold them together. We will refer to the three layers from outside to inside as core 1, core 2, and core 3, respectively. For this design, in order to make core 1 a continuous part with a full inner hollow cylinder, we have chosen to increase its width from the 28 mm of the original design to 33.1 mm. In order to save cost, we also increased the outer diameter of core 1 from the original 37.2 mm to 38.1 mm (1.5 inch) so a standard sized rod could be used. These modifications are done just for manufacturing convenience. From the perspective of the flux circuit and torque constant, the original width of 28 mm and outer diameter of 37.2 mm are adequate for this application.

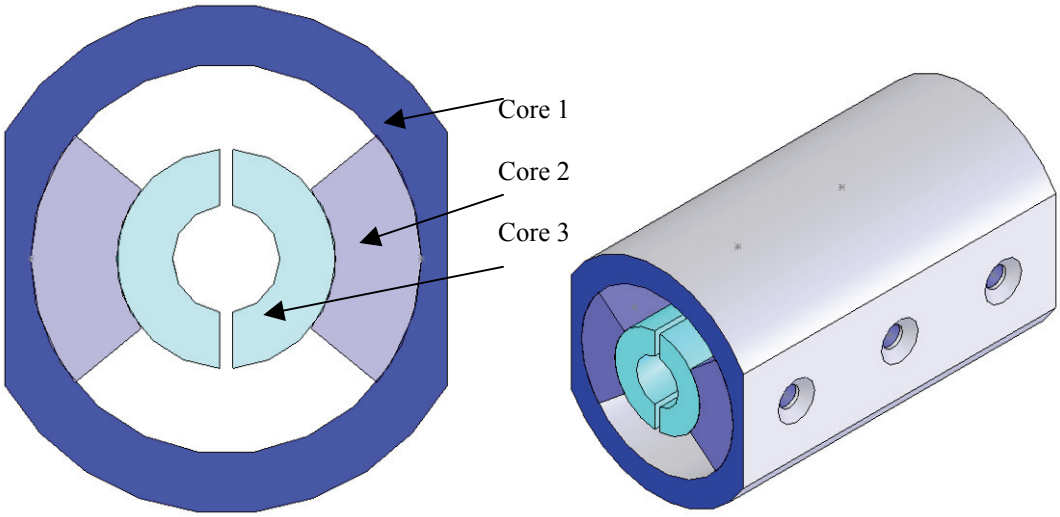

Fig. 8.17. Three-layer and five-piece design of the iron yoke.

8.3.2 Shaft and Bearings

Since the armature is the only moving element of the actuator, it is preferred to use a shaft with a large diameter to increase the ruggedness of the armature-shaft structure. For our design, the diameter of the shaft is 5/16 in, very close to that of the first motor (3/8 in) and much larger than that of the second motor (3/16 in). The shaft is made from a stainless steel rod with a tight dimensional tolerance and a precision ground finish (Mcmaster 8934K23).

Ball bearings support the shaft at both ends in order to minimize friction. To avoid a complicated and bulky bearing housing outside of the actuator, the ball bearings are press fit into the inner layer of the iron yoke. Hence, we need to modify core 3 with a properly sized cavity at both ends to accommodate the ball bearings, as shown in Fig. 8.18, where the bearings are represented by a pink hollow cylinder. A Maxwell® simulation has been done to ensure that no calculated reduction of torque output is expected due to this modification of core 3. The stainless steel ball bearing (Mcmaster 57155K358), has an inner diameter (ID) of 5/16 in, an outer diameter (OD) of 1/4 in, and a width of 5/32 in.

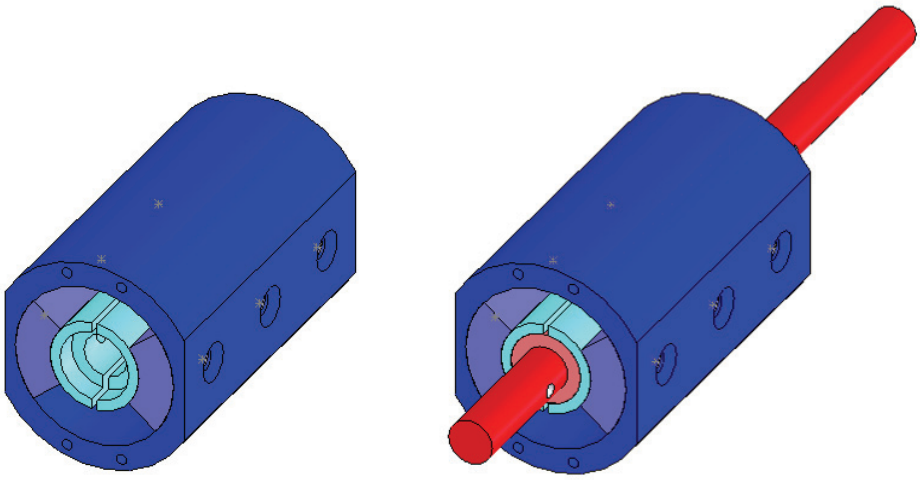

Fig. 8.18. Modified core 3 to accommodate ball bearing to support shaft.

8.3.3 Permanent Magnets and Magnet Spacers

The high temperature grade Neodymium-Iron-Boron (NdFeB) permanent magnets are used for high flux excitation. Those high temperature grade NdFeB permanent magnets are purchased from NingBo Zhaobao Magnet Co, LTD, China. The magnets are specified as an arc section of a hollow cylinder, which has an ID of 16.4 mm, an OD of 25.4 mm, hence a radial thickness of 4.5 mm, and an arc range of 90^{o}.

To prevent the magnets from moving axially or rotating with respect to the axis during or after the actuator is assembled, an aluminum magnet spacer is used to hold the magnets in the desired positions during and after the assembling procedure. The spacers are fixed to

the inner layer of the iron yoke via screws, as shown in Fig. 8.19, where the spacers are represented by the gray area and the magnets are shown in yellow.

8.3.4 Encoder and Mounting Bridge

As mentioned in Chapter 4, we need θ position feedback to monitor and control the transition trajectory. In order to get this information, a micro hollow shaft optical encoder (2MCH from Scancon Incremental Encoders, USA) is used. This encoder can only accommodate a shaft with a diameter of no more than 1/8 inch. The encoder is designed to be installed using a mounting plate included in the encoder package. A mounting bridge is used to connect the stationary mounting plate of the encoder to the stationary part of the actuator --- the outside layer of the iron yoke. Further, we need to reduce the encoder end of the shaft to a diameter of 1/8 inch to fit the rotating part of the encoder. Figure 8.20 shows more details about this design consideration.

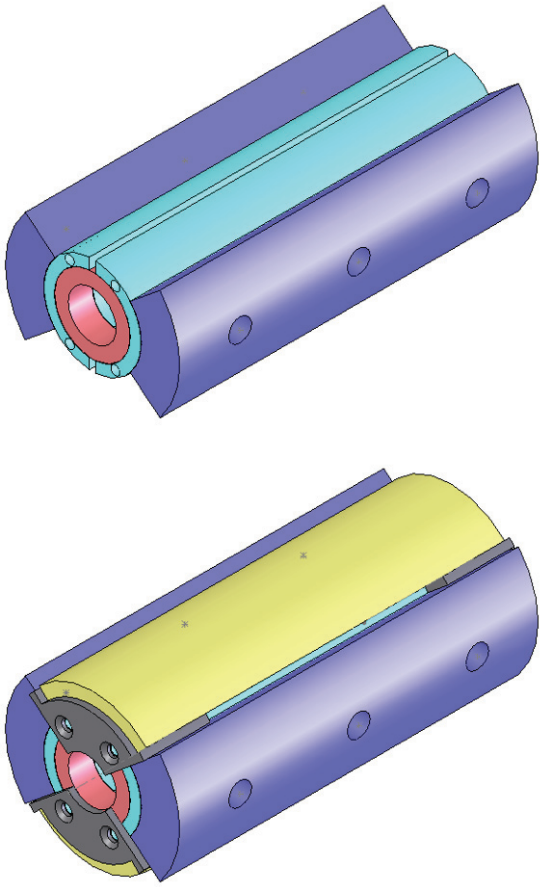

Fig. 8.19. Permanent magnets and magnet spacers.

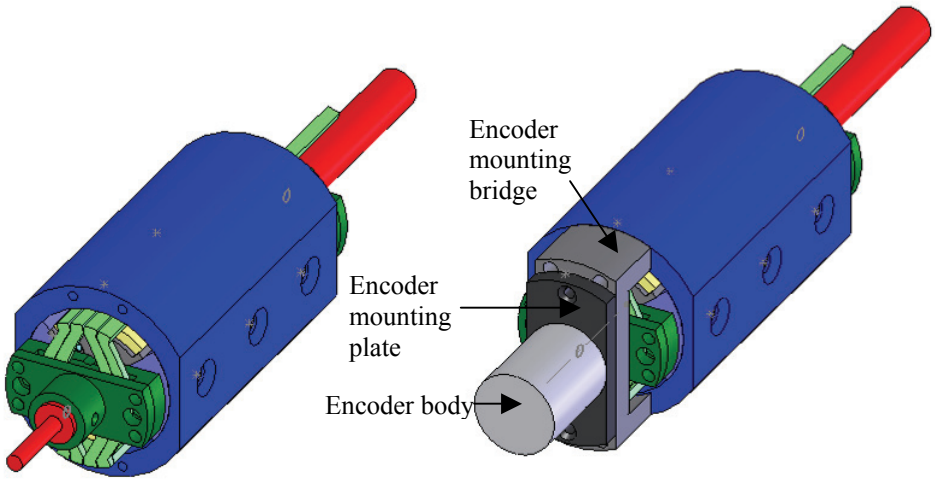

Fig. 8.20. Shaft and core 1 modification for encoder installation.

8.4 Assembling the Actuator

In this section we discuss how to assemble all the parts to obtain a functional actuator. We start assembling by attaching the two pieces of core 3 and the two pairs of magnet spacers together, as shown in Fig. 8.21. Two slim plastic spacers with a thickness of 1mm and proper height and length are inserted into the air gaps between the two pieces of core 3 before assembling. These two plastic spacers are the yellow element in Fig. 8.21. Then the two ball bearings shown in pink are pressed into the core.

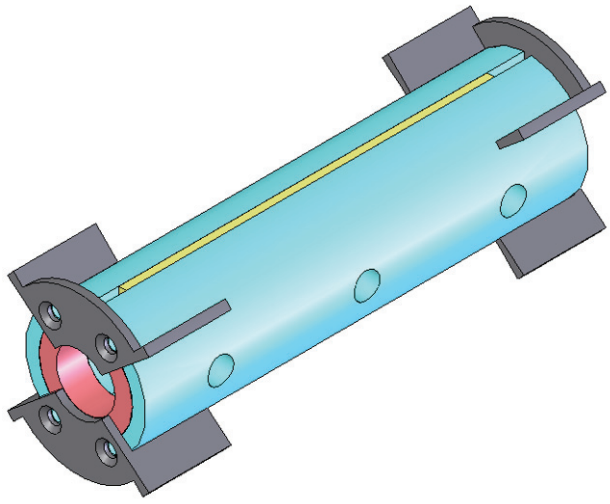

Fig. 8.21. Assembling of core 3, core spacers and magnet spacers.

A pair of permanent magnets is then put into the positions defined by the magnet spacers, as shown in Fig. 8.22.

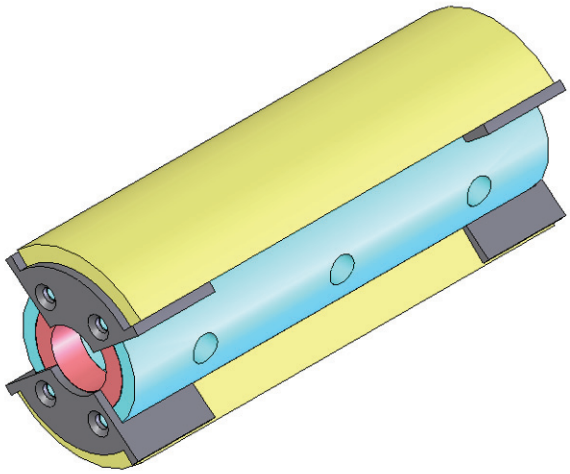

Fig. 8.22. Assembling with permanent magnets added.

The rotor, i.e., the armature-shaft structure, is installed next. At this point the shaft is not fixed to the front end clamps. As shown in Fig. 8.23, the armature is placed on top of the partial assembly. The orientation of the armature will allow it to slide over the partial stator assembly. The shaft, which goes through the end clamps of the armature and the clearance hole within core 3, is then installed. The armature is next rotated 90^{o} with respect to the partial stator assembly so that it is positioned with the active turns centered on the permanent magnets, as shown in Fig. 8.24. Spring pins are then used to permanently connect the rotor shaft and end clamps.

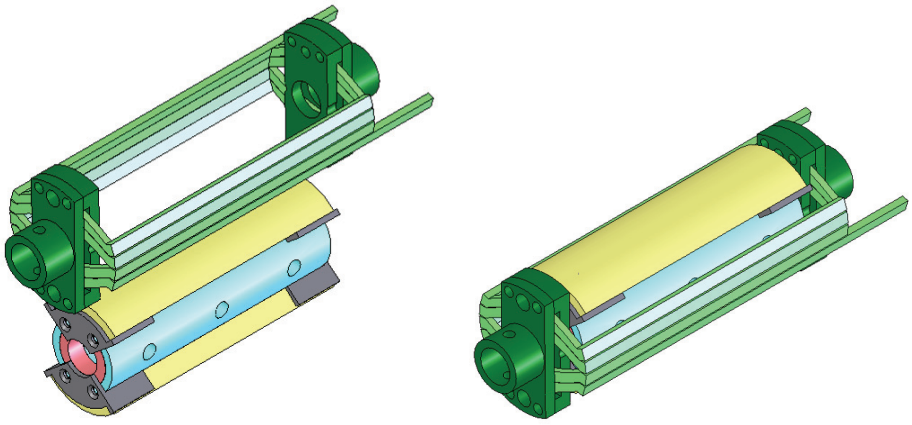

Fig. 8.23. The first two steps of assembling the armature and partial core.

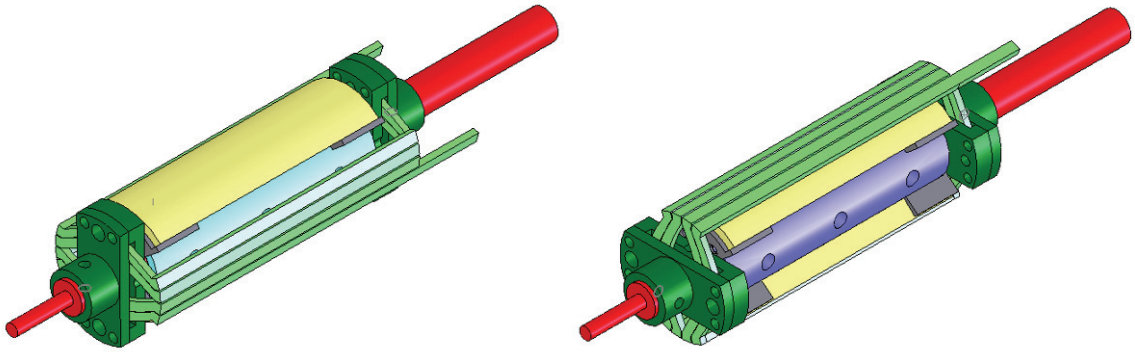

Fig. 8.24. The last two steps of assembling the armature.

After fitting the armature into the partial stator assembly, we are ready to put on the second layer of the iron yoke by putting the two pieces of core 2 into the positions defined by the magnet spacers and the two pieces of core 3, as shown in Fig. 8.25.

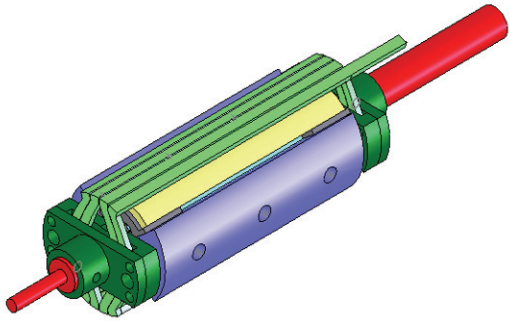

Fig. 8.25. Core 2 and core 3 added to the partial stator assembling.

The outside layer of the iron yoke (core 1) is now slid on from either end and connected to core 2, and core 3 by flat-head screws, as shown in Fig. 8.26.

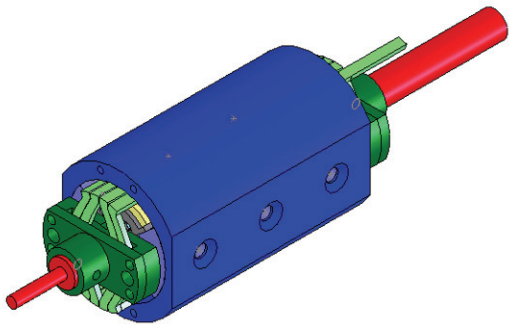

Fig. 8.26. Core 1 installed completing the stator assembling.

Finally, we installed the encoder and its accessories in the following sequence. First, the mounting bridge is connected to the core 1 by screws; then, the mounting plate is connected to the mounting bridge also by screws; and lastly, the rotating part of the encoder is connected to the shaft by a set screw and the stationary part of the encoder is fixed to the mounting place by a flat spring. This process is shown in Fig. 8.27. Note that the set screw and flat spring in the last step are not shown in Fig. 8.27.

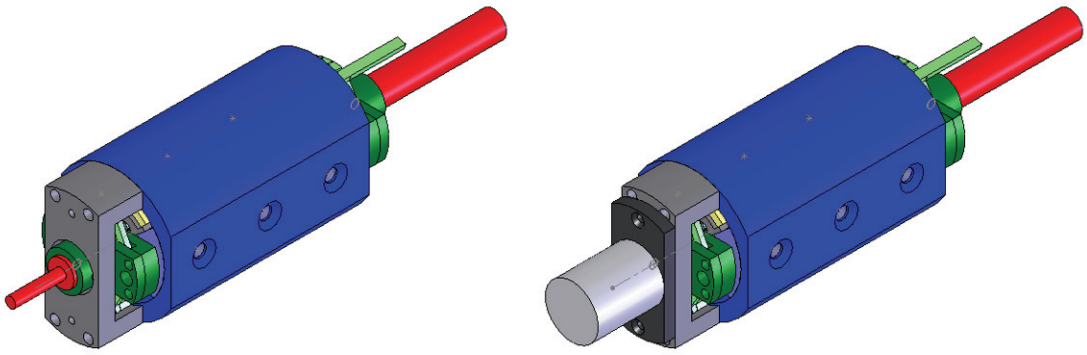

Fig. 8.27. The encoder installed on the actuator.

The picture of the fully assembled actuator is shown in Fig. 8.28.

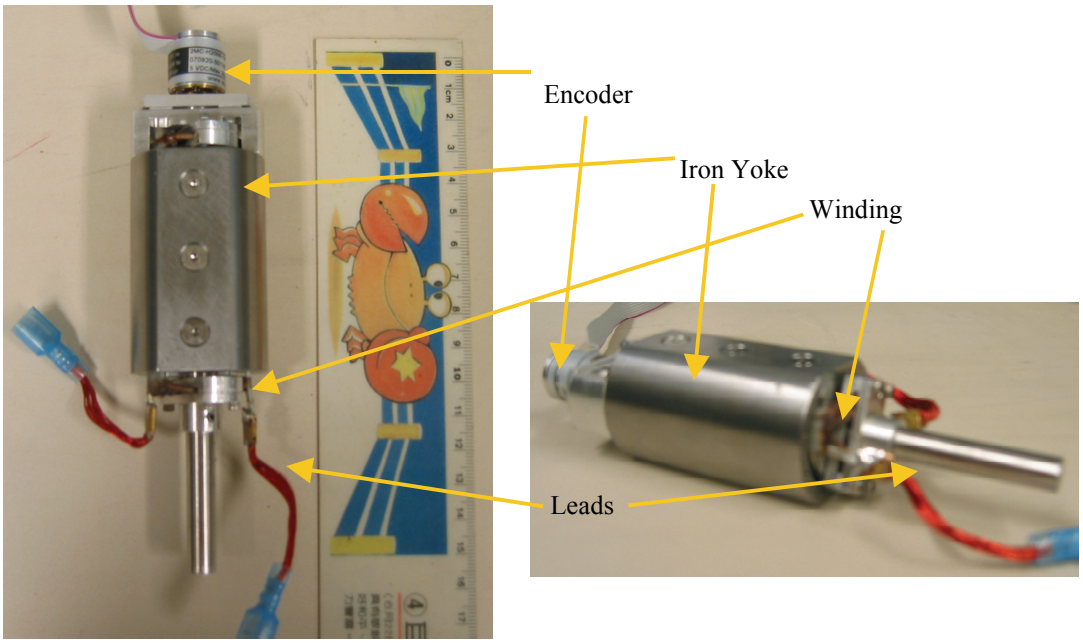

Fig. 8.28. The fully assembled limited-angle actuator.

Note that for our convenience, a pair of stranded leads is soldered to the winding ends as the electrical leads connected to the outside power supply. Future development of a more professional lead design is desired. With this prototype of the limited-angle actuator, we can conduct experimental tests on the actuator alone and the EMV system with the actuator installed, as will be discussed in Chapter 9.

CHAPTER 9 EXPERIMENTAL EVALUATION

9.1 Introduction

In Chapter 8, the construction of the limited-angle actuator was discussed. In this Chapter, some experimental evaluations are reported which confirm our theoretical analysis and simulation prediction of the actuator performance.

This Chapter first reports mechanical and electrical tests of the armature. Then measurements of torque constant, rotor inertia, friction coefficients, and other parameters of the actuator are described, followed by presentation of successful valve actuation with satisfactory system performance. Finally, projection of a full engine valve actuation will be presented based on experimental results of intake valve actuation and simulation results of both intake and exhaust valves actuation.

9.2 Armature Evaluation

After each armature was fabricated, we examined its dimensional accuracy, tested its mechanical ruggedness, and measured its electrical parameters.

9.2.1 Armature Dimensions

The most critical armature dimensions include its outer diameter, inner diameter (or armature thickness), angle range, and end-to-end distance.

Accurate outer and inner diameters are very important to keep the 0.2 mm clearance between the armature and the iron yoke outside, and the permanent magnets inside in order to ensure smooth movement of the active portion of the armature. We used a caliper to measure the outer diameter of the armature before and after we took it off the mold. Because it is very hard to measure the inner diameter of the armature directly, we use an alternative method to make sure the inner diameter is correct. As shown in Fig. 9.1, we made a cylinder of hard plastic with both sides cut off, whose outer diameter is the same

as the outer diameter of the permanent magnets. The cylinder also includes a through-hole in order to accommodate the shaft. After the armature is removed from the mold, we insert the plastic cylinder into the armature with the flat sides facing the active windings. The shaft is then inserted into the armature and the plastic cylinder, which is rotated with respect to the shaft so the round sides of the cylinder face the active windings. By rotating the cylinder back and forth, one can feel the resistance if any. If the rotation feels very smooth without the resistance then we conclude that the clearance between the armature and the permanent magnets is enough for our purpose although we don't have a specific measurement of the inner diameter.

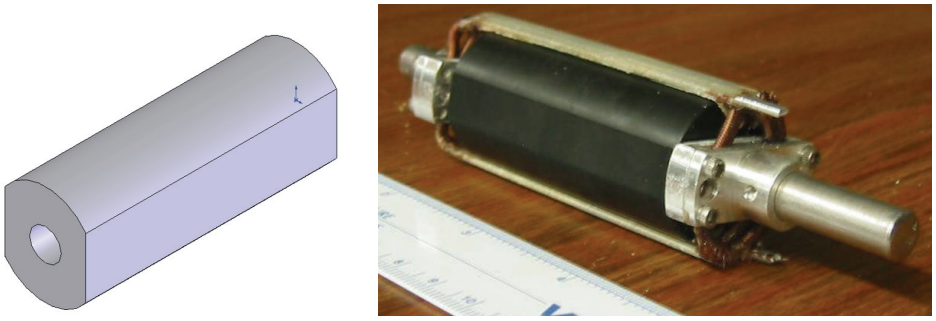

Fig. 9.1. The cylinder for testing the inner armature diameter.

The angular spread of the armature is also a very crucial parameter, as discussed in Chapters 7 and 8. The angular range of the current armature is 45°. By assuming that the axis of the armature is at the expected position and that the outer diameter of the armature measured previously is well controlled, we are able to measure the width of the active portion of the armature from the outside edge of the first turn to the outside edge of the fourth turn with a caliper, as shown in Fig. 9.2, and then translate that number into degrees.

The end-to-end distance of the armature is defined as the distance between the inner surfaces of the two inner end clamps of the armature, as shown in Fig. 9.3. We need to make sure this distance is sufficient to accommodate the iron yoke and permanent magnets without causing any undesired friction.

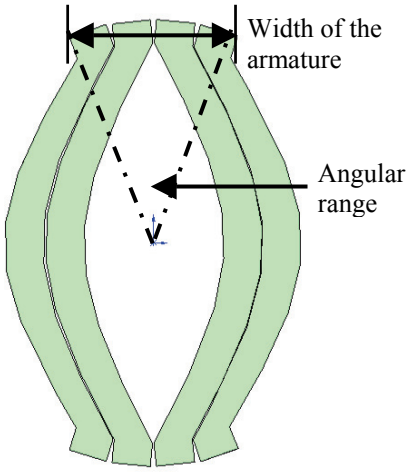

Fig. 9.2. Relation between the width of the armature and its angular range.

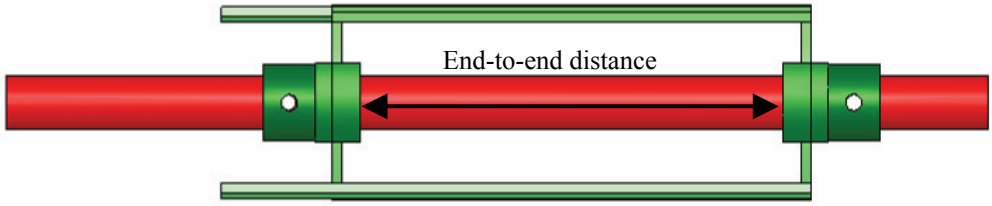

Fig. 9.3. The end-to-end distance of the armature.

The results of all dimensional measurements are summarized in Table 9.1, which shows excellent accuracy of the actual dimensions compared with the desired ones and proves the effectiveness of the armature mold.

We now describe the so-called "pulling test" to make sure that the armature is strong enough from a mechanical point of view.

TABLE 9.1. SUMMARY OF THE ARMATURE DIMENSIONS.

	Designed Value	Measured Value
Outer diameter (mm)	28.80	28.81~28.84
Inner diameter (mm)	25.80	N/A
Thickness (mm)	1.50	1.45~1.50
Width (mm) /Angle range (degree)	11.31 /45^{o}	11.30~11.38 /44.96^{o}~45.28^{o}
End-to-end distance (mm)	63.00	62.99~63.03

9.2.2 Mechanical Strength (Pulling Test)

As mentioned in Chapter 8, we have made windings with two kinds of insulation structures which also offer mechanical support. The cross section of the two insulation patterns, where the light green represents conductor and the dark blue presents pre-preg tape as insulation, are shown in Fig. 9.4, which is copied from Chapter 8 for the reader's convenience. As discussed in Chapter 8, the main difference between these two patterns in terms of winding fabrication is that pattern (a) needs separate treatment of the active portion and the end turns while pattern (b) treats the active and end-turn parts of the winding simultaneously. Undoubtedly, pattern (b) is much more convenient for fabrication purposes. However, it is readily appreciated that the requirement of adequate mechanical robustness of the winding is more important than fabrication simplicities. In order to make sure the armature is strong enough and to determine which insulation structure is stronger, we have done a pulling test as described below for both insulation designs.

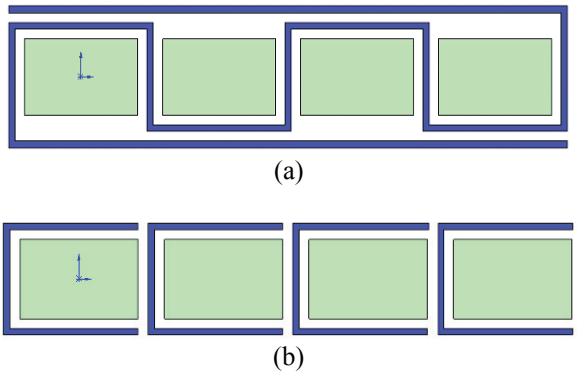

Fig. 9.4. Two different insulation patterns.

A vice was used to hold three turns of the 4-turn winding. The fourth turn of the winding was connected to a spring scale via a clamp. This turn was then pulled until it began to distort or pull apart from the rest of the winding. The spring scale reading at that moment was recorded. The same test was done repeatedly to each armature we made, including the one fitted into the actuator prototype, and consistent results were obtained. The armature of pattern (b) could be easily torn apart while the clamp lost its hold on the armature with pattern (a) before any sign of distortion or parting was observed. In the

later case, we recorded the maximum spring scale reading. The experimental data are shown in Table 9.2.

Note that in Table 9.2, we also set up a lower limit of force for failure of the winding in our pulling test. The failure limit is set at 10 times the force generated by each half turn when producing the rated torque of the actuator (0.38 N-m from Maxwell® simulation and is rounded to 0.4 N-m for our calculation), as shown in (9.1), where T is the rated torque, D_m is the mean diameter of the armature, and N is the number of turns.

$$F = 10 \cdot T / (D_m \cdot N) \tag{9.1}$$

Obviously, the winding with pattern (a) has a much stronger mechanical structure in the mechanical sense while the winding with pattern (b) can barely meet our strength requirement. Therefore, we choose to use pattern (a) for the final winding. Next we will validate the electrical parameters, mainly the resistance and inductance, of the armature.

TABLE 9.2. COMPARISON OF TWO INSULATION PATTERNS.

	Force (N)
Winding with insulation pattern (a)	> 80
Winding with insulation pattern (b)	35~40
Lowest requirement (discussed in text)	36.6

9.2.3 Electrical Parameters (Resistance and Inductance)

- **Armature Resistance**

The resistance of the four-turn winding was expected to be 6.8 mΩ given its height of a 1.3 mm and its width of a 2.3 mm. However, the aluminum conductor we received actually has a height of 1.2 mm and a width of 2.2 mm. This increases the winding resistance to about 7.7 mΩ, which is still quite small and causes inconvenience in our measurements and experiments, because any contact resistance and/or lead resistance can easily exceed the winding resistance, as will be shown shortly.

We used a high-resolution meter (Model 2002 Multimeter from Keithley) and the four-probe method to measure the resistance. Repetitive measurements for the armature resistance have been done and the mean value of all measurements is 8.0 $m\Omega$, as shown in Table 9.3. This result is satisfactory compared to the calculated value of 7.7 $m\Omega$. It is also observed that the contact resistance and lead resistance are much larger than the winding resistance. Therefore we are prepared to see a much larger total resistance when we fit the actuator into our EMV system and connect the armature to the actuator drive. This will cause a higher total power loss, as will be discussed in a later section of this Chapter. It is anticipated that this problem can be solved by either paying more attention to reducing lead and contact resistance and/or by redesigning a winding with more turns and hence higher resistance but lower current.

TABLE 9.3. ARMATURE RESISTANCE

	Resistance (mΩ)
Four-wire measurement	8.0
Calculated Value	7.7

- **Armature Inductance**

The inductances of the armature before and after it is assembled into the iron yoke, i.e., with air core and iron core, respectively, were measured by an impedance analyzer at a frequency of 100 Hz. As shown in Table 9.4, the inductances of the armature with air core and with iron core matched our estimates based on first order approximations fairly well.

TABLE 9.4. ARMATURE INDUCTANCE WITH AIR CORE OR IRON CORE.

	Armature inductance with air core (μH)	Armature inductance with iron core (μH)
Estimates based on first order approximation	1.03	4.8
Measurement by Impedance Analyzer	1.10	5.0

9.3 Actuator Evaluation

Based on these results, we expect to have a satisfactory armature in every respect. After we assemble this armature into the iron yoke together with the permanent magnets and the position encoder, following the steps discussed in Chapter 8, we have our specially designed actuator ready to fit into our EMV system. Before carrying out valve actuation experiments, we performed some tests to make sure the actuator has the desired torque constant, rotor inertia, and friction coefficients.

9.3.1 Torque Constant

In order to test the torque constant of the actuator and compare it with the estimated torque constant (5.09 mN-m/A), we have performed two kinds of tests, a dc static test and a free-oscillation dynamic test, as discussed below.

- **DC Static Test**

In a dc static test, we connect the armature of the actuator to a current-controlled dc power supply. One end of a lever clamps the shaft of the actuator while the other end is connected to a spring scale. A schematic of the test is shown in Fig. 9.5. We use the power supply as a current source by controlling its current limit. With current injected into the armature, the rotor of the actuator will tend to rotate. However, the spring scale counteracts the motor torque and keeps the lever at a fixed position. We record the reading of the spring scale and then estimate the torque generated by the actuator based on the length of the lever. With the input current already known, we can easily estimate the torque constant of the actuator. In order to avoid any offset from the spring scale, a set of experiments with different current inputs have been done for the torque constant estimation.

- **Free-oscillation Dynamic Test**

We also carried out another test called a free-flight dynamic test to confirm the torque constant of the actuator. In this test, the actuator is mechanically connected to the spring-valve assembly but electrically disconnected from the actuator drive. We first force the system into its fully open or fully closed position, and then give the system some outside

initial impetus manually so the system will oscillate freely as a spring-mass system. During the system oscillation, the back EMF, the position, and the velocity of the armature are captured by an oscilloscope via a voltage probe and position sensor. From these data, we can estimate the torque constant, which is equivalent to the back EMF constant if using international units, from either the back EMF and the rotor velocity or the integral of the back EMF and the rotor position.

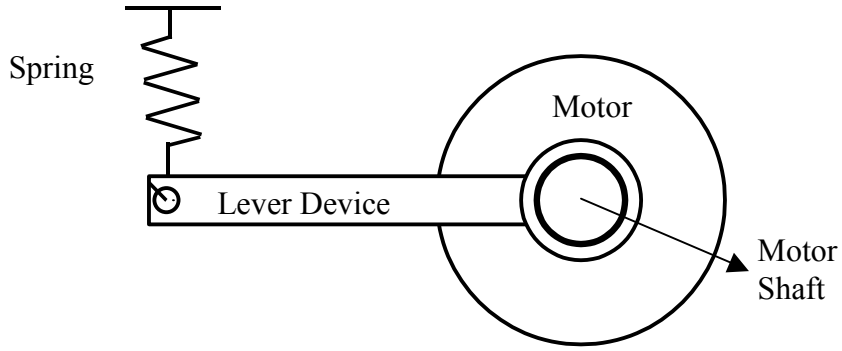

Fig. 9.5. Schematic of dc static test of actuator torque constant.

As shown in Table 9.5, the test results from both approaches are quite consistent with each other and a little bit higher than our calculated value. This is possibly because the actual residential flux density of the permanent magnets (1.27 T), as measured by a flux meter) is a bit higher than what is stated in its specification (1.23 T).

TABLE 9.5. THE TORQUE CONSTANT OF THE ACTUATOR.

	Torque constant (mN-m/A)
Dc static test	5.25
Free-oscillation dynamic test	5.20
Calculated value in Maxwell®	5.09

9.3.2 Rotor Inertia and Friction Coefficients

Because of the physically limited rotational range and the nonlinear friction of the actuator, we cannot use the traditional method, such as applying a constant current and measuring the final rotating speed or the rise time from standstill to full speed, to estimate the rotor inertia and friction coefficients.

Instead, we will obtain the rotor inertia in two ways. One way is to calculate the inertia of each part of armature using SolidWorks®, including the winding ($1.3 \cdot 10^{-6}$ Kg·m^2/s), two outer end clamps ($3.14 \cdot 10^{-7}$ Kg·m^2/s), two inner end clamps ($3.92 \cdot 10^{-7}$ Kg·m^2/s), the shaft ($3.8 \cdot 10^{-7}$ Kg·m^2/s), and the encoder ($2.5 \cdot 10^{-8}$ Kg·m^2/s), and then add them up for the total rotor inertia ($2.41 \cdot 10^{-6}$ Kg·m^2/s).

Another approach is to repeat the free-oscillation tests, using different initial current pulses instead of a manual impetus. By matching the experimental profile with the simulated profile, we are able to extract the total inertia (rotor inertia and cam inertia) and the friction coefficients, as discussed in Chapter 4. As shown in Table 9.6, the best-fit system inertia is a little larger than the value calculated by SolidWorks®, probably due to the external leads of the armature (discussed in Chapter 8 and shown in Fig. 8.28) and the screws used to fasten the winding to the end clamps and shaft. We are able to obtain an excellent fit to the data while keeping the bearing friction coefficient and cam friction coefficients the same as the values measured previously. For the valve friction, the best-fit coefficient is reduced by 50% for unknown reasons. One example of fitting the simulation and experimental free-oscillations is shown in Fig. 9.6.

TABLE 9.6. EXTRACTED MECHANICAL ACTUATOR PARAMETERS.

	Expected Value		Extracted Value
$J_{\theta rotor}$	$2.41 \cdot 10^{-6}$ Kg·m^2/s	$1.47 \cdot 10^{-5}$ Kg·m^2/s in total	$1.8 \cdot 10^{-5}$ Kg·m^2/s in total
$J_{\theta cam}$	$1.23 \cdot 10^{-5}$ Kg·m^2/s		
$B_{\theta b}$	500 μN-m·s/rad		500 μN-m·s/rad
$B_{\theta v}$	10 μm·s/rad		10 μm·s/rad
$B_{\theta c}$	8 μm·s/rad		8 μm·s/rad
B_z	12 N-m/s		6 N-m/s

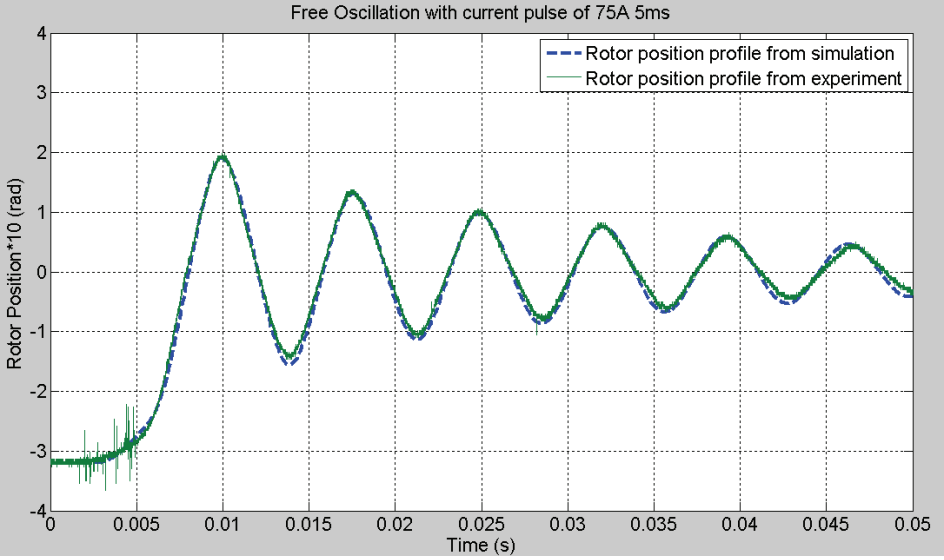

Fig. 9.6. Fitting the simulated and experimental free-flight trajectory.

9.3.3 Simulation with Measured Actuator Parameters

Using the actuator parameters measured in the previous sections, we have done another set of simulations, which show improved performance with respect to power consumption and transition time owing to the higher torque constant and lower valve friction, relative to the old simulation results with calculated parameters discussed in Chapter 7. The simulation results are shown in Fig. 9.7. The comparison of the new and old simulations is presented in Table 9.7. We see that for the same transition time, the power consumption is reduced by about 6% for the new simulation with the measured parameters of our actuator.

TABLE 9.7. COMPARISON OF THE NEW AND OLD SIMULATION.

	Old Simulation	New Simulation
Torque Constant (mN-m/A)	5.09	5.25
Current Pulse (A, ms)	75 A, 9 ms	75 A, 7 ms
Power Consumption (W)	56	49
Transition Time (ms)	2.8	2.7

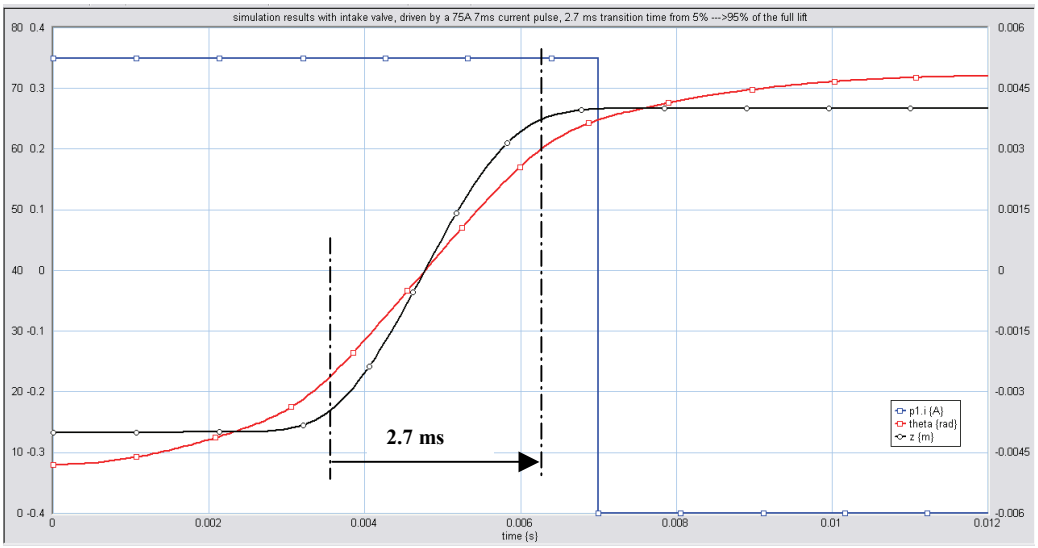

Fig. 9.7. Simulation with the measured actuator parameters.

9.4 EMV System Evaluation

After fully testing our actuator mechanically and electrically, we now evaluate our EMV system with the limited-angle actuator in place.

9.4.1 Full Experimental Setup

The full experimental setup is shown in Fig. 9.8. Note that the armature of the actuator is directly connected to the outside drive via two stranded wires for simplicity, as discussed in Chapter 8. For a more practical design, some alternative device, such as a pair of elastic spring leads, can be used to connect the rotating armature and outside power supply. Also note that between the drive and the actuator, there is an extra inductor inserted for the purpose of maintaining an appropriate switching frequency, as discussed before. However, the resistance of the inductor is much higher than that of the armature, causing more power loss due to the system operation. The extra inductance slows down the rise of the current as well. Therefore, instead of 12 V, we apply 20 V to the drive to obtain a consistent 75 A output with satisfactory rise time. It is possible to design an inductor specially for this purpose without such strong negative effects on power consumption and slew rate. Also, we have to admit that we could do a better job in terms of impedance matching for our armature design. The present armature has a rather low

resistance and inductance even for 12V input. An armature with more turns could serve our purposes better.

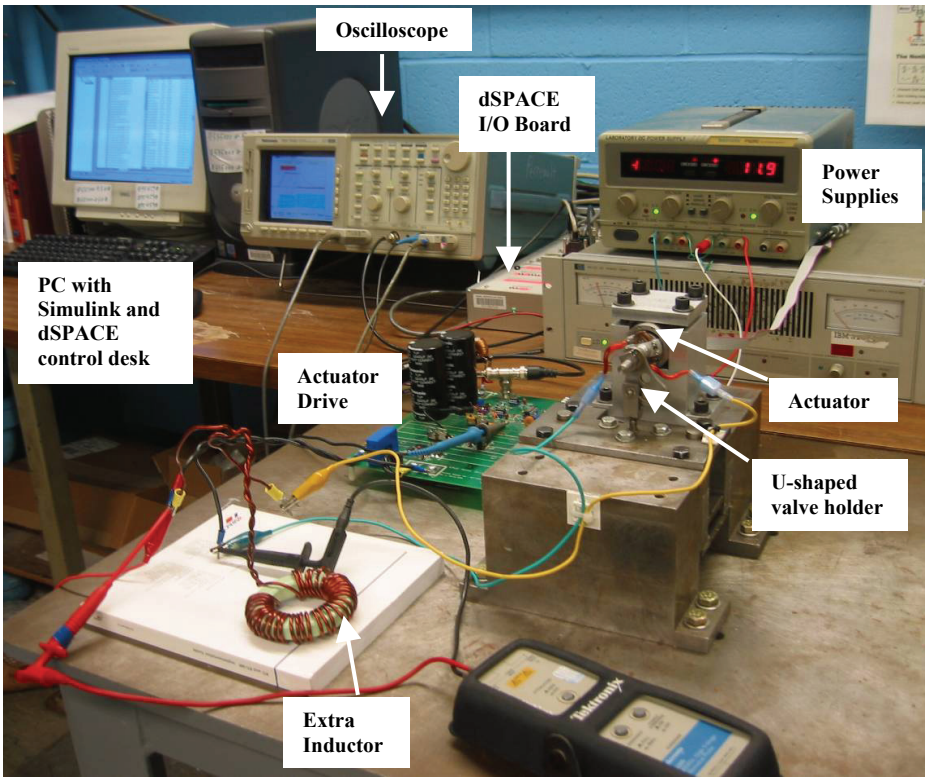

Fig. 9.8. The experimental setup with the limited-angle actuator.

It should also be noted that besides the different cam and actuator design, the U-shaped valve holder represents another improvement to the hardware design in this experimental setup, as compared to the L-shaped valve holder used in Dr. Chang's Ph.D. thesis [17] and Dr. Parlikar's M.S. thesis [18], as reviewed in Chapter 3 and shown in Fig. 3.3. The original L-shaped valve holder frequently results in an asymmetric force and inevitable bending during transitions, while the revised U-shaped valve holder is much more satisfactory in those respects. Both the new U-shaped valve holder and the old L-shaped valve holder are shown in Fig. 9.9.

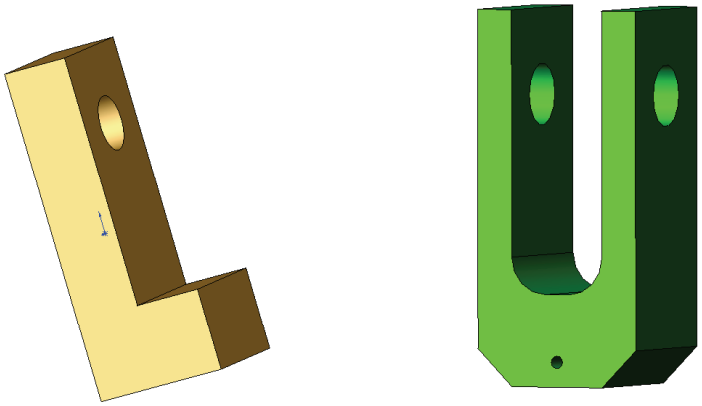

Fig. 9.9. The old L-shaped and the new U-shaped valve holders.

- **A Note about the Actuator Drive**

In order to accommodate the high current output (no less than 75 A), high slew rate (no less than 75 A/ms), high switching frequency (no less than 300 kHz), and low current ripple (no more than 5 A), the drive with hysteretic controller used for the first dc brush motor was modified to meet our requirements, as shown in Fig. 9.10. The details about the original drive design can be found in Mr. Michael Seeman's B.S. thesis [21]. In this thesis, only the modifications that have been made will be described as follows.

An extra capacitance of 1500 pF was added to the original 1000 pF of the capacitors C1 and C2, which increases the dead time between the switching off of one MOSFET and the switching on of the other on the same bridge leg. We found this necessary to prevent shoot-through due to a much higher current output (75 A vs. 20 A). As shown in Figs 9.11 and 9.12, the dead time before and after we added the extra capacitance to C1 and C2 was about 50 ns and 125 ns respectively. Experimentally, before we added the extra capacitance, the MOSFETs suffered shoot-through failures several times. After we made this revision, the drive worked properly up to 75 A output.

Fig. 9.10. The drive used for the limited-angle actuator.

We also replaced the current sensor (originally LEM part LEM-55P), which can sense current up to 50 A, with LEM part LEM-100P, which can sense current up to 100 A. Also, since we are using a ± 12 V power supply to power the sensor, the LEM-100P has a lower upper bound for resistance (50 Ω) connected to its output pin compared to that of the LEM-55P (100 Ω). Therefore the original 68 Ω sampling resistance (R30) was no longer appropriate. We replaced it with a 1% resistance of 39.2 Ω, which was chosen because it meets the 50 Ω limit and was readily available.

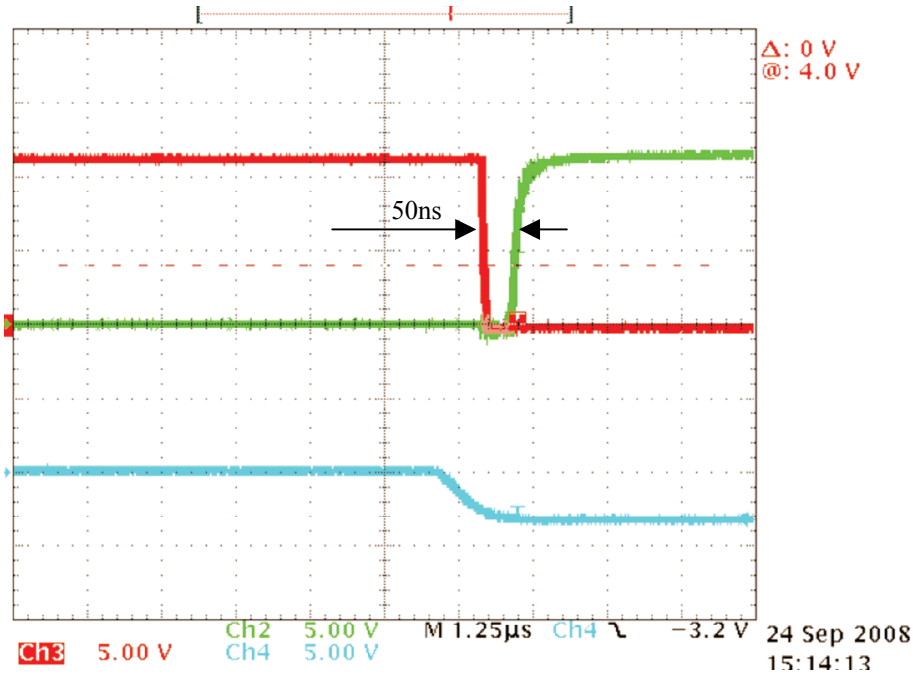

Fig. 9.11. 50 ns dead time before increasing C1 and C2.

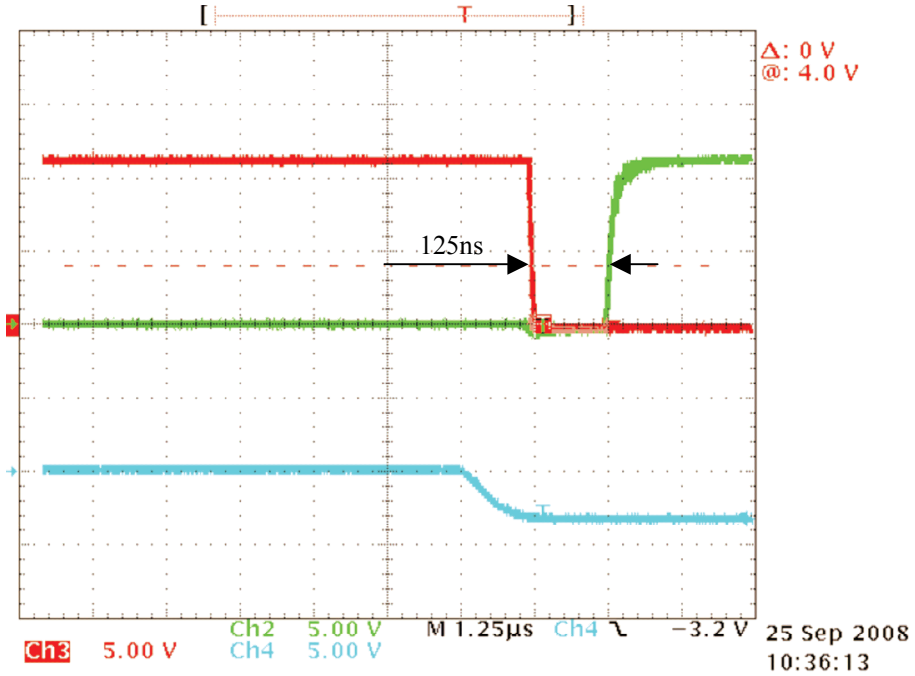

Fig. 9.12. 125 ns dead time after increasing C1 and C2.

Finally, we needed to adjust the controllable current range of the drive. Originally, the drive was designed to output up to ± 20 A with a ± 10 V command input. The original current sensor (LEM-55P) had a 1000:1 conversion ratio and a sampling resistance of 68

Ω. We needed to change some resistances in the feedback loop of the control circuits, including R2, R3, and R6-R9. The new conversion ratio (2000:1) of the LEM-100P and the new sampling resistance (39.2 Ω) also need to be taken into consideration. Based on calculation and the available 1% resistors at hand, we made the following changes. Increase R3 from 200 Ω to 499 Ω, R7 from 100 Ω to 249 Ω, and R8 from 1.5 kΩ to 1.8 kΩ while keeping R2, R6, and R9 unchanged. With the new conversion ratio (2000:1) and the new sampling resistance (R30 = 39.2 Ω), we will have a ± 10 V command input representing about ± 140 A current output, which is big enough for our purpose.

Note that all revisions to the current drive are for the purpose of increasing its output to 75 A in order to demonstrate valve actuations in the shortest time. Therefore a custom design of the actuator drive with 12 V nominal voltage input, minimized loss, fast rise time, etc, will be an interesting project in the future.

9.4.2 Experimental Results with Intake Valve

Here we demonstrate valve actuation with our newly designed limited-angle actuator and the modified actuator drive. Following the open-loop control strategy discussed in Chapter 5, we use a single current pulse to complete the valve actuation. Current pulses with different amplitudes and durations have been used and the resulting transition times and different amounts of power recorded. Two examples are shown below. The first shown in Fig. 9.13 is a transition achieved using a 75 A, 6.5 ms current command and result in a transition time of 2.6 ms and power consumption of 49.41 W. The second shown in Fig. 9.14 is a transition achieved with a 60 A, 9 ms current command and result in a transition time of 2.7 ms and power consumption of 44.68 W. Note that at the end of the each transition, the rotor and the roller-follower parked at different location within the extended flat area. In the first transition, the rotor and the roller-follower parked approximately the far end of the extended flat area while in the second transition, they parked approximately in the middle of the flat area after turning around from the end of the flat area.

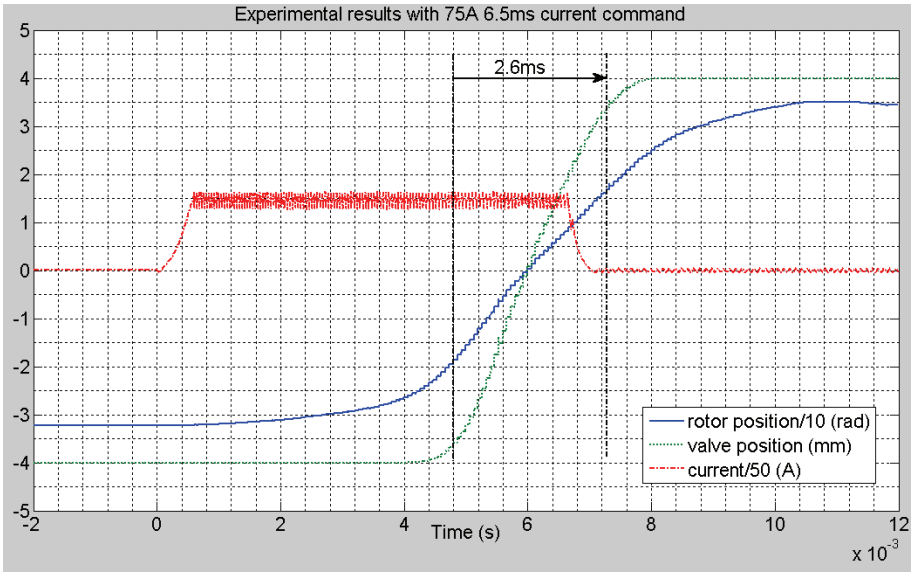

Fig. 9.13. Experimental results with 75 A, 6.5 ms current command.

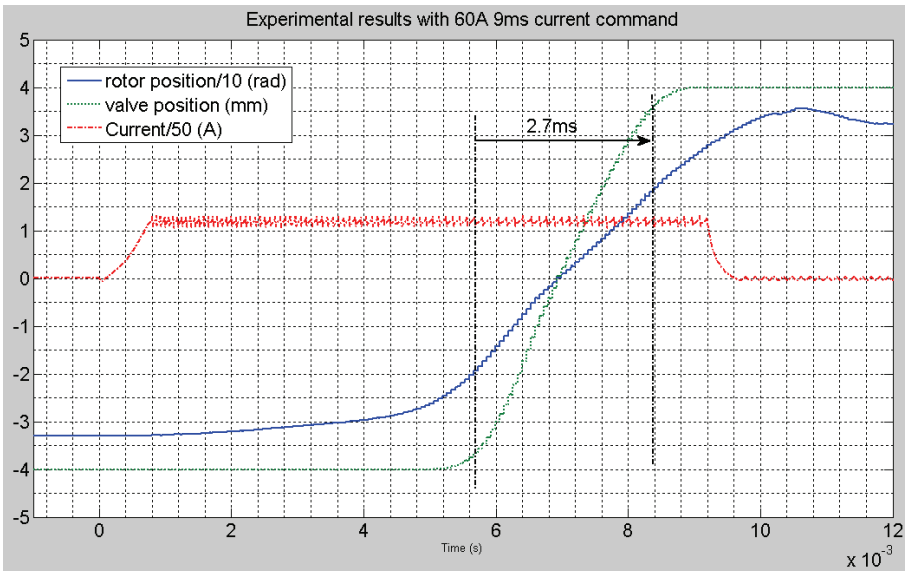

Fig. 9.14. Experimental results with 60 A, 9 ms current command.

As discussed in Chapter 4, the average power dissipation over one cycle is calculated based on an engine speed of 6000 rpm. These two transitions are summarized in Table 9.8, which further confirms that we can achieve successful transitions with different transition times and power consumptions by adjusting the amplitude and duration of the current pulse.

Note that the total power provided by the power supply is much larger than the power consumed by the limited-angle actuator and hence the EMV system. We accept these losses because they are external to the system being evaluated. The detailed distributions of power for these two cases discussed above are listed in Table 9.8.

TABLE 9.8. SUMMARY OF THE TRANSITION TIME AND POWER DISTRIBUTION.

	20 V bus, 75 A, 6.5 ms current command	15 V bus, 60 A, 9 ms current command
Transition time (ms)	2.6	2.7
Actuator Winding loss (6.8 mΩ) (W)	24.86	21.68
EMV system frictional loss (W)	25.08	23.00
Total power loss within the EMV system (Sum row 2 and row 3) (W)	49.94	44.68
Loss due to leads resistance, inductor resistance, and contact resistance (0.1 Ω) (W)	357.80	318.82
Total loss beyond the motor drive (Sum row 4 and row 5) (W)	407.74	363.50
Total power output by the motor drive (W)	401.30	358.26
Total power input from power supply (W)	435.88	379.42
Loss due to the motor drive, mainly the MOSFETS (Subtract row 6 from row 7) (W)	34.58	21.16

9.4.3 Simulation Results with Exhaust Valve

Due to the limited experimental setup, we did not conduct experiments on opening of the exhaust valve against a large gas force. However, we did simulate exhaust valve with a simulated gas force at 6000 rpm. The gas force simulation package is provided by Prof. Wai Cheng of Sloan Automotive laboratory at MIT [24]. The original profile of gas force versus crank angle, i.e., time, was translated into the profile of gas force versus valve position, as shown in Fig. 9.15. The simulation results shown in Fig. 9.16, confirm that this actuator is capable of opening an exhaust valve with a transition time of 2.9 ms and a power consumption of 102 W over half cycle. If we assume that the closing transition of an exhaust valve will be similar to the closing transition of an intake valve, making the

average power consumption over one cycle (one opening transition and one closing transition) about 76 W (half of the sum of the 102 W power consumption for opening transition plus the 50 W power consumption for closing transition), which is still reasonable compared to our 100 W bench mark.

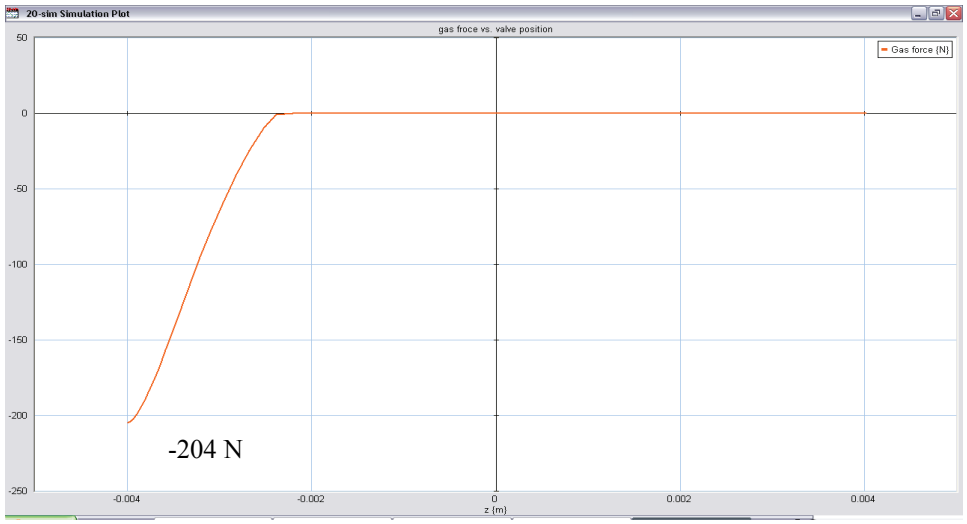

Fig. 9.15. Gas force versus valve position @ 6000 rpm.

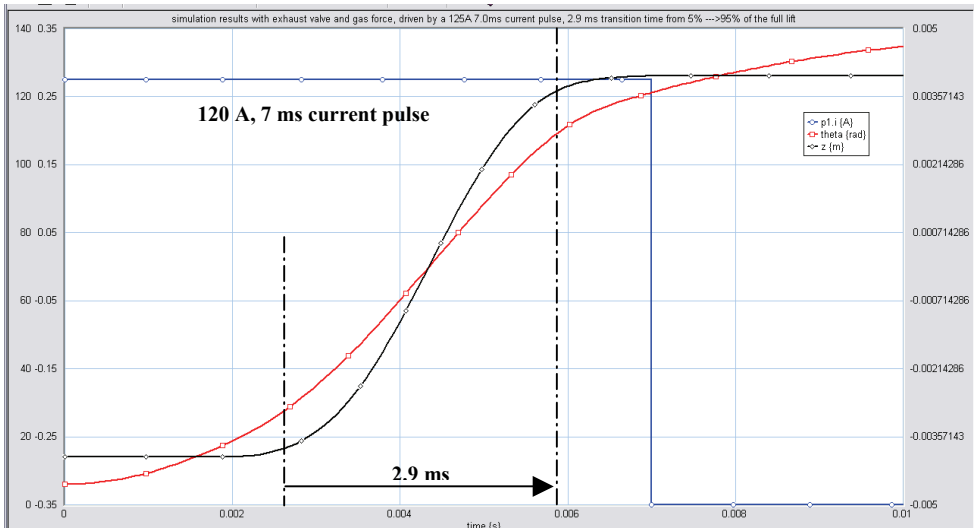

Fig. 9.16. Simulation of exhaust valve opening transition with gas force.

9.4.4 Projection for Full Engine Valve Actuation

From the simulation of valve actuation with gas force disturbance and the experiment of valve actuation without gas force disturbance, we can project the performance of a full engine valve actuation system with independent valve actuation for each intake and exhaust valve, as summarized in Table 9.9. Again, note that all average power is estimated at 6000 rpm engine speed where half cycle for one transition is 10 ms and one cycle for two transitions (open and then close) is 20 ms.

TABLE 9.9. COMBINED EXP. AND SIM. RESULTS FOR A COMPLETE EMV ACTUATION SYSTEM.

	Transition time (ms)	Average power consumption over half cycle (W)		Average power consumption of intake valve over one cycle (W)	Average power consumption of exhaust valve over one cycle (W)	Average power consumption of a 4-cylinder 16-valve engine over one cycle (W)
Valve actuation without gas force	2.6	49.94		49.94	75.97	1007.28
Valve actuation with gas force	2.9	102				

The projection above is based on our own experimental setup, assuming both intake and exhaust valves have the same full lift of 8 mm and the same weight. However, this is not the common practice in the real world. Next, we will do a more practical projection using simulations based on a real engine with different intake and exhaust valve actuation parameters. These parameters shown in Table 9.10 were provided by Industrial Technology Research Institute (ITRI) in Taiwan.

The simulation results of three cases---opening (and closing) transitions of the intake valve, closing transition of the exhaust valve, and opening transitions of the exhaust valve with gas force present---are shown in Figs. 9.17-9.19, respectively, and are summarized in Table 9.11, which again illustrates the practical feasibility and promising future of our EMV system in a real engine environment up to an engine speed of 6000 rpm. As

discussed before, all power estimations are based on 6000 rpm engine speed. Also note that opening and closing transitions are identical if no gas force presents.

TABLE 9.10. SPECIFICATION OF ITRI'S 2.2 L ENGINE (FOR ONE CYLINDER)

Working principle	4-stroke SI
Fuel injection	Gasoline port injection
No. of valve	4
Bore/Stroke	Φ86 × 94.6 mm
Displacement volume	0.55 liter
Compression ratio	10
Intake/ Exhaust valve actuator	DOHC, shimless tappet
Exhaust valve diameter	29 mm
Max. intake valve lift	9.3 mm
Max. exhaust valve lift	8.6 mm
Intake valve mass	47.4g
Exhaust valve mass	41.7g
Valve pitch	37.5 mm

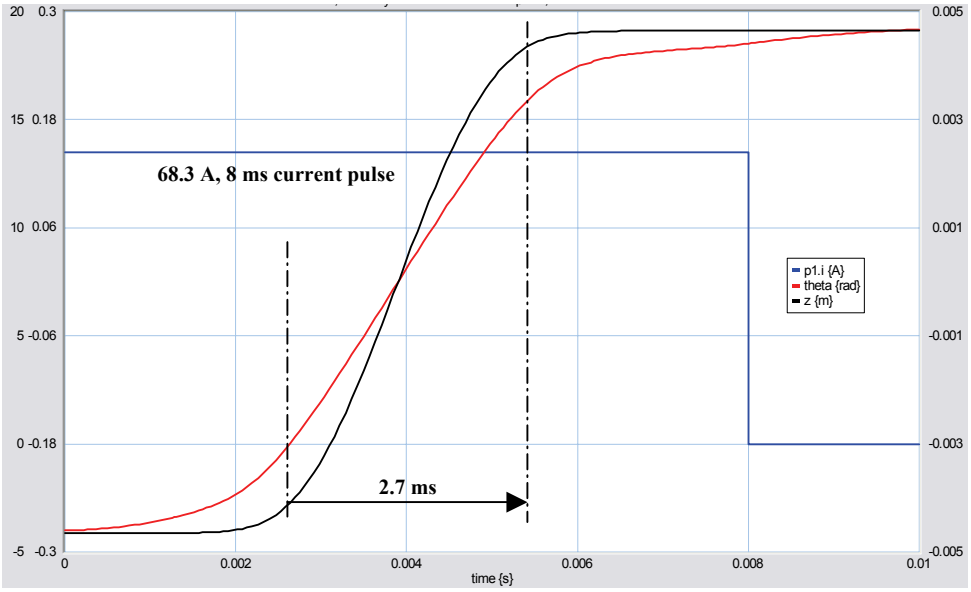

Fig. 9.17. Position and current profiles of intake valve opening.

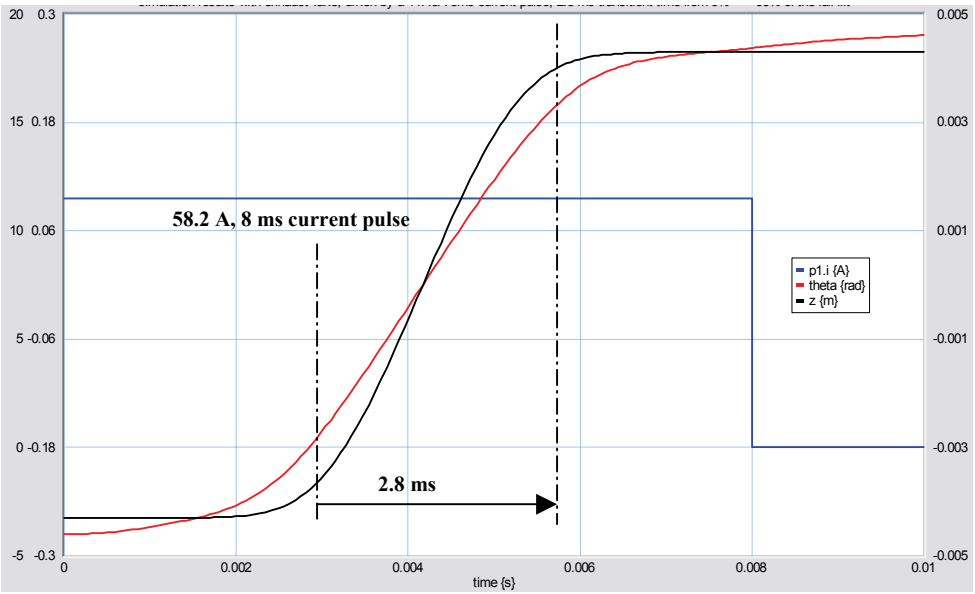

Fig. 9.18. Position and current profiles of exhaust valve opening w/o gas force.

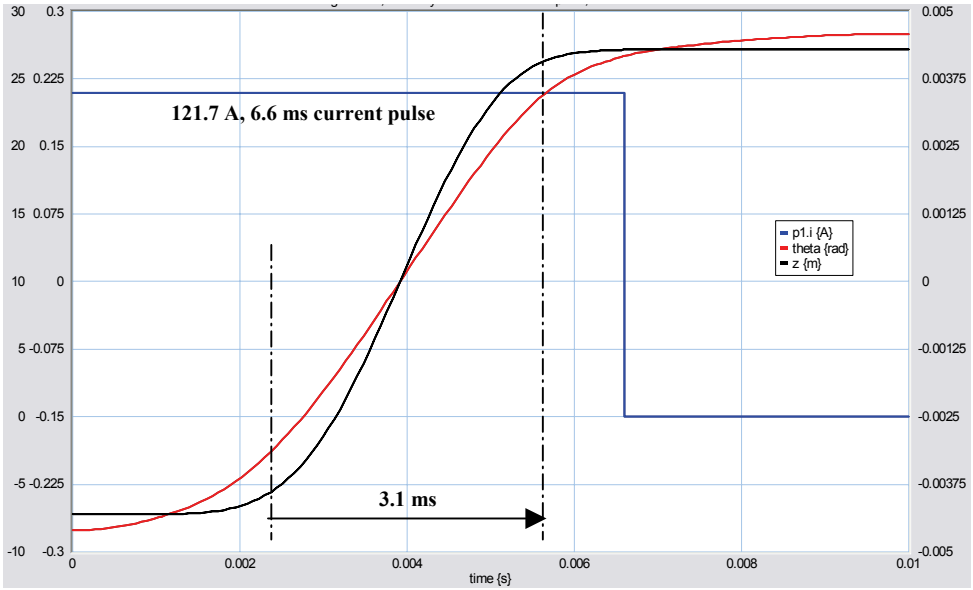

Fig. 9.19. Position and current profiles of exhaust valve opening against gas force.

The research staff at ITRI also packaged our EMV system over their engine head in a SolidWorks® design, as shown in Fig. 9.20. This clearly demonstrates the possibility of realizing independent valve actuation for each valve using our EMV system.

At this point, we have successfully demonstrated the capability of our EMV system with a limited-angle actuator based on advanced system modeling, control, design, and experiment. The goal of this thesis has been satisfactorily achieved. In the next chapter, we will conclude the thesis and then offer some thoughts on possible future work.

TABLE 9.11. SIMULATION RESULTS WITH ITRI'S VALVE PARAMETERS.

	Transition time (ms)	Average power consumption over half cycle (W)	Average power consumption over one cycle (W)	Average power consumption of a 4-cylinder 16-valve engine over one cycle (W)
Case I: Open/close intake valve without gas force	2.7	52	52	1056
Case II: Close exhaust valve without gas force	2.8	40	80	
Case III: Open exhaust valve with gas force	3.1	120		

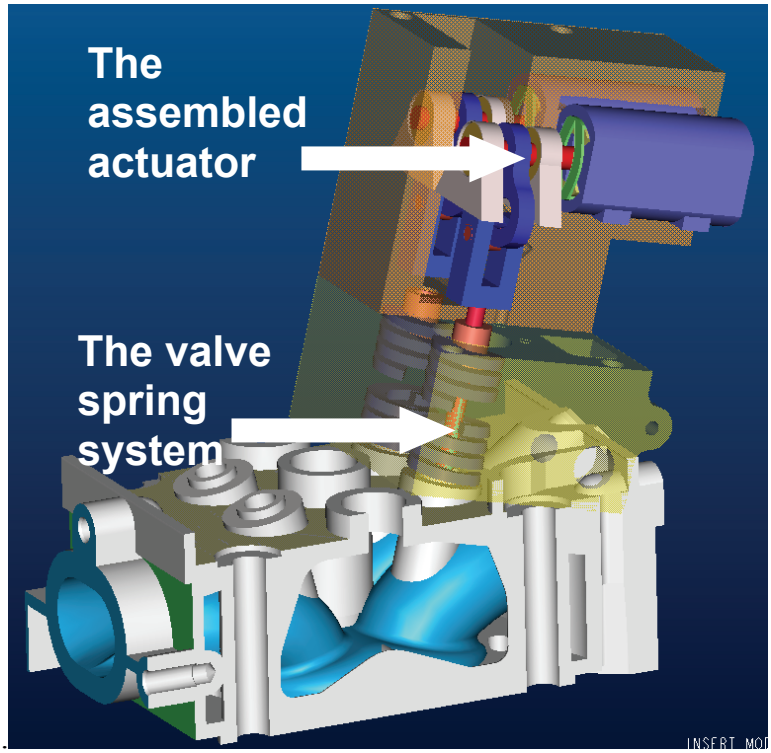

Fig. 9.20. SolidWorks® illustration of the EMV system mounted on an engine head.

CHAPTER 10 CONCLUSIONS AND FUTURE WORK

10.1 Introduction

In this chapter, we will conclude with an evaluation of how the original thesis objectives have been met, and a discussion of future work on the MIT EMV project.

As noted earlier, from August 2002 we have been working on improving system performance of a novel EMV system for internal combustion engines, which was proposed by Dr. Chang and his colleagues in MIT's Laboratory for Electromagnetic and Electronic Systems (LEES). This MIT EMV system is an electromechanical valve drive incorporating a NMT [17]-[20]. Dr. Chang et. al. proved its feasibility for engine valve actuation by demonstrating inherent soft landing and valve transition fast enough for 6000 rpm engine speed. The ultimate goal of this thesis was to bring the EMV system performance to a much more practical level, including achieving a smaller actuator, lower power consumption, faster valve transition, and addressing the effect of gas force disturbance. Extensive research in advanced system modeling, control, and design has been conducted in order to achieve this goal.

We will evaluate how the objectives of this thesis have been met in section 10.2, and discuss possible future work in section 10.3.

10.2 Evaluation of Thesis Objectives

As discussed in Chapter 1, the objectives of this thesis can be summarized as follows: First, to establish a more accurate system model for better guidance in system control and design; Second, to explore different control strategies and cam designs in order to identify the most appropriate control strategy and cam design for achieving a lower torque requirement, reduced power consumption and faster transition time; Third, to design and build a limited-angle actuator for the valve actuation application in order to reduce actuator size while maintaining the necessary torque and power output; Fourth, to

evaluate the EMV system experimentally and numerically with the limited-angle actuator in place, and with gas force disturbance taken into consideration.

All four primary objectives described above have been fulfilled.

A more accurate system model has been presented in Chapter 4, including the dynamic system model, loss flow and distributions, and a nonlinear friction model. They resulted in a detailed and trustable simulation setup for our EMV system.

Different control strategies, including pure closed-loop control, combination of closed-loop and open-loop control, and pure open-loop control, have been compared in Chapter 5. Although the pure closed-loop control is more stable, the use of open-loop control reduces the torque requirement and power consumption significantly while maintaining satisfactory stability. It is possible to increase the robustness of the open-loop control by iterative learning and the use of outer closed-loop control based on crank angle, as will be discussed in the next section.

In Chapter 6, we outlined design considerations for the disk cam before presenting two possible directions in order to find a better cam design --- different functional design and different angular range design. A new cam has been designed and built based on angle range optimization. The new cam confirms all the benefits predicted by simulation, including a lower torque requirement, lower power consumption, and faster transition time.

The design and fabrication of a custom limited-angle actuator have been discussed in Chapters 7 and 8. Chapter 7 focuses on the basic idea and conceptual design of the limited-angle actuator after presenting the design challenges of an actuator for this application. The designed actuator shows excellent performance through simulation. Chapter 8 demonstrated how to build the actuator components, especially the armature and the iron yoke, and how to assemble all the components into a working actuator.

Finally, in Chapter 9, we experimentally confirmed all the benefits of the nonlinear system modeling, the open-loop control strategy, the optimal cam design, and the custom actuator design. A promising future of full engine valve actuation for a real engine at the end is also predicted in Chapter 9.

10.3 Recommendations for Future Work

With the improvements that we have made in modeling, control, and actuator designs, our EMV system is now a much more practical system for automotive application. However, there is room for developing an even better system. Within this interesting project, there still are several intriguing issues that still need to be addressed.

10.3.1 Control

As discussed in Chapter 5, the pure open-loop control is a simple control scheme to implement and maintain. It not only reduces the power consumption and torque requirement substantially, but also offers a way to trade off transition time and power consumption under different engine speeds by adjusting the amplitude and duration of the current pulse. Although its stability is satisfactory in our laboratory setup, we would like it to be more robust for a real engine environment where all kinds of disturbances could be present, such as when friction forces change, when gas force varies, and when a valve fails to seat. A possible solution is to introduce iterative learning and outer closed-loop control with respect to crank angle position into our current control structure. Development of an effective algorithm to select the current pulse parameters (duration and amplitude) and system performance, including transition time and power consumption, will be another attractive topic to work on in the future.

10.3.2 Linkage

As mentioned in Chapter 6, using the roller follower and disk cam with a fixed lift is only one convenient way to implement the NMT (NMT). It is not necessarily the best way, however. Future research could explore other possible options to realize the desired nonlinear feature. The optimal linkage design should offer low friction, low cost, flexible lift control, ease of assembly and maintenance, long life span, and so on. Three possible

NMT design directions have been presented in section 6.5 of Chapter 6---a two-step lift design, a special asymmetric design for the exhaust valve, and a four-bar linkage. However, future researchers should not limit themselves to these design alternatives.

10.3.3 Actuator and Drive

As discussed in Chapter 9, although the actuator and the drive electronics we built have done an excellent job proving the effectiveness of our advanced modeling, control, and design for the EMV system, there is still room to achieve an even better outcome by looking at them as a single system. This is mainly because, first, the drive electronics were not specially designed for the limited-angle actuator, and second, the actuator (especially the armature) design did not do a good job of matching the drive impedance. These resulted in the huge external losses due to resistance outside of the actuator, including lead resistance, contact resistance, and winding resistance of the extra inductor, as described in Chapter 9. Therefore it is necessary to treat the actuator design and drive design as a whole, such that these external losses are reduced to a negligible level compared to the power consumption of our EMV system. This could be achieved through a slightly re-designed actuator with more turns for appropriate impedance matching and a custom drive design with 12 V nominal voltage input. Also, a more appropriate interconnect design should be included in this project, as discussed in Chapters 8 and 9.

10.3.4 Low-cost and Robust Position Sensing

As described throughout the whole thesis, we have been relying on an optical encoder to obtain rotor position directly. However, the use of an optical encoder will be a big challenge because of cost and maintenance in an unfriendly automotive environment. Our EMV system would be a more promising system if we could obtain the position information via a cheaper but reliable way. This could be accomplished in two ways. One is to get position information directly by using some other type of position sensor, such as an anisotropic magnetoresistive (AMR) sensor, which is fairly cheap and yet is able to survive the automotive environment. It is possible to revise the design of the armature of our limited-angle actuator in order to make use of the AMR sensor, as discussed in

Chapter 7. The alternative way is through indirect position sensing, i.e., to extract the position information from real time voltage, back EMF, and current data.

10.3.5 Lash Adjuster

Unlike conventional valvetrains, the spring force is zero in the middle of the stroke in the MIT EMV system, and lash adjusters for conventional valvetrains do not work in this case because valve springs always under compression transmit the compressed force to the lash adjusters in conventional valvetrains. Therefore, a custom designed lash adjuster will eventually be needed for our EMV system to compensate for temperature change, wear, and manufacturing tolerances of the valvetrain.

10.3.6 Thermal Analysis and Cooling System Design

We have not done a through study on cooling of the EMV system, especially the limited-angle actuator. For practical automotive application, it is necessary to conduct a detailed thermal analysis of the system and design a proper cooling system.

10.3.7 Setup on a Real Working Engine

All the work we have done to date is based on our laboratory setup. It would be exciting to set up the EMV system on a real engine head and conduct research based on the real automotive environment. For the same reason, all research work suggested above would be the most meaningful if done with the EMV system installed on the top of a working engine.

Furthermore, if were we to advance to the stage of full engine valve actuation, there will be numerous multi-disciplinary research subjects remaining, including investigation of either independent valve or multi-valve control, study of interactions between valves and cylinders, and comprehensive surveys of durability, reliability, and cost.

APPENDIX I DERIVATION OF $\cos(\alpha)$ AT THE CONTACT POINT OF THE CAM SLOT

As discussed in Chapter 4, the normal force exerted on the rolling surface varies along the valve transition because it is affected by multiple factors, as copied in (A1.1),

$$F_n = (K_s z - f_z - m_z \frac{d^2 z}{dt^2}) \cdot \cos(\alpha) \tag{A1.1}$$

where $K_s z$ is the spring force, f_z is the friction force in the z-domain, $m_z \frac{d^2 z}{dt^2}$ is the inertia force, and α is angle between the contact surface in direction C-C and the plane in direction A-A perpendicular to valve motion in direction B-B at the contact point, as shown in Fig. A1.1, where F is the total force exerted at the contact point in direction B-B, F_t is the portion of F in the direction parallel to the tangent line at the contact point, and F_n is the portion of F in the direction perpendicular to the tangent line.

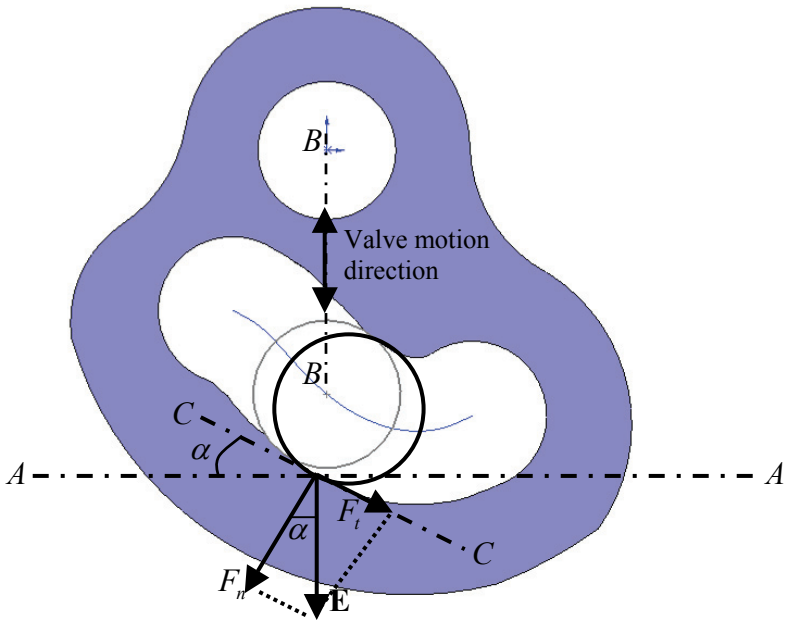

Fig. A1.1. The tangent angle α at the contact point.

In Chapter 4, we have asserted that $\cos(\alpha)$ is a nonlinear function of θ position as in (A1.2),

$$\cos(\alpha) = 1/\sqrt{1+(a\cdot b\cdot\cos(b\cdot\theta)/(a\cdot\sin(b\cdot\theta)+h))^2} \quad |\theta| \le \pi/2b \tag{A1.2}$$

where $a = z_{\max}$, $b = \pi/(2\theta_{\max})$, and as shown in Fig. A1.2, $2z_{\max}$ is the full lift of the valve, $2\theta_{\max}$ is the total effective rotation range of the motor, and h is the vertical distance between the motor shaft center and the roller center when the roller as well as the valve is in the middle of the stroke, i.e., the equilibrium point of the whole system.

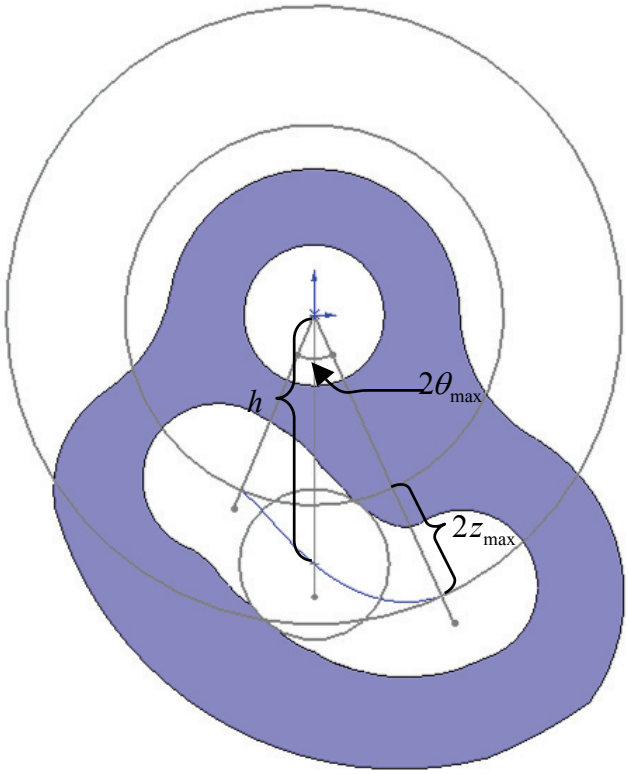

Fig. A1.2. Upper surface, lower surface, and center trajectory of the cam slot.

This appendix will present the derivation of the relation between $\cos(\alpha)$ and θ as shown in (A1.2).

First of all, let us assume that we have a given NMT function as shown in (A1.3),

$$
\begin{aligned}
z &= f(\theta) = a \cdot \sin(b \cdot \theta) \\
a &= z_{\max} \\
b &= \pi / 2\theta_{\max}
\end{aligned}
\tag{A1.3}
$$

where $z_{\max}$ is half the stroke of valve transition and $\theta_{\max}$ is half of the total effective angular range of rotor rotation within one transition.

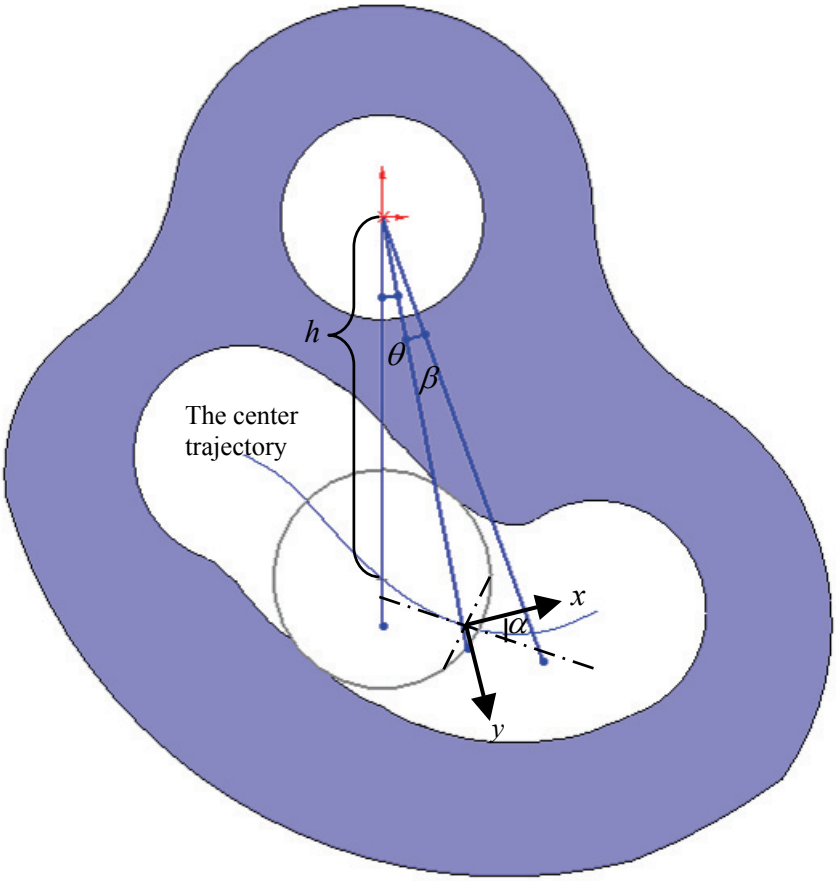

Fig. A1.3. The coordination and cam parameters to estimate $\cos(\alpha)$.

We also need another important assumption to simplify our analysis. During each transition, the real contact points between the roller follower and the cam slot will be located either on the upper surface or the lower surface of the cam slot. Generally, when spring force is pulling up the contact point will be on the upper surface and when the spring force is pushing down, the contact point will be on the lower surface. There will be

a moment and position where the contact point was on upper surface in the previous moment, is contacting nowhere in the current moment, and will jump to the lower/upper surface in the next moment. However, from (A1.1), we can see that the inertia force of the valve and any other *z*-domain force will cause this transition not to occur exactly at mid stroke (as it would in a quasi static case). The exact instant and location of the transition would be difficult to model. Therefore, instead of using the real upper and lower surface curve profile, we will assume that the center of the cam follower follows the center curve used to generate the cam, as shown in blue in Fig. A1.2 and Fig. A1.3. Mathematically and numerically it turns out to be a very good estimation, which is practically very useful in latter system design process.

Now let us estimate $\tan(\alpha)$. As shown in Fig. A1.3, we define the origin of a set of rectangular coordinates at the center of the roller follower (when the follower is at angle θ), y-axis in the direction of valve motion, and x-axis in the direction perpendicular to the valve motion. Now we can derive the displacements in both x and y directions of the center of the roller follower when it rotates from θ to $\theta+\beta$ within the cam slot, as shown in (A1.4),

$$\begin{aligned} x_\beta &= (a\cdot\sin(b\cdot(\theta+\beta))+h)\cdot\sin(\beta) \\ y_\beta &= (a\cdot\sin(b\cdot(\theta+\beta))+h)\cdot\cos(\beta)-(a\cdot\sin(b\cdot\theta)+h) \end{aligned} \tag{A1.4}$$

where θ is the current angular position of roller follower, β is a tiny angular displacement of roller follower from the current position, x_β and y_β are the displacements in x and y directions respectively due to the angular movement of the roller follower, h is the vertical distance between the centers of motor shaft and roller follower when the roller follower is rest at the equilibrium point, i.e., at the point where $\theta=0$.

Therefore, it is quite straightforward that $\tan(\alpha)$ can be estimated as in (A1.5),

$$\tan(\alpha) = \lim_{\beta \to 0} \frac{y_\beta}{x_\beta} \tag{A1.5}$$

From basic math knowledge, we know that if $\beta \to 0$ then we will have $\cos(\beta) \to 1$, $\cos(b \cdot \beta) \to 1$, $\sin(\beta) \to \beta \to 0$, and $\sin(b \cdot \beta) \to b \cdot \beta \to 0$. These implications will allow us to estimate $\underset{\beta \to 0}{x_\beta}$ and $\underset{\beta \to 0}{y_\beta}$ as in (A1.6) and (A1.7),

$$\begin{aligned} \underset{\beta \to 0}{x_\beta} &= (a \cdot \sin(b \cdot (\theta + \beta)) + h) \cdot \sin(\beta) \\ &= (a \cdot (\sin(b \cdot \theta) \cdot \cos(b \cdot \beta) + \cos(b \cdot \theta) \cdot \sin(b \cdot \beta)) + h) \cdot \sin(\beta) \\ &= (a \cdot (\sin(b \cdot \theta) + \cos(b \cdot \theta) \cdot b \cdot \beta + h) \cdot \beta \\ &= (a \cdot (\sin(b \cdot \theta) + h) \cdot \beta \end{aligned} \tag{A1.6}$$

$$\begin{aligned} \underset{\beta \to 0}{y_\beta} &= (a \cdot \sin(b \cdot (\theta + \beta)) + h) \cdot \cos(\beta) - (a \cdot \sin(b \cdot \theta) + h) \\ &= (a \cdot (\sin(b \cdot \theta) \cdot \cos(b \cdot \beta) + \cos(b \cdot \theta) \cdot \sin(b \cdot \beta)) + h) \cdot \cos(\beta) - (a \cdot \sin(b \cdot \theta) + h) \\ &= (a \cdot (\sin(b \cdot \theta) + \cos(b \cdot \theta) \cdot b \cdot \beta) + h) - (a \cdot \sin(b \cdot \theta) + h) \\ &= a \cdot \cos(b \cdot \theta) \cdot b \cdot \beta \end{aligned} \tag{A1.7}$$

Plug $\underset{\beta \to 0}{x_\beta}$ and $\underset{\beta \to 0}{y_\beta}$ into (A1.5), we will have $\tan(\alpha)$ as shown in (A1.8),

$$\tan(\alpha) = \lim_{\beta \to 0} \frac{y_\beta}{x_\beta} = \frac{a \cdot \cos(b \cdot \theta) \cdot b \cdot \beta}{(a \cdot \sin(b \cdot \theta) + h) \cdot \beta} = \frac{a \cdot b \cdot \cos(b \cdot \theta)}{a \cdot \sin(b \cdot \theta) + h} \tag{A1.8}$$

Accordingly, we can derive $\cos(\alpha)$ from $\tan(\alpha)$ since $\cos(\alpha) = 1/\sqrt{1 + \tan(\alpha)^2}$. Therefore we can conclude $\tan(\alpha)$ and $\cos(\alpha)$ within the effective angular range, as shown in (A1.9) and (A1.10),

$$\tan(\alpha) = (a \cdot b \cdot \cos(b \cdot \theta)) / (a \cdot \sin(b \cdot \theta) + h) \quad |\theta| \le \pi / 2b \tag{A1.9}$$

$$\cos(\alpha) = 1/\sqrt{1 + (a \cdot b \cdot \cos(b \cdot \theta) / (a \cdot \sin(b \cdot \theta) + h))^2} \quad |\theta| \le \pi / 2b \tag{A1.10}$$

To verify this development, we carry out some simple checks at special positions like $\theta = 0$ and $\theta = \pm\pi / 2b$, as shown in (A1.11) and (A1.12),

$$\begin{aligned} &\theta = 0 \\ &\tan(\alpha) = a \cdot b / h \\ &\cos(\alpha) = 1/\sqrt{1 + (ab/h)^2} \end{aligned} \tag{A1.11}$$

$$\begin{aligned} &\theta = \pm\pi / 2b \\ &\tan(\alpha) = 0 \\ &\cos(\alpha) = 1 \end{aligned} \tag{A1.12}$$

Figs. A1.4 and A1.5 plot $\cos(\alpha)$ vs. θ along the full effective angular range of the old cam and the new cam respectively. From these figures, we can see that $\cos(\alpha)$ of the new cam has a smaller minimum and mean value compared to that of the old cam. This apparently contributes to the smaller friction force and hence smaller torque requirement and power consumption with the new cam.

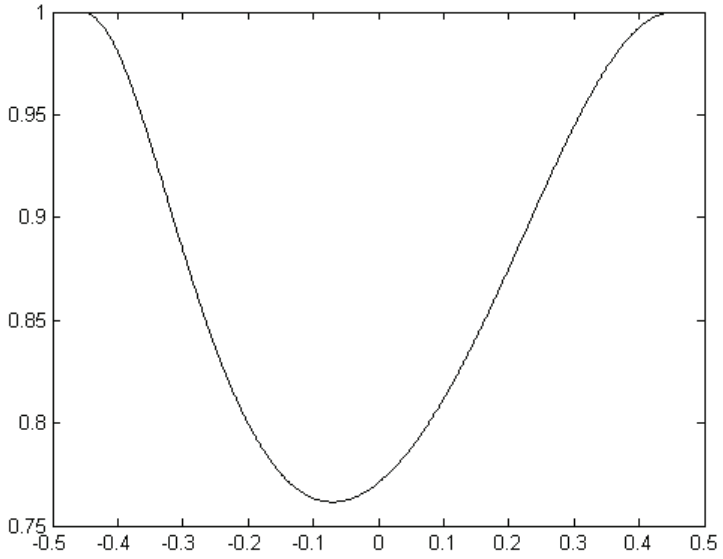

Fig. A1.4. The plot of $\cos(\alpha)$ vs. θ of the old cam.

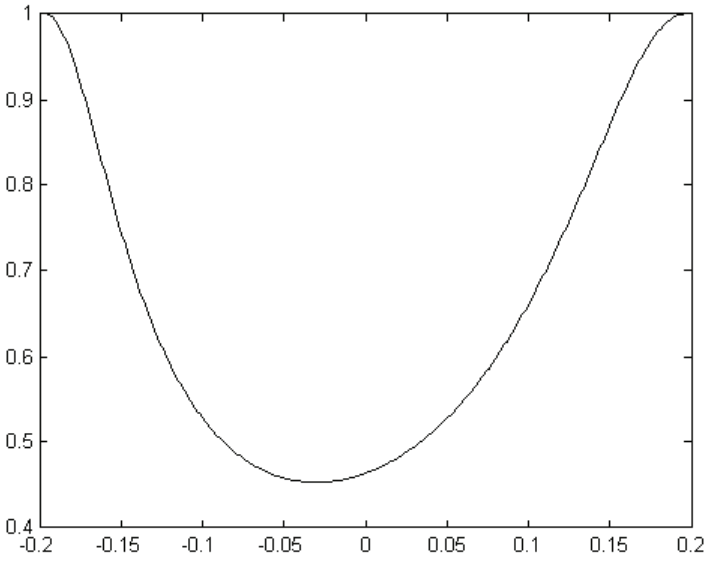

Fig. A1.5. The plot of $\cos(\alpha)$ vs. θ of the new cam.

APPENDIX II SOLIDWORKS® DRAWINGS OF HARDWARE

This Appendix contains the SolidWorks® drawings of the hardware designed during the whole thesis work, including valve holder, disk cam, armature mold parts, actuator parts, and actuator mounting parts.

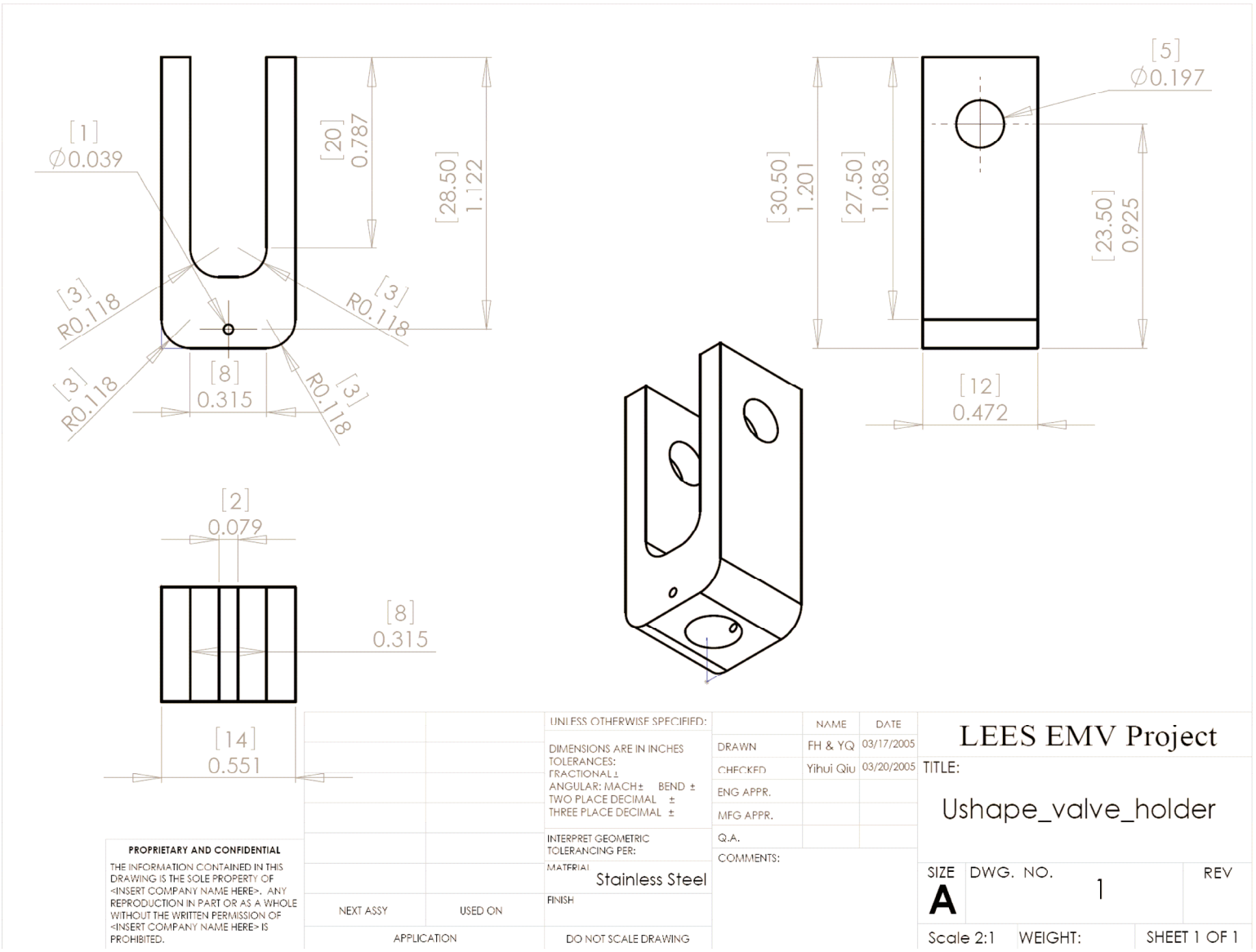

Fig. A2.1. U-shape valve holder.

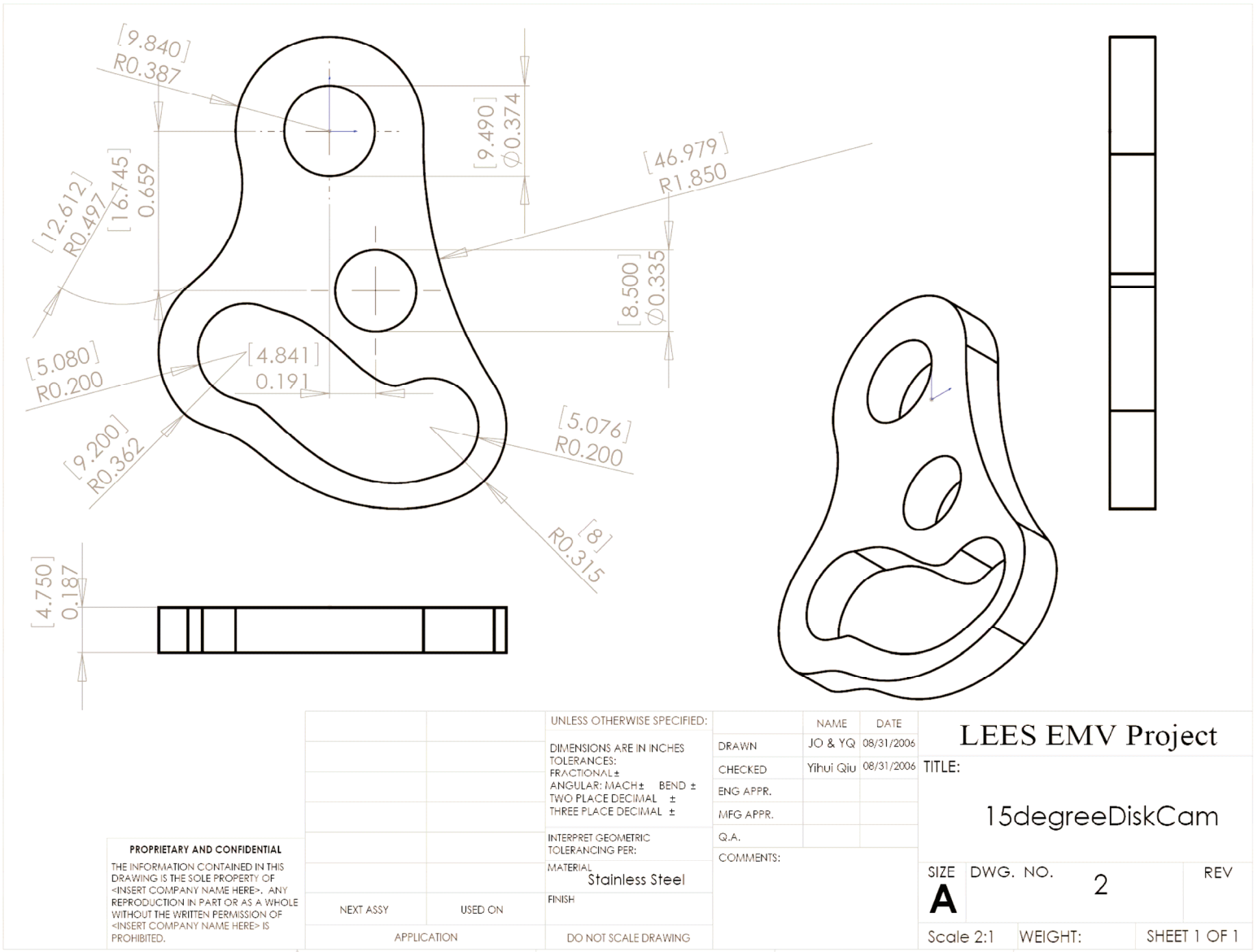

Fig. A2.2. 15-degree disk cam.

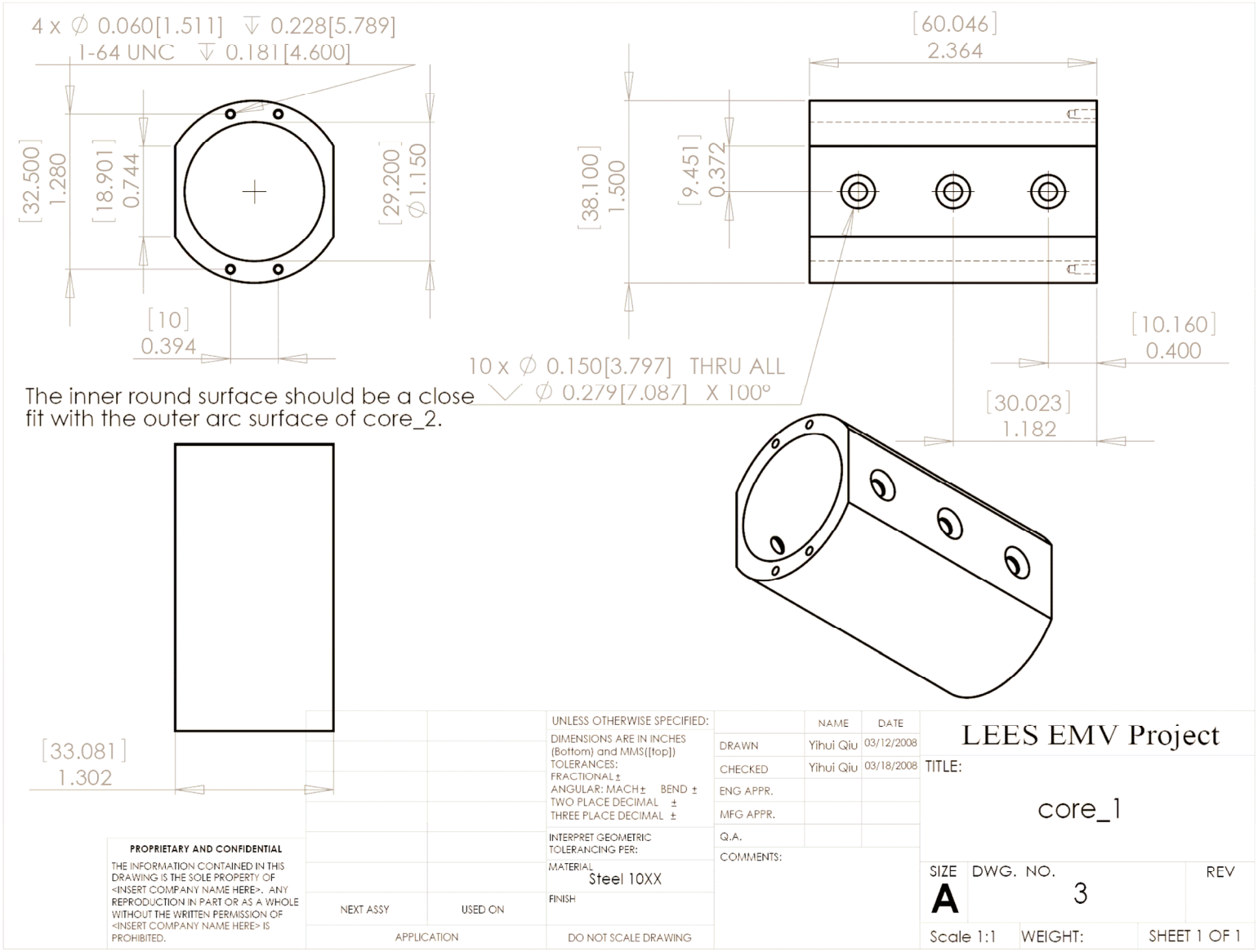

Fig. A2.3. Outer layer of iron core for the actuator.

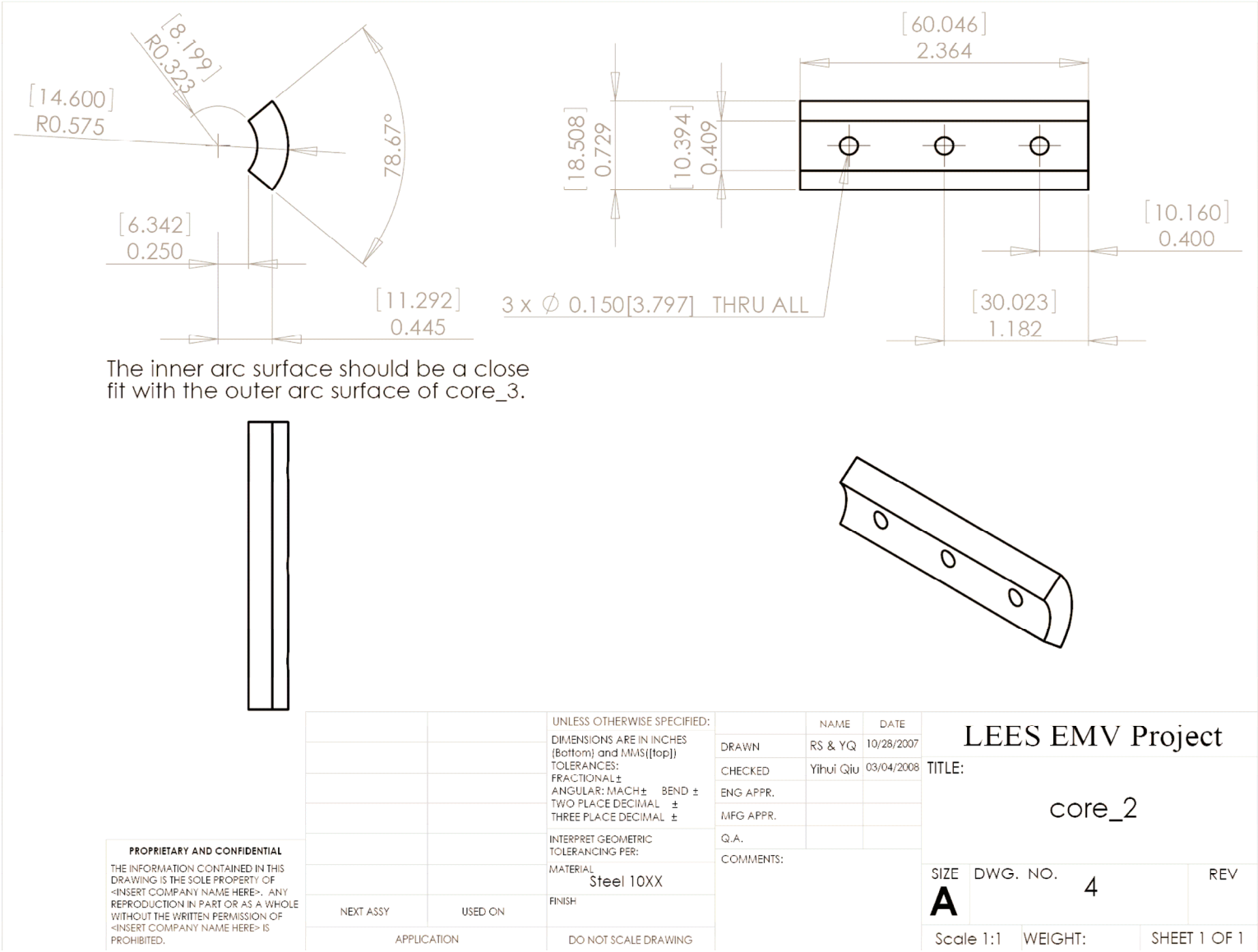

Fig. A2.4. Middle layer of iron core for the actuator.

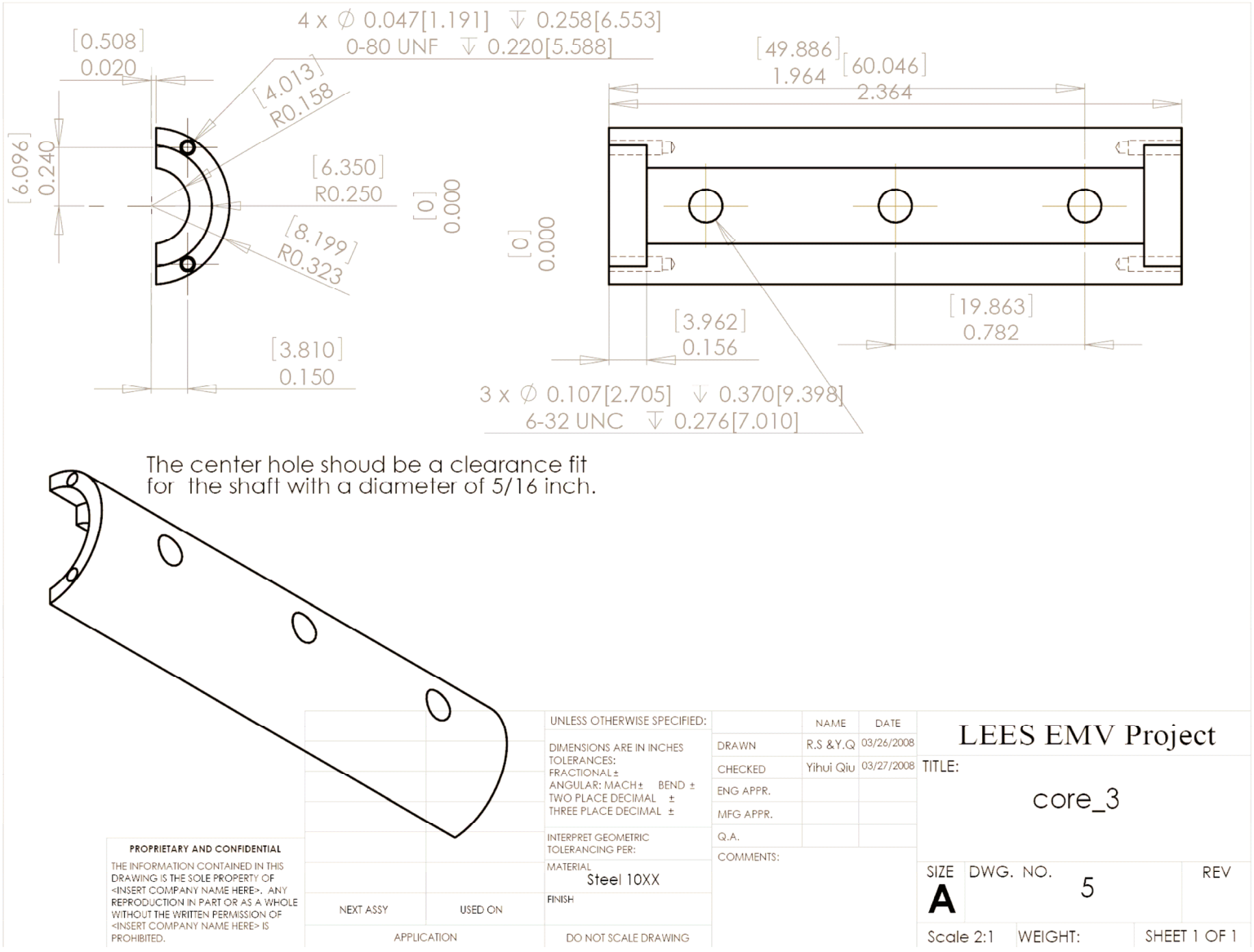

Fig. A2.5. Inner layer of iron core for the actuator.

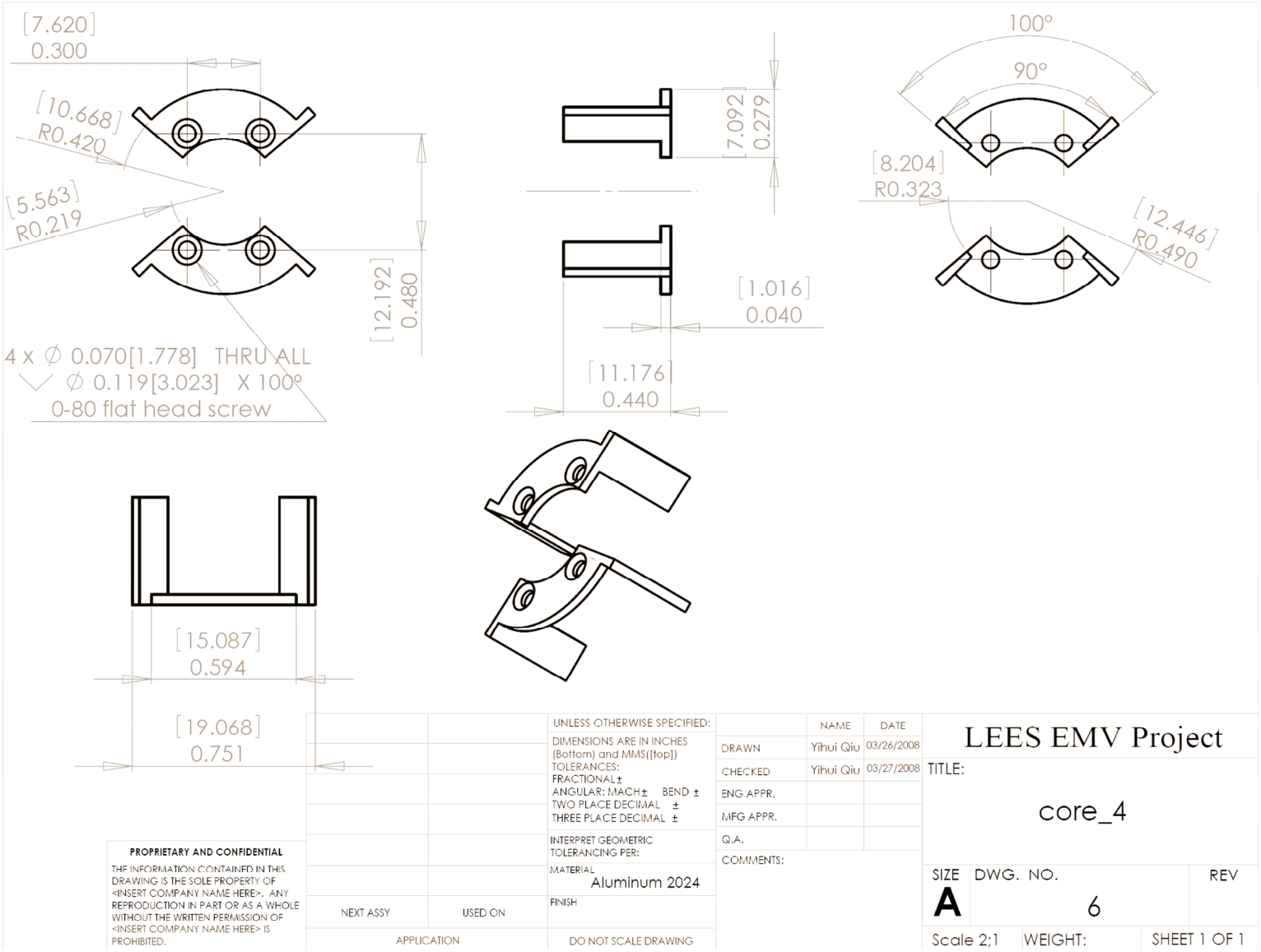

Fig. A2.6. Magnet spacers for the actuator.

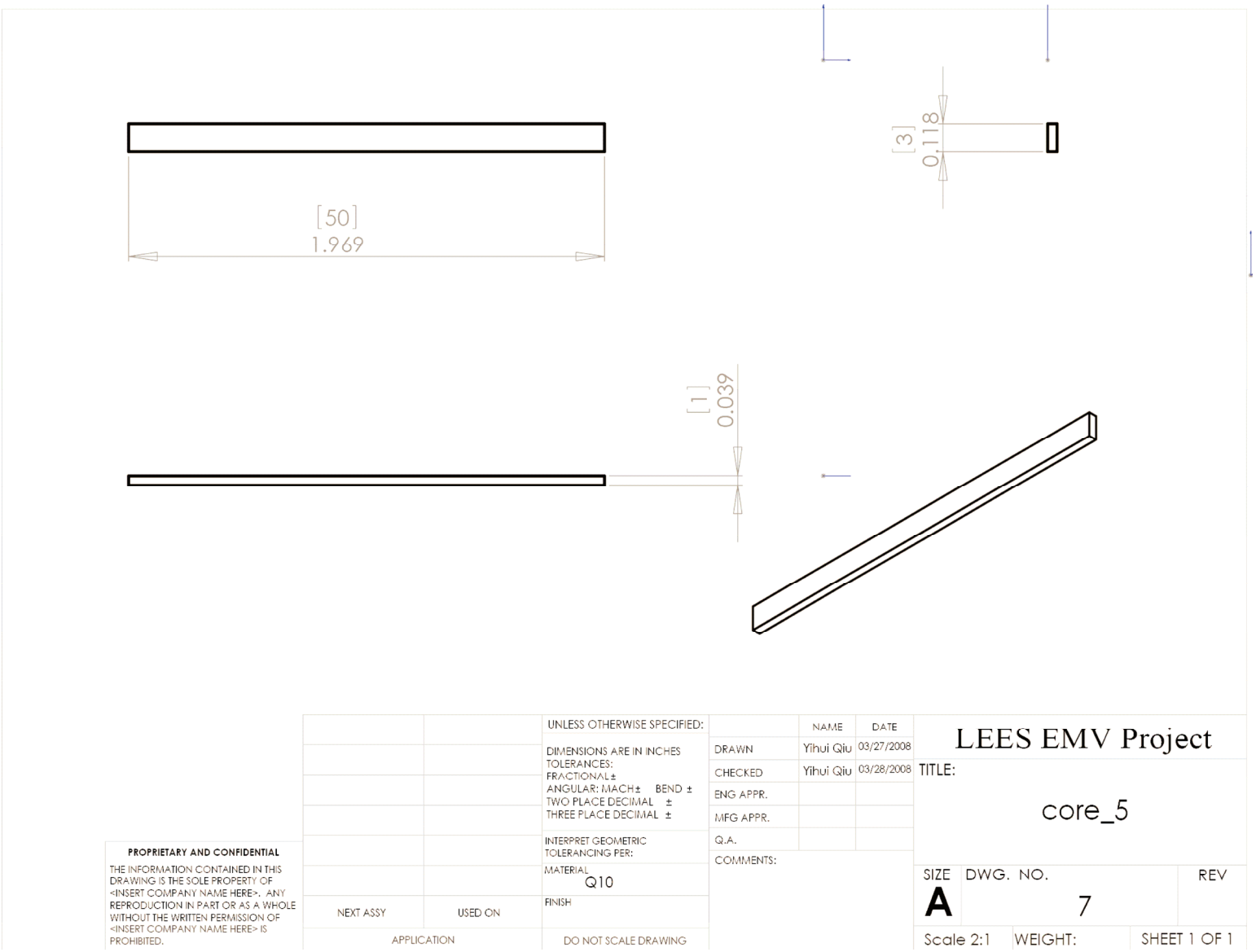

Fig. A2.7. Core spacer for the actuator.

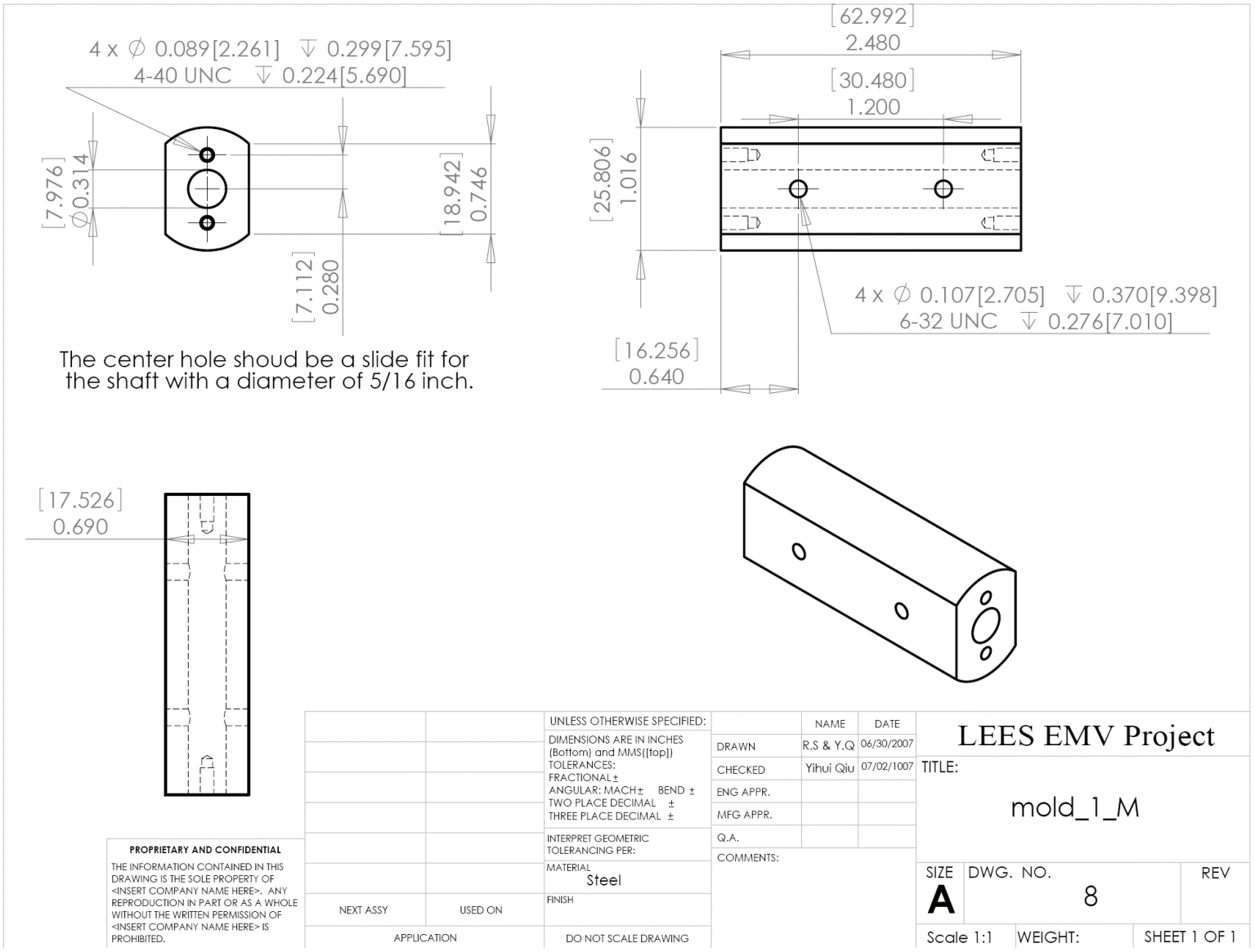

Fig. A2.8. Mold part 1 for the armature making.

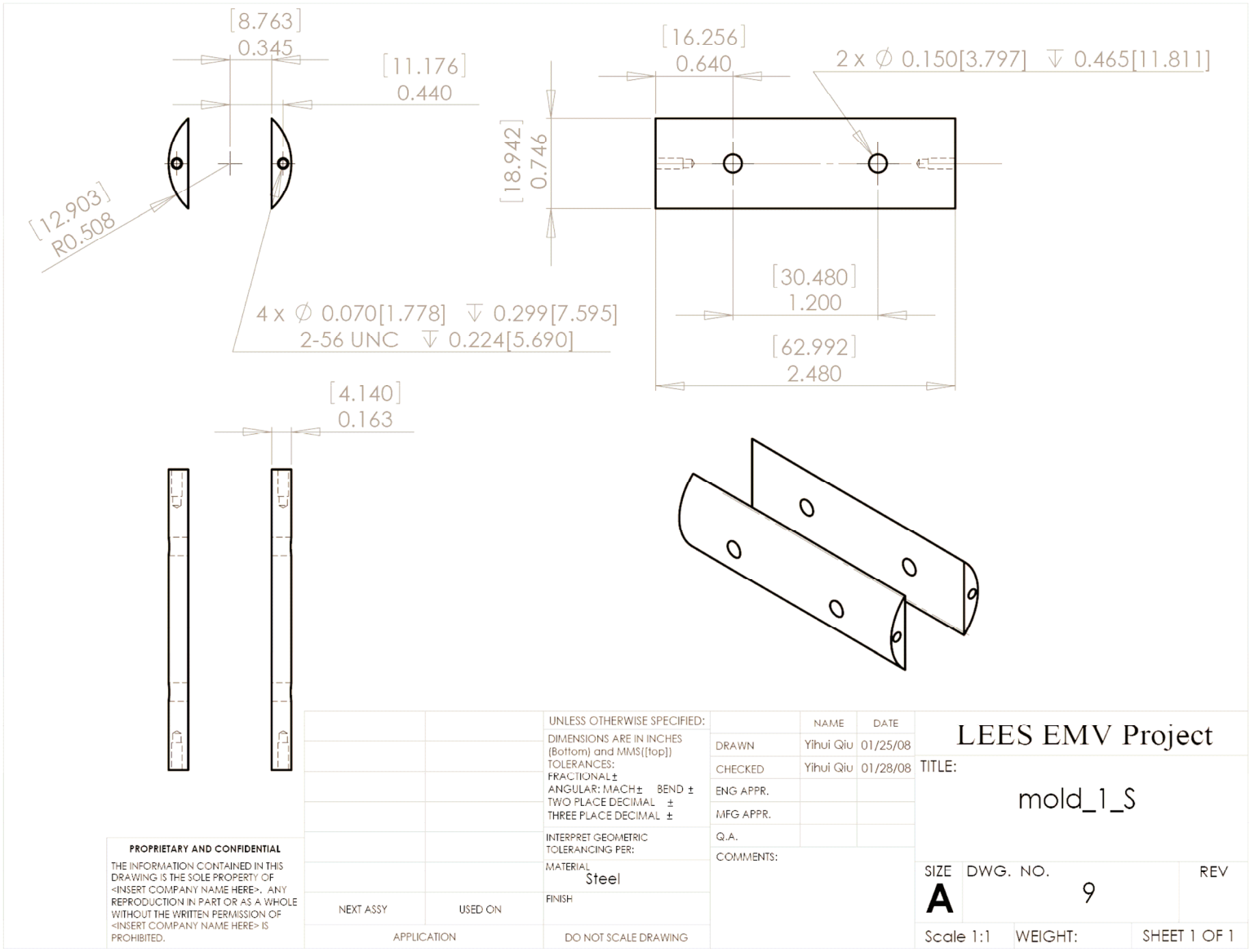

Fig. A2.9. Mold part 2 for the armature making.

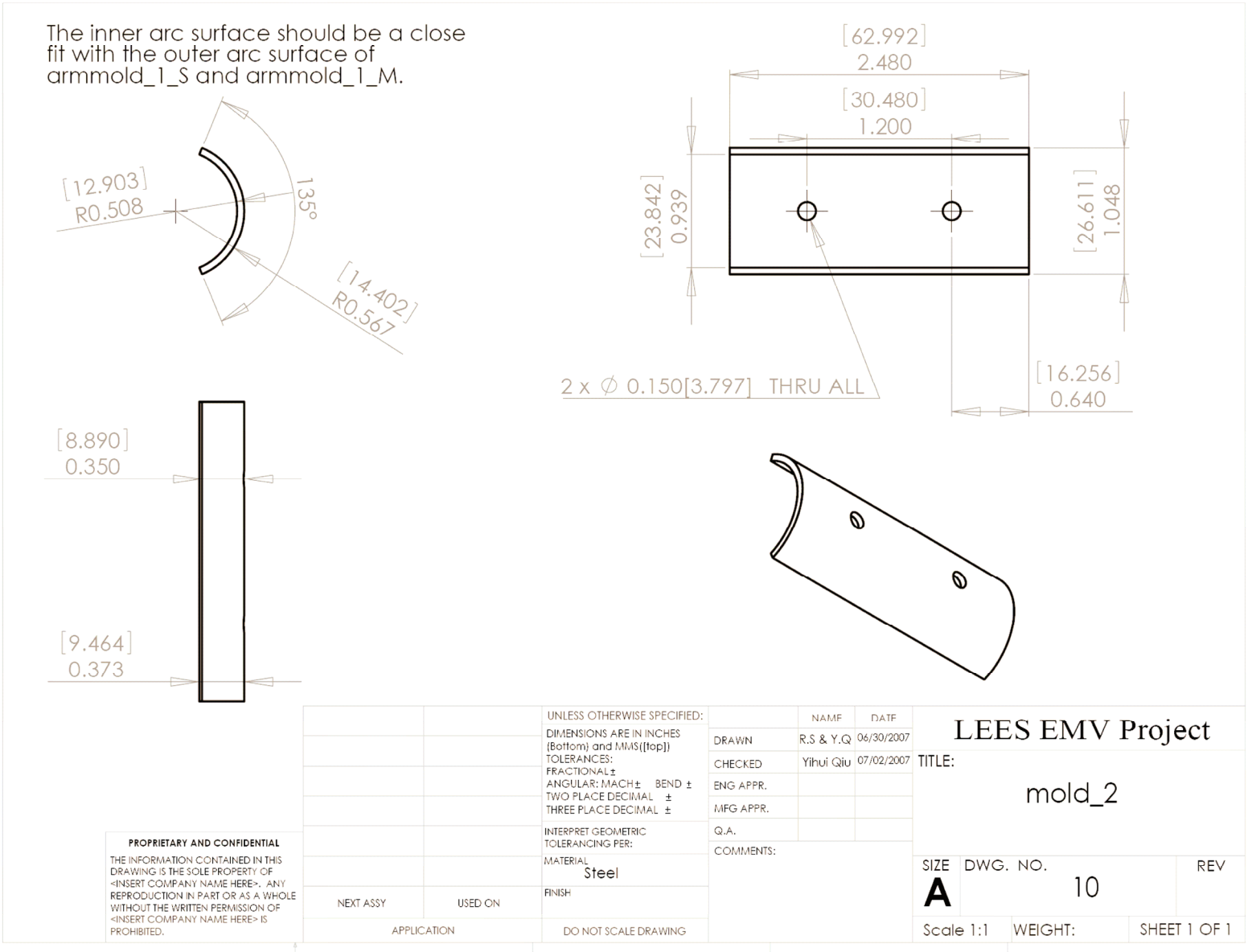

Fig. A2.10. Mold part 3 for the armature making.

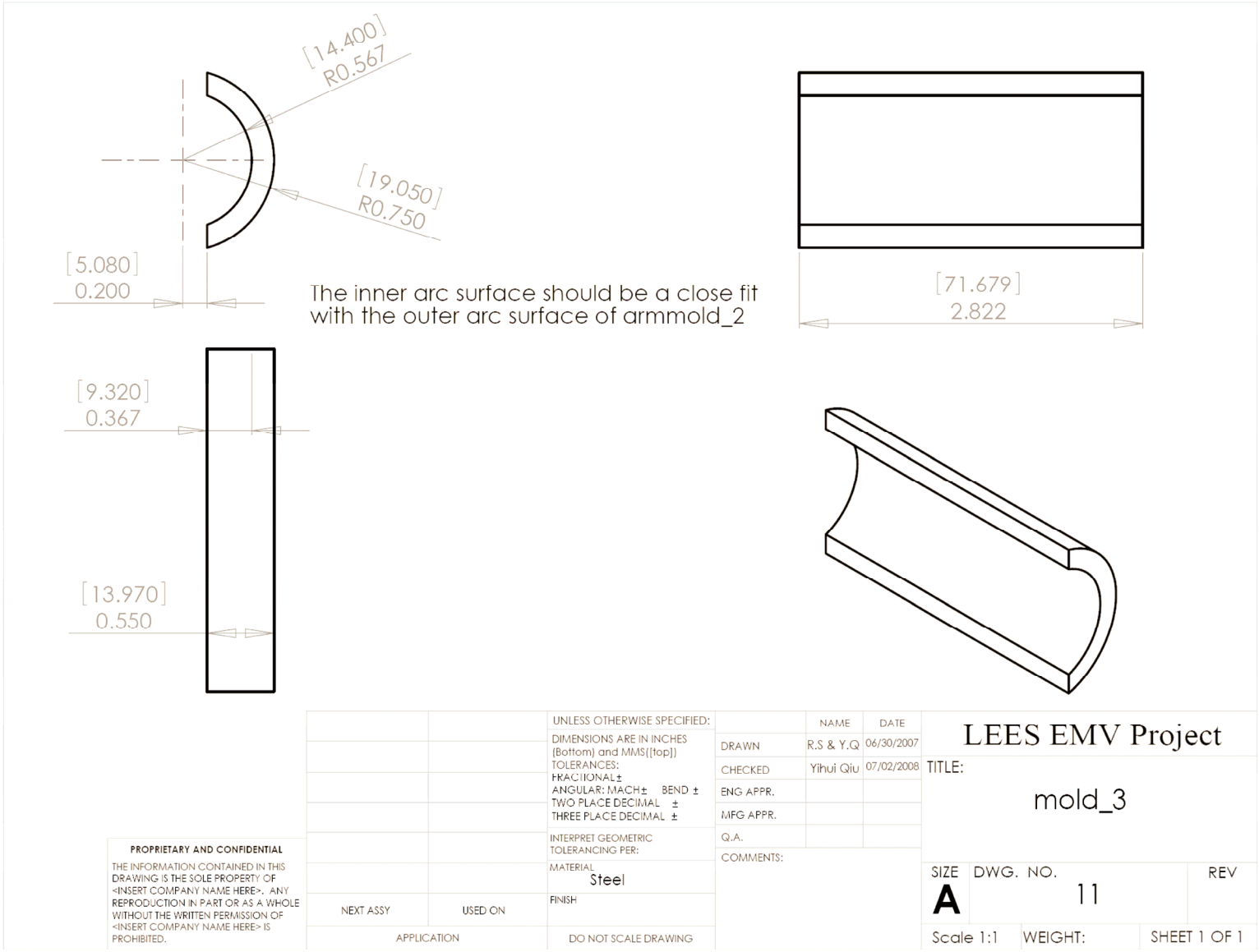

Fig. A2.11. Mold part 4 for the armature making.

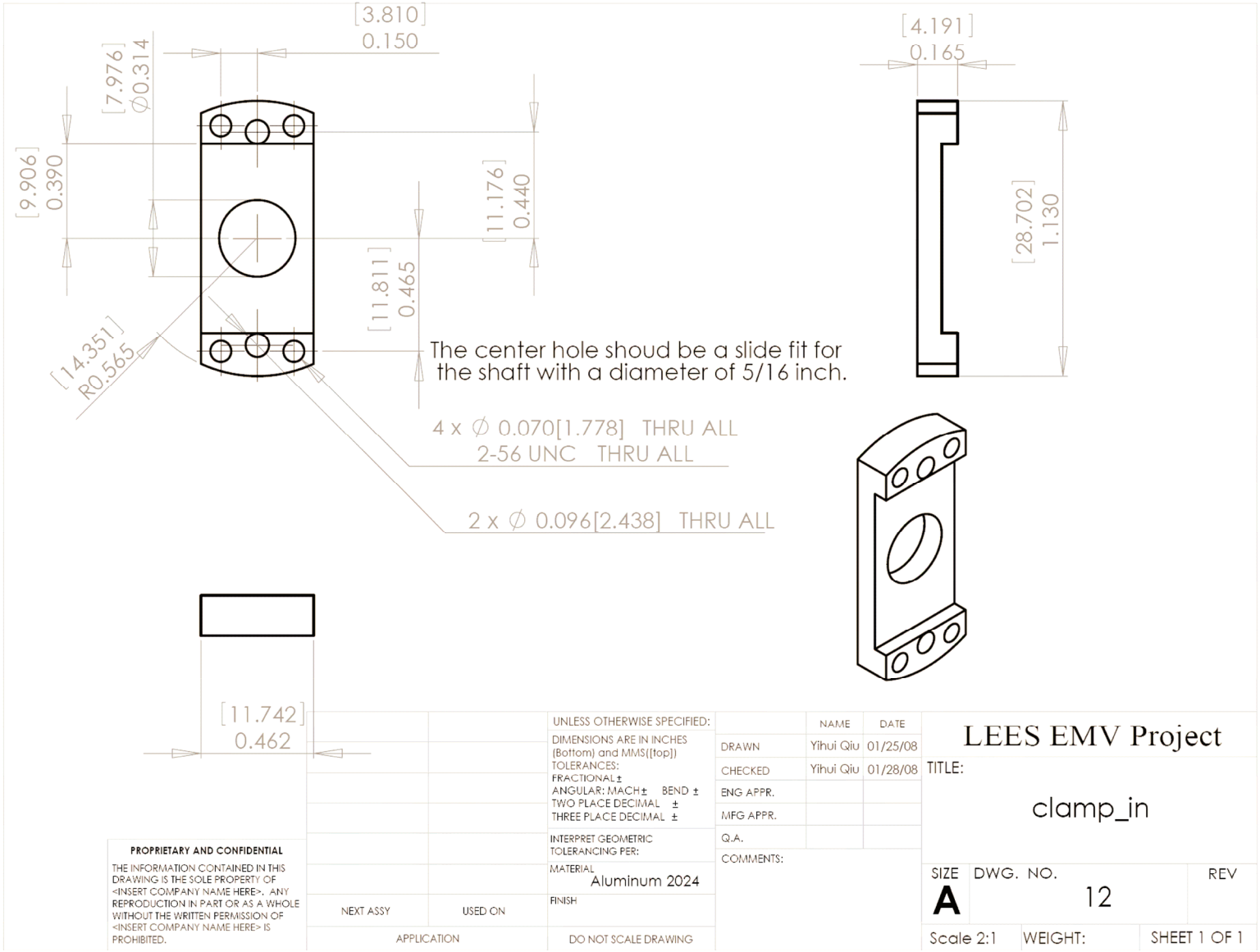

Fig. A2.12. Inner clamp for the armature.

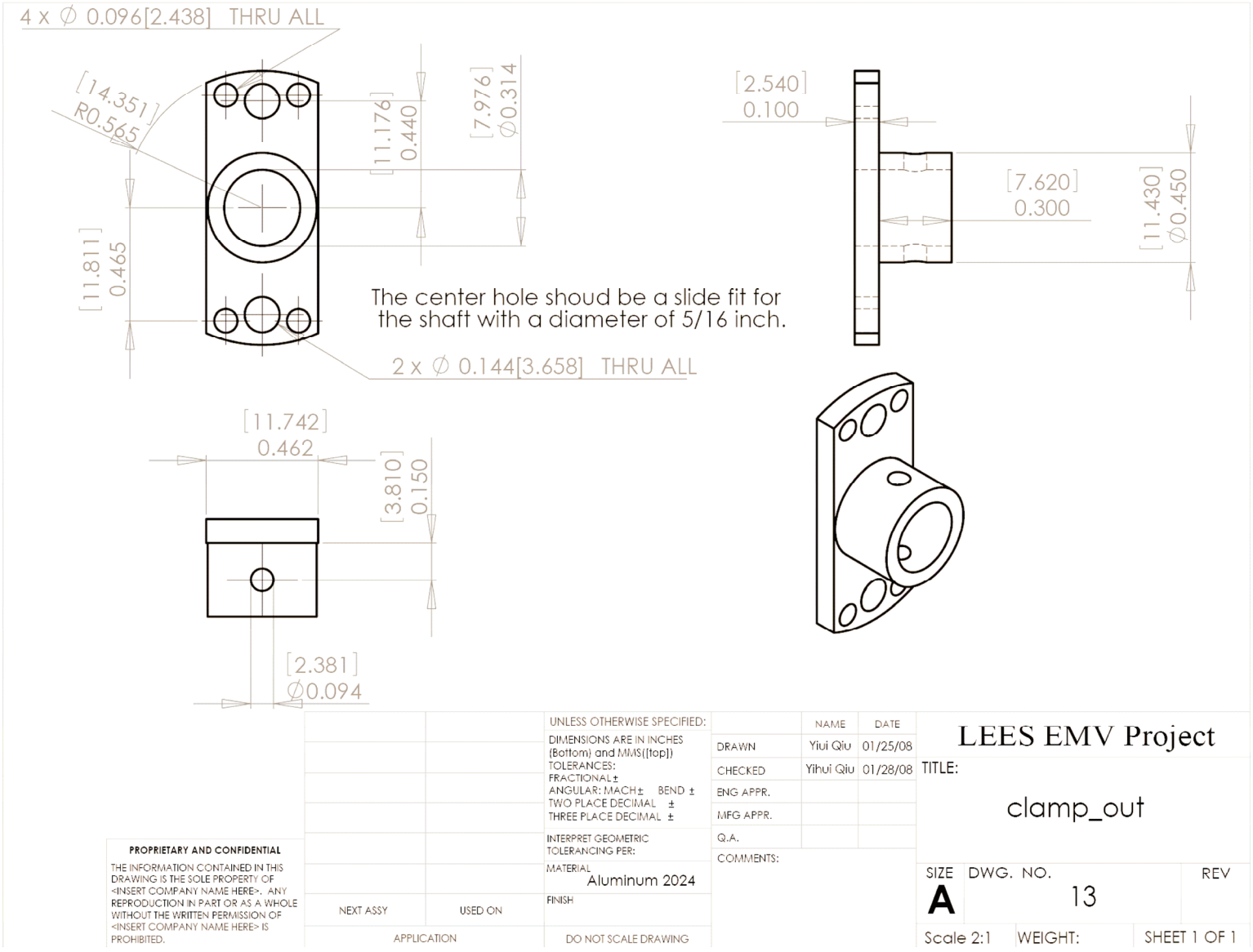

Fig. A2.13. Outer clamp for the armature.

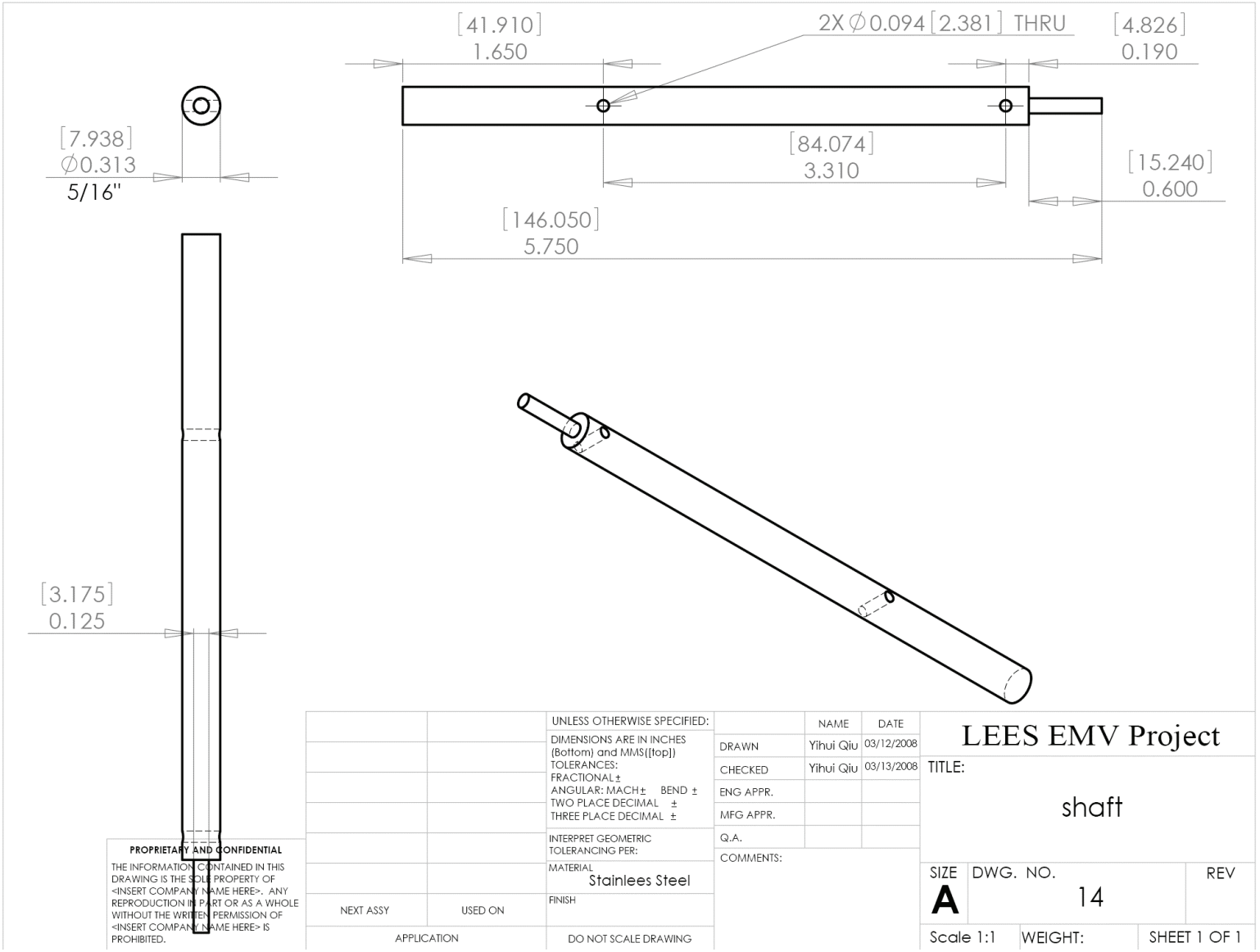

Fig. A2.14. Shaft for the armature and actuator.

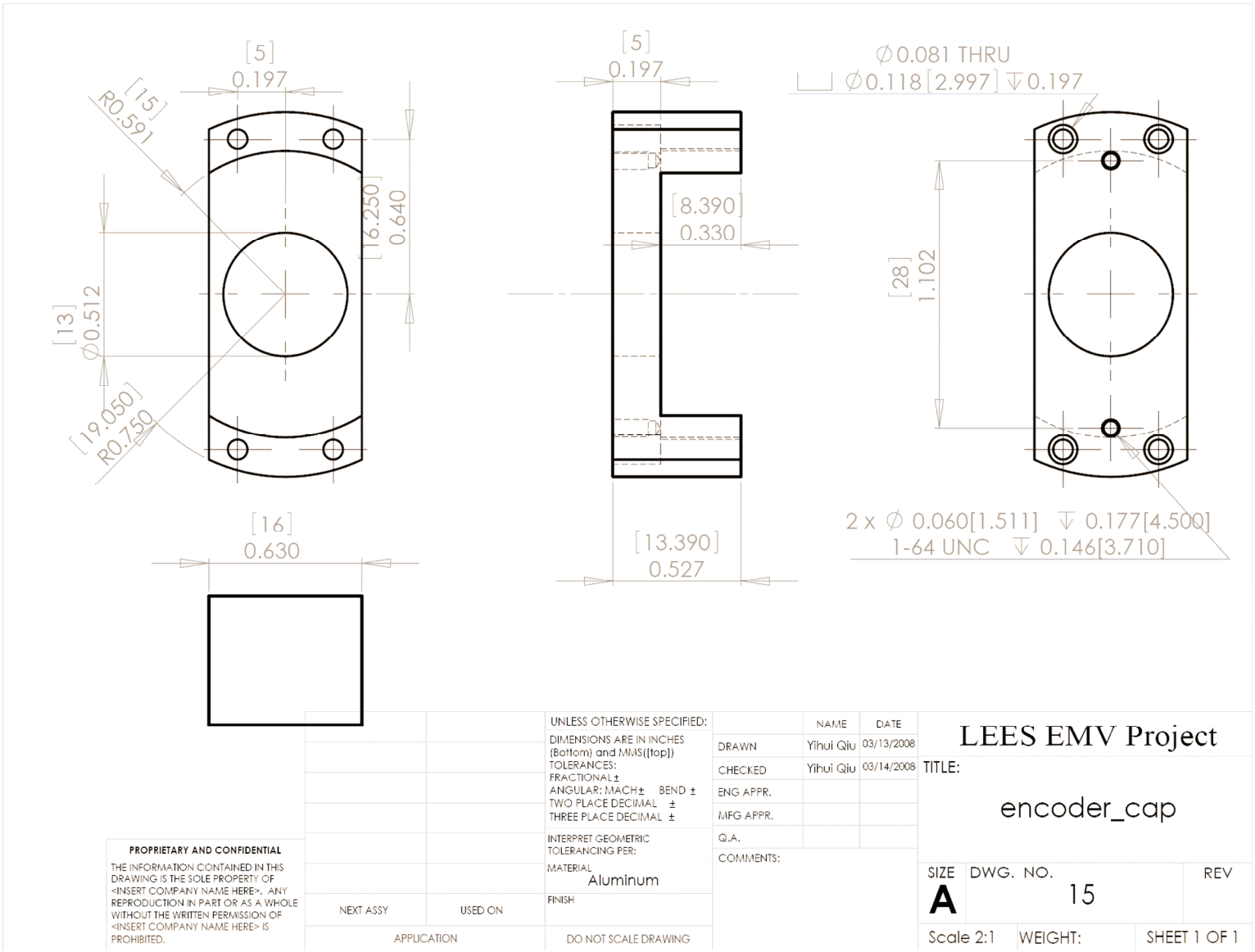

Fig. A2.15. Cap to connect the stator to the stationary part of the encoder.

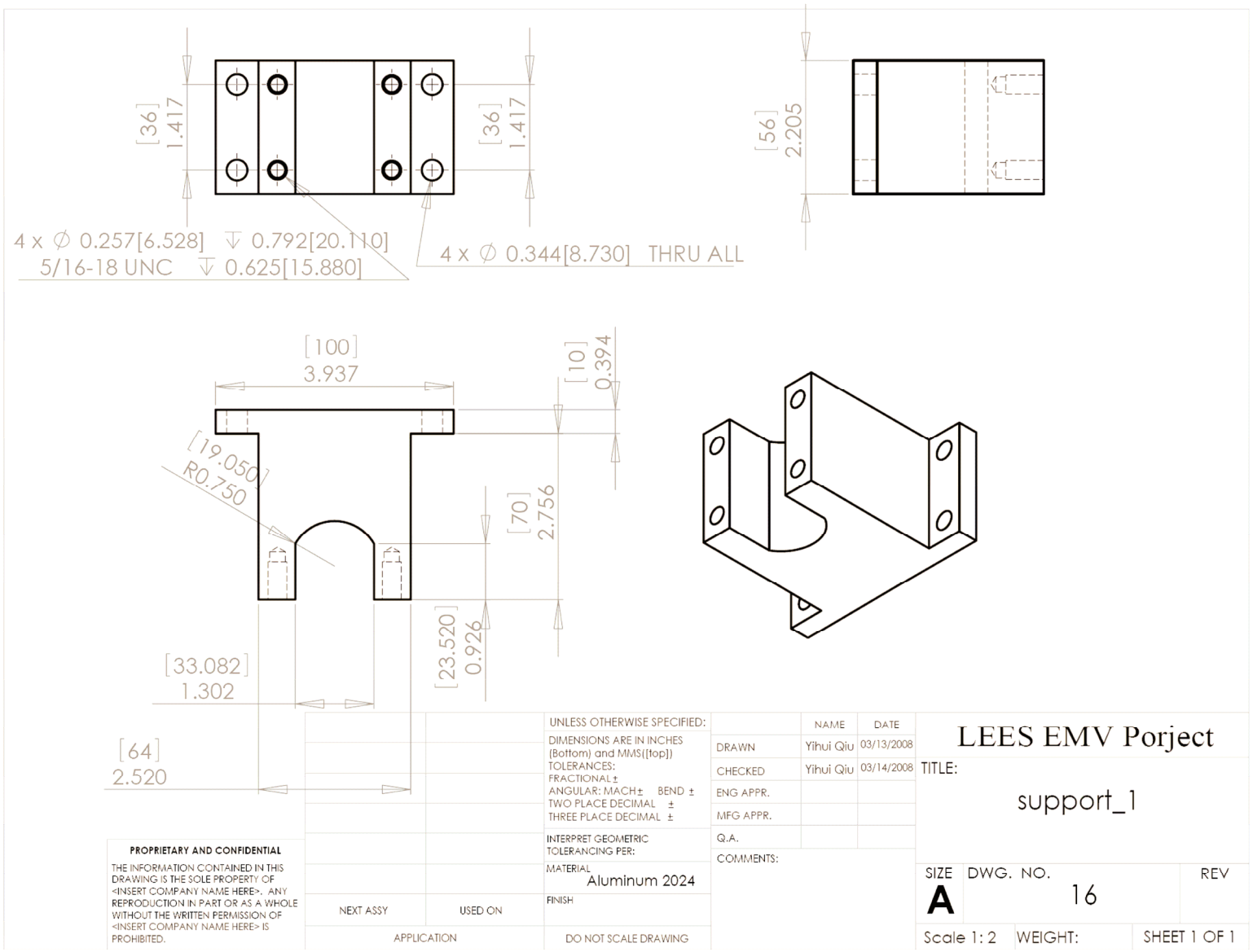

Fig. A2.16. Supporting part 1 for the actuator.

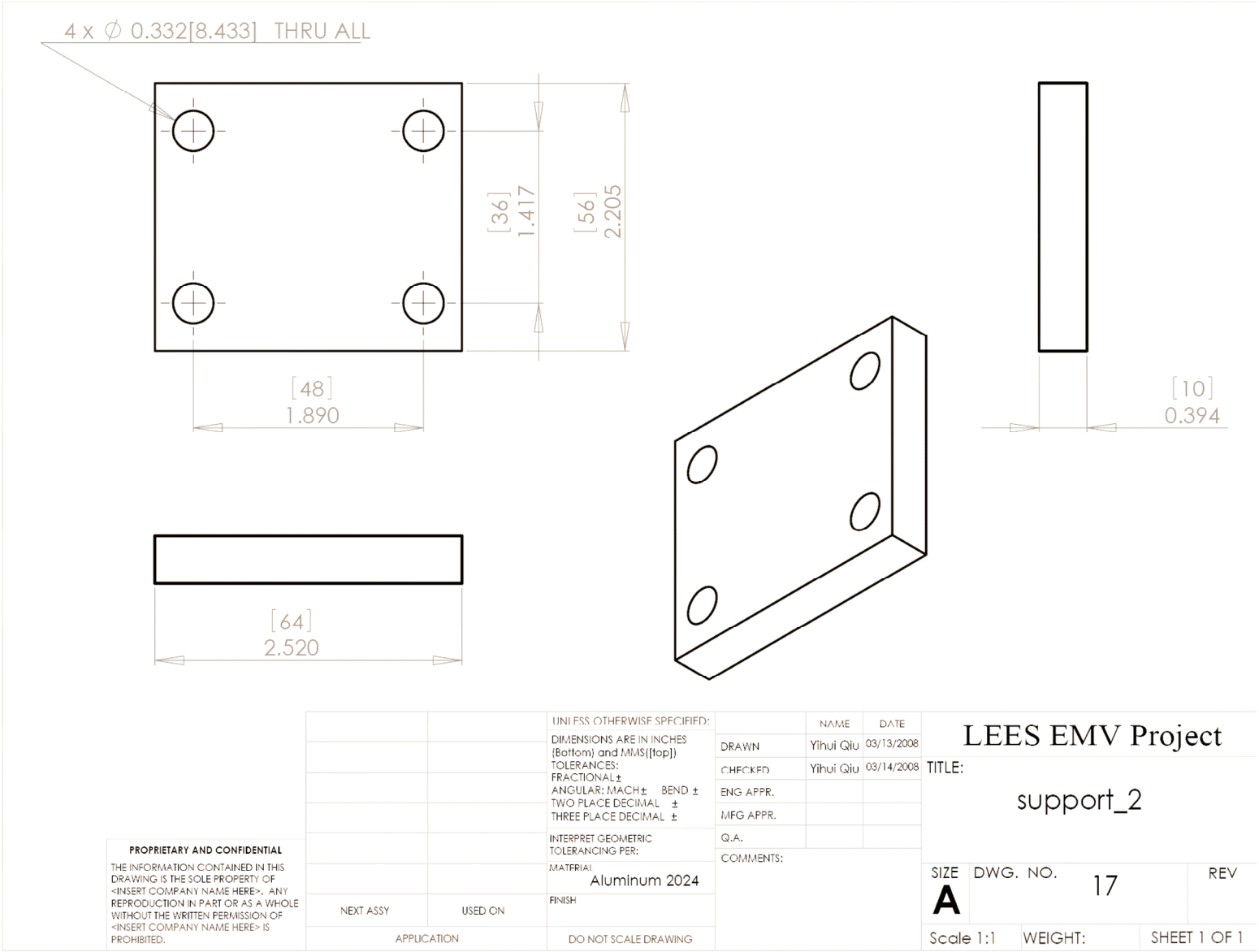

Fig. A2.17. Supporting part 2 for the actuator.

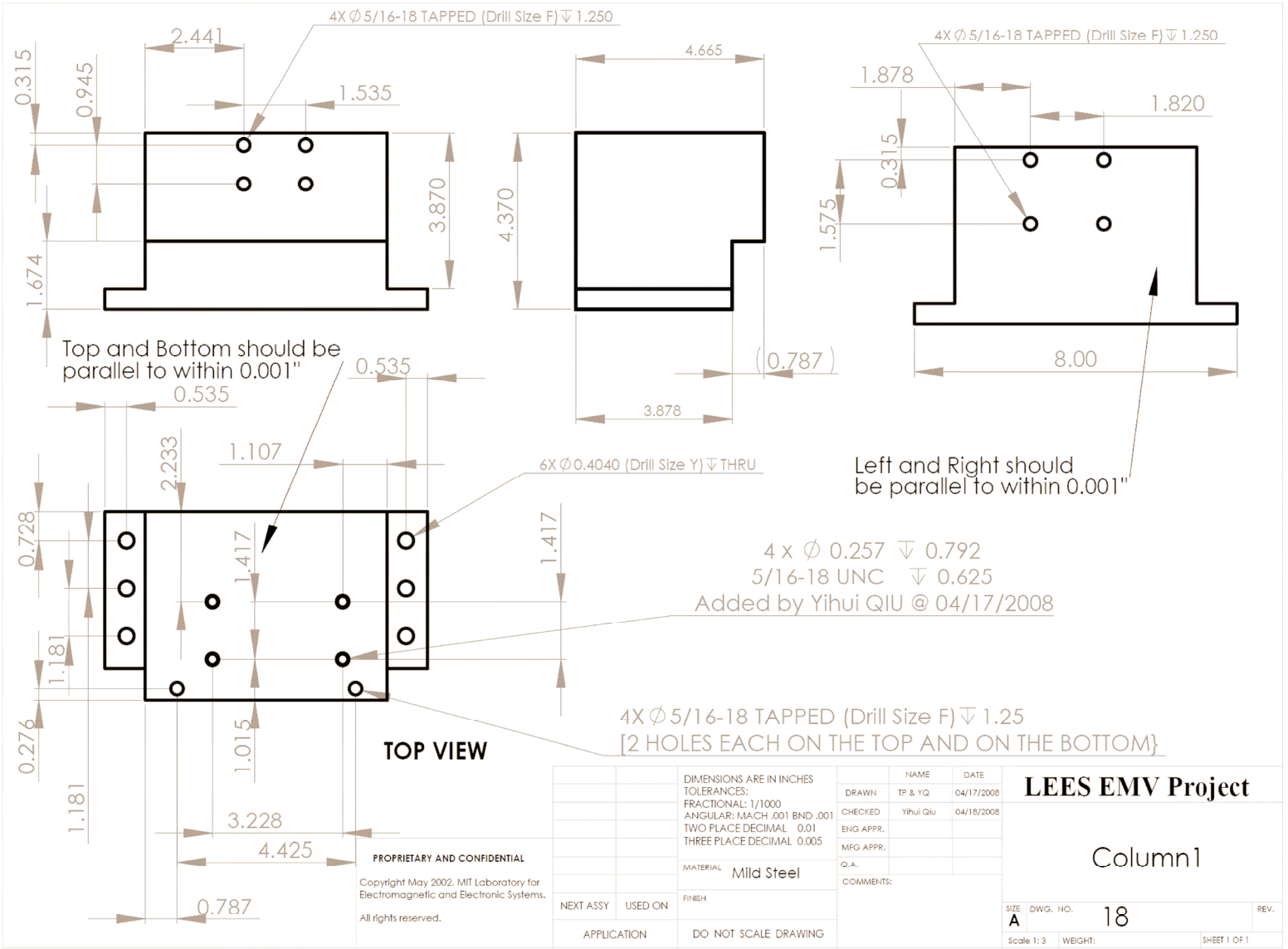

Fig. A2.18. Four threaded holes added to column 1 [18] for the actuator support.

APPENDIX III SIMULATION SCHEMATICS IN 20-SIM®

This Appendix contains the simulation schematics in 20-sim® developed during the whole thesis work, including simulation schematics with pure closed-loop control, combination control, and gas force disturbance. The blocks used in those schematics, including NMT modulus generator, sinusoidal position reference generator, free-flight trajectory generator, and lead compensator, are also attached in this appendix. Note that in the simulation schematics of combination control, it is optional to turn off either the initial open-loop current pulse or the closed-loop control at later stage to implement the pure closed-loop or pure open-loop control independently.

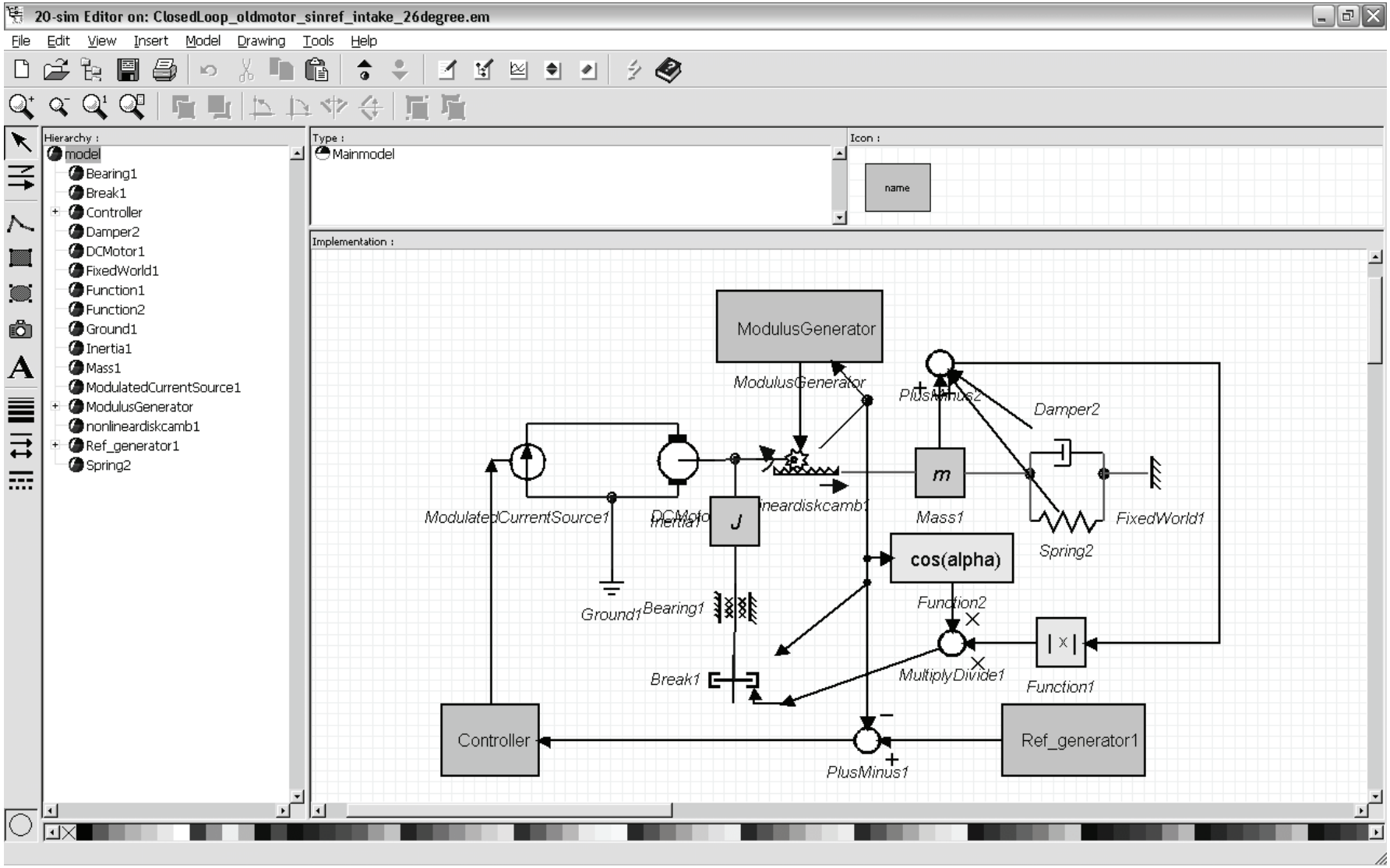

Fig. A3.1. Simulation schematic with pure closed-loop control.

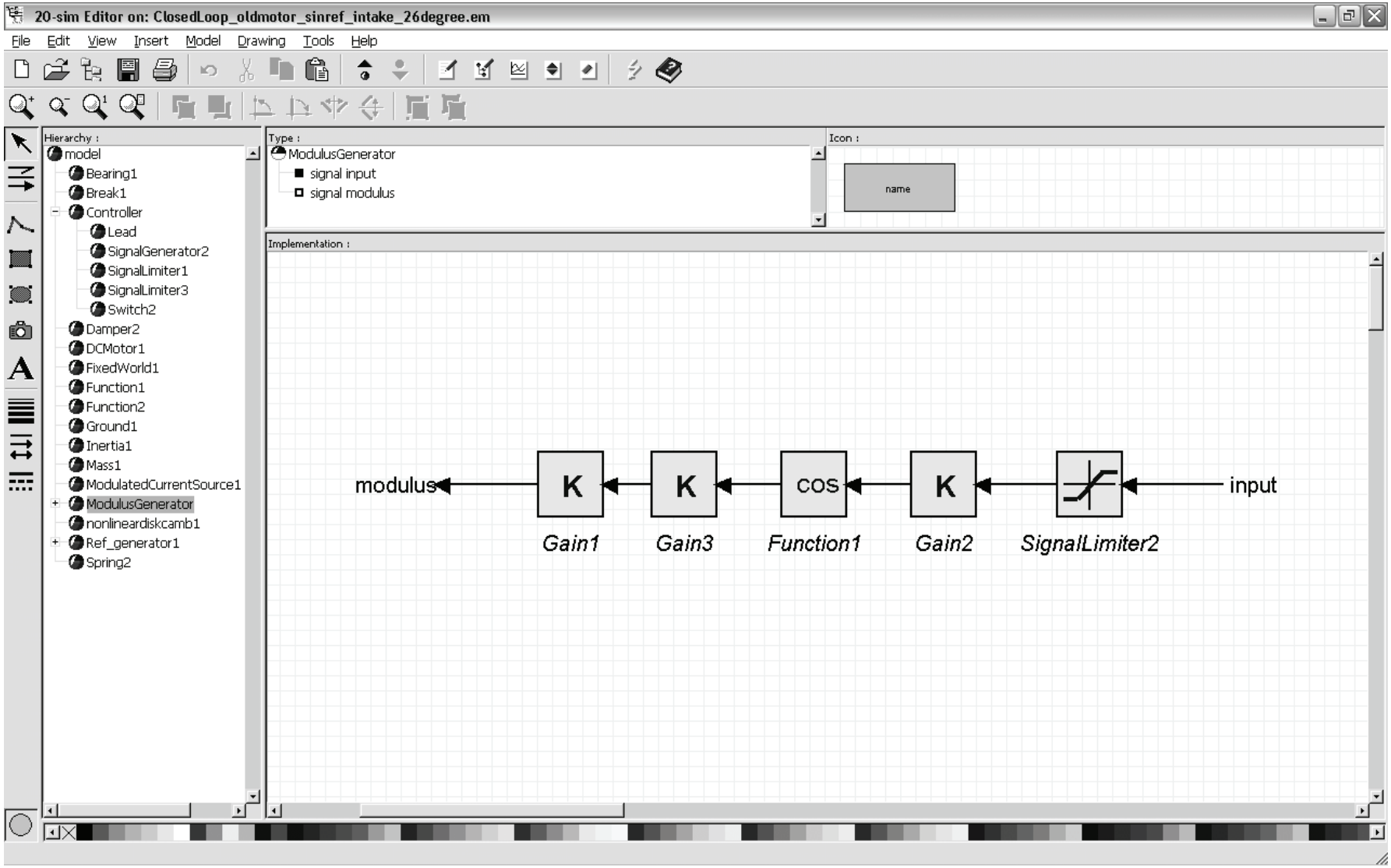

Fig. A3.2. Modulus generator for the nonlinear transformer.

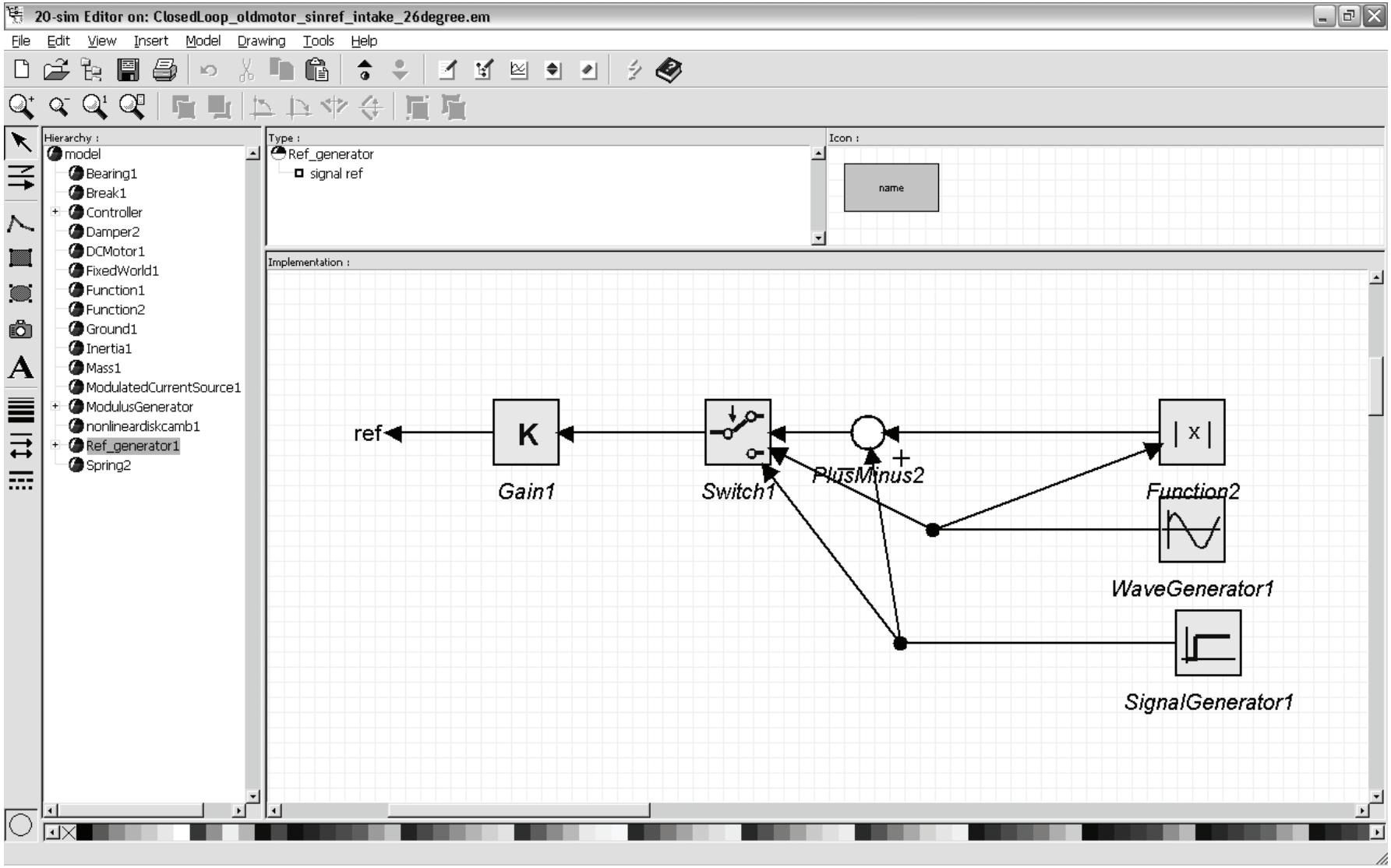

Fig. A3.3. Sinusoidal position reference generator.

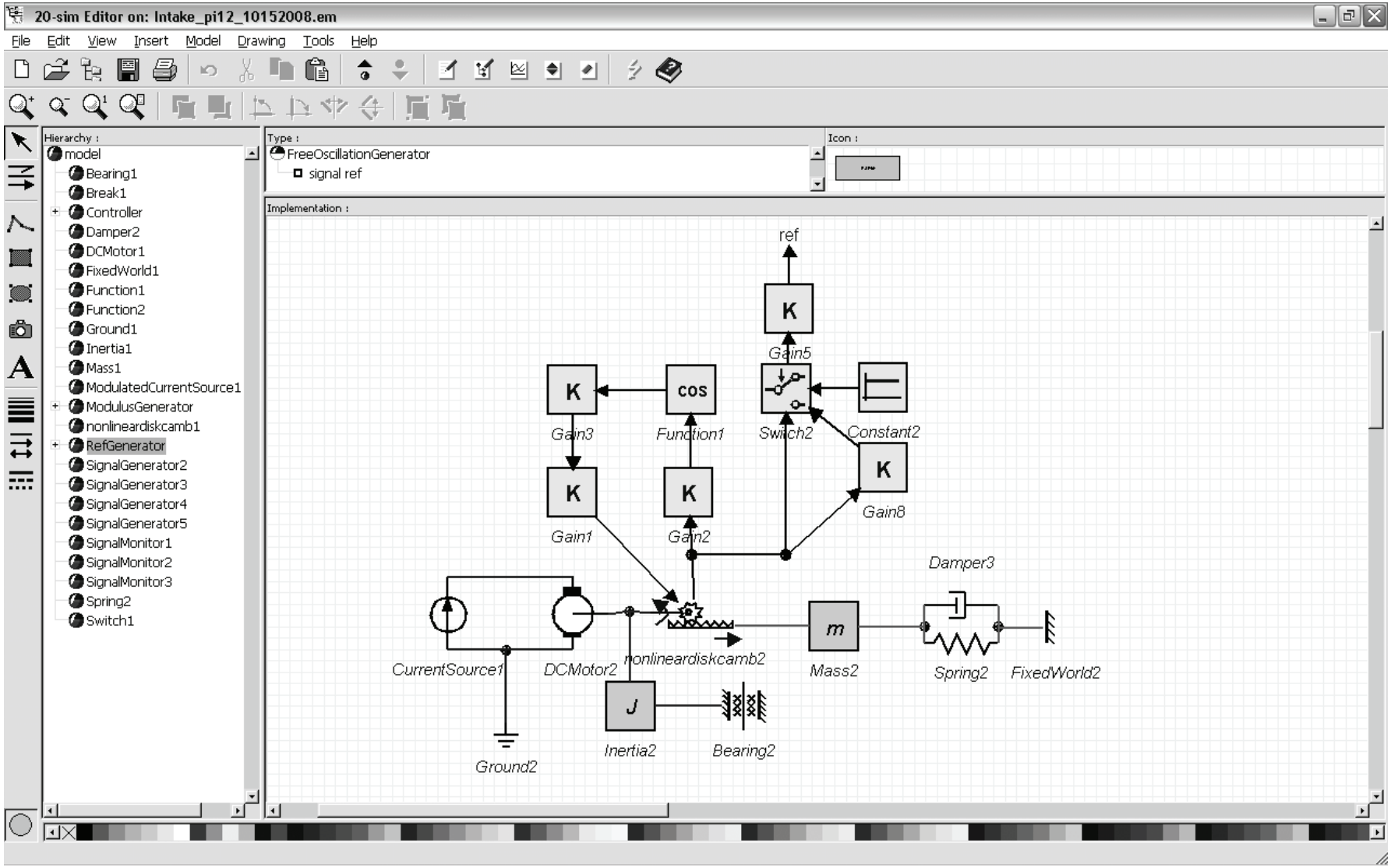

Fig. A3.4. Free-flight position reference generator.

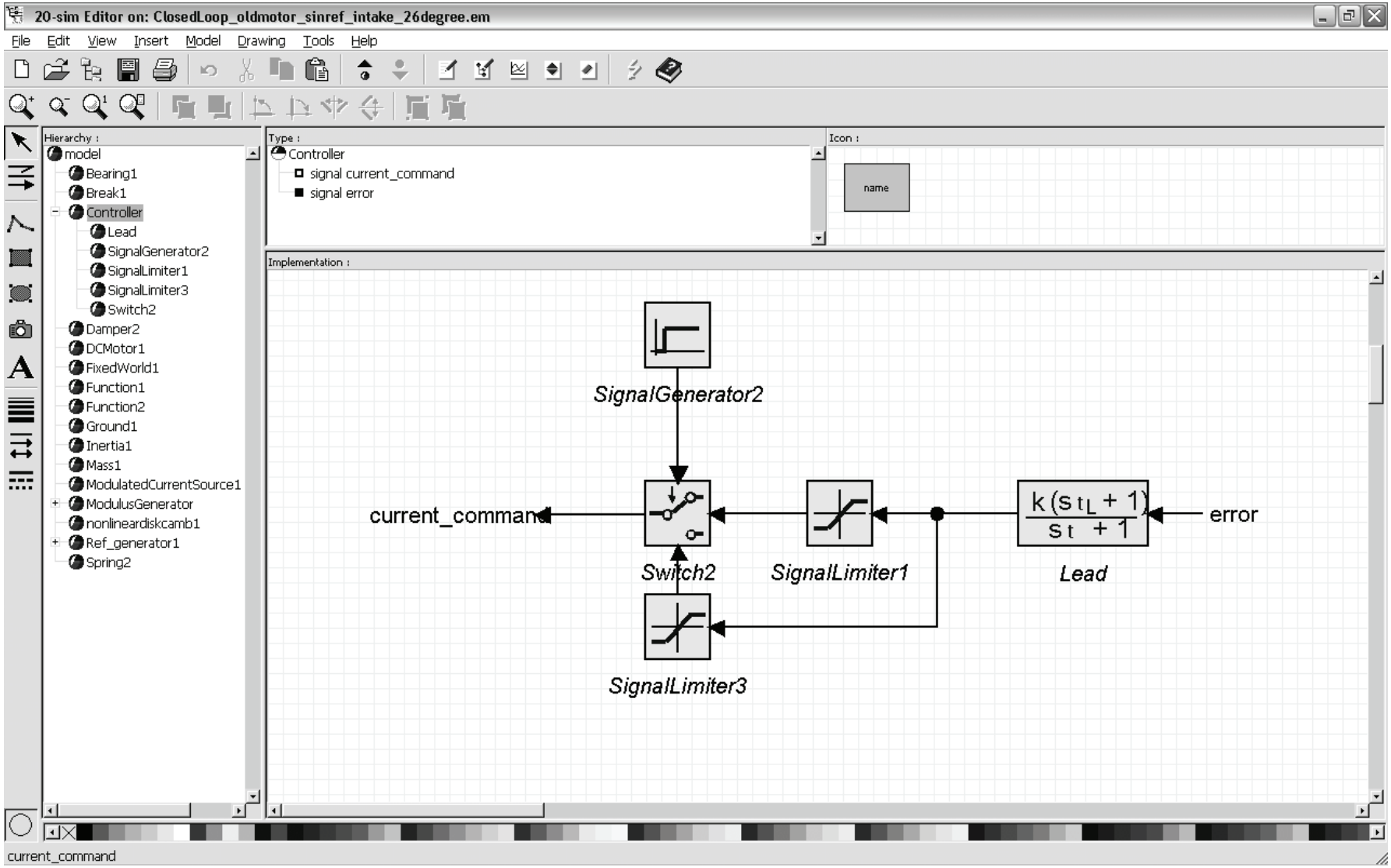

Fig. A3.5. Lead compensator plus current clamper.

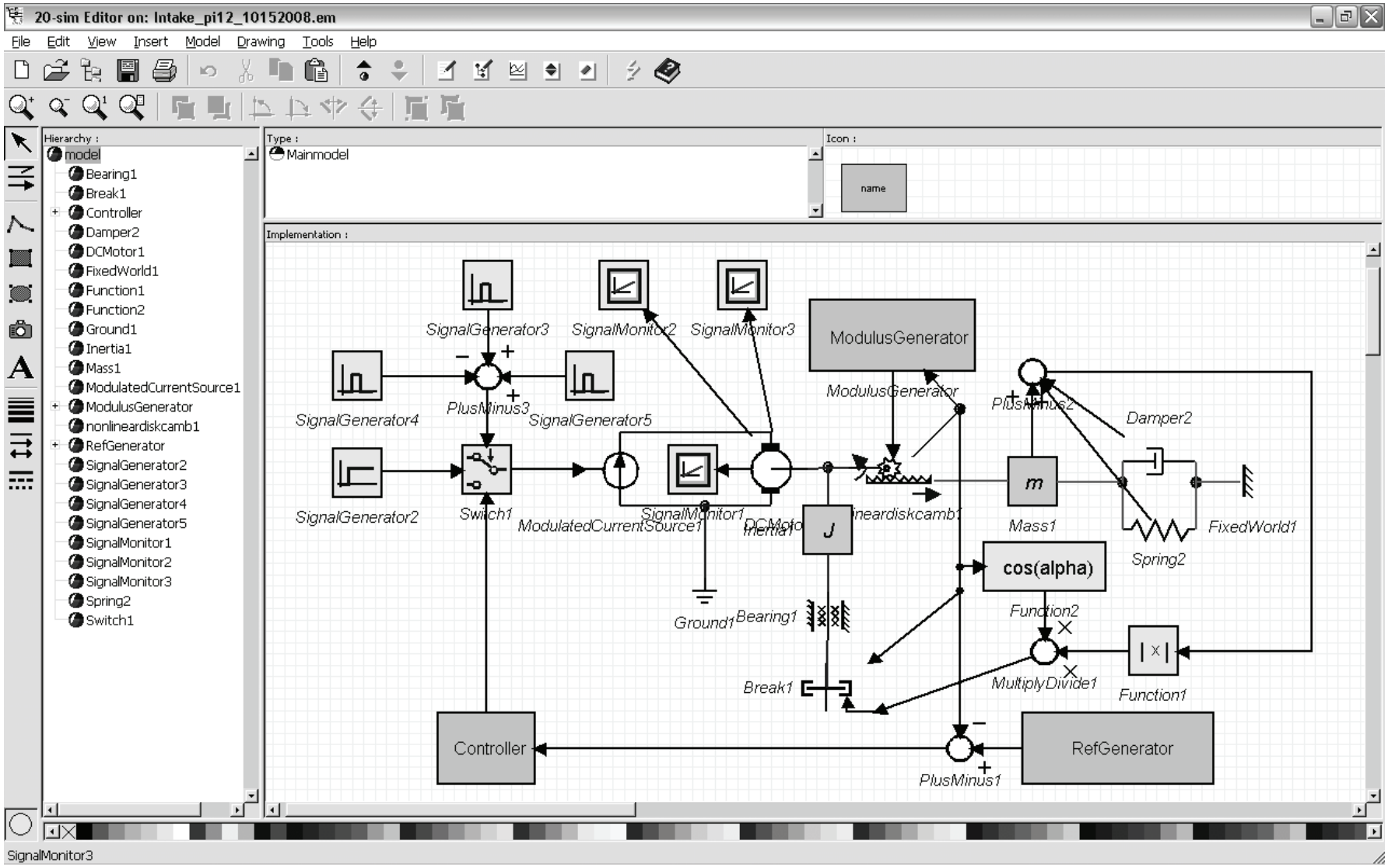

Fig. A3.6. Simulation schematic with combination control.

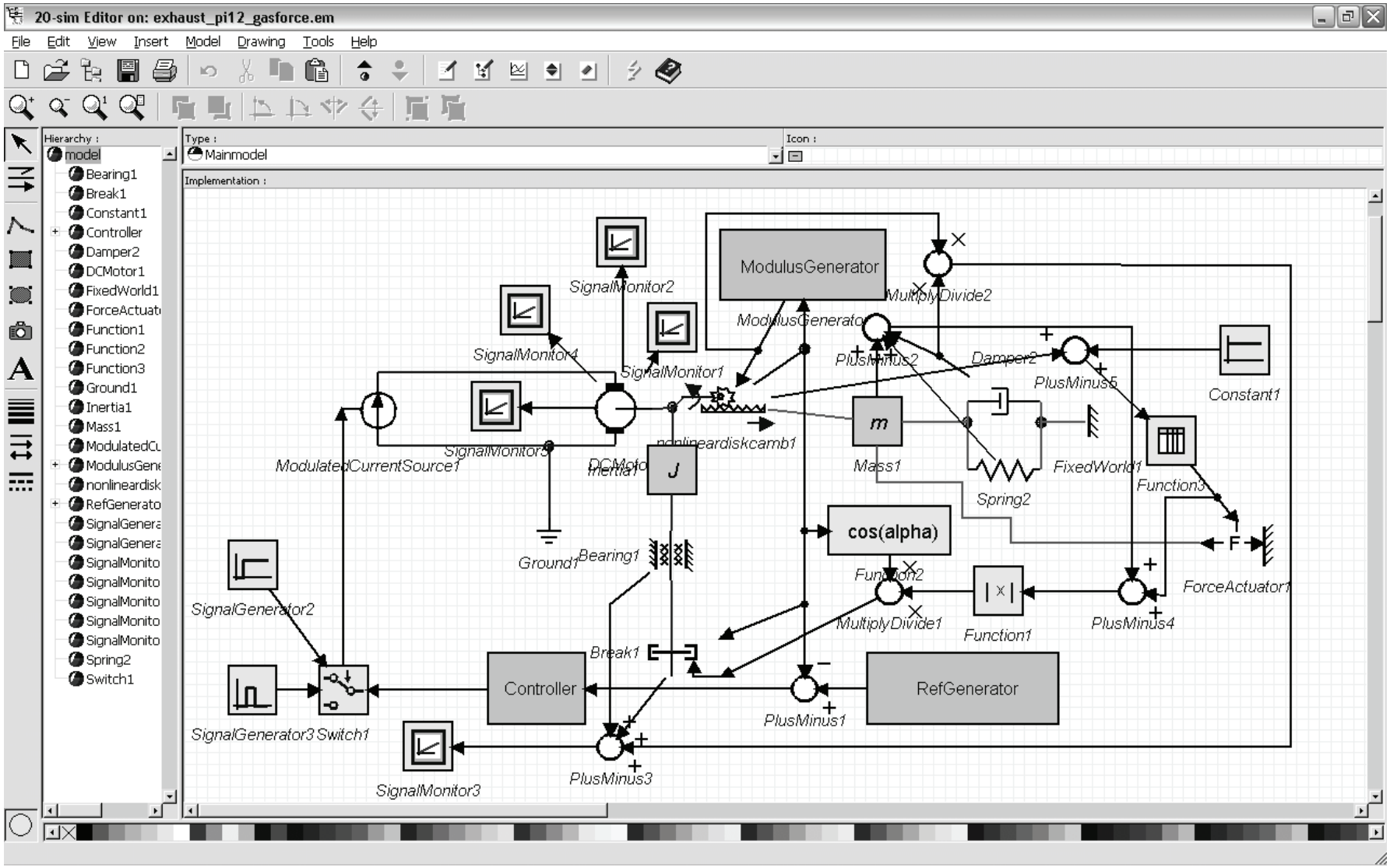

Fig. A3.7. Simulation schematic with gas force disturbance.

APPENDIX IV MATLAB® DESIGN PROGRAM FOR THE ±15° DISK CAM

This Appendix contains the MATLAB® file that was used to generate the profile for the disk cam roller-follower. The curves generated by this program were used in SolidWorks® to create a 3-dimensional design for the disk cam.

```
%%%%%%%%%%%%%%%%%%%%%%%%%%%%%%%%%%%%%%%%%%%%%%%%%%%%%%%%%%%%%%%%%%%%%%%%%%%%%%%%
% EMV Project                                                                    %
% Yihui Qiu                                                                      %
% April 2005                                                                     %
% Name of file: 15degreediskcamprofile.m                                         %
% Purpose: to generate a slot in the disk cam of +/- 15 degrees for   %
% the roller                                                                     %
%%%%%%%%%%%%%%%%%%%%%%%%%%%%%%%%%%%%%%%%%%%%%%%%%%%%%%%%%%%%%%%%%%%%%%%%%%%%%%%%

clc;
clear all;

% Enter the equation for the NTF relating the z and theta domains
lift=0.008; %full stroke of the valve
alpha=6;
beta=0.99;
r=0.02875; % distance between shaft center and roller center when the
system is in its equilibrium point
r0=0.005075; % roller radius
h=lift/(2*sin(beta*pi/2));
endpt=15;
endpt1=endpt+5;
endpt2=endpt+4;
n=2*(endpt1+endpt2)+1;
theta=linspace(-endpt1,endpt2,n);
for i=1:length(theta)
    if abs(theta(i)) <= endpt
        z1(i)=h*sin(alpha*theta(i)*pi/180);
    else
        if theta(i) >endpt
        z1(i)=h*sin(alpha*endpt*pi/180);
        else
        z1(i)=-h*sin(alpha*endpt*pi/180);
        end
    end
end


figure; %Figure1: z-theta characteristics
plot(theta,z1);
title('Z=f(\theta)') ;
xlabel('\theta (degrees)');
ylabel('Z (mm)');
```

```
grid;


% Translate by +r
for i=1:length(theta)
    if abs(theta(i)) <= endpt
        z2(i)=h*sin(alpha*theta(i)*pi/180)+r;
    else
        if theta(i) >endpt
        z2(i)=h*sin(alpha*endpt*pi/180)+r;
        else
        z2(i)=-h*sin(alpha*endpt*pi/180)+r;
        end
    end
end
figure; %Figure2: (z+r)-theta characteristics
plot(theta,z2);
title('Z=f(\theta)+r');
xlabel('\theta (degrees)');
ylabel('Z(mm)');
grid;

% Convert from the Polar Coordinates to the x-y Coordinates
x=1*z2.*cos(theta*pi/180);
y=z2.*sin(theta*pi/180);

%Flip x and y and make y=-y
x0=y;
y0=-1*x;


% Generation of Top and Bottom Surface Profiles:

% Find the derivatives of each point of the slot
dy_dxnum=gradient(y0)./gradient(x0);
zeta=atan(dy_dxnum);

% Find the x-y coordinates for each point of the slot
for i=1:length(x0)

        x1num(i)=x0(i)-r0*sin(zeta(i));
        y1num(i)=y0(i)+r0*cos(zeta(i));
        x2num(i)=x0(i)+r0*sin(zeta(i));
        y2num(i)=y0(i)-r0*cos(zeta(i));

end


% Plot the top curve, bottom curve, and the center curve of the roller
slot
figure;%Figure 3: Show the top curve, bottom curve, and the center
curve
plot(x0,y0,'k',x1num,y1num,'yellow',x2num,y2num,'green');
grid
title('Cam Roller Profiles')
legend('Center of roller', 'Top contact point(analytical)','Bottom
contact point(analytical)');
xlabel('Horizontal Displacement - x (meters)');
```

```
ylabel('VerticalDisplacement - y (meters)');


%Generate the disk slot by rolling the roller vitually from one end to
the
%other end
figure; %Figure 4: Show the disk slot by rolling the roller from end to
end
for i=1:length(theta)
    circ(x0(i),y0(i),r0);
end
hold on
plot(x0,y0,'green',x1num,y1num,'b',x2num,y2num,'b') ;
title('y=g(x)');
xlabel('x');
ylabel('y');
axis equal
grid


%Generate Profile Data and Save in Text Files

 for i=1:length(x0)
     profileC(:,i)=1000*[x0(i); y0(i); 0;]; %convert to mm
     profileT(:,i)=1000*[x1num(i);y1num(i);0]; %convert to mm
     profileB(:,i)=1000*[x2num(i);y2num(i);0]; %convert to mm
 end

 %Coordinations of center curve to diskC.txt
 fid=fopen('E:\HardwareDesign\Cam\15degrees\diskC.txt','w');
 fprintf(fid,'%6.2f  %6.2f   %6.2f\n',profileC);
 fclose(fid);
 %Coordinations of top curve to diskT.txt
 fid=fopen('E:\HardwareDesign\Cam\15degrees\diskT.txt','w');
 fprintf(fid,'%6.2f  %6.2f   %6.2f\n',profileT);
 fclose(fid);
 %Coordinations of bottom curve to diskB.txt
 fid=fopen('E:\HardwareDesign\Cam\15degrees\diskB.txt','w');
 fprintf(fid,'%6.2f  %6.2f   %6.2f\n',profileB);
 fclose(fid);
```

APPENDIX V MATLAB® PROGRAM FOR EXPERIMENTAL DATA ANALYSIS

This Appendix contains the MATLAB® file that was used to analyze experimental data, especially focusing on estimation of winding loss, frictional loss, and total power consumption during one transition at 6000 rpm engine speed. The raw data are captured by digital oscilloscope and recorded by Labview® as binary files. Due to possible different capturing setting of the oscilloscope and different motor parameters at each experiment, the effective length of the raw data could be different for different experiments. Therefore, the algorithm below applies for the general purpose stated above but carefully setting up the desired data length and motor resistance and torque constant will be necessary for each experiment.

```
%%%%%%%%%%%%%%%%%%%%%%%%%%%%%%%%%%%%%%%%%%%%%%%%%%%%%%%%%%%%%%%%%%%%%%%%%%%%%%%%
% EMV Project                                                                    %
% Yihui Qiu                                                                      %
% May 2004                                                                       %
% Name of file: PowerAnanlysis.m                                                 %
% Purpose: to estimate winding loss, frictional loss, and total                  %
%power consumption during one transition at 6000 rpm engine speed                %
% the roller                                                                     %
%%%%%%%%%%%%%%%%%%%%%%%%%%%%%%%%%%%%%%%%%%%%%%%%%%%%%%%%%%%%%%%%%%%%%%%%%%%%%%%%


% Read in raw data of each waveforms
[t1a,thetaA]=readbin('ref.bin');
[t1b,thetaB]=readbin('pos.bin');
[t1c,current]=readbin('cur.bin');
[t1d,voltage]=readbin('vol.bin');


%power data calculated offline from cur and vol data
power=current.*voltage;


%pictures of 10ms full transition
figure;
subplot(2,2,1);
plot(t1a,thetaA,t1b,thetaB);
subplot(2,2,2);
plot(t1c,current);
subplot(2,2,3);
plot(t1d,voltage);
subplot(2,2,4);
plot(t1a,power);
```

```
%Average power, loss on i2r and total energy consumed
r=0.89; %This is the winding resistance of the first brush dc motor
AVGP20ms=mean(power)
AVGP10ms=mean(power(5800:30800))
Eloss=sum(current.*current)*4*10^-7*r
E=sum(power)*4*10^-7
figure
plot(t1a(5800:30800),current(5800:30800),t1a(5800:30800),thetaA(5800:30
800),t1a(5800:30800),thetaB(5800:30800));

%picture of valve position profile as well as transition time
for i=1:length(t1a)
    if abs(thetaB(i)-3.3)>2.618
        z(i)=4*sin(sign(thetaB(i)-3.3)*pi/2);
    else
        z(i)=4*sin((thetaB(i)-3.3)*6/10);
    end
end

figure
plot(t1a,thetaB-3.3,t1a,z)
figure
plot(t1a,thetaA,t1b,thetaB,t1c,current)


%distribution of avg power per 100us, i2r loss and T*omega
for i=1:50000
    i2r(i)=current(i)^2*r;
end   %instantaneous i2r

%filtering rotor position and get rotor speed as well as valve position
%accordingly
Fs=2500000;%Sampling frequency

%design filter for position and omega filtering
[B,A] = ELLIP(1,0.1,40,[1 100]*2/Fs); thetaC=thetaB;
for i=50001:100000
thetaC(i)=thetaB(100001-i);
thetaC(i+50000)=thetaB(i-50000);
end

%construct a period signal from one transition profile such that we got
%right filtered signal from beginning
t3c=[t1a (t1a+0.02) (t1a+0.04)];

%filter position profile
YC=filter(B,A,thetaC);

%get omega from position profile
omegaC=diff(YC)*Fs/10;

%fill in the missing last spot for omega vector
omegaC(150000)=0;

%filter omega profile
```

```
YYC=filter(B,A,omegaC);


figure;
plot(t3c,YC,t3c,YYC/100)

%valve position from filtered rotor position
for i=1:length(t1a)
    if abs(YC(i+100000)-3.3)>2.618
        zf(i)=4*sin(sign(YC(i+100000)-3.3)*pi/2);
    else
        zf(i)=4*sin((YC(i+100000)-3.3)*6/10);
    end
end
figure
plot(t1a,YC(100001:150000)-3.3,t1a,zf)


Kt=0.07; %torque constant of the first brush dc motor
Tw=Kt*current.*YYC(100001:150000);%instantaneous torque work
ElossN=sum(current(23500:31000).*current(23500:31000))*4*10^-7
%energy loss on resistance after the current turns negative
ETwN=sum(Tw(23500:31000))*4*10^-7
%torque energy after the current turns negative


%avg power and i2r per 100us
for i=1:100
    for j=((i-1)*500+1):(i*500)
        avgpower(j)=mean(power(((i-1)*500+1):(i*500)));
        avgi2r(j)=mean(i2r(((i-1)*500+1):(i*500)));
        avgTw(j)=mean(Tw(((i-1)*500+1):(i*500)));
        avgcurrent(j)=mean(current(((i-1)*500+1):(i*500)));
    end
end


%avg current per 10us
for i=1:1000
    for j=((i-1)*50+1):(i*50)
        avgcurrent2(j)=mean(current(((i-1)*50+1):(i*50)));

    end
end


%avg power and i2r per 100us
avgpowerDCr=0.8*avgcurrent.*avgcurrent;
ACcurrent=(current-avgcurrent2);
powerACr=31*ACcurrent.*ACcurrent;
for i=1:100
    for j=((i-1)*500+1):(i*500)
        avgpowerACr(j)=mean(powerACr(((i-1)*500+1):(i*500)));
    end
end
figure
plot(t1a,avgpower,t1a,avgpowerDCr,t1b,avgpowerACr,t1c,avgTw);
```

APPENDIX VI SIMULINK® SCHEMATICS FOR EXPERIMENTAL EVALUATIONS

This Appendix contains the SIMULINK® schematics in MATLAB® developed during the whole thesis work for the purpose to evaluate the EMV system experimentally. The schematics include pure closed-loop control, combination control, and pure open-loop control. Again, in the scheme of combination control, it is optional to turn off either the initial open-loop current pulse or the closed-loop control at later stage to implement the pure closed-loop or pure open-loop control independently.

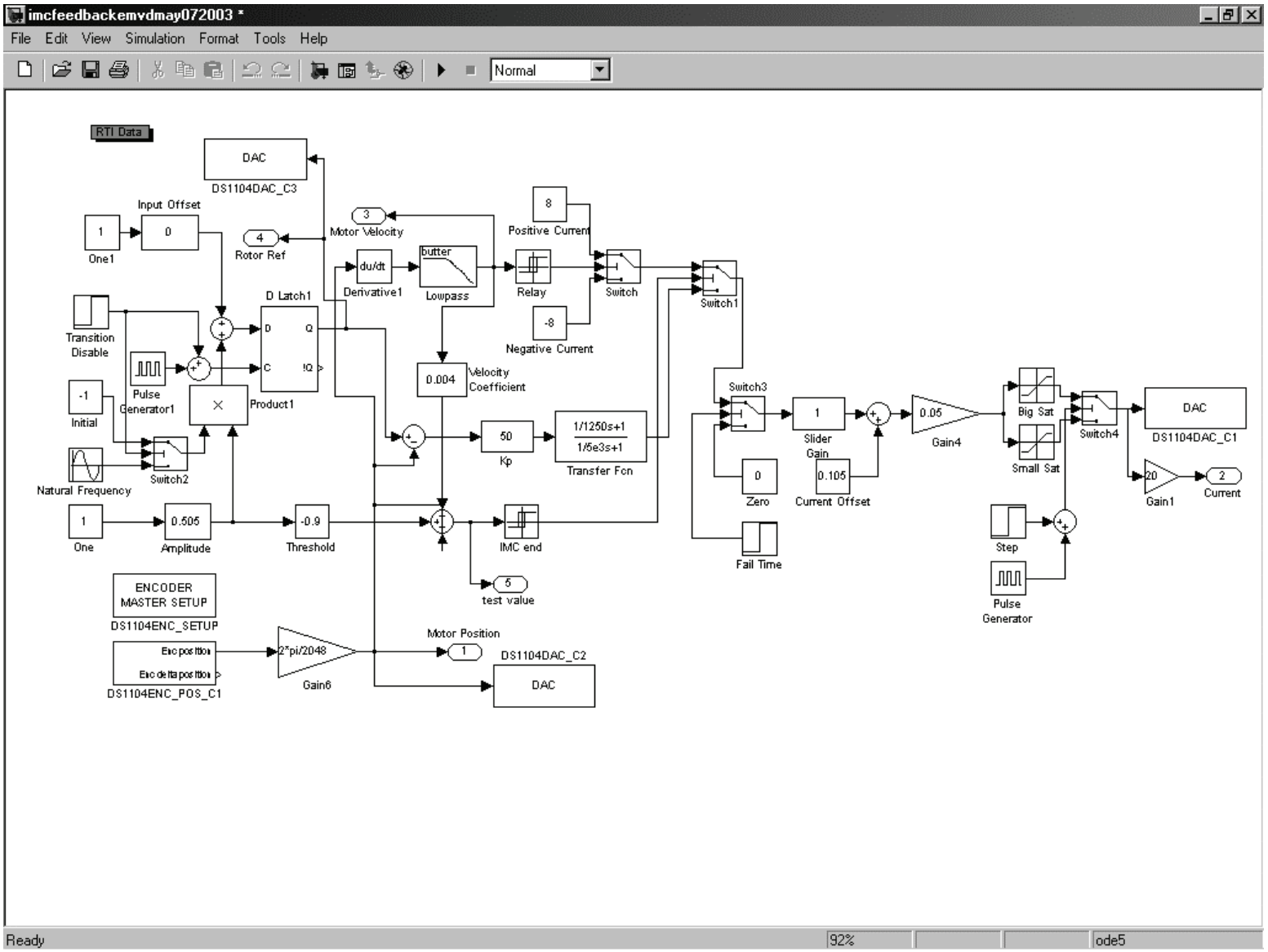

Fig. A6.1. Pure closed-loop control with sinusoidal position reference.

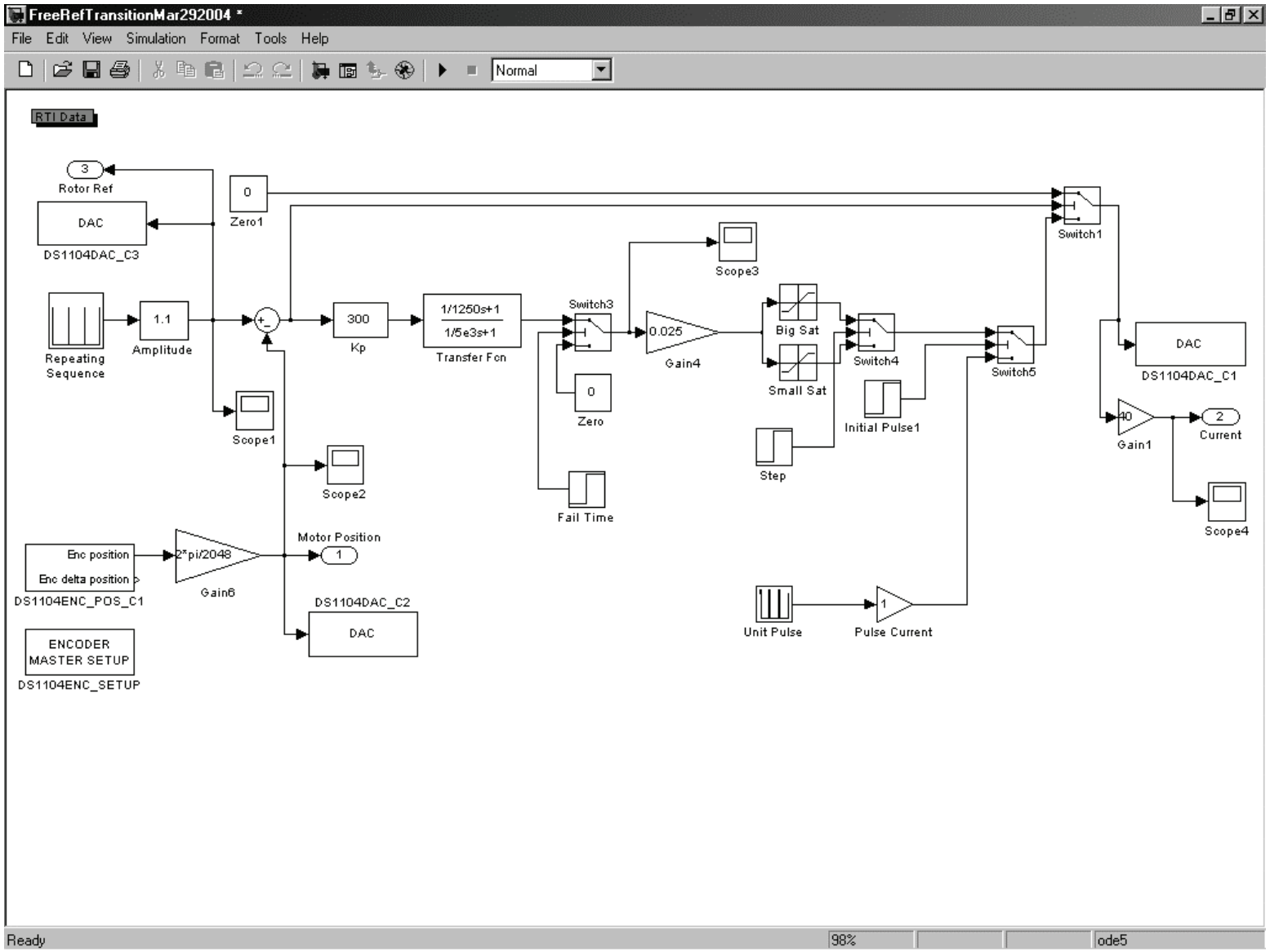

Fig. A6.2. Combination control with free-flight position reference and initial pulse.

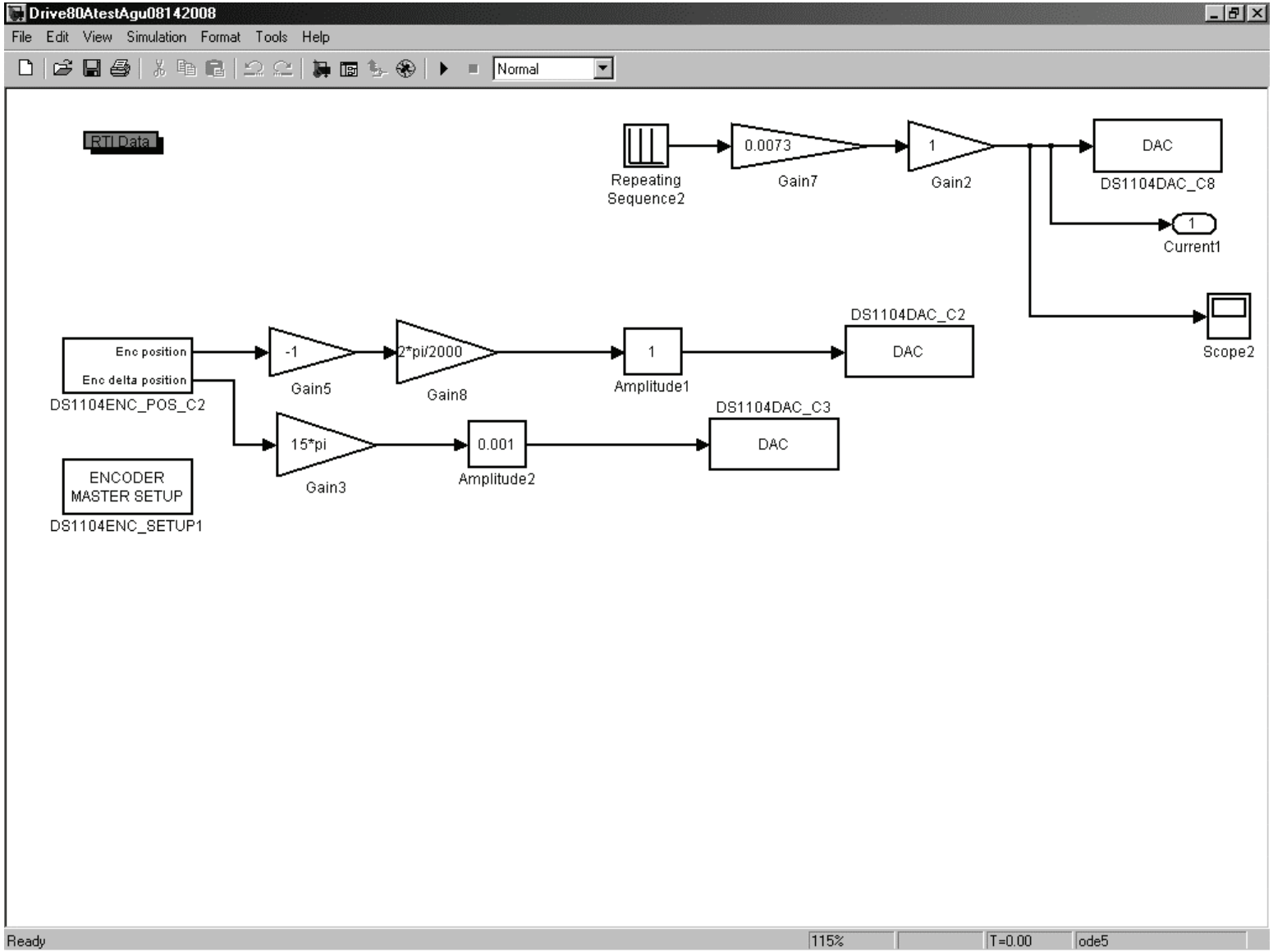

Fig. A6.3. Pure open-loop control with a current pulse.

REFERENCES

[1] M. B. Levin, and M. M. Schlecter, "Camless Engine", *SAE Technical Paper Series*, Paper 960581, 1996.

[2] P. Barkan, and T. Dresner, "A Review of Variable Valve Timing Benefits and Modes of Operation," *SAE Technical Paper Series*, Paper 891676, 1989.

[3] T. Ahmad, and M. A. Theobald, "A Survey of Variable-Valve-Actuation Technology," *SAE Technical Paper Series*, Paper 891674, 1989.

[4] M. Pischinger, et. al., "Benefits of the Electromechanical Valve Train in Vehicle Operation," *SAE Technical Paper Series*, Paper 2001-01-1223, 2001.

[5] C. Tai, et. al., "Increasing Torque Output from a Turodiesel with Camless Valve Train," *SAE Technical Paper Series*, Paper 2002-01-1108, 2002.

[6] M. Sellnau, and E. Rask, "Two-Step Variable Valve Actuation for Fuel Economy, Emissions, and Performance," *SAE Technical Paper Series*, Paper 2003-01-0029, 2003.

[7] G. B. Parvate-Patil, et. al., "An Assessment of Intake and Exhaust Philosophies for Variable Valve Timing," *SAE Technical Paper Series*, Paper 2003-32-0078, 2003.

[8] R. Steinberg, et. al., "A Fully Continuous Variable Cam Timing Concept for Intake and Exhaust Phasing", *SAE Technical Paper Series*, Paper 980767, 1998.

[9] F. Pischinger, et. al., "Electromechanically Operating Actuators," *U.S. Patent 4,455,543*, 1984.

[10] F. Pischinger, et. al., "Electromechanical Variable Valve Timing," *Automotive Engineering International*, 1999.

[11] M. Gottschalk, "Electromagnetic Valve Actuator Drives Variable Valvetrain," *Design News*, November 1993.

[12] R. Flierl, and M. Klüting, "The Third Generation of Valvetrains --- New Fully Variable Valvetrains for Throttle-Free Load Control," *SAE Technical Paper Series*, Paper 2000-01-1227, 2000.

[13] S. Butzmann, et. al., "Sensorless Control of Electromagnetic Actuators for Variable Valve Train," *SAE Technical Paper Series*, Paper 2000-01-1225, 2000.

[14] K. Peterson, et. al., "Nonlinear Self-tuning control of Soft Landing of an Electromechanical Actuator," *Proc. 2nd IFAC Conference on Mechatronics Systems*, Berkeley, CA, 2002.

[15] K. Peterson, et. al., "Rendering the electromechanical valve actuator globally asymptotically stable," *Proc. 42nd IEEE Conference Decision and Control*, Maui, HI, Dec. 2003, pp. 1753–1758.

[16] D. Durrieu, et. al., "Electro-Magnetic Valve Actuation System: First Steps Toward Mass Production," *SAE Technical Paper Series*, Paper 2008-01-1360, 2008.

[17] W. S. Chang, "An Electromechanical Valve Drive Incorporating a Nonlinear Mechanical Transformer," *Ph.D. thesis*, Massachusetts Institute of Technology, 2003.

[18] T. A. Parlikar, “Experimental Implementation of an Electromagnetic Engine Valve”, *Master Thesis*, Massachusetts Institute of Technology, 2003.

[19] Y. H. Qiu, et. al., “Design and Experimental Evaluation of Ann Electromechanical Engine Valve Drive,” in *Proceedings of the 35th IEEE Power Electronics Specialists Conference*, pp. 4838-4843, Aachen, Germany, June, 2004.

[20] T. A. Parlikar, et. al., “Design and Experimental Implementation of an Electromagnetic Engine Valve Drive”, in *IEEE/ASME Transaction on Mechatronics*, Vol.10, NO.5, October 2005.

[21] M. Seeman, “Design and Implementation of a Motor Drive Amplifier”, *Bachelor Thesis*, Massachusetts Institute of Technology, 2002.

[22] F. T. Brown, “Engineering System Dynamics”, Marcel Dekker, Inc., 2001.

[23] Y. H. Qiu, et. al., “Limited-angle Actuator for Electromechanical Valve Actuation,” U.S. Patent Application Number 60,911,363, 2007.

[24] W. K. Cheng, et. al., “MATLAB Based Engine Cycle Simulation Package”, *Sloan Automotive Laboratory at MIT*.